The Pennsylvania State University

The Graduate School

Department of Mechanical and Nuclear Engineering

DESIGN AND NONLINEAR FORCE CONTROL OF A POWER-BY-WIRE PIEZOELECTRIC-HYDRAULIC PUMP ACTUATOR FOR AUTOMOTIVE TRANSMISSIONS

A Dissertation in

Mechanical Engineering

by

Gi-Woo Kim

Submitted in Partial Fulfillment
of the Requirements
for the Degree of

Doctor of Philosophy

May 2009

The dissertation of Gi-Woo Kim was reviewed and approved* by the following:

Kon-Well Wang
Adjunct Professor of Mechanical Engineering
Dissertation Advisor
Co-Chair of Committee

Chris Rahn
Professor of Mechanical Engineering
Co-Chair of Committee

Mary Frecker
Professor of Mechanical Engineering

George A. Lesieutre
Professor and Head of Aerospace Engineering

Karen A. Thole
Professor of Mechanical Engineering
Head of the Department of Mechanical and Nuclear Engineering

*Signatures are on file in the Graduate School

ABSTRACT

In this dissertation research, a new concept of actuation system and corresponding control method are developed for automotive automatic transmission (in short, AT) shift control.

A piezoelectric-hydraulic pump (in short, PHP) based actuation system can be one of the potential alternatives that can replace a current electro-hydraulic actuation system for an automatic transmission friction element such as a band brake. In this dissertation, a stand-alone prototype of the PHP actuator is synthesized with the new concept of power-by-wire actuation, with a primary emphasis on the development of required performance for AT shift control. The fundamental performance of a prototype PHP is evaluated through the measuring of the flow rate and dead-head pressures. In addition, both the effects of a Helmholtz resonator and a fluid effective bulk modulus on the performance are experimentally examined.

Next, a nonlinear sliding mode controller is developed for actuation force tracking control of the piezoelectric-hydraulic pump based actuation system. With a derived governing equation of motion of the PHP-band brake actuation system, a simple but effective switching control law is synthesized based on the sliding mode theory for the given nonlinear system. To demonstrate the effectiveness of the proposed controller, its force tracking performance for a smooth engaging of friction elements during the AT 1 → 2 up shift is validated experimentally. In addition, implementation method using a two-level driver that is appropriate for a pulse-driven actuator is established. It not only can successfully track the desired force trajectory for AT shift control with small tracking

error, but also provides a new opportunity for pressure control of fluid power systems, eliminating three traditional hydraulic components: oil pump, regulating valve, and control valve. These promising results demonstrate the potential of the PHP actuator as a new controllable actuation system for AT friction elements.

Finally, the PHP actuator and controller are applied to the automatic transmission shift control scenario to examine the effectiveness of the new power-by-wire actuation concept. To do this, a real time automotive power train model is first synthesized to develop the simulation model for hardware-in-the-loop simulation. Only power on 1 → 2 up shift model using band brake as on-coming friction element and one-way clutch as off-going friction element is provided for evaluating the single actuator performances. In addition, both fill volume control to prevent over-fill and the desired force trajectory learning control for AT shift controller are designed to achieve the enhanced shift performance. With the real time power train model and the PHP actuator, the whole structure of HILS is constructed, and its successful use in the development of AT shift control system is presented to demonstrate the feasibility and benefits of using the new PHP actuator.

TABLE OF CONTENTS

LIST OF FIGURES

LIST OF TABLES

NOMENCLATURE

A	cross section area of PZT stack
A_1	ram (effective) area of head side in double-acting hydraulic cylinder
A_2	ram area (effective) area of rod side in double-acting hydraulic cylinder
A_p	diaphragm area
A_o	orifice area
A_R	orifice area of reed valve
b	damping constant
C	capacitance, Hydraulic compliance
C_d	discharge coefficient for orifice flow
c	specific heat of PZT stack
c_1,c_2	damping constant of return spring and band brake
c_p	damping constant of PZT stack transducer
c_R	damping constant of reed valves
d_{33}	piezoelectric constant
e	tracking error
F_a	actuation force
F_e	external forces
F_f	friction force
$F_{d,}\dot{F}_d$	desired force and derivative of desired force
f, f_c	pulse (driving) and control frequency
G_c	control flow gain

G_l leakage flow gain

I current

I_{sub} inertia of subscript

K Lipschitz constant

K_e effective hydraulic spring rate

K_r opening gain of reed valve

K_g control gain

k conductivity of PZT stack

k_1, k_2 spring rate of return spring and band brake

k_p stiffness of PZT stack transducer

k_R **s**tiffness of reed valves

m effective mass of hydraulic cylinder

m_p effective mass of PZT stack transducer

m_R effective mass of reed valve

n number of multilayered PZT stack transducer

P_1 actuation pressure

P_2 accumulator pressure

P_p pumping pressure

ΔP pressure difference

Q_o discharge (outlet) flow rate

Q_i suction (inlet) flow rate

Q_l leakage flow rate

Q_c control flow rate

s	Laplace operator
T_p	pulse duration time
T_{sub}	torque of subscript
$T(r)$	temperature of PZT stack
t	thickness
t_p	pulse period time
t_d	delay time
t_1 $t_{2,}$	start and finish time of feedback control interval
u	switching control input
V_t	voltage
$V_i(f)$	control input voltage with pulse frequency f
V	volume
V_o	control volume of head side in double-acting cylinder
V_c	control volume of pumping chamber
w	orifice area gradient
$x, \dot{x}$	displacement (stroke) and velocity of hydraulic cylinder
x_o	pre-loaded length of return spring
$x_p, \dot{x}_p$	displacement (stroke) and velocity of PZT stack transducer
x_s	dead (fill) stroke
x_R	opening displacement of reed valves
Y_E	piezoelectric admittance
Z	impedance
Z_c	characteristic impedance

Z_E	piezoelectric impedance
Z_M	mechanical impedance
α, η	strictly positive constant
β_e	effective bulk modulus of working fluid
ψ	final gear ratio
τ	time constant
ρ_c	density of hydraulic oil
ρ	density of PZT stack
ω_{sub}	angular velocity of subscript
$\omega(k)$	sampled angular velocity
ζ	damping ratio

ACKNOWLEDGEMENTS

I am very pleased to have this opportunity of extending my best gratitude, first of all, to my thesis advisor Dr. Kon-Well Wang for his mental guidance, teaching efforts, and financial support throughout my Ph. D program. I am also very grateful to Dr. Chris Rahn, Dr. Mary Frecker, and Dr. George A. Lesieutre for their serving as my doctoral committee members. In particular, I would like to express my thanks to Dr. Rahn for his encouragement about my late Ph. D pursuing.

I also would like to express my sincere appreciation to Dr. Yuji Fujii, Gregory M. Pietron, James W. McCallum, Robert O. Bukhart, Seung-Hoon Lee at the Ford Scientific Research Laboratory and Dr. William E. Tobler (retired) for the ceaseless sponsoring and valuable discussion. My lab colleagues also have been helpful for completing my Ph. degree. In addition, I might not be able to finish my experimental work without assistance of all staffs, especially machinist Philip.

My heartfelt thanks extend to my father, mother, and all of my family members. Without their persistent support and understanding, I would not have been completed Ph. D program. Finally, I would like to share my achievements with my lovely two sons, Gyu-Won and Jun-Won.

Chapter 1

Introduction

1.1 Background and Motivation

Over the past decades, there has been the growing demand for cost-effective, highly efficient, and reliable automotive power train. The transmission, especially an automatic transmission (in short, AT), is a key element in a power train, which plays a pivoting role in satisfying the higher consumer expectations for high-performance vehicles [Deiss et al., 2006]. Hence, significant research efforts have been performed and various innovative technologies have been explored to reduce the cost and improve the reliability, shift quality and fuel economy of automatic transmissions [Zongxuan and Hebbale, 2005]. In particular, the actuation system for engaging friction elements (e.g., band brakes and clutches) is a critical component to ensure good shift quality and high fuel economy [Turner et al., 2004 and Cao et al., 2004]. For actuating the friction elements, current actuation systems in AT consist of many electro-hydraulic components, such as the rotor type oil pump, the pressure regulating valve and pressure control valves including solenoid valves such as the variable force solenoid (in short, VFS) and pulse width modulation (in short, PWM) solenoid. Because of these many components, the electro-hydraulic control circuit for AT can be very complicated, as shown in Figure **1-1**.

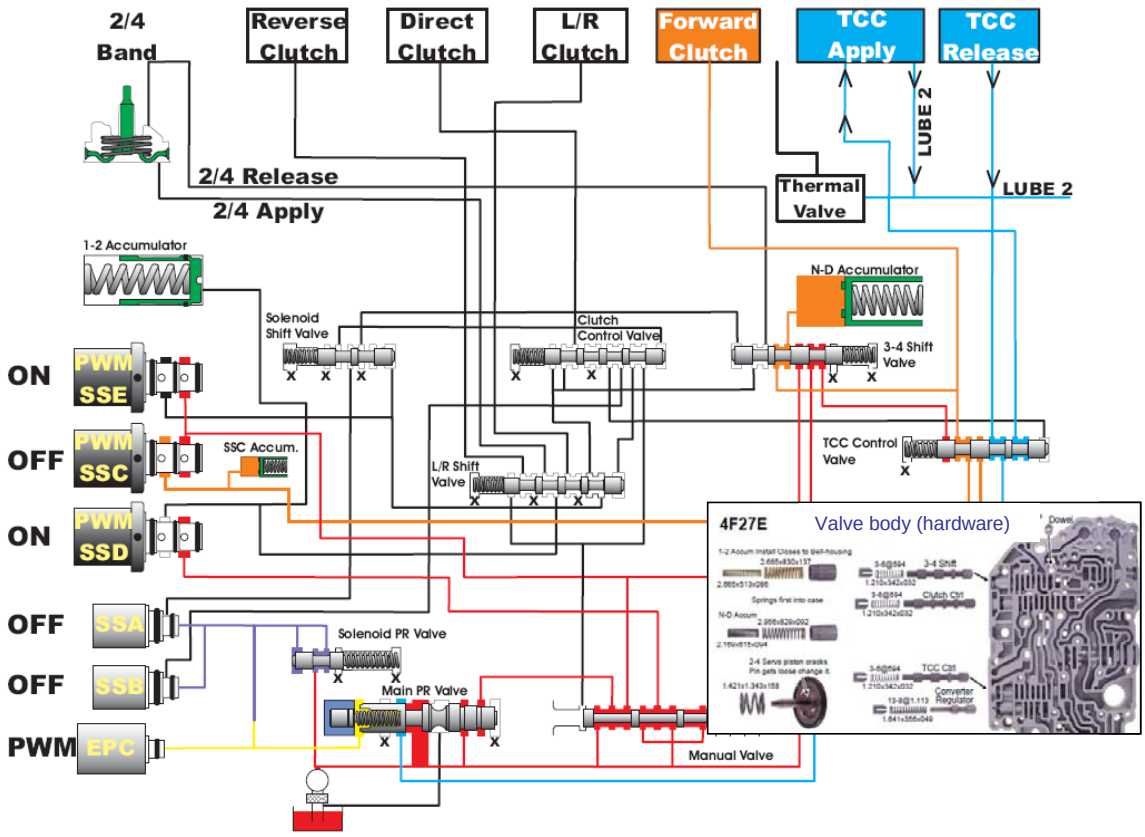

Figure 1-1: Typical hydraulic control circuit for D-1 position [Ford Motor Co., 2006]

In general, the structure of traditional hydraulic control circuits illustrated in Figure **1-1** consists of two main parts: the central hydraulic power unit (i.e., the engine, rotor type oil pump, and pressure regulating valve) and the electro-hydraulic control/actuation system (i.e., valve body). The schematic of a conventional electro-hydraulic actuation system is illustrated in Figure **1-2**. This structure also requires distributed transmission lines to connect the actuation system with each friction element, requiring fluid passage in the transmission case or fluid pipes. As a result, it negatively affects the product size and manufacturing cost of the AT. The actuation pressure is modulated through two processes in current electro-hydraulic actuation systems. The

inlet flow rate from the oil pump is first regulated by the exhausting flow through the regulating valve. This regulated pressure is also controlled by the exhausting flow through the control valves with solenoid valves. It is obvious that this pressure regulating and control method using the continually exhausting flow can negatively affect the size of oil pump. Furthermore, while current AT friction element actuation systems have been operational, it has been recognized that they have the following technical limitations for enhanced performance:

(a) The oil pump (3 kg to 5 kg) and valve body (7 kg to 10 kg) are relatively heavy.

(b) The energy loss is mainly due to the engine-driven oil pump.

(c) The electro-hydraulic actuator does not provide high precision controllability.

It is obvious that the fuel economy of engine will be affected by items (a) and (b). Item (c) will negatively affect the shift quality.

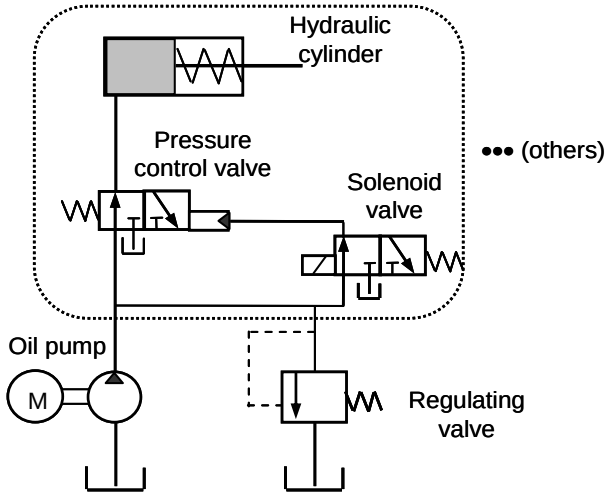

Figure 1-2: Schematic of conventional electro-hydraulic actuation (control) systems

1.2 Literature Review

To address the aforementioned problems, alternative actuation systems featuring simpler structure and compact size have been introduced recently to replace the current complex electro-hydraulic actuation systems. This section describes previous and current studies relevant to the development of these alternative actuation systems.

Numerous smart materials-based systems have been recently synthesized with particular focus on the development of innovative actuators incorporating smart materials such as piezoelectric materials, electro/magneto-rheological (in short, ER/MR) fluids, and shape memory alloys (in short SMA) [Chopra, 2002]. One of the promising applications featuring smart materials is a direct clutch/brake system, with the elimination of traditional auxiliary actuation systems. For instance, a proportional drum brake actuated by PZT stack was developed by using compliant-mechanism-based transmission device as shown in Figure **1-3** [Gogola and Goldfarb, 1999]. They achieved 180 N-mm level of braking torque with a voltage input of 200 Volts. Despite its enhanced controllability, using smart materials, however, has still many technical limitations such as small stroke of piezoelectric material based actuators and particle segmentation of ER/MR fluids.

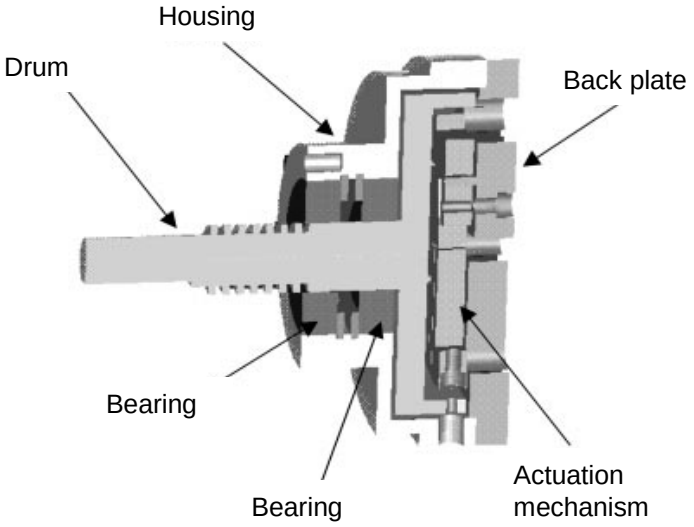

Figure 1-3: A proportional drum brake actuated by PZT stack [Gogola and Goldfarb, 1999]

Recently, a high force electromechanical linear actuator for automated manual transmissions was developed to satisfy the force requirement of 1 kN over a 16 mm stroke, as shown in Figure **1-4**. Using such devices for actuating friction elements, however, has critical disadvantages such as low power density due to the heavy permanent magnets.

Figure 1-4: A high force electromechanical linear actuator [Turner et al., 2006]

A two stage actuation system by combining classical actuators (e.g., DC motors) and piezoelectric actuators was recently developed for controllable brakes and clutches, as shown in Figure **1-5**. Using this hybrid type high-bandwidth actuator, the large actuation force by a PZT stack actuator (3.5 kN) was achieved within the short fill time by the motors. This hybrid concept extended to the development of a hydraulic-piezoelectric actuator for positioning control systems with large stroke achieved by a hydraulic cylinder and high accuracy obtained by PZT stacks [Chiang et al., 2005]. However, electric motors feature relatively low power density, which is a critical drawback for automotive and aerospace applications.

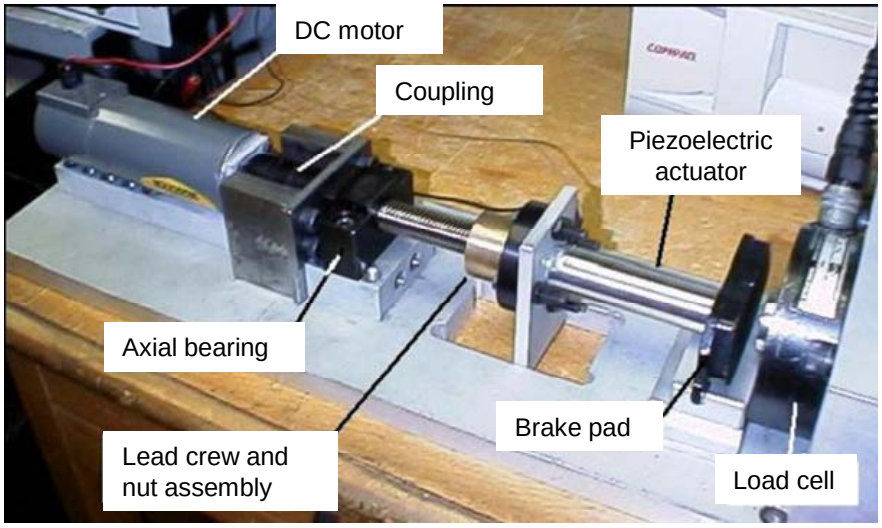

Figure 1-5: Two stage actuation system [Neelakantan et al., 2005].

Another potential hybrid alternative is to utilize a piezoelectric-hydraulic pump (in short, PHP). The main idea of the piezoelectric-hydraulic pump is to combine the advantages of piezoelectric transducers (i.e., high power density and large load authority) and hydraulic systems (i.e., large stroke and large actuation force). Therefore, it is highly

possible to satisfy both performance requirements (i.e., large stroke and large actuation force). Furthermore, it features high power density with low weight compared with conventional actuators, as shown in Figure **1-6**.

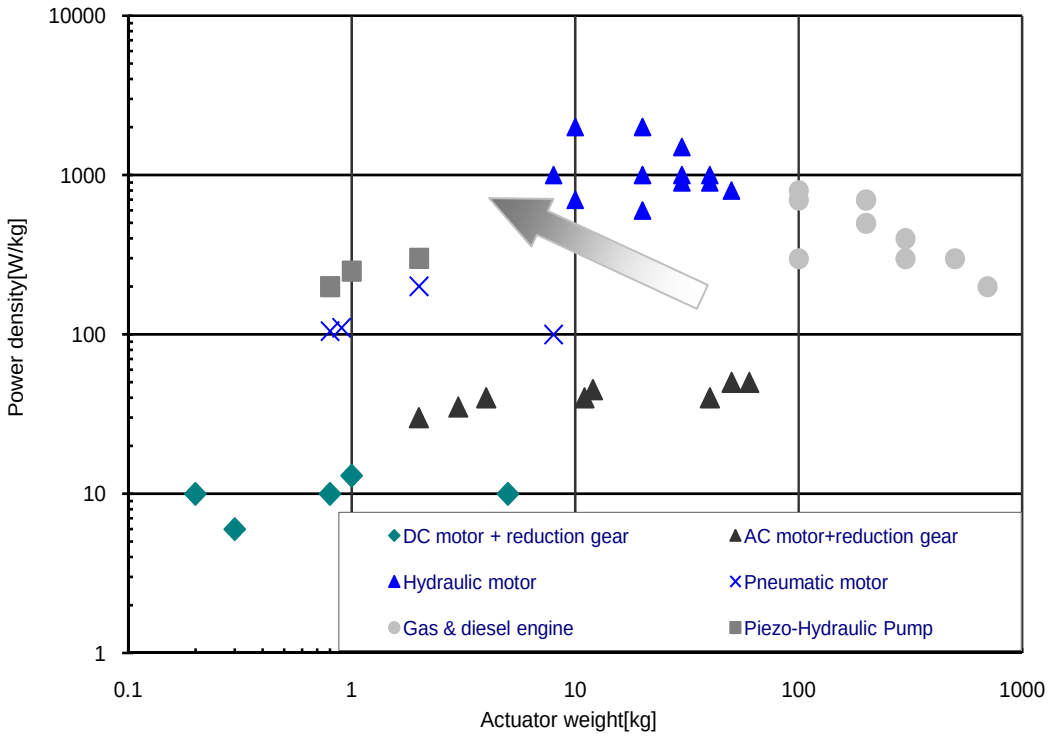

Figure 1-6: Power density vs. actuator weight of various conventional actuators and piezoelectric-hydraulic pump [Hirose et al., 1989]

In the last decade, several prototypes of the piezoelectric-hydraulic pump based actuators have been introduced by researchers. Konishi et al. [1993] have developed the first macro-scale piezoelectric-hydraulic pump using a piezoelectric stack actuator, and recognized that using a flexible diaphragm in the pumping chamber could increase its output and reduce the bandwidth. Mauck and Lynch [1999, 2000] developed various versions of new actuation systems consisting of a piezoelectric-hydraulic pump driven by

a high voltage piezoelectric stack (1000 Volt) and hydraulic cylinders, and achieved the maximum 7.25 cc/s flow rate and 271N blocking force under 800 Volt, 350 psi accumulator pressure and 60 Hz. Nasser et al. [2000] identified the effect of the pre-charge using an accumulator on the reducing of friction in the commercial hydraulic cylinder. Oates et al. [2000, 2001] developed a dynamic model to identify bandwidth limitations. Sirohi et al. [2001, 2003] drove the co-fired type piezo stacks at higher frequencies to more effectively utilize their high power using their customized driver. The no-load flow rate was achieved by the 2.2 cc/s at 300 Hz, 50 psi accumulator pressure. In addition, they replaced the ball-type check valves with reed valves to extend the bandwidth of the one-way valves. A multi-stage reed valve is also incorporated to improve the bandwidth of passive reed valves [Janen et al., 2003].

To overcome the limitations of passive one-way valves, active check valves have been investigated by some researchers [Lee et al., 2004]. They developed a pump that consists of a piezoelectric stack actuator and two piezoelectric unimorph disc valves acting as one-way valves. Based on Lee's research, in-house passive check valve arrays fabricated using MEMS technology were developed to improve the performance of conventional passive check valves [Tieck et al., 2005]. At operating frequency of 150 Hz and accumulator pressure of 80 psi, about 0.91 cc/s flow rate was achieved. Chapman et al. [2005] developed three compact, low cost piezo-hydraulic pumps using the co-fired type piezoelectric actuators. However, the achieved maximum flow rate (6scc/s) was similar with their earlier versions. Novel techniques utilizing resonance were also introduced by some researchers [Park et al., 1999, and Keller, 2004].

Recently, researchers and engineers have built on these previous research efforts and investigated the possibility of using piezoelectric-hydraulic pumps in a wide range of industries. For instance, Choi et al. [2005] demonstrated the applicability of an actuator driven by piezo-hydraulic pump for a positioning system. A MEMS valves based high performance PHP (piezoelectric-hydraulic pump) system was developed by Kinetic Ceramics [O'Neill, 2007]. The performance of this system was successfully tested in a remotely piloted flight vehicle. Aerospace engineers have attempted to develop piezoelectric material based pumps for the new trailing edge flaps or morphing wing systems on airplanes [Yoo et al., 2003, Lhermet et al, 2006, and Sneed et al., 2007].

1.3 Problem Statement and Research Objectives

While the potential of piezoelectric-hydraulic pump based actuators has been recognized, it is not clear that such devices can be synthesized and effectively controlled for automotive applications. As illustrated in Figure **1-7**, typical piezoelectric-hydraulic pump based actuation systems are still bulky and complex, for they consist of various mechanical components such as a gas accumulator, a hydraulic cylinder, and control valves. Therefore, the main objective of this research is to build upon previous studies and to explore the feasibility of synthesizing a self-contained piezoelectric-hydraulic pump based actuation system, with primary focus on achieving the required performance for AT shift control. To achieve this aim, a compact piezoelectric-hydraulic pump should be first developed.

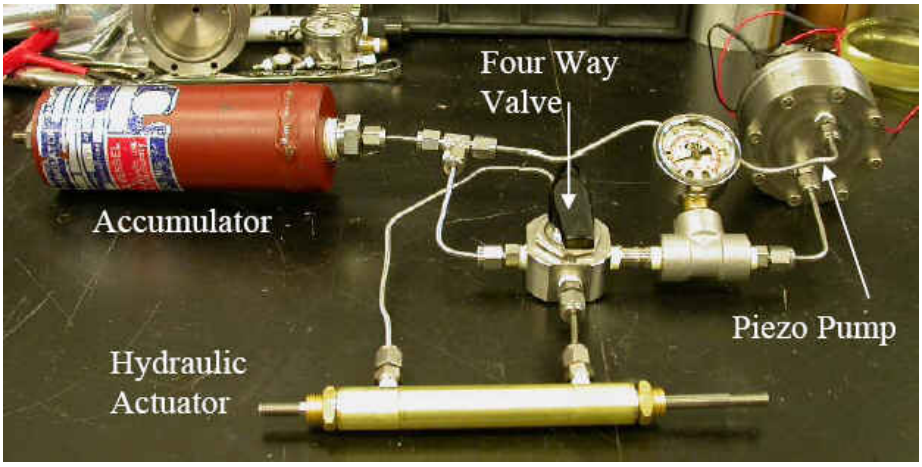

Figure 1-7: Piezoelectric-hydraulic pump based actuation system [Keller, 2004]

With a compact stand-alone PHP-based actuator, the new actuation concept of a power-by-wire system is suggested, as shown in Figure **1-8**. Compared with conventional electro-hydraulic actuation systems, this concept allows for distributed power-by-wire operation through the independent piezoelectric-hydraulic pump based actuator. It is obvious that this system can replace the conventional electro-hydraulic control system with the compact piezoelectric-hydraulic pump actuator controlled by electronic control systems. Hence, traditional hydraulic components such as the engine-driven oil pump, control valves and fluid lines can be eliminated. The additional practical advantages are the elimination of exhausting flow and the on-demand actuation system, and more flexibility in installation, as opposed to conventional systems.

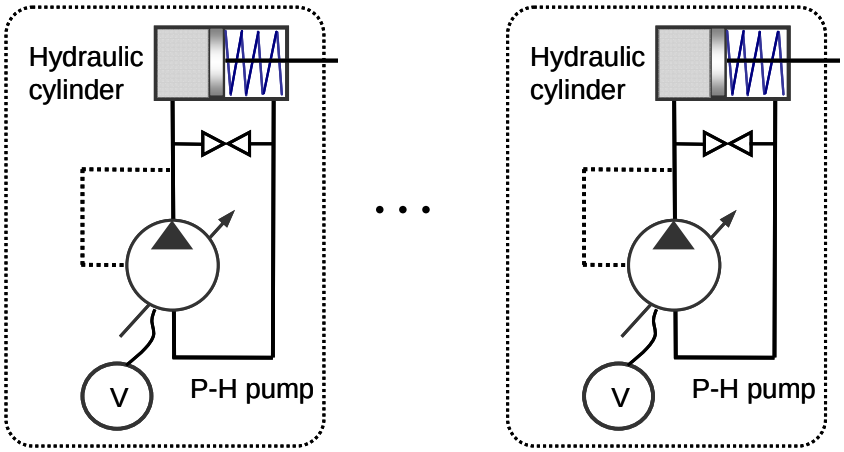

Figure 1-8: New concept of actuation system featuring power-by-wire drive

The piezoelectric-hydraulic pump based actuator, however, should satisfy the performance requirements for actuating current friction elements before the establishment of this new conceptual actuation system. In this thesis, the band brake is first selected as the test-bed friction element. Figure **1-9** shows the typical band brake and servo system that is still widely used in current AT due to its relatively superior packaging capability and the large torque capacity [Cao et al., 2004 and Gu et al., 2006]. Most AT friction elements have dead stroke due to the gap between components. In case of the 4-speed AT for low input torque capacity, it is in the range of 3 mm to 4 mm. As a result, considerable flow rate is required to fill up this cylinder volume. Figure **1-10** shows the digital mock-up model for band brake actuation system with completely developed piezoelectric-hydraulic pump.

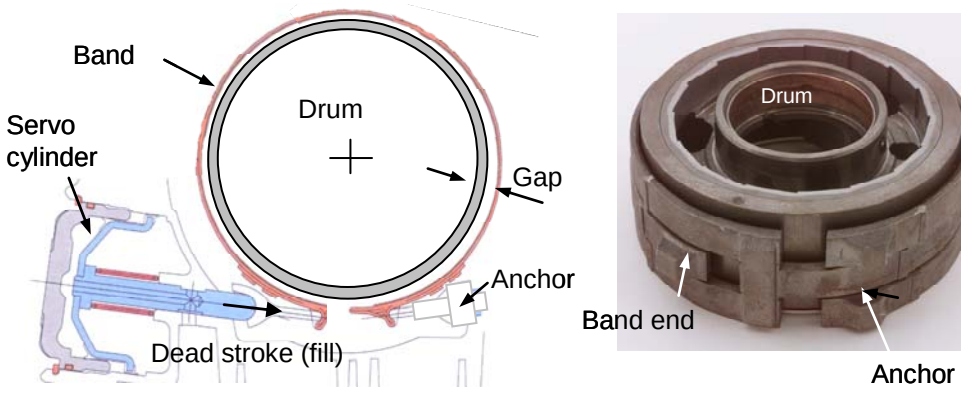

(a) schematic (b) band brake assemble

Figure 1-9: The configuration of the band brake and servo system used in Ford AT

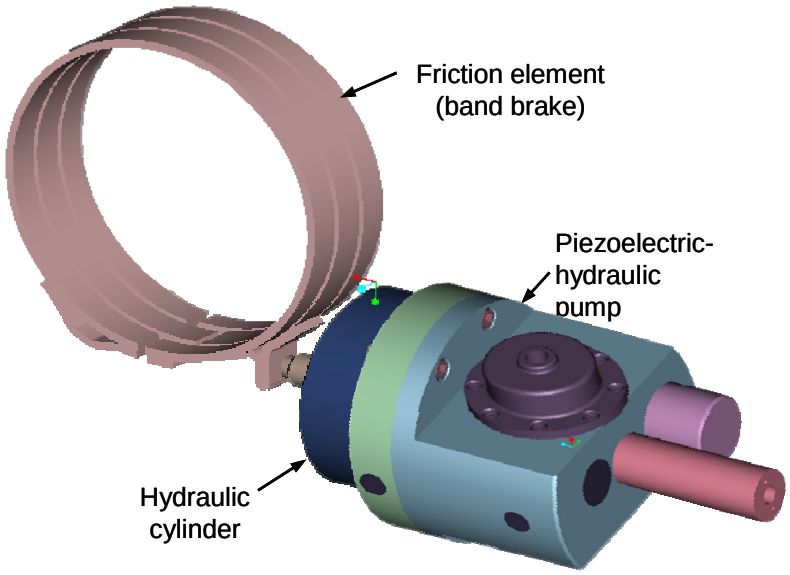

Figure 1-10: Digital mock-up model for band brake actuation system using PHP actuator

For simplicity, only the power-on 1 → 2 up shift of a Ford 4-speed AT for passenger car is first considered in this research. In this Ford AT, the engaging friction

element, which is the on-coming member related with a new speed ratio, is the band brake. The disengaging friction element, which is off-going member related with current speed ratio, is the one-way clutch (overrunning clutch) that has the automatic synchronizing ability. The typical power/on 1 → 2 up shift procedure of an AT using band brakes and one-way clutch is illustrated in Figure **1-11** [Fujii et al., 2002]. The shift event can be divided into three phases: the fill, torque and inertia phase. During the fill phase, the pump flow rate should be sufficient to ensure a short fill that should be finished within 0.3 seconds. The actuation pressure gradient should be controlled so that the transient output (shaft) torque can be changed smoothly in the inertia phase. After finishing the shift, the applied pressure should be higher than the required engaging pressure to prevent the slippage of the band brake.

Based on the above discussion, some of the nominal performance levels that the actuation system needs to provide for AT band brake control can be identified as follows:

(a) To achieve the desired fill time, the corresponding required flow rate should be approximately in the range of 20 cc/s with the servo cylinder of 50 mm bore size.

(b) To ensure a complete shift, the required actuation force should be controlled in the range of 600 N and the required actuator authority should be in the range of 1 kN to lock the band brake.

(c) To guarantee improved shift quality, actuation force has to be controlled since the output torque heavily depends on the actuation pressure profile.

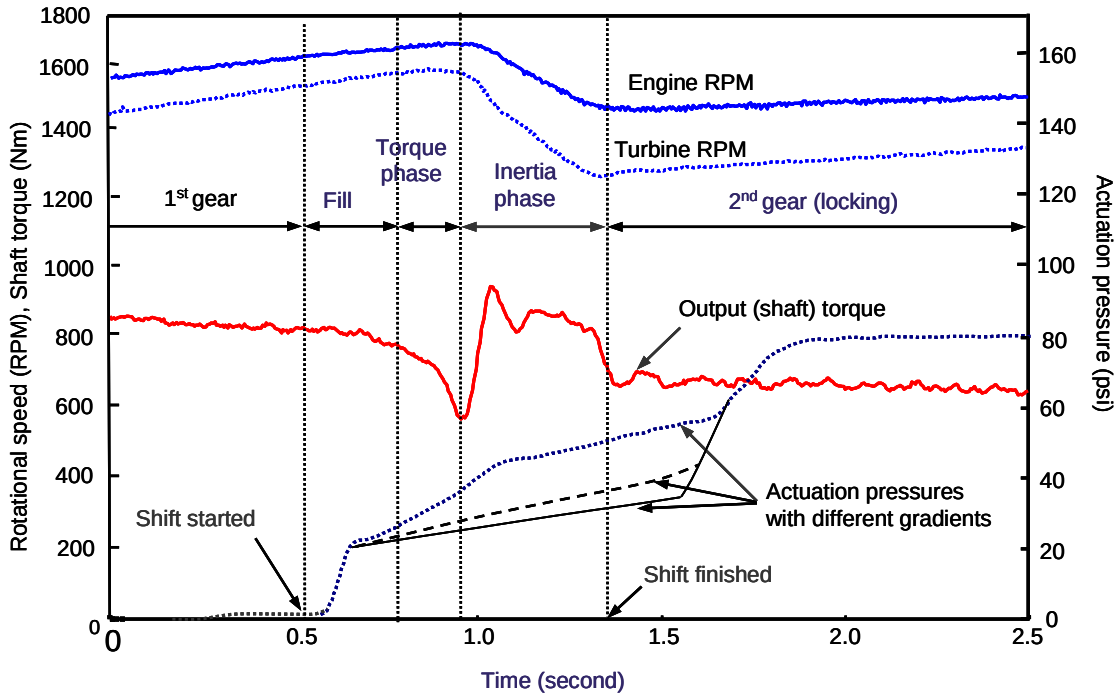

Figure 1-11: Typical power on 1→ 2 up shift of AT using one-way clutch and band brake

1.4 Overview of Dissertation

The major tasks of this thesis are identified to be the development of prototype actuation system, nonlinear force tracking control of the piezoelectric-hydraulic pump based actuator, and its application to 1 → 2 shift control of AT application. The thesis organization is described in detail as follows:

In Chapter **2**, the development of a prototype actuation system is presented. This chapter provides the design, fabrication and performance evaluation of the prototype in detail. The key performance index of pump systems, flow rate and dead-head pressure, are experimentally evaluated and improved through the design modifications. Next, a

nonlinear controller for tracking the desired actuation force is synthesized based on the sliding mode theory; the controller design and implementation is presented in Chapter **3**. Simulation efforts are also presented to confirm the effectiveness of the proposed controller. In Chapter **4**, the application of PHP actuator is extended into an AT test-bed to validate the effectiveness of the new power-by-wire actuation concept. Both nonlinear sliding mode control for force tracking of the PHP actuator and hardware-in-the-loop simulation (in short, HILS) are performed to demonstrate the potentials of the PHP actuator. A power train system model is developed and presented in detail. The model is utilized to synthesize the real time simulation process for HILS. Finally, the research efforts and main contributions of this thesis investigation are summarized in Chapter **5**. Recommendations for future research are also provided.

Chapter 2

Design and Performance Investigation of Piezoelectric-hydraulic Pump Actuator

This chapter is organized in five sub sections. In Section **2.1**, key characteristics of piezoelectric-hydraulic pump are described. The detail design of the piezoelectric-hydraulic pump based actuator, which includes the characteristics of the piezoelectric transducer is described in Section **2.2**. In addition, the fundamental property of working fluid, effective bulk modulus, is discussed in Section **2.3**. The results of performance evaluation and enhancements are presented and summarized in Section **2.4** and Section **2.5**, respectively.

2.1 Characteristics of Piezoelectric-hydraulic Pump

2.1.1 Positive Displacement Type Pump

In fact, piezoelectric-hydraulic pump is a positive-displacement type pump that causes a fluid to move into the discharge side by trapping a fixed amount of it, which is known as displacement. According to the method for moving a fluid, types of positive-displacement pumps can be classified as reciprocating, metering, and gear pumps [Karassik et. al., 2001]. Figure **2-1** shows the typical gear (rotor) type oil pump, which is commonly used in automotive industry. As illustrated, the ratio of maximum trapped

volume (V_{max}) to minimum volume (V_{min}) is generally 30 to 50. This large ratio will enable us to generate the sufficient negative pumping pressure for suction.

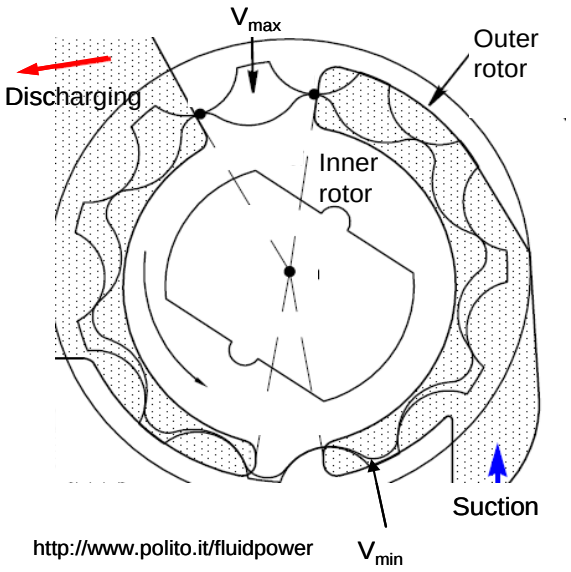

Figure 2-1: Volume variation of typical internal gear (rotor) type oil pump

Figure **2-2** shows the working principle of the piezoelectric-hydraulic pump. Compared to conventional reciprocal type pumps, the difference is the driving method of diaphragm. With piezoelectric material based transducers, the fast stroking with high frequency is possible. In case of suction, the relatively large pressure difference between pumping chamber and inlet port is required to suction due to the inertia of inlet one-way valve. Contrary to the general positive type pumps, the ratio of maximum trapped volume (V_{max}) to minimum volume (V_{min}) is, however, nearly one due to the small strain of PZT stack transducer ($50 \sim 90\ \mu m$), which is too small to generate the negative pressure for sufficient suction. Accordingly, using accumulator pressure is an essential component to increase initial pumping pressure in piezoelectric-hydraulic pump.

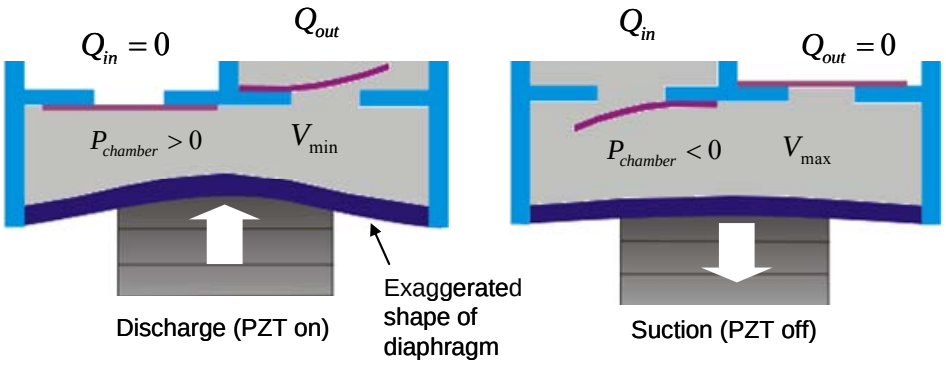

Figure 2-2: Working principle of piezoelectric-hydraulic pump

2.1.2 Inchworm Motion Principle

Another feature of piezoelectric-hydraulic pump is inchworm motion due to the one-way valve action, as shown in Figure **2-3**. Due to the inchworm principle with high frequency, small strain of PZT stack can rectify into the large stroke (theoretically infinite). Average gradient stands for the flow rate and increases linearly with frequency.

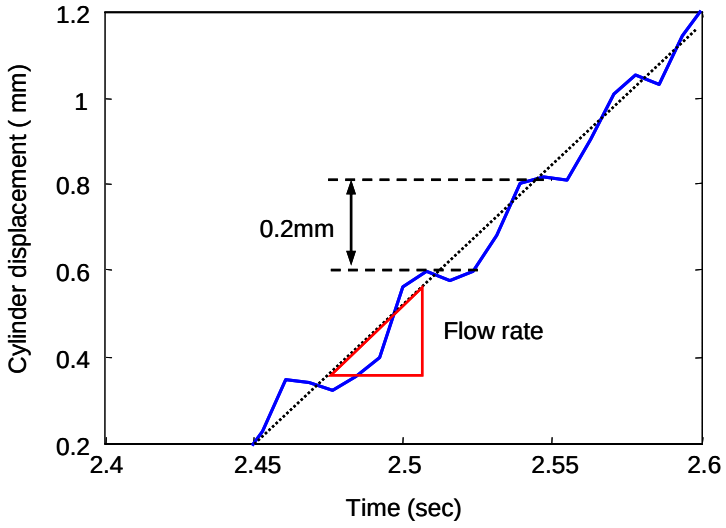

Figure 2-3: Typical measured inchworm stroke (cylinder displacement)

2.1.3 Mechanical Transmission

As shown in Figure **2-4**, intermediate working fluid in PHP actuator can be acted as the linear mechanical transmission during one cycle of pumping operation, assuming that the working hydraulic oil is an ideal incompressible fluid. Based on this assumption, the stroke of PZT stack can be estimated from measured cylinder displacement using the area ratio of pumping diaphragm to cylinder piston. For instance, if the area ratio is 0.25 and measured cylinder displacement per cycle is 0.2 *mm* illustrated in Figure **2-3**, the stroke of PZT stack can be roughly estimated by $50\,\mu m$, which represents the stroke amplification mechanism (mechanical advantage). Accordingly, the net output work per one cycle will be depends on the intermediate hydraulic fluid part. However, output power increases linearly with driving frequency, the level of driving voltage, and accumulator pressures. Transmission mechanism also becomes complicated if there is a hydraulic spring rate due to the fluid effective bulk modulus.

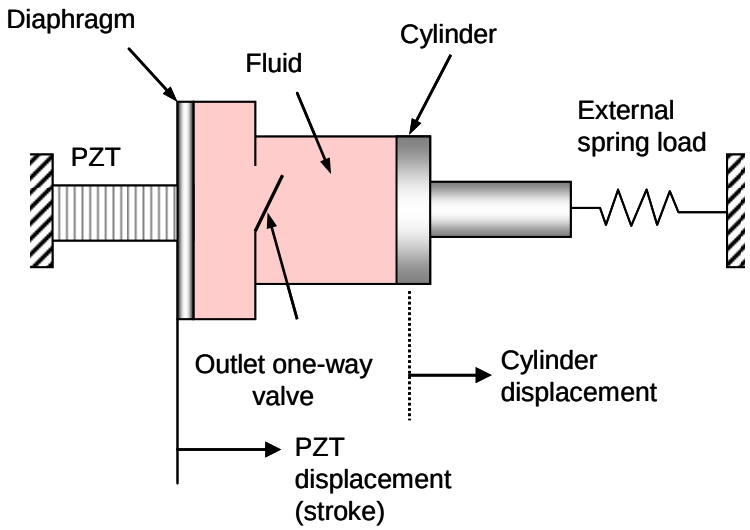

Figure 2-4: Linear mechanical transmission (stroke amplification) in PHP actuator

2.2 Design of Stand-alone Piezoelectric-hydraulic Pump Actuator

In this section, the design of PHP actuator is described in detail. Then, the fundamental performances of PZT stack transducer and new driving topology is presented. A fabricated self-contained prototype actuator is also illustrated in the last sub-section.

2.2.1 Shift Control-oriented Hydraulic Circuit

A shift control-oriented hydraulic circuit with the piezoelectric-hydraulic pump is first designed for AT shift control, as shown in Figure **2-5**. The gas accumulator is primarily used to provide pumping function. In addition, it provides various essential functions, which include cavitation prevention, pre-loading to PZT stack transducer, and improvement of the dead head pressure. A hydraulic transmission line is connected to the chambers on both sides of the double-acting hydraulic cylinder to cancel out the initial actuation force caused by the accumulator pressure. A PZT stack transducer generates the fast oscillating stroke by the input control voltage with high frequency. With the stroke of the PZT stack, the alternating pumping pressure is generated by the changing of chamber volume. Two reed valves will convert this alternating action into one way flow through the opening and closing operations of reeds. Because of the incompressibility of fluid, the piston of hydraulic cylinder will move with large stroke. Fluid line will be pressurized immediately after stroking. The band brake will be eventually engaged by this generated actuation pressure force.

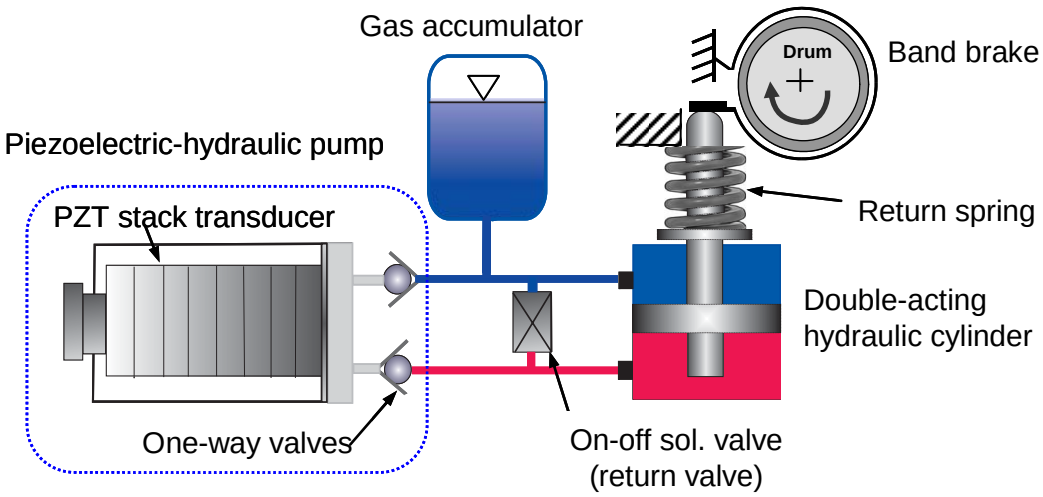

Figure 2-5: Schematic of shift control-oriented hydraulic circuit for piezoelectric-hydraulic pump based band brake actuation system

For AT shift control, there should be three operation modes: the engaging mode, the locking mode, and the disengaging mode, as illustrated in Figure **2-6**. The actuation pressure can be controlled by modulating the driving frequency of the PZT stack transducer in the engaging mode (engaging mode). Because of the incompressibility of the small amount of fluid and the sealing by one-way check valve, the cylinder piston will be locked until the actuation pressure is released, although the driving voltage for PZT stack transducer is off (locking mode). Since the bi-directional control action is not required for AT shift control, the normally closed type on-off solenoid valve is incorporated for releasing of the actuation pressure. With this return valve opened, the two pressures become equal and the piston will be returned by the return spring force (disengaging mode).

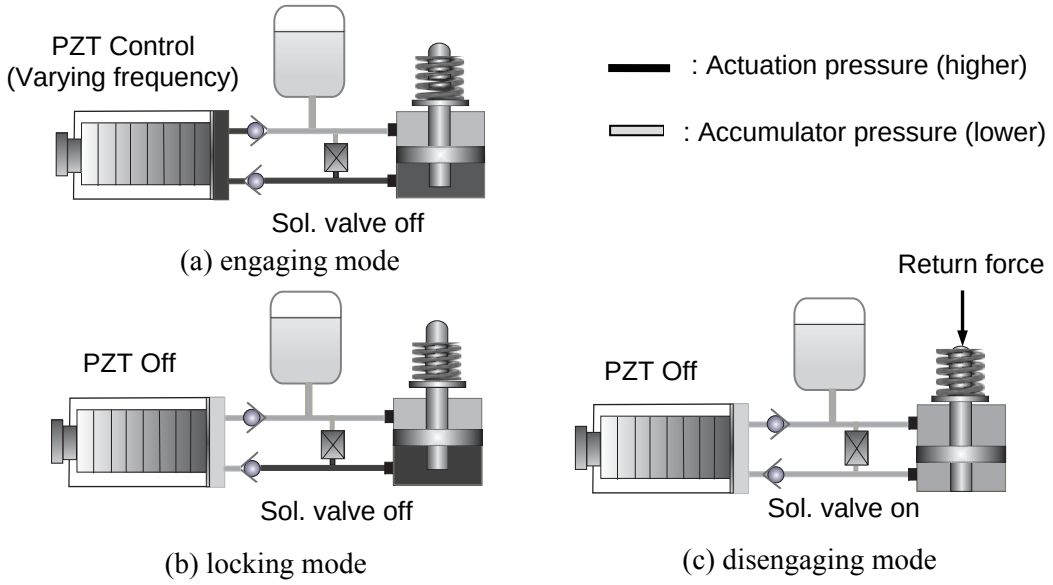

Figure 2-6: Three operation modes for piezoelectric-hydraulic pump based actuator

Based on the compactness requirement, self-contained hardware configuration for prototype is designed, as illustrated in Figure **2-7**. It consists of two main parts: upper valve body and lower valve body.

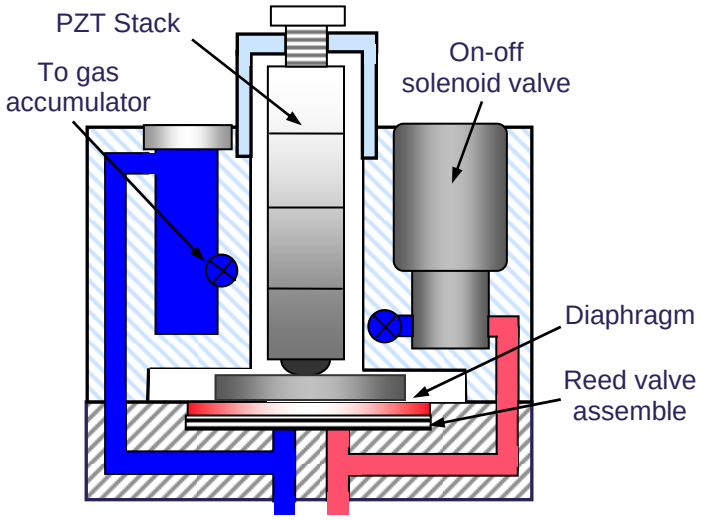

Figure 2-7: Hardware configuration of stand-alone type piezoelectric-hydraulic pump

2.2.2 Main Components

2.2.2.1 Diaphragm

A pumping diaphragm (ϕ 0.053m) is a key component for flexible stroking in positive displacement type pump. It is fabricated by using blue tempered & polished spring steel (C1095, t = 0.1 mm), since this alloy features the combination of maximum fatigue limit and the highest tensile stress. Fatigue limit can be calculated by stress-life method using S-N curve and following equation

$$\frac{\Delta S}{2} = S_f^{'}(N^f)^b \qquad (2.1)$$

where ΔS is stress amplitude (i.e., max. Von Mises stress at $80\,\mu m$), $S_f^{'}$ and b are the intercept and the slope in Figure **2-8**. Fatigue limit of 281 MPa is validated to be higher than maximum Von Mises stress (171 MPa) at 9×10^9 cycles (150 Hz X 30,000 shift times). As a result, spring steel can be used for diaphragm within fatigue limit cycles.

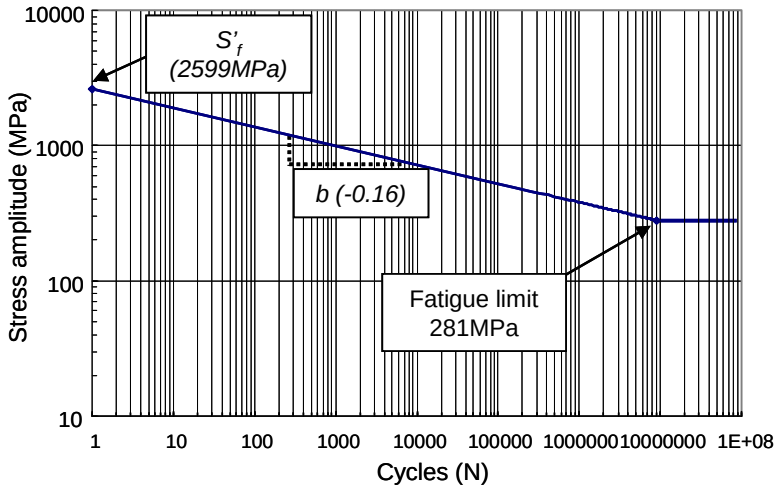

Figure 2-8: Stress-life method for fatigue analysis of spring steel reed using S-N curve

2.2.2.2 Gas Accumulator

The compactness requirement rules out the option of using standard commercial gas accumulators. Miniature gas accumulator using bead type rubber diaphragm is designed instead of them. Gas volume (approximately 2.8e-5 m^3) can be easily filled with Nitrogen gas or compressed air through the gas valve, as shown in Figure **2-9**.

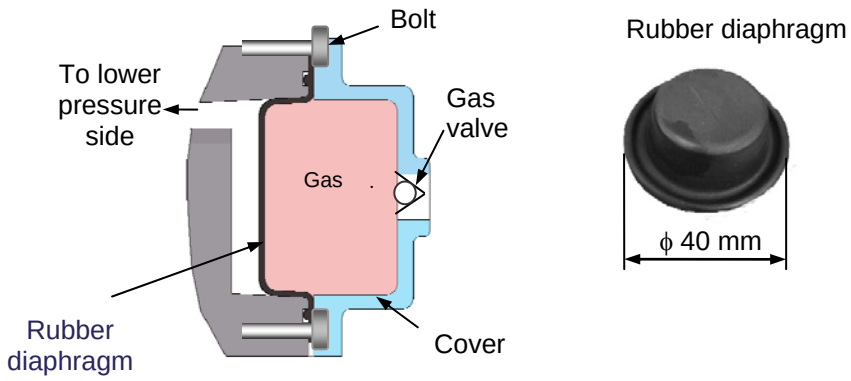

Figure 2-9: Cutaway of miniaturized gas accumulator and rubber diaphragm

2.2.2.3 One-Way Valve

Of the three feasible types of one-way valve (i.e., check valve, reed valve, and active valve), a reed valve is employed in this PHP-based actuator since it has more broad bandwidth than check valve, and simpler structure than active valve using piezoelectric materials. Like diaphragm, two reed valves are made up of blue tempered & polished spring steel (C1095, t = 0.1 mm), as shown in Figure **2-10** . In order to operate a pumping system at a frequency range of 200 Hz, the reed valves should have a natural

frequency above 200 Hz. The valves can be assumed to be a cantilevered beam clamed at one end. Then, their 1st natural frequency can be estimated by following equation

$$\omega_1 = \frac{3.52}{2\pi}\sqrt{\frac{EI_r}{m_r L^3}} \tag{2.2}$$

where m_r is the reed mass, E is the Young's modulus of reeds, L is the length, and I_r is the inertia of reed valve can be defined by

$$I_r = \frac{b_r t^3}{12} \tag{2.3}$$

In the above equation, b_r is the width of the reed valve, and t is the thickness. Using this equation, dimensions are determined by 7.5 mm (b_r) x 14 mm (L) x 0.1mm (t) to be have the 1st natural frequency of 390 Hz. According to a finite element analysis (FEA) using ANSYS, the maximum Von Mises stress (171 MPa) turned out to be lower than the yield strength of 590 MPa [Norton, 2000] at opening displacement of 79 μm, as shown in Figure **2-11**. Fatigue limit of reed turned out to be nearly same as that of diaphragm.

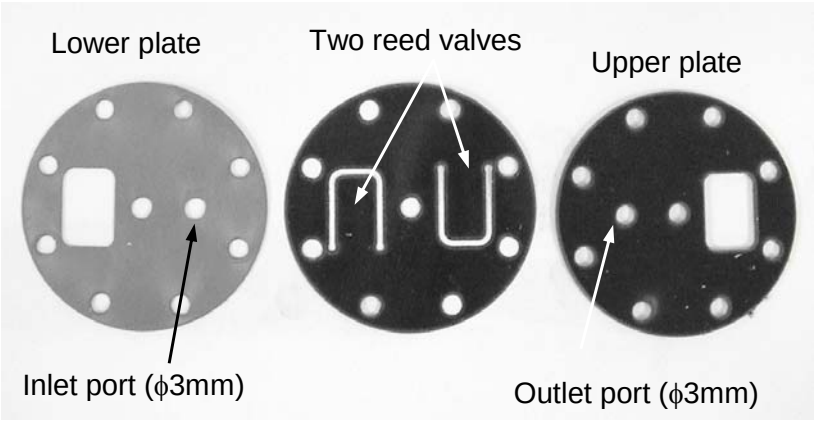

Figure 2-10: Configuration of reed valve assembly

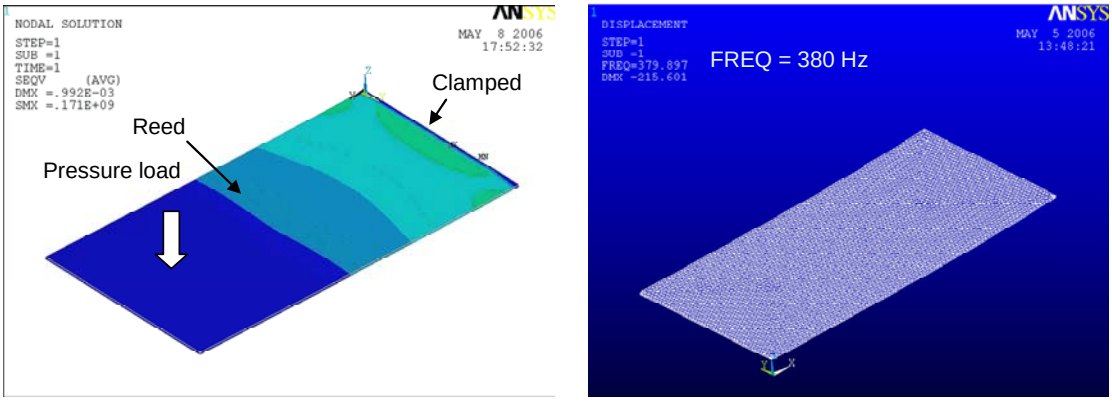

(a) stress (b) modal

Figure 2-11: Finite element analysis (FEA) result of reeds

2.2.3 PZT Stack Transducer

A co-fired type PZT stack (model: APC PSt150, 81 mm, 10 mm X 10 mm) is used as piezoelectric transducer in the PHP actuator, as illustrated in Figure **2-12**. There should be some important considerations for mounting in piezoelectric transducer applications. The clamping is first of all not recommended. Instead of clamping, surface contacting using round caps are used to decouple the unexpected bending moment. In addition, the PZT stack transducer should be aligned axially using urethane form retainer to prevent the excessive stress concentration due to the imperfection. To facilitate rapid cooling of PZT stack, the retainer is eliminated in the middle of PZT stack and many ventilation holes are drilled out in the PZT stack housing.

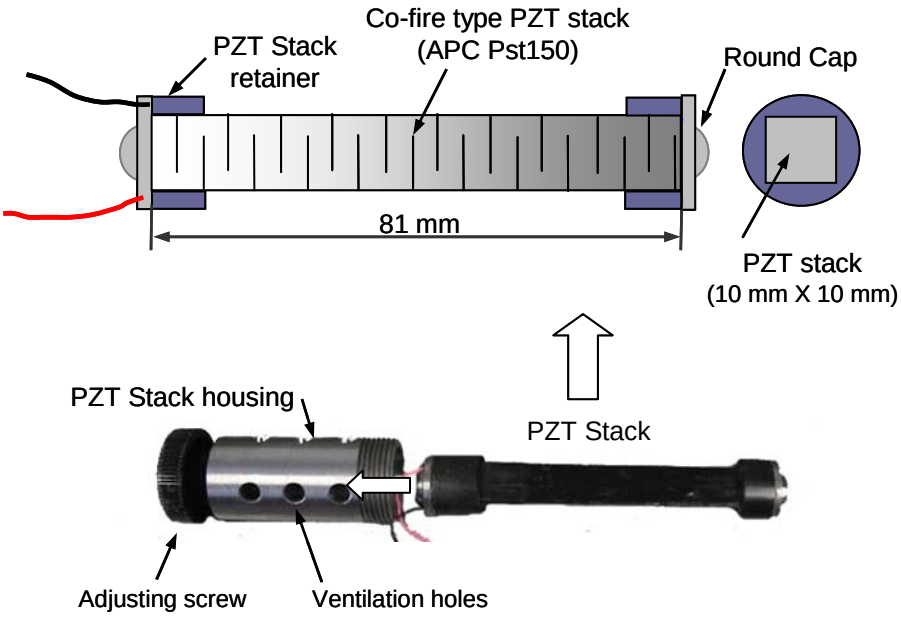

Figure 2-12: Configuration and photograph of PZT stack transducer assemble

2.2.3.1 Free Stroke and Block Force

According to the performance test results performed by product vendor, the PZT stack can achieve a free stroke of 90 μm when maximum 150 Volt is applied, as shown in Figure **2-13** . Using the test result for the 30 Volt line and its free stroke, the maximum block force is estimated by 20 kN as shown in Figure **2-14**. Typically, the mechanical energy transfer efficiency from the PZT stack transducer into the external system (i.e., pumping chamber) can be maximized under the impedance matching condition. Accordingly, the stiffness of external loads due to the accumulator pressure is designed as nearly same as the stiffness of PZT stack ($230\,N/\mu m$). As a result, the final

effective stroke is achieved around 50 μm. This preloading also can prevent the failure of PZT stack largely due to the excessive tensile stress [Yury et al., 2007].

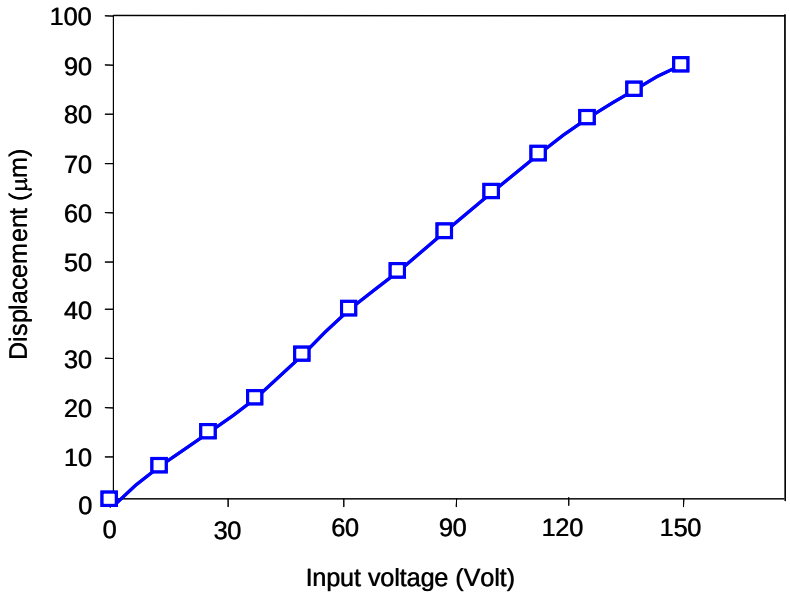

Figure 2-13: Characteristic curves for the PZT stack: Input voltage vs. displacement

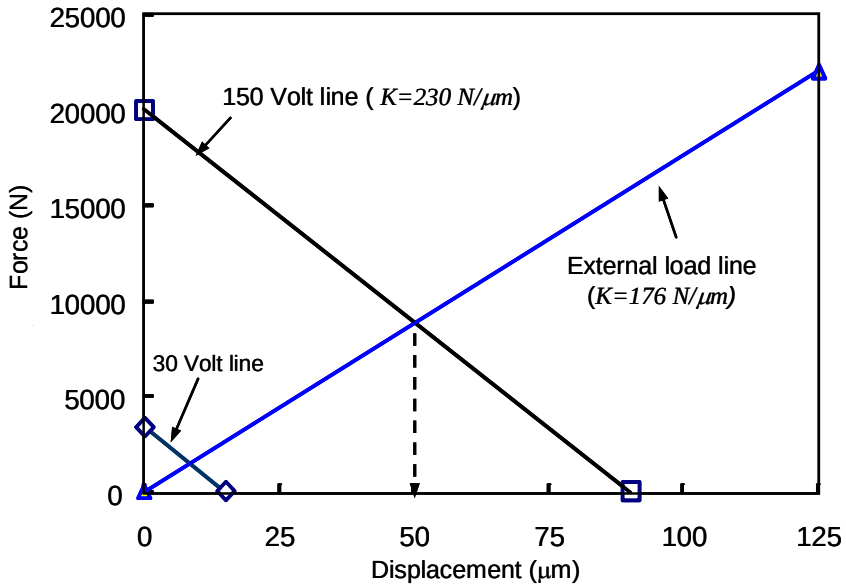

Figure 2-14: Characteristic curves for PZT stack transducer: Displacement vs. force

2.2.3.2 PZT Stack Driver

A piezoelectric material itself is a capacitor, which has the purely reactive impedance so-called capacitance. The measured capacitance of the PZT stack transducer illustrated in Figure **2-12** is approximately 30 μF due to the relatively long length (large volume) of PZT stack. This large capacitive load of PZT stack should be fully compensated for the efficient driving of PZT stack [Lindner, 2001]. Figure **2-15** shows the characteristic curve of conventional linear power amplifier for various capacitive loads. In the case of the 30 μF loads, the output voltages are dropped around 60Hz because of the current limitation of the linear amplifier (maximum average current of 0.4 A). This voltage dropping significantly affects the flow rate performance of piezoelectric-hydraulic pump, since it heavily depends on the stroke of PZT stack.

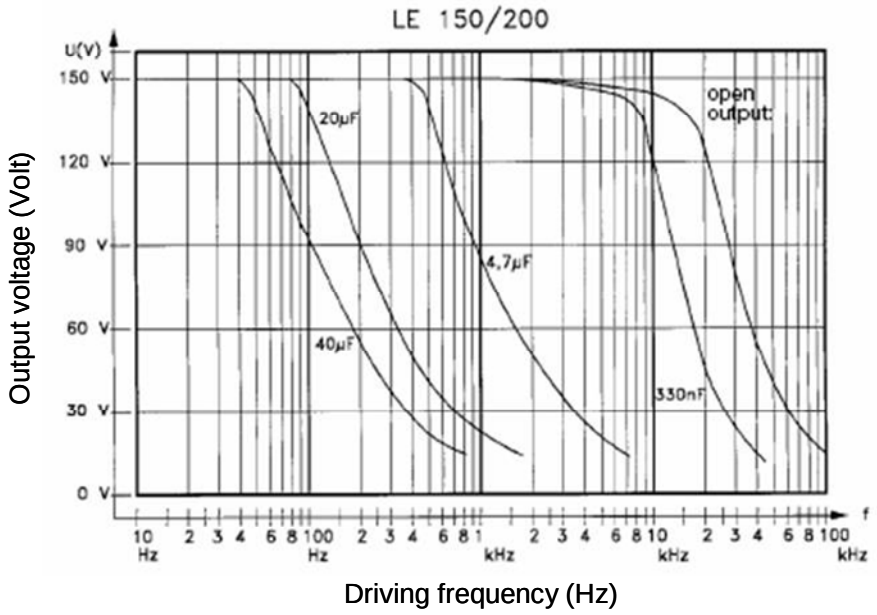

Figure 2-15: Peak output voltage vs. driving frequency for various capacitive loads of linear amplifier [Piezomechanik GmbH, Model: LE 150/200]

Typically, the required peak current capacity for compensating capacitive loads can be calculated as follows:

$$I = 2\pi f \cdot C \cdot V_{peak} = \pi f \cdot C \cdot V_p \tag{2.4}$$

where f is driving frequency (200 Hz), C is the measured capacitance ($30\,\mu F$), V_p is sinusoidal AC voltage (120 Volt). Then, the required peak current is estimated to be approximately 2.3 A in this application. However, the linear power amplifier that can fully compensate this large capacitive load has many practical disadvantages such as huge size and low efficiency. In order to overcome these technical limitations, the new driver that has different driving topology is required. Accordingly, a two-level driver is customized in this research, as shown in Figure **2-16**. This driver switches large capacitive loads between low level (e.g., -10 Volt to 0 Volt) and high level (e.g., 120 Volt to 150 Volt) in the short circuit. Thus, the TTL (transistor–transistor logic) pulse with 0 to 5 Volt is required to trigger the two-level driver. This driver provides the sufficient peak current required to produce extremely fast rise/fall times and to operate at high frequencies. With this circuitry, the wave shape of output will be pulse with quasi-sinusoidal rising and falling edges. Note that when you drive a PZT transducer with the two-level driver, there is typically a fairly high peak current, but this only occurs for a short period of time. In other words, although the PZT stack transducer needs 2 amps of current, but only draws it 10% of the time, which means the average current would still be less than 0.5 amps. Therefore, compared with conventional linear power amplifier or switching amplifier, the efficiency of this driver is relatively higher, and its overall size is more compact, which are more appropriate for automotive applications.

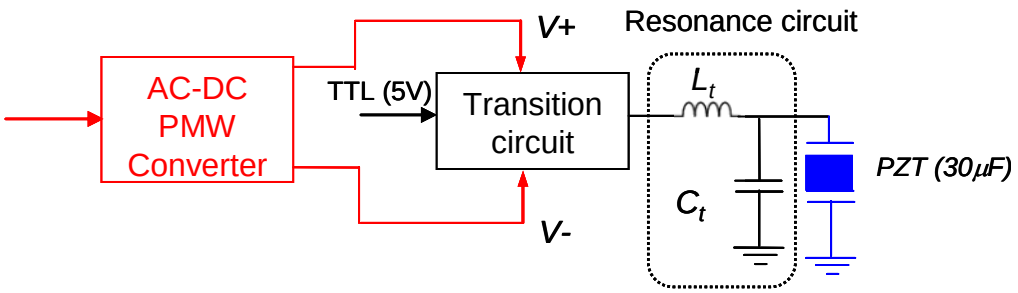

(a) block diagram of circuitry [Dynamic structure and materials LLC].

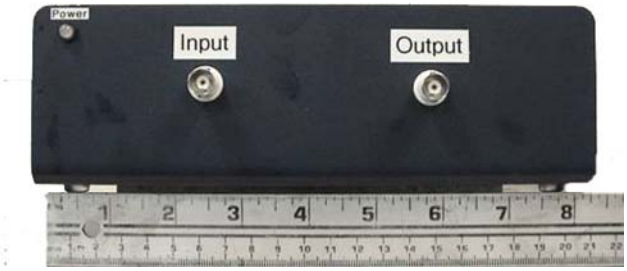

(b) photograph of driver

Figure 2-16: Customized two level driver for driving of PZT stack transducer with large capacitive loads

2.2.3.3 Self-induced Temperature Rise of PZT Stack

Typically, piezoelectric materials show the capacitive behavior under dynamic excitation conditions. One inevitable consequence of this dynamic excitation is the dissipative power loss, which will be converted into the thermal energy within the piezoelectric materials that in turn lead to the self-induced temperature rise [Zhou and Rogers, 1995]. This characteristic is of considerable concern in such pulse-driven applications as the piezoelectric-hydraulic pump since many parameters and the durability of piezoelectric materials are sensitive to the temperature rise [Mitrovic et al.,

2000]. Accordingly, the temperature rise of PZT stack has to be evaluated before its actual operation. The impedance model for piezoelectric transducer is used to predict this self-induced temperature rise. This piezoelectric impedance is defined as the inverse of the piezoelectric admittance (Y_E) [Chen et al., 1996].

$$Z_E = \frac{1}{Y_E} \tag{2.5}$$

This piezoelectric admittance can be expressed as follows:

$$Y_E = i\omega A((\tilde{\varepsilon}_{33}^T - d_{33}{}^2 \tilde{Y}_P{}^E)\frac{n}{t} + d_{33}{}^2 \tilde{Y}_P{}^E \frac{\tan(k_P \cdot t \cdot n)}{k_P \cdot t^2 (1 + Z_M / Z_P)} \tag{2.6}$$

where k_P is the wave number expressed by

$$k_P = \omega \sqrt{\frac{\rho}{\tilde{Y}_P{}^E}} \tag{2.7}$$

$\tilde{Y}_P{}^E$ is the complex modulus defined by

$$\tilde{Y}_P^E = Y_P^E (1 + \eta_m i) \tag{2.8}$$

The mechanical impedance of the PZT stack (Z_P) is

$$Z_P = -\frac{K_P \cdot k_P \cdot t \cdot n}{\omega \tan(k_P \cdot t \cdot n)} i \tag{2.9}$$

where the static stiffness of the piezoelectric material K_P is

$$K_P = \tilde{Y}_P^E \frac{a}{t \cdot n} \tag{2.10}$$

The complex dielectric permittivity ($\tilde{\varepsilon}_{33}{}^T$) with constant strain (free) is

$$\tilde{\varepsilon}_{33}^T = \varepsilon_{33}^T (1 + \eta_e i) \tag{2.11}$$

In general, the real part of the piezoelectric admittance described in Eq. **2.6** is contributed to the generation of heat of PZT stack. As a result, the relationship between the piezoelectric admittance and the dissipative power (W_D) can be written as follows:

$$W_D = \frac{V^2}{2}\mathrm{Re}(Y_E) \tag{2.12}$$

where V is the applied voltage. Generated heat energy per unit volume can be defined as:

$$Q_{generated} = \frac{W_D}{V_S} \tag{2.13}$$

where V_s is the volume of the PZT stack. According to the conservation law of energy, heat energy balance equation can be obtained as follows:

$$Q_{generated} = Q_{dissipated} + Q_{stored} \tag{2.14}$$

Using heat transfer equation, Eq. **2.14** can be rewritten as follows:

$$Q_{generated} = hA_s(T_{stack} - T_{ambient}) + \frac{d}{dt}(\rho \cdot V_s \cdot c \cdot T_{stack}) \tag{2.15}$$

where h is the convective heat coefficient for the given system, A_s is the surface area of the stack, c is the specific heat of the stack, and ρ is the density of the stack. Figure **2-17** shows an approximated thermal model used for the temperature rise analysis. Steady-state temperature rise can be approximately predicted in Eq. **2.15**. For an infinitely long cylinder of radius *r*, the temperature distributions will be governed as follows:

$$T(r) = T_{amb} + \frac{Q_{generated} r_o^{\,2}}{4k}\left[1 - \left[\frac{r}{r_o}\right]^2\right] \tag{2.16}$$

where k is the thermal conductivity of the PZT stack transducer.

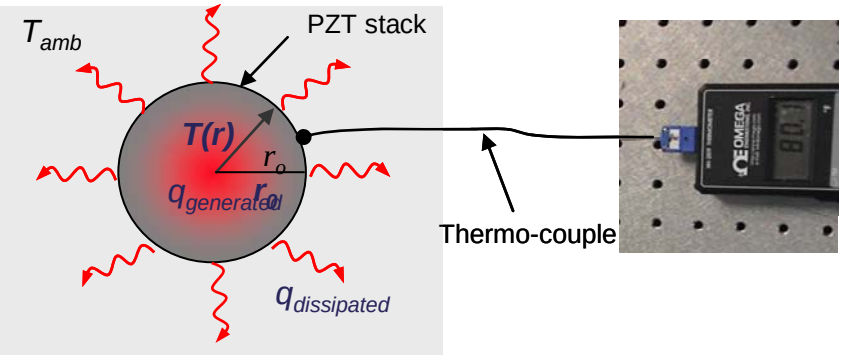

Figure 2-17: Approximated thermal model used for temperature rise of PZT stack

Based on this approximated thermal model, frequency response curve is plotted as Figure **2-18**. These simulation results are compared with test data for 27 mm PZT stack obtained from PZT stack manufacturer [Piezo Systems, Inc.]. The nominal values of parameter for simulation are listed in Table **2-1**. The simulation results at surface of PZT stack are in good agreement with the test results. At the nominal operational ranges (0 to 200 Hz), about 23 °C rise is expected when 100 Volt is applied.

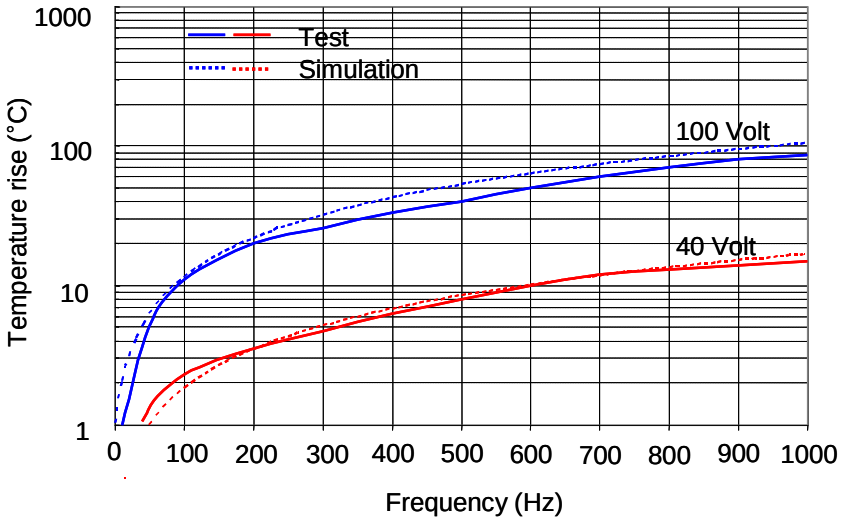

Figure 2-18: Frequency response for temperature rise of PZT stack transducer under dynamic operation conditions.

In order to predict the transient response of PZT stack transducer, the first order transfer function is derived from Eq. **2.15** as follows:

$$T_{stack}(s) = \frac{K \cdot G}{K + s} \tag{2.17}$$

where $K = \frac{h \cdot A_s}{\rho_s \cdot V_s \cdot c}, G = \frac{Q_{generated}}{h \cdot A_s} + T_{ambient}$ In Figure **2-19**, the test result and simulation results for 200 Hz driving frequency are compared. Two results show good agreement at low frequency ranges. As shown, a short operation time (about one minute) is recommended to avoid the steady-state temperature rise. In addition, the temperature rise of the piezoelectric material tends to increase at resonance frequency [Sherrit et al., 2004]. Hence, the normal operational frequency should be within the off-resonant ranges in view of the reliability of PZT stack transducer.

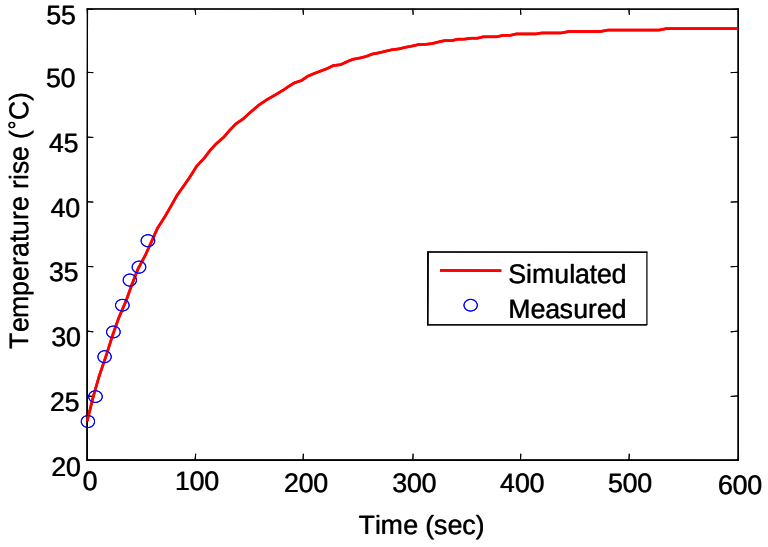

Figure 2-19: Transient response of temperature rise of PZT stack transducer under dynamic operation conditions (100 Volt, 200 Hz, 81 mm PZT stack)

Table 2-1: Material properties and dimensions for predicting of temperature rise

Symbol	Definition	Value (SI)
t	Thickness of layers	500e-6 m
n	Number of layer	162 (81 mm)
A	Cross section area of PZT stack	1e-4 m^2
ρ	Density of PZT stack	7800 kg/m^3
Y^E	Young's modulus of PZT	4.4e10 Pa
η_m	Mechanical loss	0.01(assumed)
ε_{33}^T	Dielectric permittivity	7.7e-7 (F/m)
η_e	Electrical loss	0.01(assumed)
d_{33}	Piezoelectric constant	540e-12 m/V
h	Convective heat transfer coefficient of air	100
c	Specific heat of the PZT stack	380
k	Thermal conductivity of the PZT stack	0.14

2.2.4 Prototype Fabrication

In this research, several versions of prototype were developed based on different hardware configurations. Figure **2-20** illustrates the assemble diagram of the final version of prototype pump and digital mock-up model designed based on the Figure **2-9**. In addition, a compact miniature hydraulic cylinder is customized to reduce the stick-slip friction forces between piston and cylinder using air cylinder since large stick-slip friction force will affect the flow rate performance and force tracking control performance. In order to minimize these friction forces, the tight o-ring in the piston is replaced with low friction U-cup seal and the diameter of piston is also reduced from 20 mm into 8 mm.

The final outlook of prototype pump with compact hydraulic cylinder is illustrated in Figure **2-21.** Its overall length is about 150 mm and weight including hydraulic oil is approximately 0.5 kg. This stand-alone prototype allows us to eliminate the fluid line dynamics and minimize the opportunity of air inflow through the many hydraulic couplings, and to install easily on the AT. Furthermore, it features compact size, light weight, and high performance, especially flow rate largely due to the simple and short flow path. As illustrated, this integrated actuation system is much simpler than the current band brake actuation system. With this power-by-wire actuation system, such more advanced AT shift strategies as clutch-to-clutch control also can be more easily implemented.

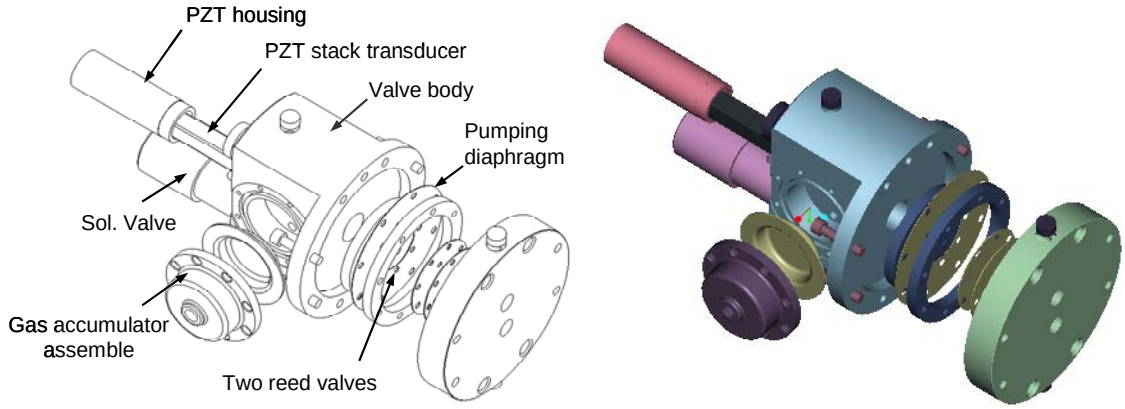

(a) assemble diagram (b) digital mock-up model

Figure 2-20: Assemble diagram and digital mock-up model of stand-alone prototype

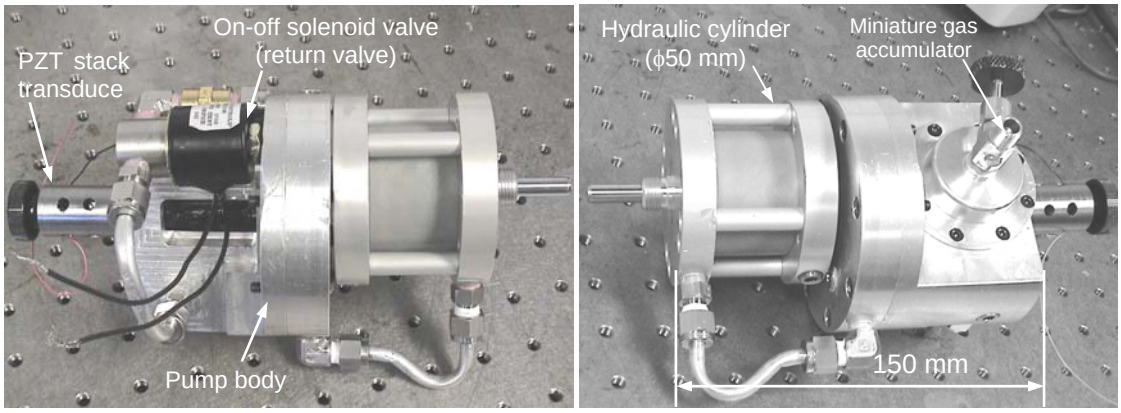

(a) left view (b) right view

Figure 2-21: Photographs of fabricated stand-alone prototype actuator

2.3 Effective Bulk Modulus of Working Fluid

In fact, most potential applications using piezoelectric-hydraulic pump will probably be operating in wide pressure and temperature ranges. Such operation conditions may cause the variation of fluid properties. In particular, since a pre-pressurized (biased) accumulator is an essential component for this actuating system, pressure will affect the property of working fluid such as the effective bulk modulus. However, the effective bulk modulus is assumed to be constant in most studies on the performance of the piezoelectric-hydraulic pump. The varying effective bulk modulus of Hydrolubric® oil primarily used for the working fluid in this research is described.

2.3.1 Review of Fluid Effective Bulk Modulus

The fluid effective bulk modulus is an important fluid property for determining the pump dynamic characteristics such as response time etc. It has been identified that it is a combination of the bulk modulus of air-free fluid and the bulk modulus of entrapped air. As a result, it varies widely with pressure and temperature and depends on the ratio of entrapped air to the total volume [Watton, 1986]. To represent this observation, various types of theoretical models have been developed. Assuming the entrapped air and fluid are modeled as serial springs and the container is a rigid, a simple model for the effective bulk modulus can be derived as follows:

$$\frac{1}{\beta_e} = \frac{V_a}{V_T}\frac{1}{\beta_a} + \frac{1}{\beta} \tag{2.18}$$

where, β_a is the bulk modulus of the air, β is the bulk modulus of fluid and V_a is the volume of the entrapped air, V_T is the total volume. From this definition, the fluid effective bulk modulus is typically measured statically in chamber with a piston that can vary the volume of the fluid. As the fluid is pressurized, its compressibility can be determined. This method, however, requires a precision test apparatus because the volume change is very small. Furthermore, it is difficult to online measure the effective bulk modulus experimentally in hydraulic control system under actual operating conditions because the current measuring devices are too bulky and complex for real time measurement.

In this research, new measuring method is developed based on the fact that the fluid effective bulk modulus has been recognized to be a main parameter for determining the natural frequency of the hydraulic control system [Merrit, 1967]. Consider the cylindrical control volume in the valve system consisting of the spool valve, spring and pressure chamber. After integrating of the pressure-rise equation, substituting it into the equation of motion for spool valve yields the following natural frequency:

$$\omega_n = \sqrt{\frac{k + \frac{\beta_e A_p^{\,2}}{V_o}}{M}} \tag{2.19}$$

where M is the mass of spool valve, k is the spring constant, β_e is the effective bulk modulus, A_p represents the ram area, and V_o is the control volume of chamber. The second term of the numerator in Eq. **2.19** is frequently referred as hydraulic spring rate.

The relationship between the effective hydraulic spring rate (K_e) and the effective bulk modulus is therefore [Niezrecki et al, 2004]

$$K_e = \frac{\beta_e \cdot A_p^{\,2}}{V_o} = \frac{\beta_e \cdot A_p^{\,2}}{A_p \cdot \ell_p} = \frac{\beta_e \cdot A_p}{\ell_p} \tag{2.20}$$

where ℓ_p is the height of fluid cavity and A_p is the area of diaphragm, as described in Figure **2-22**. From Eq. **2.20,** it is clear that the spring rate is an explicit function of the effective bulk modulus. As the effective bulk modulus of the fluid changes, the hydraulic spring rate will change accordingly. This change also will affect the system resonant frequencies. The proposed new technique is developed based on this relationship.

2.3.2 Piezoelectric Impedance Method

The impedance of the piezoelectric material is introduced to measure the hydraulic spring rate. Piezoelectric materials are widely used in a variety of applications such as vibration control, damage detection, and active noise control. When a piezoelectric transducer is integrated with solid host structures, interfacial boundary conditions are imposed on the transducer material by the coupled structure. This coupling effect generates an electrical load, the so called admittance (the inverse of impedance), which will in turn deviate significantly from the normal piezoelectric capacitive behavior at resonant frequencies. This phenomenon generates the peak resonance frequency, which will depend on the characteristics (e.g., stiffness) of the coupled host structure and the interfacial boundaries [Liang et al., 1996]. In a similar manner, when a piezoelectric transducer is coupled with a structure containing working

fluids, resonance frequencies of the integrated system will change with the fluid spring rate (which is directly related to the fluid effective bulk modulus).

To develop and illustrate this new piezoelectric impedance-based effective bulk modulus measuring technique, a simple configuration is used as test bed, as shown in Figure **2-22**. A hollow cylinder type PZT stack transducer (L = 27 mm, ϕ = 14mm), which will help the dissipation of generated heat under high frequency operations (e.g., above 2000 Hz) is attached to the end of a thin spring steel diaphragm with steel stiffener, while the other end is clamped. The measuring device is connected to an accumulator, which is used here to represent a pressurized hydraulic cylinder, since the pressure of the fluid cavity and hydraulic system can be easily adjusted by the biased accumulator pressures. With such an arrangement of the measuring device, the effects of the hydraulic control systems are eliminated due to the one-way valve action. Consequently, this new method is effective for the local areas of interest to be monitored (e.g., at the threshold of hydraulic cylinder shown)

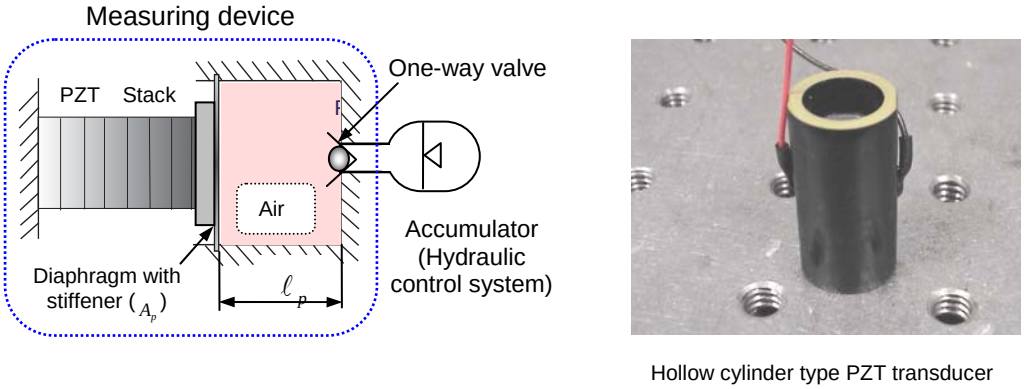

Figure 2-22: Schematic diagram of fluid effective bulk modulus measuring device

To generate the sensitivity curve characterizing the relationship between the effective bulk modulus and the impedance resonant frequency, either reliable off-line numerical simulation/calibration or off-line experimental calibration can be used. In this research, a numerical simulation model is developed to illustrate the proposed new method and obtain the sensitivity curve; the curve can then be used for monitoring the working fluids bulk modulus in an on-line manner. The proposed measuring device can be modeled using a coupled electromechanical impedance model, which consists of a mechanical impedance the coupled fluid-structure system (the measuring device excluding the PZT stack transducer), Z_M, and the piezoelectric impedance, Z_E, as illustrated in Figure **2-23**. Since we focus on the behavior of coupled fluid-structure system that the operating frequency of interest for the measuring device is tuned to be relatively low (e.g., a few kHz), the effect due to the mechanical impedance of the PZT stack transducer at higher frequency ranges or the impedance matching will not be considered in our analysis.

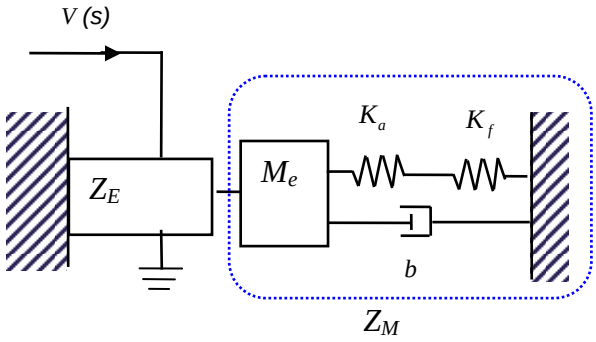

Figure 2-23: Simplified coupled electro-mechanical impedance model for measuring device

The mechanical impedance Z_M can be represented by the three elements, namely mass (Z_m), spring (Z_k) and damper (Z_c). The mass element (*M*) is represented by the effective mass of the diaphragm and stiffener. The fluid mass is negligible since the calculated fluid mass from the fluid density and tiny control volume is so small compared with the effective mass of the diaphragm and stiffener. According to Eq. **2.20**, the spring element for coupled fluid-structure system can be represented by the effective hydraulic spring rate (K_e) of working fluid contained in the measuring device, which represents the combined effect of the air and the fluid spring rates (K_a and K_f). Since the spring force due to the hydraulic spring rate is mainly dominant for the restoring force and the flexible diaphragm is very soft, the diaphragm stiffness is neglected in this study. The stiffness of thick steel stiffener (t=0.003 m) is also neglected because it can be assumed as a rigid body with mass. The damper element (damping constant *C*) represents the effective damping in the system, which will affect the shape of piezoelectric impedance around the resonant peak frequency.

The piezoelectric impedance (Z_E) is mainly generated from the electrical properties of the piezoelectric transducer and defined from Eq. **2.6** to Eq. **2.11**. The aforementioned mechanical impedance for the various elements in coupled fluid-structure system can be derived as:

$$\begin{aligned} Z_c &= b \\ Z_m &= i\omega M_e \\ Z_k &= \frac{-K_e i}{\omega} \end{aligned} \tag{2.21}$$

In the analysis of impedance, it is often convenient to combine basic elements as follows:

$$Z_M = \sum_i^n Z_i = b + i(\omega M_e - \frac{K_e}{\omega}) \tag{2.22}$$

Finally, the overall piezoelectric impedance Z when coupled with the fluid-structure system can then be obtained using standard impedance block manipulation method:

$$Z = \frac{Z_E \cdot Z_M}{Z_E + Z_M} \tag{2.23}$$

The coupled impedance of the piezoelectric transducer also can be experimentally measured, typically, using an impedance analyzer. In this research, a simple alternative approximation method is used [Peairs, 2004]. Instead of the impedance analyzer, a dynamic signal analyzer and a sensing resistor are used for measuring the impedance. A unit sensing resistor is connected in series with the piezoelectric measuring device as shown in Figure **2-24** (a). Then, impedance of the measuring device can be defined as follows:

$$Z = \frac{V_t}{I} \tag{2.24}$$

where I is the current across the sensing resistor which can be defined as:

$$I = \frac{V_d}{R_s} = V_d \tag{2.25}$$

where R_s is a sensing resistor ($1\,\Omega$) and V_d is the voltage drop. Substituting Eq. **2.25** into Eq. **2.24**, the impedance becomes the ratio of the input voltage to output voltage as follows:

$$Z = \frac{V_t}{V_d} \tag{2.26}$$

The impedance with respect to frequency can be easily obtained from the frequency response function between two voltages. Figure **2-24** illustrates the photograph of the piezoelectric measuring device connected with the accumulator and sensing resistor.

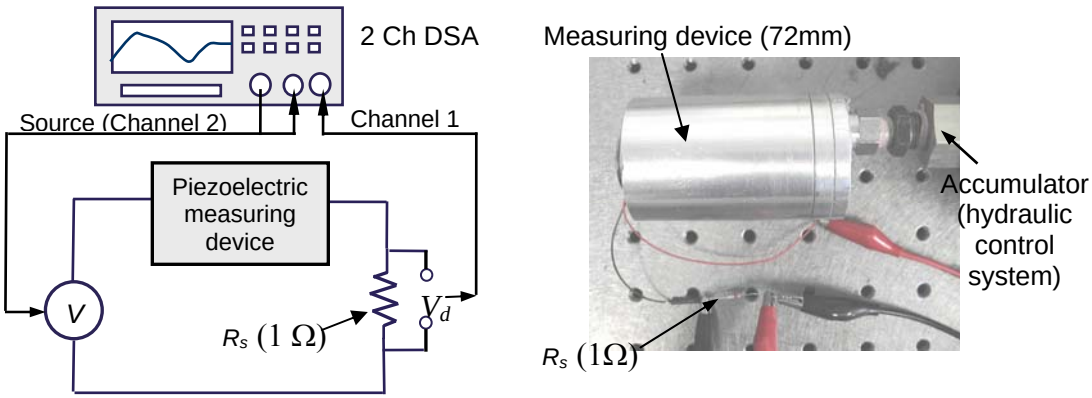

(a) overall configuration (b) photograph

Figure 2-24: Schematic and photograph of piezoelectric impedance measuring set-up

In this thesis, a Hydrolubric® oil, which is known as water-based hydraulic oil, is used for working fluid for piezoelectric-hydraulic pump, since the effective bulk modulus of water-based hydraulic oil is generally higher than that of petroleum-based hydraulic oil such as DEXRON-III® ATF (automatic transmission fluid) reported in [Kim et al., 2007]. In Figure **2-25**, the measured piezoelectric impedances are plotted as a function of the exciting frequency with respect to three different pressures. For the illustrating example, as the pressure of the accumulator is increased from 0.4 MPa to 0.7 MPa, the impedance peak induced by resonance is shifted from 2.9 kHz to 3.1 kHz due to the variation of fluid stiffness caused by different effective bulk modulus. The effective bulk modulus corresponding to the given accumulator pressures are adjusted in the simulation model so

that the predicted peak resonant frequencies can match with that measured, as shown in Figure **2-26**. Material properties and dimensions of the PZT stacks used in the simulation are listed in Table **2-2** . Note that one can also utilize off-line calibration test instead of the numerical simulation to obtain the sensitivity curve. Compared with a petroleum-based hydraulic oil such as DEXRON-III® ATF (automatic transmission fluid), which is a well-known reference oil [Kim et al., 2007], the effective bulk modulus of the Hydrolubric oil is higher than that of ATF at the same pressure (0.4 MPa). This type of phenomenon has been noted in previous literatures [Houghton, 2008].

Table 2-2: Material properties and dimensions of the PZT stack and measuring device

Symbol	Items	Value (SI unit)
t	Thickness of layers	500e-6 m
n	Number of layer	54
A	Cross section area of PZT	7.5398e-5 m^2
ρ	Density of PZT	7800 kg/m^3
Y_E	Young's modulus of PZT	4.4e10 Pa
η_m	Mechanical loss	0.01(assumed)
ε_{33}^T	Dielectric permittivity	7.7e-7 (F/m)
η_e	Electrical loss	0.01(assumed)
d_{33}	Piezoelectric constant	540e-12 m/V
A_p	Area of diaphragm	7.1e4 m^2
ℓ_p	Height of fluid cavity	10 mm
M_e	Effective mass	31 g
b	Damping constant	20 (assumed)

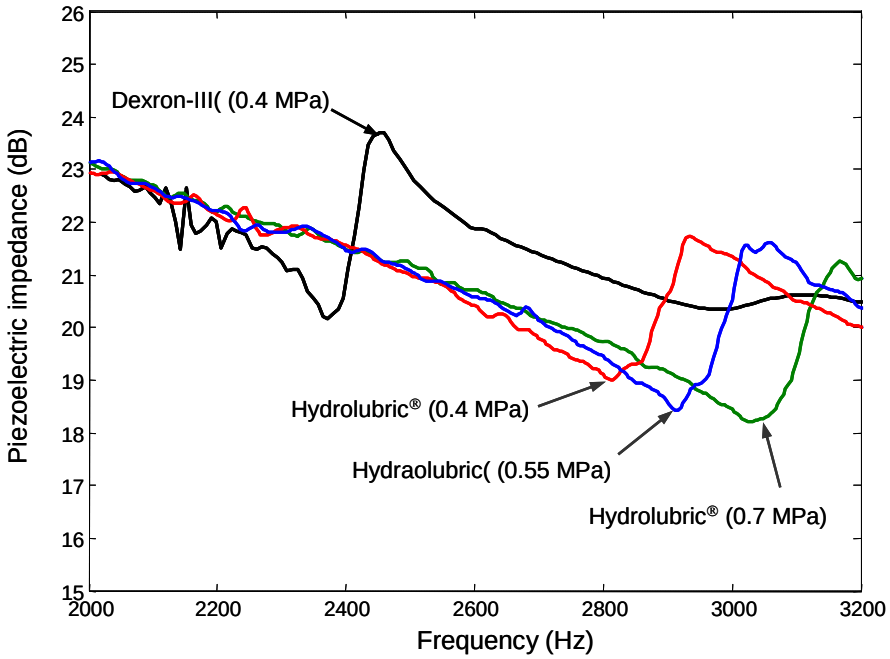

Figure 2-25: Comparison results of the measured piezoelectric impedances

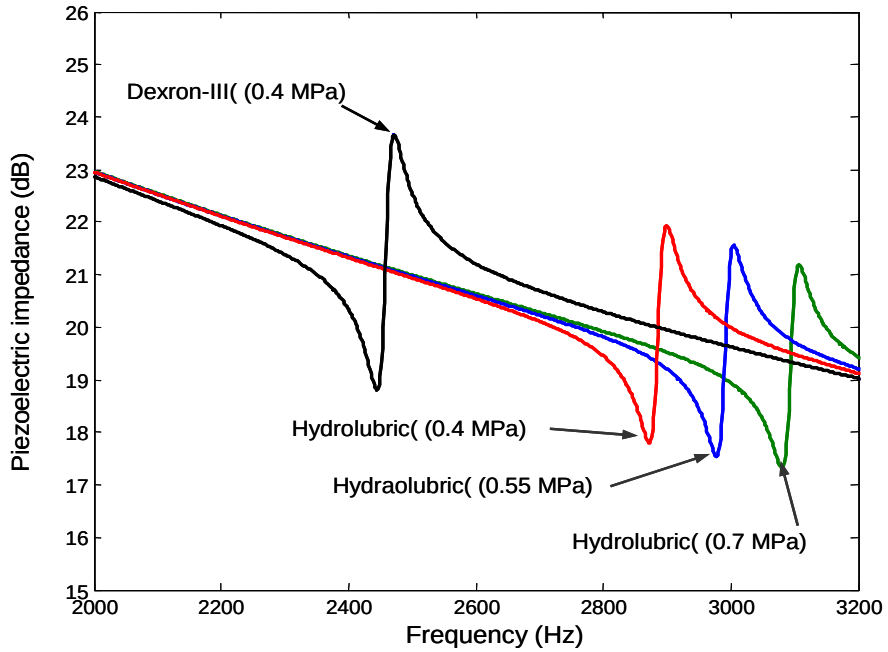

Figure 2-26: Comparison results of the simulated piezoelectric impedances

The estimated effective bulk modulus are shown in Figure **2-27**, where the sensitivity curve for on-line monitoring can be obtained by following curve fitting (solid line in Figure **2-27**).

$$y = 7 \times 10^{-6} \cdot x^{2.2} \tag{2.27}$$

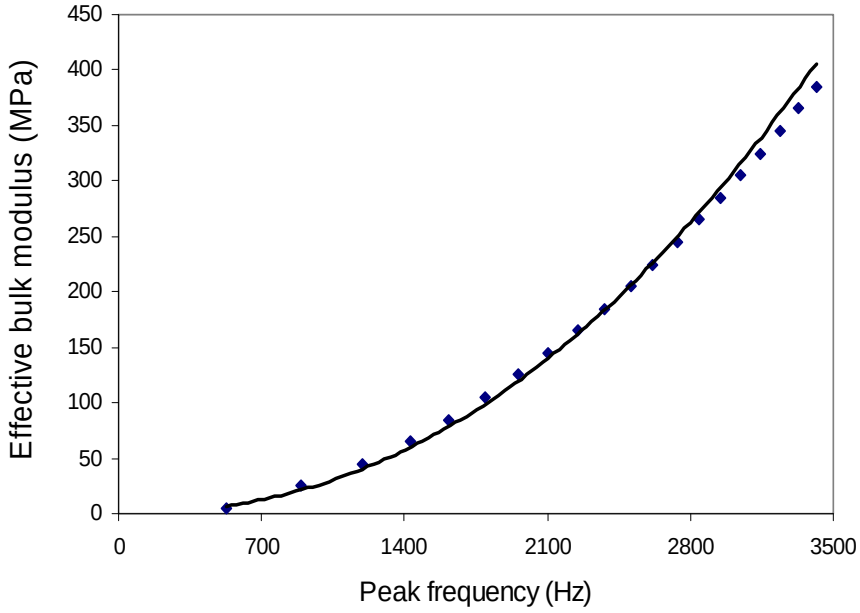

Figure 2-27: Sensitivity curve developed using the new device and simulation model (solid line: fitted; dots: measured)

2.4 Performance Investigation and Enhancements

In this section, in order to investigate the characteristics of the piezoelectric-hydraulic pump based actuator, a series of measurements for the flow rate and dead head pressures are performed and its performance is enhanced through design modifications.

2.4.1 Performance Test Apparatus

In fact, flow meter is required for measuring the flow rate of the PHP actuator. In this thesis, instead approximation method using hydraulic cylinder attached on the PHP actuator is used. In general, pressure-rise rate of hydraulic cylinder with small external loads is nearly zero during the stroking.

$$\dot{P} = \frac{1}{C}(Q_A - A_1\dot{x}) \approx 0 \tag{2.28}$$

where C is the hydraulic compliance, A_1 is the effective (ram) area of cylinder, $\dot{x}$ is the velocity of cylinder, respectively. From the Eq. **2.28,** the flow rate can be estimated from the average velocity of cylinder from as follows;

$$Q_A \approx A_1\dot{x} \tag{2.29}$$

Figure **2-28** represents the configuration diagram of performance evaluation set-up. The piston of cylinder is connected with the linear variable displacement transducer (LVDT, Omega DP25B) to measure the stroke for velocity estimation. The dead-head pressure was also measured by high resolution pressure transducer installed at the bleed port of high pressure side. These sensing signals are analyzed and stored through the dynamic

signal analyzer (HP35665A). The record length is set as above 500Hz to avoid the beat phenomenon. The driving frequency is selected in the TTL pulse generator (model: FG3B) and an on-off switch is also used to toggle the TTL signal. Figure **2-29** shows photograph of the piezoelectric-hydraulic pump mounted on the performance test stand.

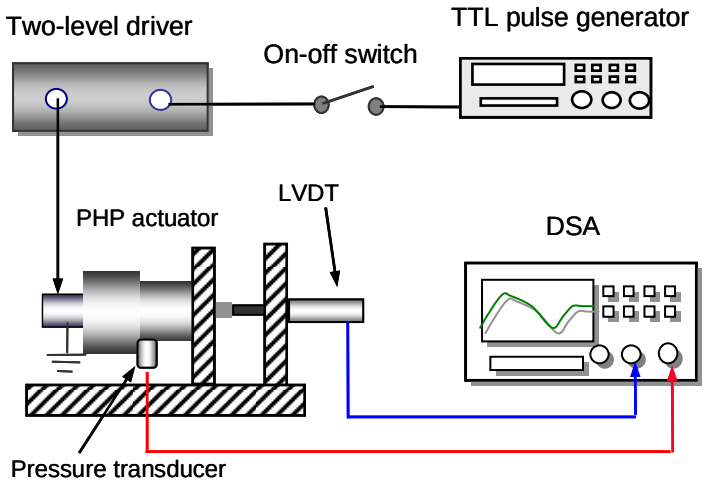

Figure 2-28: Configuration diagram of performance test set-up

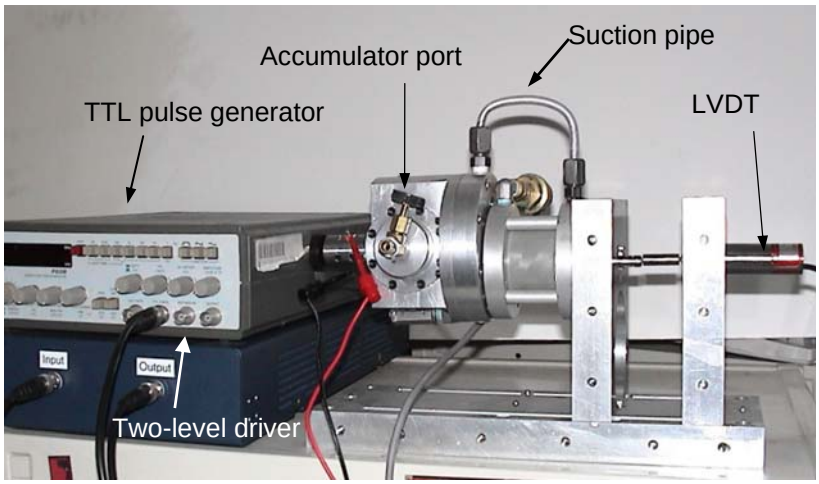

Figure 2-29: Photograph of overall performance test stand

2.4.2 Volumetric Efficiency

For more precision velocity (flow rate) measurement, thin air cylinder with ϕ 38 mm bore size is primarily used to minimize the effect of friction force in cylinder, as shown in Figure **2-30**.

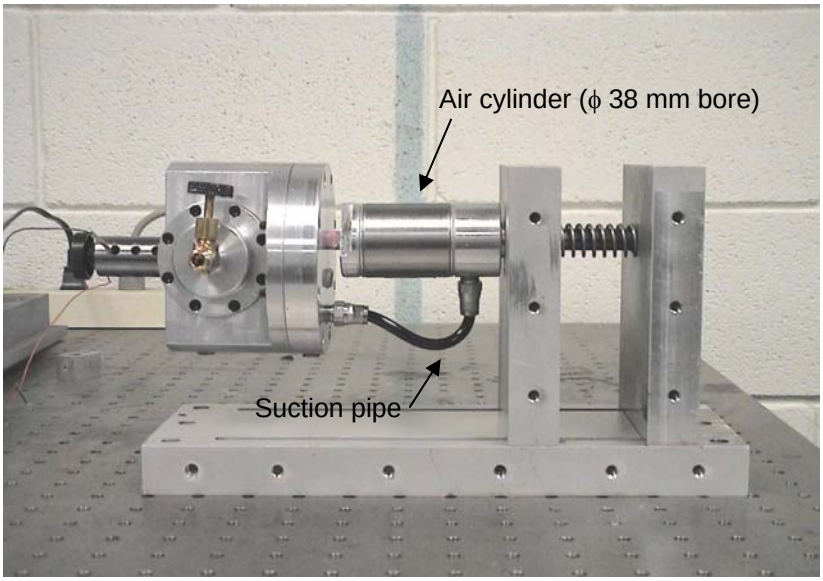

Figure 2-30: Photograph of piezo-hydraulic pump with cylinder bore size of ϕ 38 mm

The measured flow rate characteristic curves for various accumulator pressures are shown in Figure **2-31**. There is narrow dead-band in the range of 5 Hz because of the friction of hydraulic cylinder. The bandwidth of valve opening turned out to be within the 150 Hz. Because of the bandwidth and system uncertainties, flow rate is dropped around 170 Hz. At higher driving frequency, outlet port in reed valve becomes the orifice which leads to the recovery of flow rate due to the large pressure difference and higher driving frequency.

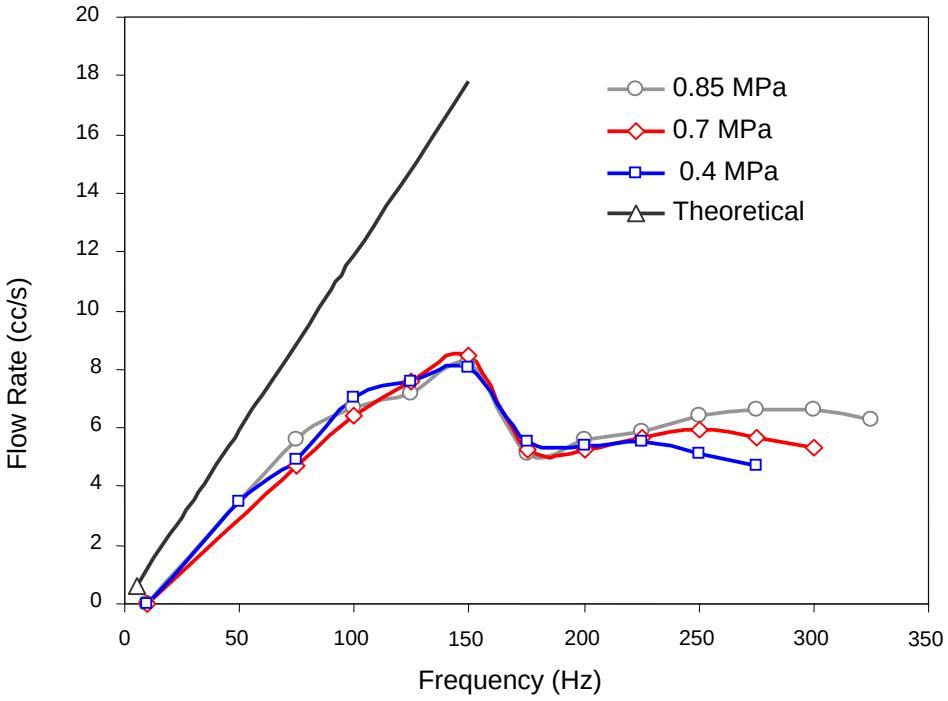

Figure 2-31: Flow rate characteristic curves for various accumulator pressures

In fact, the piezoelectric-hydraulic pump is a positive displacement type pump that uses a combination of the reciprocating action of a flexible diaphragm and one-way check valve. This type pump enables a fluid to displace by trapping a fixed amount of fluid into the discharging side. As a result, theoretical flow rate can be expressed as follows:

$$Q_{TH} = \delta \frac{\pi D^2}{4} f \qquad (2.30)$$

where δ is the stroke of PZT stack ($50\,\mu m$), D is the diameter of pumping chamber (0.053m), f is the driving frequency (Hz). This theoretical flow rate is designed based on the performance requirement of flow rate. Accordingly, the volumetric efficiency (η) is a key factor for evaluating of positive displacement type pump.

$$\eta = \frac{Q_A}{Q_{TH}} \tag{2.31}$$

where Q_A is the actual measured flow rate calculated from Eq. **2.29**. From the Figure **2-31**, the volumetric efficiency is approximately calculated by 0.5 at 150 Hz. The factors that can affect the volumetric efficiency of the pump are leakage into back flow direction, external loads and dynamic characteristic of inlet flow and so on.

Most researches have focused on the driving at the high frequency range to enhance flow rates of the piezoelectric-hydraulic pump based on the fact that the pump flow rate will be proportional to the driving frequency [Sirohi et al., 2003a]. However, at higher frequency (above 200 Hz), the flow rate shows irregular behavior due to the effect of the one-way valves, pumping chamber, and hydraulic circuit and so on. Furthermore, the driving of soft piezoelectric material at higher frequency has the many technical limitations such as driving issues. Thus, the improvement of the volumetric efficiency at relatively lower frequency range is more appropriate way to improve the flow rate performance. Unlike the general pumping system, the proposed actuation system is formed by closed loop, as illustrated in Figure **2-32.** The volumetric efficiency is then affected by the suction flow dominated by the suction pipe size and length etc. At some frequency range, the small size of the suction pipe may cause a restriction (i.e., impedance increasing) and the volumetric efficiency may be deteriorated.

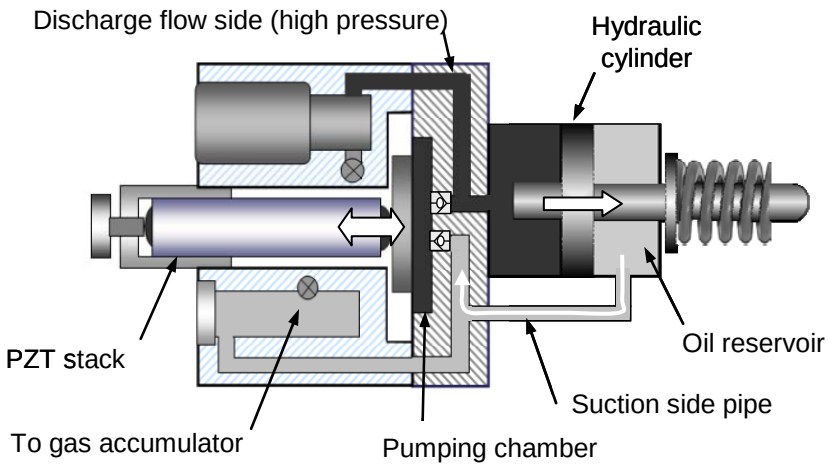

Figure 2-32: Circulating flow circuit of the PHP actuator

2.4.2.1 Effect of Impedance Matching

In pump system, characteristic impedance of suction port (Z_i) and discharging port (Z_o), as denoted in Figure **2-33,** has to be matched to maximize the circulating. The characteristic impedance of pipe can be defined by the following expression.

$$Z_c = \frac{\sqrt{\rho_c \beta_e}}{A_c} \tag{2.32}$$

where ρ_c is the density of medium (fluid), A_c is the cross-section area of pipe (orifice area), and β_e is the effective bulk modulus of fluid. The characteristic impedance of the discharging flow side ($\phi 5\ mm$ equivalent orifice) is $2.5\times10^{10}\ Nm^{-2}/m^3 s^{-1}$, which is well-known standard value in hydraulic control system [Watton, 1989]. The main factor for determining characteristic impedance is the cross sectional area of pipe (i.e., pipe size).

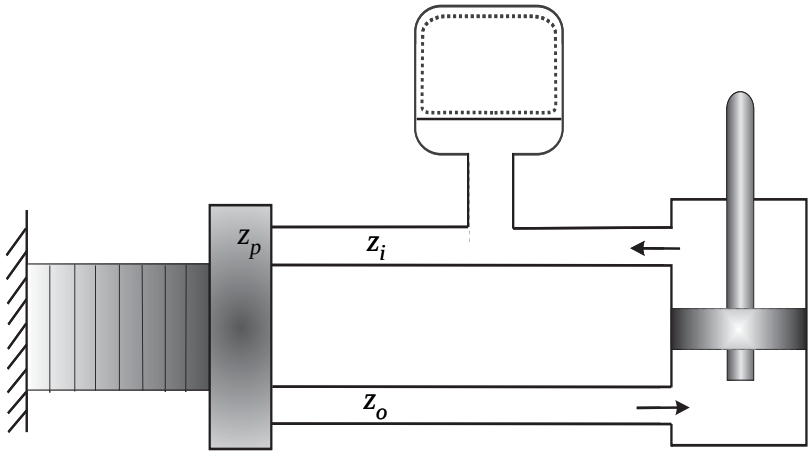

Figure 2-33: Schematic of circulating flow circuit of PHP actuator

To demonstrate the effect of impedance matching, the flow rates with respect to different pipe sizes of suction side are shown in Figure **2-34**. Square dots represent the measured flow rate using plastic (elastic) tube of $\phi 2\ mm$ pipe size. Circle dots represent the result for aluminum (rigid) tube of $\phi 5\ mm$ pipe size. In both case, the pipe size of discharging side (aluminum) of $\phi 5\ mm$ is used. In case of the aluminum tube (equal to the suction pipe), flow rate is much closer to the theoretical displacement of pump system, which implies that the volumetric efficiency is significantly improved. It is self-evident that the different pipe size between suction and discharge may lead to the impedance mismatching that adversely affects the volumetric efficiency of the pump system [Rinderknecht et al., 2005].

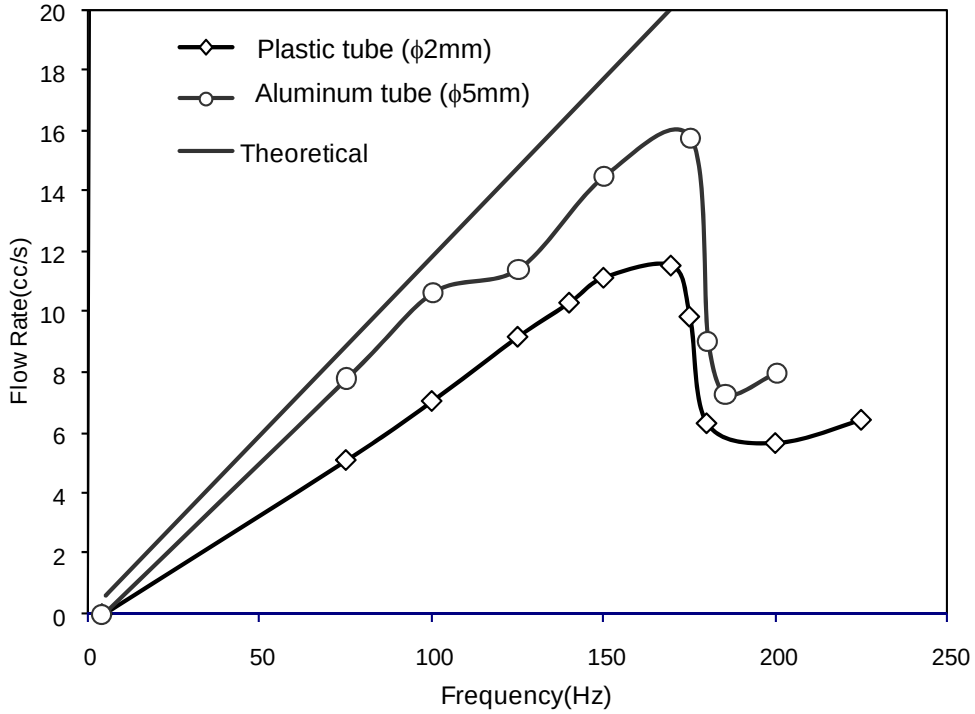

Figure 2-34: Measured flow rates with respect to different suction pipe sizes (0.55 MPa accumulator pressure, 120 Volt)

2.4.2.2 Effect of Accumulator

As noted in Chapter **1**, the gas accumulator is an essential component for pumping in piezoelectric-hydraulic pump. However, the compliance of gas in accumulator may also affect on the flow rate performance. In order to demonstrate the effect of gas accumulator, pipe of $\phi 5\,mm$ in the front of gas accumulator is restricted by the orifice size of $\phi 1.5\,mm$ to minimize the effect of gas accumulator, as depicted in Figure **2-35**. Measured flow rates with respect to different configuration are compared in Figure **2-36**. In case of restricted orifice, volumetric efficiency is lower than the case of without orifice

(i.e., original configuration) except for the vicinity of 150 Hz. Obviously, gas accumulator helps not only to provide the pumping but also to increase the volumetric efficiency. Dropping around 175 Hz can be explained by other effect discussed in the next section.

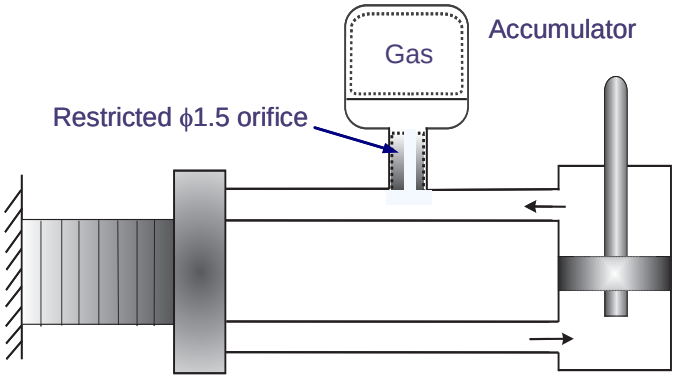

Figure 2-35: Schematic of gas accumulator with restricted orifice

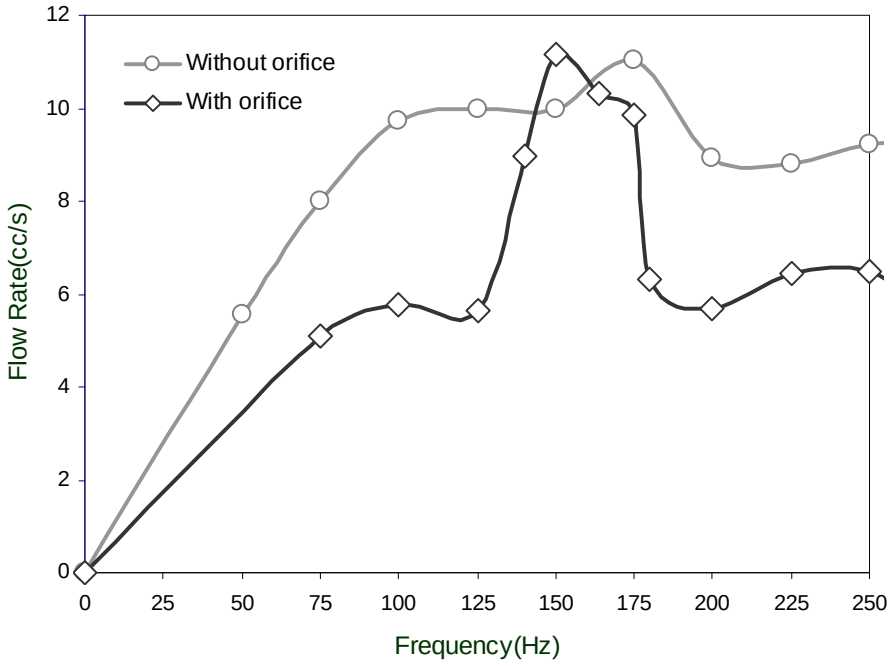

Figure 2-36: Measured flow rates with respect to different accumulator orifices (0.55 MPa accumulator pressure, 120 Volt)

2.4.2.3 Effect of Helmholtz Resonator

In general, the air intake process significantly affects the performance of an internal combustion engine since the generated power depends on the capability of a large mass flow at intake manifolds. In order to achieve the large mass flow during the suction stroke, a Helmholtz resonator which consists of a large cavity and duct with small diameter is widely used in current internal combustion engines. In a similar manner, the characteristic of suction flow has a great effect on the flow rate performance of the positive displacement type pump since discharging flow rate depends on the capability of circulating the working fluid as shown in Figure **2-32.** Figure **2-37** shows the simplified representation of a suction flow side to explain the Helmholtz resonator. It is no doubt that the chamber on the low pressure side of the double acting hydraulic cylinder could be acted as the Helmholtz resonator if the suction side is connected to the double-acting hydraulic cylinder for oil reservoir [Kinsler et al., 2000]. As a result, the behaviors of this resonator will affect the suction flow. It often causes the sudden drop of discharged flow rate at certain frequency ranges.

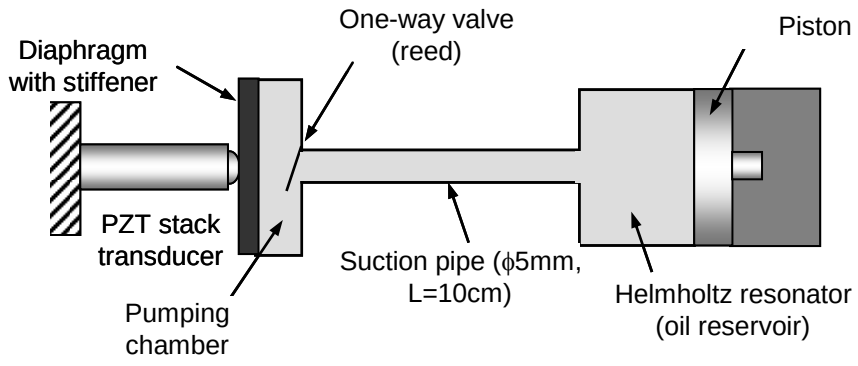

Figure 2-37: Simplified representation of suction flow side

The equivalent lumped model is developed to identify the sharp dropping frequency, focusing on the only simplified suction flow side in the piezoelectric-hydraulic pump based actuation system as shown in Figure **2-38.**

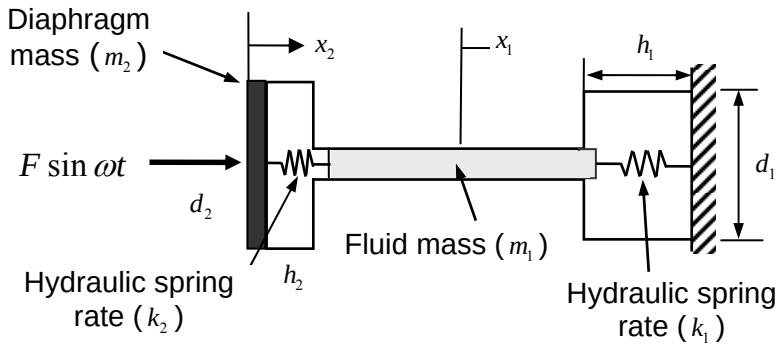

Figure 2-38: Equivalent lumped system model for simplified suction flow side

The governing equation for this lumped model can be written as follows:

$$\begin{aligned} m_1\ddot{x}_1 + b_1\dot{x}_1 + k_1x_1 + b_2(\dot{x}_1 - \dot{x}_2) + k_2(x_1 - x_2) &= 0 \\ m_2\ddot{x}_2 + b_2(\dot{x}_2 - \dot{x}_1) + k_2(x_2 - x_1) &= F\sin\omega t \end{aligned} \tag{2.33}$$

where m_1 is the fluid mass in suction pipe, m_2 is the mass of diaphragm with stiffener, k_1 and k_2 represent the hydraulic spring rate of the Helmholtz resonator and pumping chamber, respectively. Taking the Laplace transform of Eq. **2.33** results in following frequency response function of the exciting force to the velocity (flow rate).

$$\frac{V_1(s)}{F(s)} = \frac{b_2s^2 + k_2s}{a_4s^4 + a_3a^3 + a_2s^2 + a_1s + a_0} \tag{2.34}$$

where $V_1(s)$ represents the velocity of fluid ($\dot{x}_1$), $F(s)$ represents the exciting actuation force, $s = j\omega$ and

$$
\begin{aligned}
a_4 &= m_1 m_2 \\
a_3 &= m_1 b_2 + b_1 m_2 + b_2 m_2 \\
a_2 &= m_1 k_2 + b_1 b_2 + k_1 m_2 + k_2 m_2 \\
a_1 &= b_1 k_2 + k_1 b_2 \\
a_0 &= k_1 k_2
\end{aligned}
\tag{2.35}
$$

The four-pole system in Eq. **2.34** possesses two resonant frequencies, ω_{n1} and $\omega_{n2} > \omega_{n1}$ that are related to the natural frequency of pumping chamber with diaphragm and the Helmholtz resonator frequency, respectively. The k_1 and k_2 can be rewritten from the definition of the hydraulic spring rate shown in Eq. **2.20**.

$$
k_1 = \frac{\beta_e \cdot A_1}{h_1}, \quad k_2 = \frac{\beta_e \cdot A_2}{h_2} \tag{2.36}
$$

where A_1, A_2 and h_1, h_2 are the diameter and height of the two fluid cavities, β_e is the fluid effective bulk modulus (0.3 MPa), as described in Figure **2-38**. It is clear that hydraulic spring rates are introduced from the time-varying compliance of a working fluid. However, they can be treated as constant because the portion of volume change on the compliance is so small. Then, they can be main parameters for tuning of the resonance frequency. To identify the effect of different hydraulic spring rate, the flow rates are compared with respect to two different ram areas of the hydraulic cylinder (A_2), 38 mm and 50 mm, respectively, as shown in Figure **2-39**. The frequency response function for Helmholtz resonator is simulated with respect to different cylinder sizes in Figure **2-40**. As the diameter of hydraulic cylinder is changed from 38 mm into 50 mm, the first peak frequency is shifted from the 170 Hz into higher ranges (above 220 Hz). The second resonance frequency associated with pumping chamber is also identified to the 2 kHz, as

described in Figure **2-25**. Dimensions for simulation are listed in Table **2-3**. Experimental results also indicate the shift of the peak frequency from 175 Hz into the 220 Hz. From this result, it is concluded that the exciting force will be absorbed between two resonance frequency (200 Hz to 2 kHz), which leads to the flow rate drop.

Table 2-3: Dimensions for the simulation of the Helmholtz resonator effect

Symbol	Items	Value (SI unit)
m_2	Diaphragm mass (including stiffener)	0.02 kg
m_1	Fluid mass	0.017 kg
d_1	Cylinder bore diameter	0.038 m and 0.05 m
h_1	Cylinder height	0.03 and 0.01 m
d_2	Diaphragm diameter	0.054 m
h_2	Chamber height	0.003 m
b_1, b_2	Damping constant	0.2 (assumed)

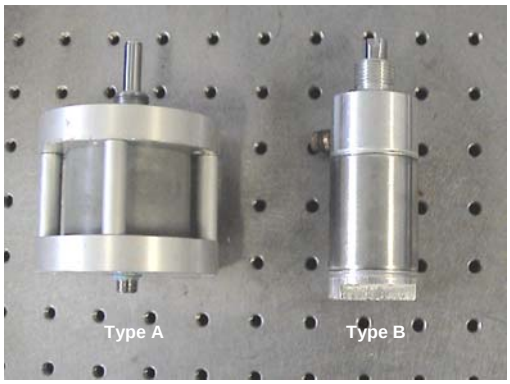

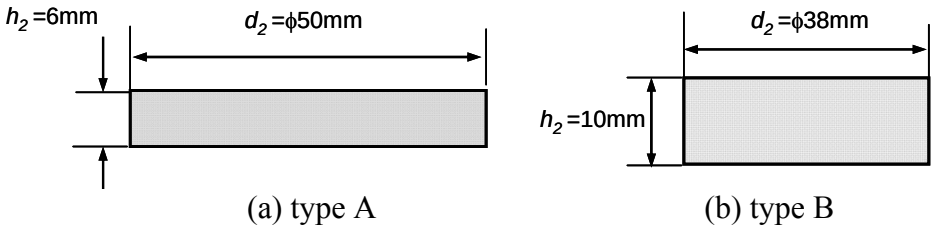

(a) type A (b) type B

Figure 2-39: Different Helmholtz cavities of hydraulic cylinders

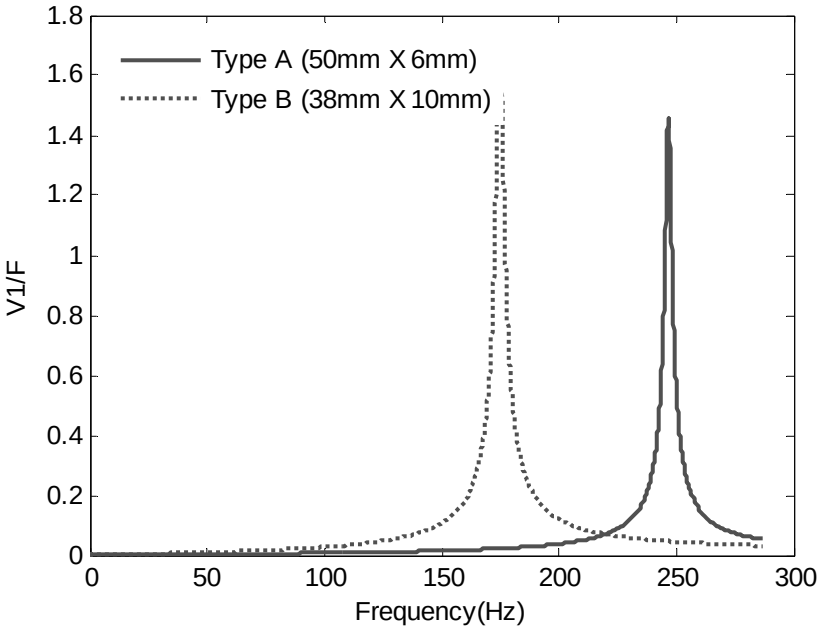

Figure 2-40: Simulated frequency responses with respect to different bore sizes

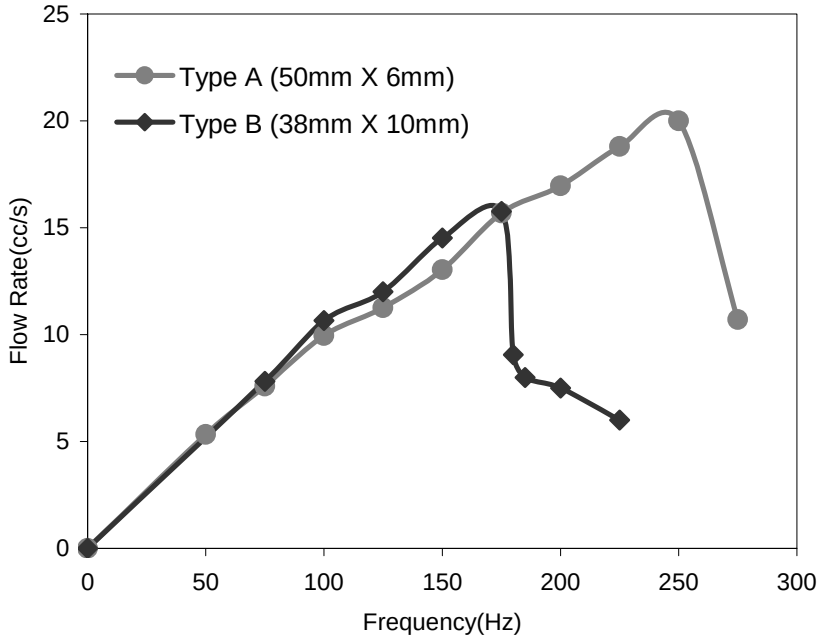

Figure 2-41: Measured flow rate curves as a function of driving frequency with respect to different bore sizes (0.55 MPa accumulator pressure, 120 Volt)

2.4.3 Dead-head Pressure and Resolution

Typically, the generated maximum actuation pressure can be evaluated by the dead-head pressure in pump applications. As shown in Figure **2-42**, dead-head pressure is defined by the pressure difference between initial accumulator pressure and generated actuation pressure (RMS) at zero flow rate (i.e., blocking of piston). The dead-head pressure is developed during the outlet reed valve opening, while pumping (PZT on). This pressure will keep remaining due to the sealing of reed valve while PZT off. As a result, generated actuation pressure will be fluctuated, which in turn result in fine pressure ripple to be minimized for control applications.

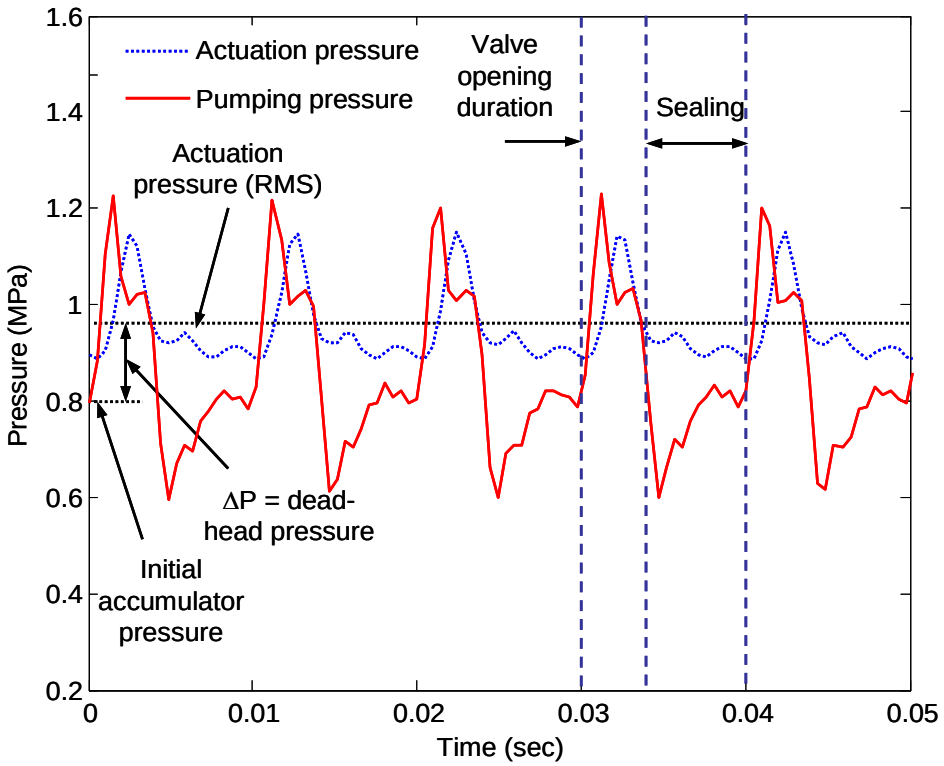

Figure 2-42: Definition of dead-head pressure and actuation pressure (100 Hz)

2.4.3.1 Effect of Effective Bulk Modulus

The dead-head pressure can be increased by using higher effective bulk modulus because dead-head pressure will be depending on the amplitude of the oscillating pumping pressure, as illustrated in Figure **2-42**. The amplitude of pumping pressure can be explained from the pressure-rise rate equation as follows:

$$\dot{P} = \frac{1}{C}(Q_o - Q_i - A\dot{x}) \tag{2.37}$$

where *C* represents the hydraulic compliance (capacitance), which is defined as:

$$C = \frac{(V_o + A_1 x)}{\beta_e} \tag{2.38}$$

where β_e is the fluid effective bulk modulus, V_o is initial control volume, A is ram area of cylinder and x is stroke of PZT stack. One of the feasible methods to make lower hydraulic compliance is to make higher effective bulk modulus. It is confirmed that the effective bulk modulus can be increased through the increasing of the initial accumulator pressure. Due to this useful fluid property, the improvements of the dead-head pressure are achieved using higher accumulator pressures. The example of comparison results with respect to different accumulator pressures are plotted in Figure **2-43**. The maximum pressure difference (i.e., dead head pressure) is approximately 0.15 MPa when the initial accumulator pressure is about 0.65 MPa. This pressure difference becomes larger (0.3 MPa) as increasing the initial accumulator pressure (0.72 MPa). From this comparison, it is recognized that the measured pressure difference depends on the initial pressure of the accumulator. However, this approach possesses the technical limitations such as the

more leakage flow due to the higher pressure. The stroke of the PZT stack also will be reduced with much higher pressure loads.

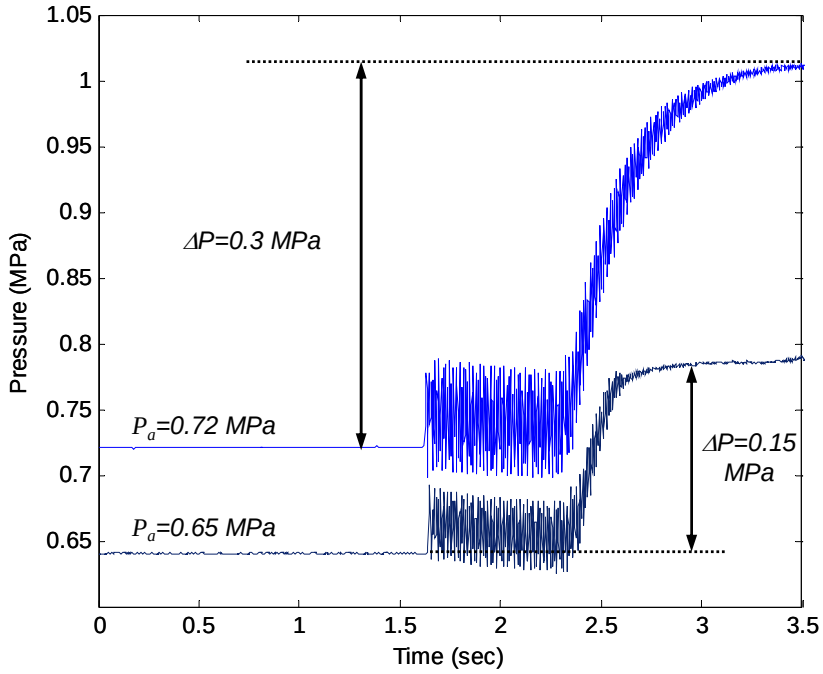

Figure 2-43: Dead-head pressures with respect to different accumulator pressures (120 V, 60 Hz)

Another possible method to increase the effective bulk modulus is to utilize the different working fluid that has higher effective bulk modulus. As described in the Figure **2-25**, the effective bulk modulus of Hydrolubric oil is higher than that of automatic transmission fluid (ATF). As a result, dead-head pressure using Hydrolubric oil turned out to be higher, as shown in Figure **2-44** .

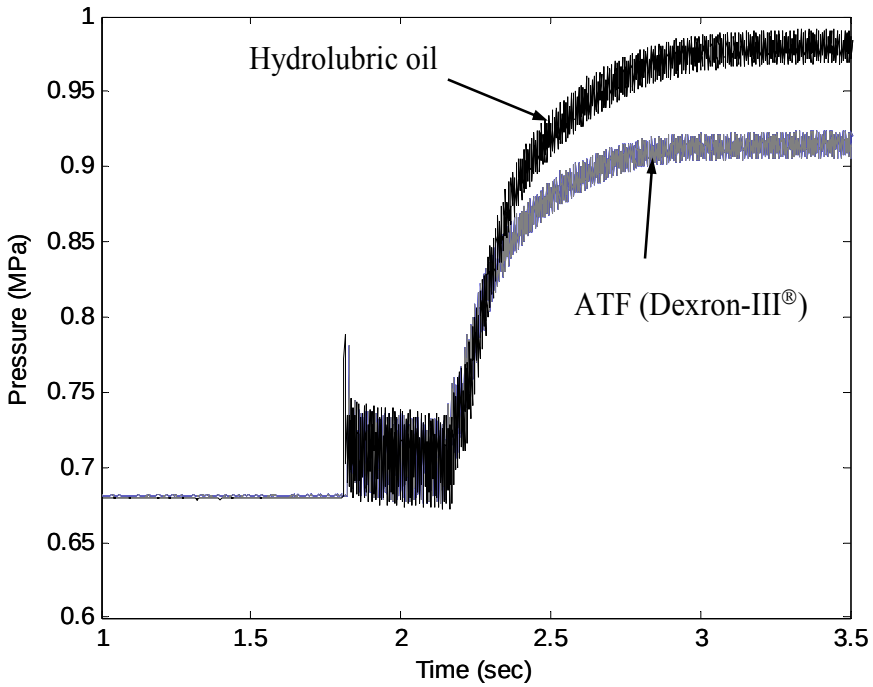

Figure 2-44: Dead-head pressures with respect to working fluids with different effective bulk modulus (120 V, 200 Hz)

2.4.3.2 Effect of Reed Valve Characteristics

Another practical way to improve the dead-head pressure is to utilize the reed valve characteristics. The amplitude of the pumping pressure will be pressure difference for the ideal one-way action. In actual situation, however, pressure difference becomes lower than the amplitude of the pumping pressure because of the reed opening duration and the leakage flow toward reverse direction, as shown in Figure **2-42**. Therefore, the quick closing motion of reed and improved sealing performance are required to resolve this problem resulting from the passive type reed valve. This drawback can be compensated via the active reed valve using active material such as piezoelectric

transducer [Tan et al., 2005]. However, such an additional active valve system adversely influences the cost-effectiveness and the benefits of high power density. The other feasible method to adjust the reed valve open timing without active valve is using different pulse width of TTL pulse. The example of TTL pulse (100 Hz) is illustrated in Figure **2-45**. In general, the pulse width of TTL pulse is defined as following duty ratio:

$$Duty\ ratio = \frac{t_p}{T_p} \cdot 100\ (\%) \tag{2.39}$$

where T_p is the period time and t_p is the pulse duration time. As a result, duration time of reed valve opening can be easily adjusted by changing the pulse duration time.

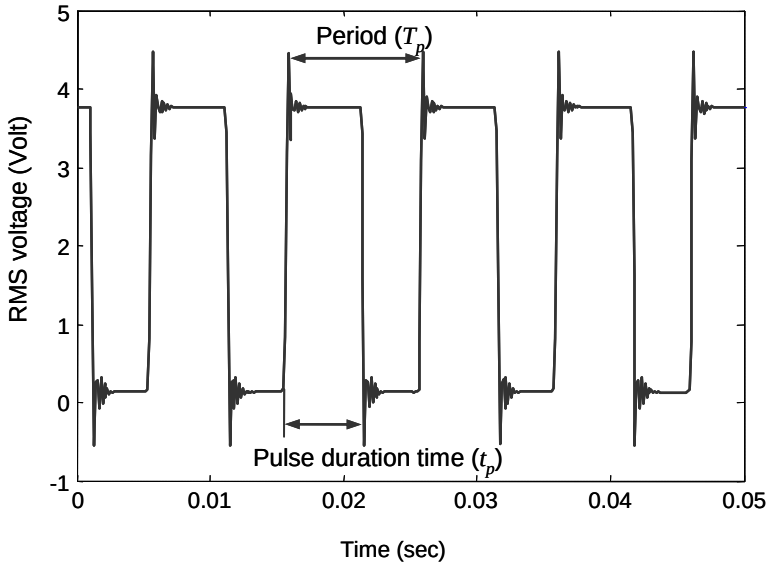

Figure 2-45: Definition of duty ratio of TTL pulse input voltage

Figure **2-46** shows the dead-head pressure with respect to different duty ratios. The duty ratio of 60 % shows the largest pressure difference (i.e., dead-head pressure). It is self-evident that open duration time of reed valve affects the amplitude of dead-head pressure.

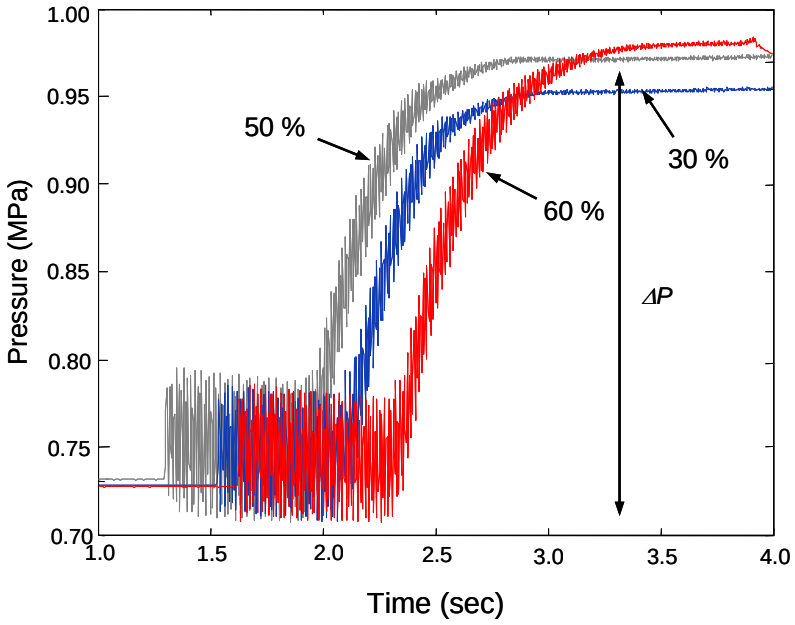

Figure 2-46: Dead-head pressures with respect to different duty ratio : 0.72 MPa accumulator pressure, 100Hz, 120 Volt

The other simple alternative way to compensate the valve timing is to change the properties of reed valve such as stiffness. One feasible way is to replace the material of reed valve from spring steel to carbon fiber, which features more responsive due to the light weight. The leakage flow also can be reduced due to the higher stiffness and fine roughness. As shown in Figure **2-47**, new reed valves are assembled by using thin carbon fiber sheet (t=0.3mm), which is widely used in two cycle combustion engine. In the case of the carbon fiber reeds, valve opening interval becomes shorter than spring steel due to the larger restoring force. Figure **2-48** shows the dead-head pressures with respect to two reed valves. Dead-head pressure for carbon fiber reeds is higher than that of spring steel reeds. However, pressure ripple becomes more evident. Experimental

results show that reed valve characteristic significantly affects the amplitude of dead-head pressure and pressure ripple.

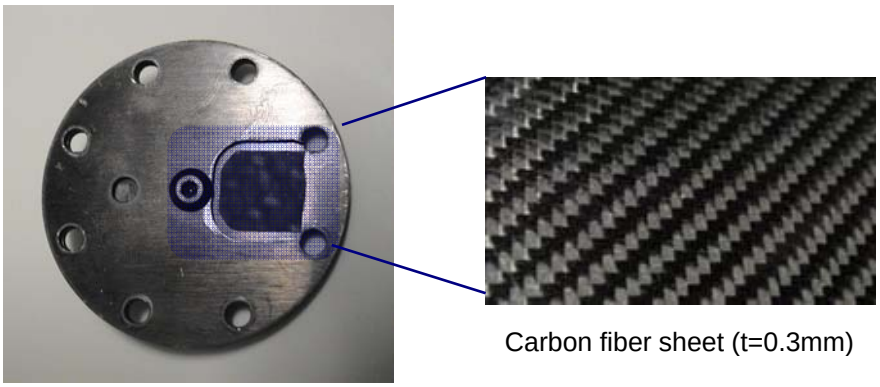

Figure 2-47: Photograph of new reed valve assemble using carbon fiber sheet

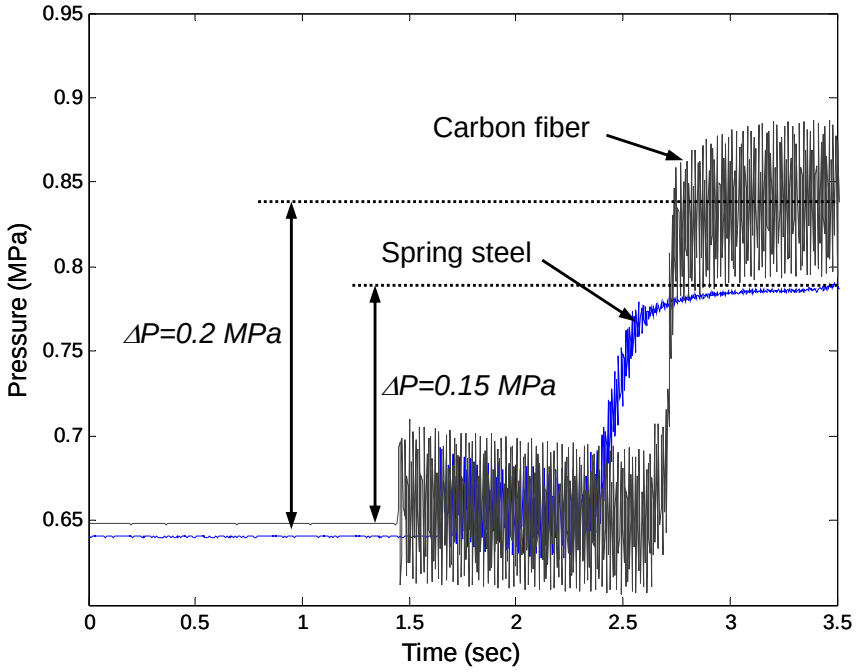

Figure 2-48: Dead-head pressures with respect to different reed valves: 0.65 MPa accumulator pressure, 100Hz, 120 Volt

In addition, the minimization of the compliance loss in the pumping chamber can be one of the most effective ways to improve the amplitude of pumping pressures. Pumping chamber volume (V_o) in the fluid compliance (C) is designed as small as possible. In this research, the pumping height is designed as 1 mm based on the previous CFD analysis [John et al., 2006].

2.4.4 Summary of Actuator Performance

As summarized in Figure **2-49**, fill time of 0.3 second corresponding to flow rate of 20 cc/s and maximum actuation pressure of 0.48 MPa are achieved. Prototype PHP actuator can satisfy the performance requirement for AT shift application.

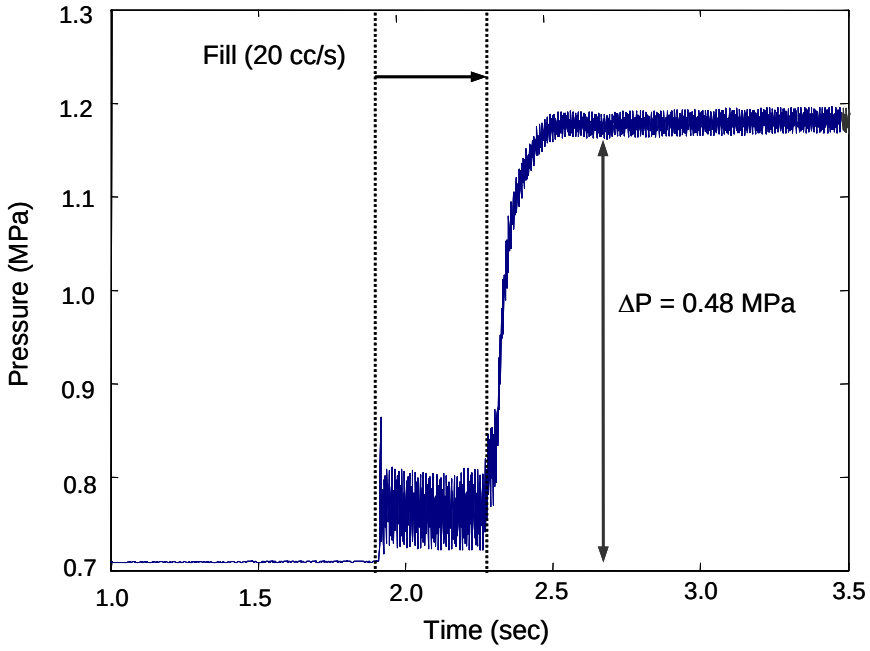

Figure 2-49: Achieved required performances: max. dead-head pressure and flow rate (0.7 MPa accumulator pressure, 145 Volt)

The performance of actuation system can be also summarized by plotting the actuation pressure versus flow rate, as shown in Figure **2-50.** Then, the interception pressure in y-axis represents the deadhead pressure. Also, the interception in x-axis stands for the no-load flow rate. The output power can be calculated by using the definition of power and Eq. **2.29.**

$$Power = F \cdot \dot{x} = (P_1 \cdot A_1)\frac{Q_A}{A_1} = P_1 \cdot Q_A \tag{2.40}$$

where P_1 is the actuation pressure, Q_A is the flow rate. The maximum output power corresponding to impedance matching line is approximately calculated by 3 Watt at the interception point between actuation line for 145 Volt and impedance matching load line.

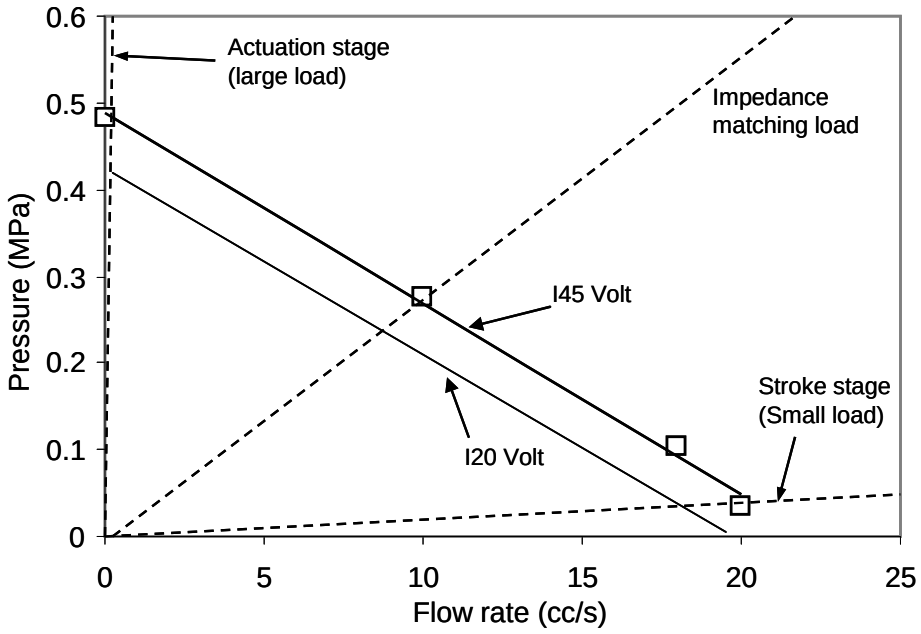

Figure 2-50: Actuator characteristic curve of piezoelectric-hydraulic pump actuator (120 Volt, 200 Hz and 0.55 MPa accumulator pressure)

2.5 Chapter Summary and Conclusions

In this chapter, the development of a piezoelectric-hydraulic pump based actuator for applying into the shift control of automatic transmissions is presented. Its fundamental performances, flow rate and dead-head pressure, are then evaluated through a series of experiments and the theoretical analysis. In Section **2.2,** the design of components and fabrication of the prototype piezoelectric-hydraulic pump actuator are described in detail. The compact, light, and self-contained prototype actuator is designed by utilizing the optimized hardware configuration and the miniature gas accumulator. To predict the self-induced temperature rise of the PZT stack transducer, the piezoelectric impedance model is derived. The effective bulk modulus of working fluid is characterized to be used in the simulation and performance analysis in Section **2.3**. In addition, using the derived piezoelectric impedance model, a new online monitoring method of the fluid effective bulk modulus is developed in this research. In Section **2.4**, the flow rate performance is measured and enhanced by design modifications. The reason for dropping of flow rate around 180 Hz is identified by introducing the Helmholtz resonator concept. Flow rate requirement (20 cc/s) corresponding to the fill time (0.3 second) for current band brake of automatic transmissions is achieved by shifting of peak frequency caused by the Helmholtz resonance. The maximum dead-head pressure of 0.45 MPa also is nearly achieved by using the useful property of working fluid and the characteristic of reed valves.

One of the main features of prototype PHP actuator is that we can successfully mount it onto the transmission without any additional devices due to the stand-alone

structure and compactness. Performance evaluation results also indicate that the performance of the new piezoelectric-hydraulic pump actuator is adequate to apply for AT shift control.

.

Chapter 3

Nonlinear Force Tracking Control of Piezoelectric-Hydraulic Pump Actuator

With the promising design of the PHP-based actuator, the goal of the research presented in this chapter is to develop a controller that can effectively control the new actuator so that the required output force (pressure) profile can be generated to guarantee a smooth and reliable shift. The major challenge here is that the PHP-based actuator is highly nonlinear and thus difficult to control with traditional approaches. The technical objective is therefore to synthesize an effective nonlinear control law that can command the piezoelectric stack actuation so that the pump actuator can track a certain force profile and actuate the band brake for AT shift control. First of all, several control issues on the actuation force control systems are briefly discussed in Section **3.1**. To achieve the research goal, a model of the PHP-based actuator is developed and presented in Section **3.2,** and a switching sliding mode controller is synthesized based on the derived model and sliding mode theory (Section **3.3)**. The actuator and controller are implemented experimentally in a lab environment to validate the analytical predictions and demonstrate the effectiveness of the proposed concept (Section **3.4).** Effort to compensate for the effect of friction force in the hydraulic cylinder is presented (Section **3.5**).

3.1 Control Issues in Piezoelectric-Hydraulic Pump Actuator

3.1.1 Force Control vs. Position Control

In the PHP actuator, the final force generating element for engaging the AT friction elements is a hydraulic cylinder, which is widely used in many control applications since it features high power density, high stiffness and fast response. The main control objective is to track the desired actuation force. Most of the research efforts on hydraulic cylinder control have been focused on position regulation and tracking based on the classical linear control or adaptive control theories. Over the past several decades, only a few studies explicitly considered the force tracking problem. The main reason for this is due to the challenging interaction problem between the actuator dynamics and the inherent nonlinear dynamics of the hydraulic cylinder system. Using a linearized model derived from the original nonlinear system and frequency domain analysis, it was recognized that zeros exist in the transfer function from the control input for the control valves to the actuation force output [Alleyne et al., 1998]. These zeros resulted from actuator dynamics in turn can be canceled out by poles in the transfer function from the force to the position of the actuation system if the output of interest is the position (displacement), as shown in Figure **3-1.** If these zeros are lightly damped in actuation system and they appear at relatively low frequency (within 10 Hz), it is difficult to design a controller to achieve high bandwidth force tracking performance [McCloy, 1980].

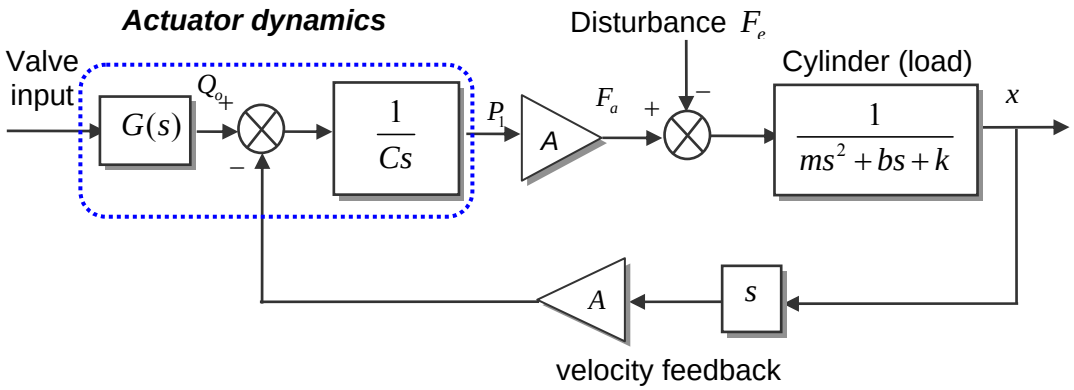

Figure 3-1: Linearized block model for standard hydraulic cylinder actuation system

These facts have led to use of more advanced control theory for hydraulic actuation force control. For example, an adaptive force control method was developed by Alleyne [1999] for active suspensions based on a Lyapunov based adaptive law. Other Lyapunov based nonlinear controllers were proposed by Sohl [1999] and Niksefat et al. [2001]. In these controls, both position and velocity measurements are required, which is a relatively expensive system and not commonly used in practical applications with harsh environments, such as in automotive AT. In addition, since an on-site force transducer is not practical to be implemented in the AT, the force tracking control will end up becoming a pressure tracking problem, where the performance may not be good due to the low resolution of the pressure transducer or inaccuracy of the force calculation.

3.1.2 Continuous Input vs. Discrete Input

Many control systems require a pulse modulating block between a controller and a plant block, as shown in Figure **3-2**. Some control systems (e.g., the thruster control

system for the attitude control of a spacecraft) use a discrete on-off signal (u), while the controller produces a continuous desired torque signal (r). It is necessary to convert the continuous control input signal from the controller to a modulated pulse signal. Likewise, for the piezoelectric-hydraulic pump based actuators, the applied voltage to the PZT stack transducer should be a discrete pulse signal by nature. Hence, a continuous control signal should be converted into a frequency modulated pulse stream that is proportional to the level of flow rate command, which implies that the averaging level of pulse input is equivalent to the continuous input command. However, since the controller is generally designed without a pulse modulator, the exact averaging model is required for converting and this *ad-hoc* approach often makes the system unstable since it may be subject to self-sustained oscillation (i.e., limit cycles) due to the nonlinearities of the given system.

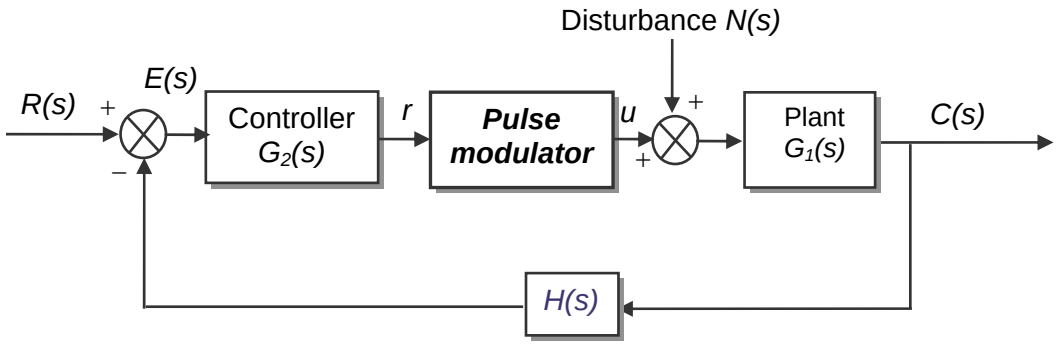

Figure 3-2: Block diagram of standard closed-loop system with pulse modulator

Another approach is to design the controller without a pulse modulation system based on the discrete control input system. Only limited amount of research, however, has considered the direct closed-loop control with discrete control input because it is difficult to guarantee stability and robustness in the discrete input system, while the pulse

width modulated electro-magnetic type valves are common actuators driven by the discrete input signal [Shen et al., 2006]. Hence, in order to utilize the piezoelectric-hydraulic pump as a force actuator, this issue should be fully addressed by either reliably converting the continuous control input or using a direct controller design to produce a discrete control input.

3.1.3 Actuation Force Response Delay

As noted in Chapter 1, electro-hydraulic actuation systems for friction elements show the inherent delay time in pressure response due to the fill process. In many investigations, this dynamics has been characterized as second order filter and the transport lag between the commanded pressure and actuated pressure based on experimental results [Yoon et al., 1997 and Wang et al., 2001]:

$$\frac{P_{actuate}}{P_{command}} = \frac{e^{-\tau_3 s}}{(1+\tau_1 s)(1+\tau_2 s)} \qquad (3.1)$$

This simple linear model is, however, valid only for limited conditions due to uncertainties and nonlinearities. It is also suitable for only frequency domain based control. Another approach is to separate the control methods according to each stage. Then, discontinuity resulting from the switching control law has to be considered for stability analysis.

3.2 System Model

To design the controller, a system model of the PHP actuator integrating with the friction element is first developed. The complete PHP actuator integrated with friction element mainly consists of the piezoelectric-hydraulic pump and the double-acting hydraulic cylinder with external loads, as depicted in Figure **3-3**.

3.2.1 Dynamic Modeling

The governing equation of the cylinder piston can be expressed by the force balance equation using Newton's second law as follows:

$$m\ddot{x} = F_a - F_e - F_f \qquad (3.2)$$

where F_f is the friction force between the piston and the cylinder, F_e is the load from the band brake, x represents the displacement of the piston and m is the effective mass of the cylinder with the piston rod, F_a represents the actuation force, which is the force difference between the two pressures sides in the hydraulic cylinder.

$$F_a = A_1 P_1 - A_2 P_2 \qquad (3.3)$$

where P_1 is actuation pressure to be controlled, and P_2 is accumulator pressure to be constant. To represent the stroke (x_s), the second spring constant (k_2) with a small additional stroke (about 0.5 mm) is introduced to emulate the band brake, for the actual band brake can be slightly deformed due to the band elongation and the compression of a friction pad. The piston will be nearly stopped due to the solid state of the second spring

after entire stroking (i.e., fully compressed). During the fill (stroking) stage, the external force is largely due to the return spring force with low stiffness. After the fill stage, the external load is mainly dominated by the reaction force of the band brake.

$$F_e = \begin{cases} k_1(x+x_o)+c_1\dot{x} & if \quad x \le x_s \\ k_1(x+x_o)+k_2(x-x_s)+(c_1+c_2)\dot{x} & if \quad x > x_s \end{cases} \tag{3.4}$$

where k_1 and k_2 are the spring constant of return spring and band brake, respectively. c_1 and c_2 are the damping constant of return spring and band brake, respectively. x_o and x_s represent the pre-loaded length and dead stroke.

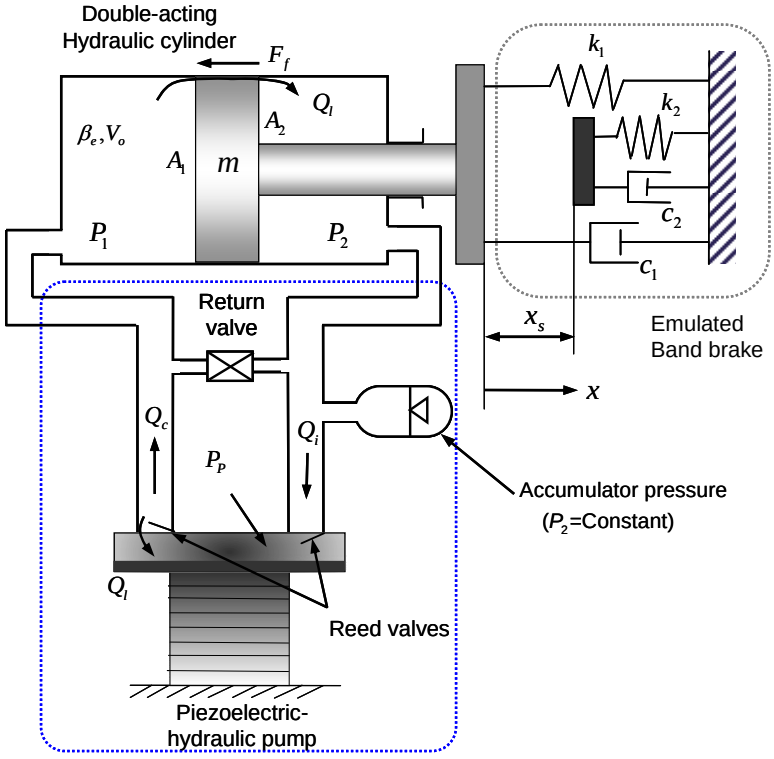

Figure 3-3: Schematic diagram of band brake actuation system

The actuation pressure is governed by the following pressure-rise rate (i.e., continuity) equation [Manring, 2005].

$$\dot{P}_1 = \frac{1}{C}(Q_o - A_1\dot{x} - Q_l) = \frac{\beta_e}{(V_o + A_1 x)}(Q_o - A_1\dot{x} - Q_l) \qquad \textbf{(3.5)}$$

where β_e is the effective bulk modulus, V_o is the control volume of the high pressure (head) side, and A_1 is the ram (effective) area of the double-acting cylinder. x and $\dot{x}$ represent the displacement and velocity of the piston, respectively. Note that C in Eq. **3.5** represents the hydraulic compliance, which is a key parameter for determining transient response time. The accumulator pressure (P_2) of the rod side is assumed to be constant in this study. Q_o is outlet (discharging) flow rate, Q_l denotes the leakage flow rate across the cylinder piston and outlet reed valve, respectively. These flow rates can be determined by following the orifice equation

$$Q = \text{sgn}(\Delta P) \cdot C_d A_o \sqrt{\frac{2|\Delta P|}{\rho_c}} \qquad \textbf{(3.6)}$$

where C_d is the discharging flow coefficient, A_o is the orifice area, ΔP is the pressure difference between up-stream and down-stream. In order to specify the outlet flow rate, the pumping pressure (P_p) of PHP is introduced by the continuity equation of the pumping chamber as follows;

$$\dot{P}_P = \frac{\beta_e}{(V_c + A_p x_p)}(Q_o - Q_i - A_p \dot{x}_p) \qquad \textbf{(3.7)}$$

where V_c is the pumping chamber volume, x_p and $\dot{x}_p$ are the displacement (stroke) and velocity of PZT stack, respectively. A_p is the area of diaphragm, Q_i is the inlet (suction) flow rate. Once the pumping pressure is generated by stroking the PZT stack transducer, the outlet flow rate and the inlet flow rate through the two reed valves can be expressed by the orifice equations as follows:

$$Q_o = C_d w \cdot x_R \sqrt{\frac{2}{\rho_c}} \sqrt{|P_P - P_1|},\ x_R = \begin{Bmatrix} x_R & if\ x_R \geq 0 \\ 0 & if\ x_R < 0 \end{Bmatrix} \quad \textbf{(}3.8\textbf{)}$$

$$Q_i = C_d w x_R \sqrt{\frac{2}{\rho_c}} \sqrt{|P_2 - P_P|},\ x_R = \begin{Bmatrix} x_R & if\ x_R \leq 0 \\ 0 & if\ x_R > 0 \end{Bmatrix} \quad \textbf{(}3.9\textbf{)}$$

where w is the orifice area gradient and x_R represents the opening displacement of the reed valve. As shown in Figure **3-4**, due to the one-way valve action, the backward flow is zero during discharging or suction, which leads to the elimination of the sign function that can be seen in Eq. **3.6**.

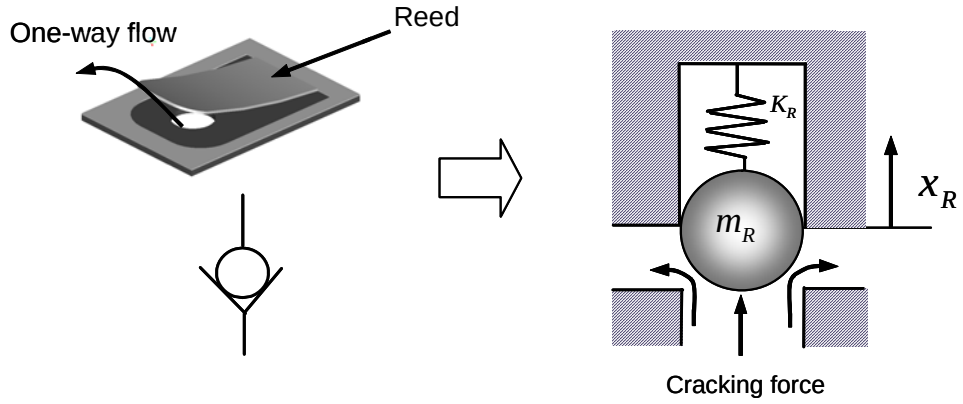

Figure 3-4: 1-DOF lumped parameter model for reed valve

The continuous dynamics PZT stack can be reduced into a single degree of freedom system by considering the only first mode shape, since the nominal operational frequency ranges (200 Hz) is much lower than the first natural frequency of the PZT stack used (e.g., about 20 kHz). Based on this assumption, the expression for the generalized displacement of the PZT stack is given by following equation [Oates et al., 2001]

$$m_p\ddot{x}_p + c_p\dot{x}_p + k_p x_p = n \cdot k_p \cdot d_{33} V_i(f) - P_p \cdot A_p \qquad \textbf{(}3.10\textbf{)}$$

where d_{33} is the piezoelectric coupling coefficient, $V_i(f)$ is the input voltage, n is the number of stack layers and m_p, c_p are the effective mass, damping constant of the PZT stack, respectively. k_p is the effective stiffness of PZT stack that can be derived from the linear constitutive law of the piezoelectric material.

For the reed valve opening (x_R) in Eq. **3.8** and Eq. **3.9**, the reed dynamics is also simplified as a single degree of freedom lumped model based on the fact that the first natural frequency of cantilever type reed valve in air is estimated to be 390 Hz. Since the nominal operational frequency (150 Hz to 200 Hz) is lower than the bandwidth of reed and will not excite the higher order modes of the reed valve, the governing equations of the reed opening displacements becomes

$$m_R\ddot{x}_R + c_R\dot{x}_R + k_R x_R = A_R \Delta P \qquad \textbf{(}3.11\textbf{)}$$

where $A_R \Delta P$ is cracking force, $m_R, c_R, k_R,$ and A_R represent the effective mass, damping constant and the effective stiffness, and the orifice (ϕ 3mm) area of the reed valve, respectively. With this approximation, reed valve can be modeled as a check ball valve,

which has narrow bandwidth, as shown in Figure **3-5**. This check valve model can be further simplified since the opening displacement of reed is limited due to the stopper to prevent the excessive deformation, which will affect the fatigue limit of spring steel reeds. In other words, it is nearly fast binary motion with fully opening of about 2 mm to be neglected the transient dynamics of reeds.

$$x_R = K_r \Delta P \qquad \textbf{(}3.12\textbf{)}$$

where K_r is the opening gain. This assumption can be verified with experimental result. As expected, measured flow rate shown in Chapter **2** shows the good linearity with driving frequency, which implies that orifice opening area of reed valve must be constant in the low frequency range (below 200 Hz) due to the fully opening. As a result, this reed valve is a passive valve, since the valve opening displacement cannot be controlled, as opposed to conventional hydraulic control valves. Like PWM solenoid valve system, only the total valve opening time can be modulated through the pulse frequency.

3.2.2 Open-loop Control Responses

Based on the derived governing equations, open-loop control response is simulated and compared with experimental results to validate the derived system model. Simulink® is used to simulate the open-loop responses of the overall system, as shown in Figure **3-5**. It consists of three main blocks: PZT stack transducer, piezoelectric-hydraulic pump, and hydraulic cylinder. The piezoelectric-hydraulic pump block also consists of pumping chamber and two reed valves. The simulation parameters and required dimensions are listed in Table **3-1**.

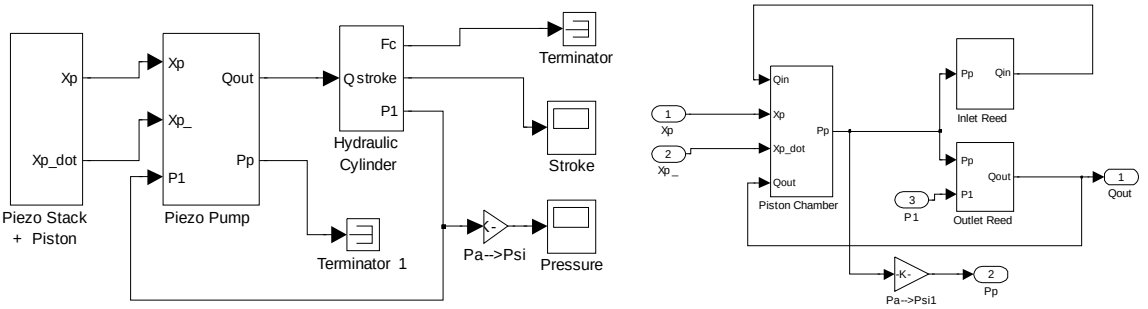

(a) piezo-hydraulic pump actuator (b) piezo-hydraulic pump

Figure 3-5: Simulink® model for simulation of open-loop control responses

In order to evaluate the time delay (i.e., fill time) and maximum pressure difference (i.e., available actuation force), step responses are examined. Figure **3-6** shows the simulation results for open-loop step responses. When the maximum step input (120 Voltage, 200 Hz) is applied around one second, the fill time for a 4 mm stroke turned out to be 0.32 second. Also, the generated maximum pressure difference 0.33 MPa is sufficient for shift control in the current AT.

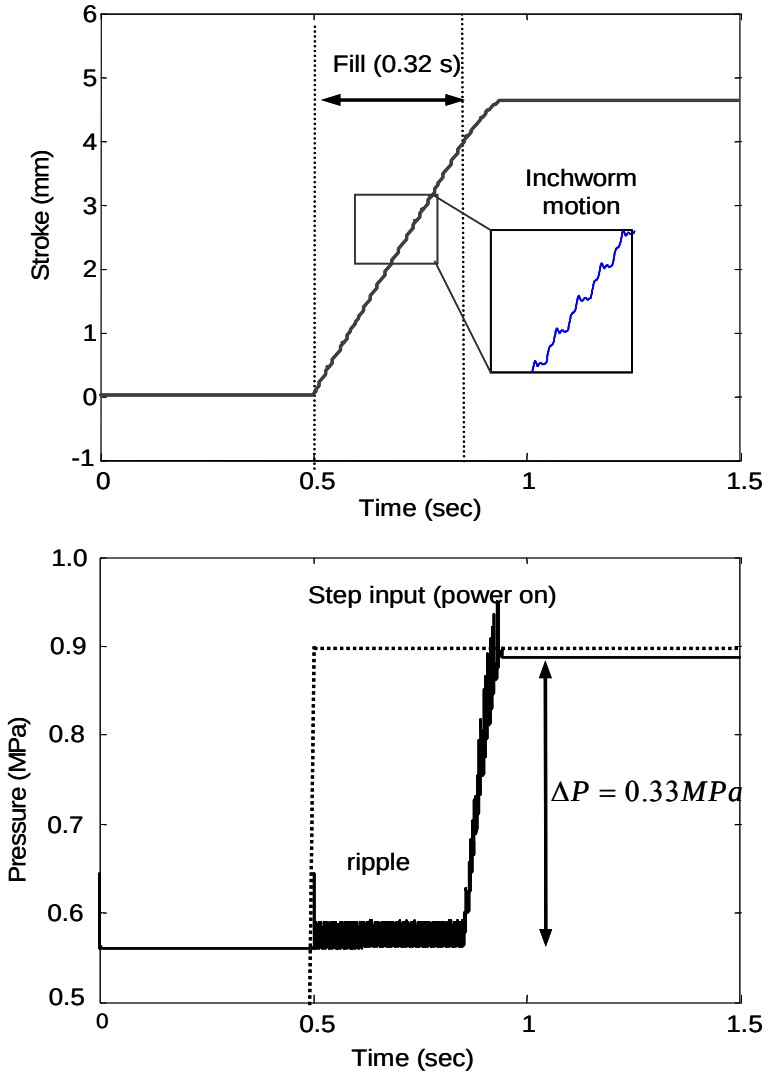

Figure 3-6: Simulation results of the open-loop step response to piezoelectric-hydraulic pump actuator

Experimental results for the open-loop step response are shown in Figure **3-7**. The pressure difference is 0.35 MPa and the fill time is 0.3 seconds. The experimental results are in good agreement with the simulation results, although there are some differences due to the uncertainties in the reed valves. From this comparison, the effectiveness of the system model is validated.

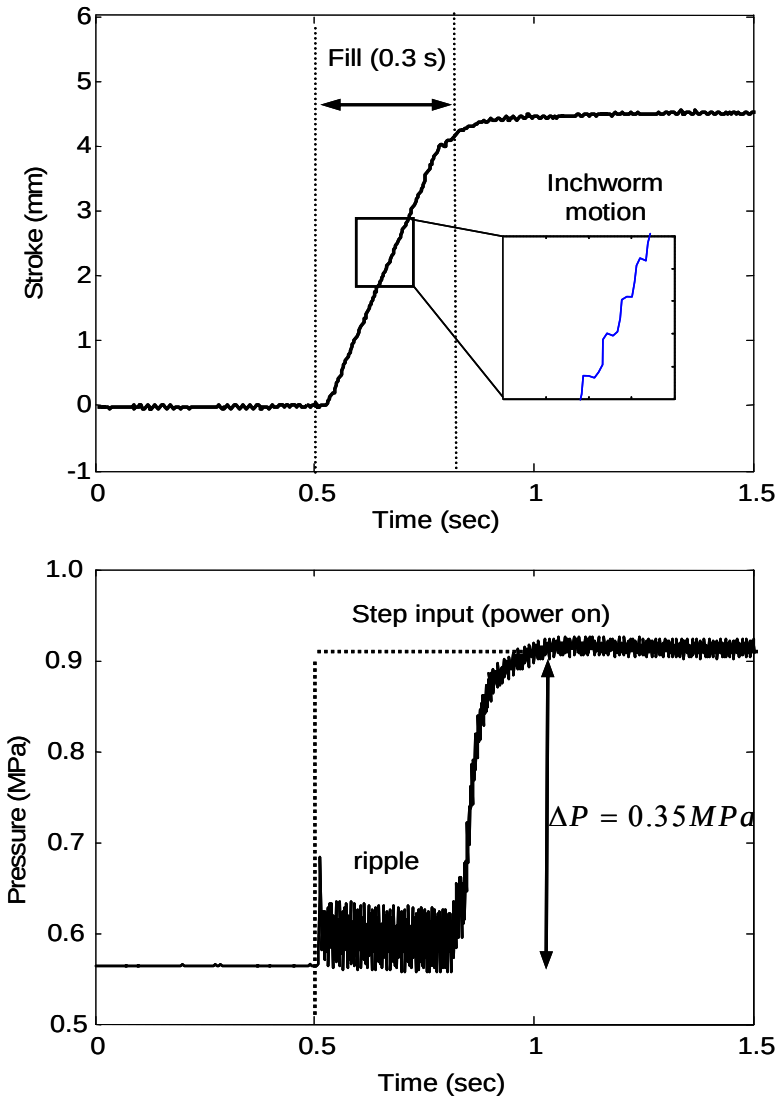

Figure 3-7: Experimental results of open-loop step response to piezoelectric-hydraulic pump actuator

3.3 Control Law Design

For controller design, the stick-slip friction force (F_f) in Eq. **3.2** and the leakage flow across the piston (Q_l) in Eq. **3.5** are assumed to be negligible, since the effect of the pre-charge using an accumulator can reduce the friction force in the piezoelectric-hydraulic pump based actuator [Nassar et al., 2000]. Moreover, the tight o-ring is replaced with a low friction U-cup seal, which is designed for superior sealing performance with minimal friction. The pumping pressure rise dynamics (i.e., Eq. **3.7**) is neglected because the control action is performed at the only steady state. Next, while the pumping pressure is oscillating due to the pulse operation of pump, as shown in Figure **3-8**, only the discharging flow rate is considered in this research by neglecting the suction flow rate for the controller design since the control action is only performed while discharging.

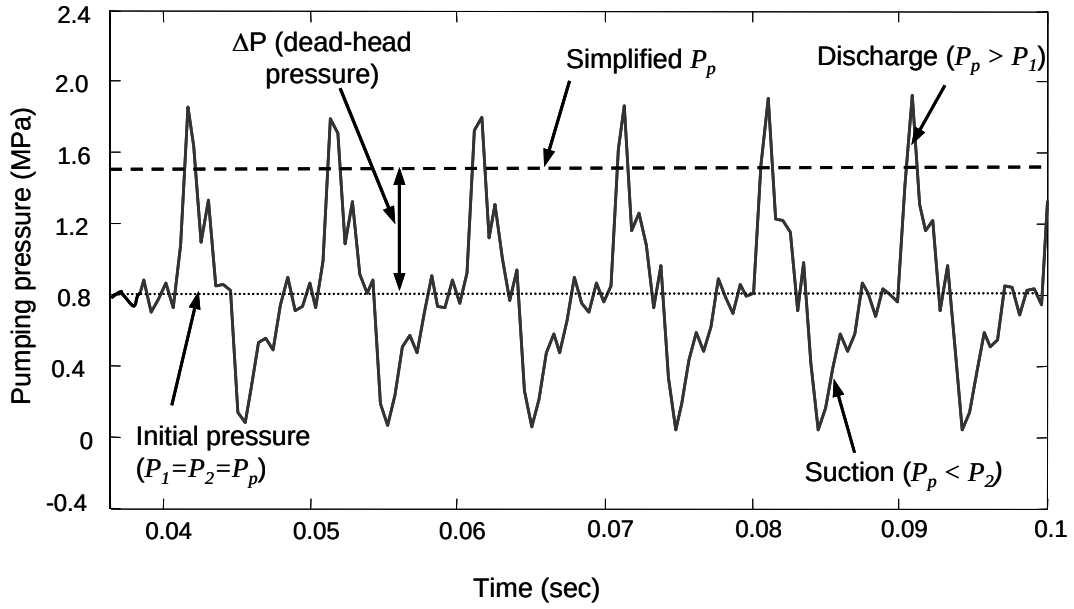

Figure 3-8: Alternating wave patterns for the pumping pressure (100Hz)

The pumping pressure is derived by taking the RMS averaging value for discharging pulse (i.e., upper part) based on the aforementioned assumption and is viewed as the supply pressure. This pumping pressure is mainly proportional to the stroke of the PZT stack (x_P) in Eq. **3.7** under the same accumulator pressure. Since the response time of a multi-layered (co-fired) type PZT stack transducer used in this thesis research (approximately $200\ \mu\text{sec}$ for square pulse of 200 V [Yury et al., 2007]) is much shorter than the pulse duration time of the operating frequency, the governing equation for the PZT stack shown in Eq. **3.10** can be simplified as the static by neglecting the transient characteristics of the PZT stack and the pressure pre-load, which is much smaller than induced block force of PZT stack

$$x_p = K_p V_i(f) \tag{3.13}$$

Substituting Eq. **3.13** into Eq. **3.12,** the opening displacement of the inlet reed valve can be treated as the control input

$$x_R = K_r \cdot K_c x_p = K_r K_c K_p \cdot V_i(f) = K_g V_i(f) \tag{3.14}$$

where $V_i(f)$ is the control input voltage pulse (120 Volt with frequency f_c), and K_g is the final control gain. By introducing these assumptions, the final governing equations for the designing of the controller can be expressed as following state equations:

$$\begin{aligned}
\dot{x}_1 &= x_2 \\
\dot{x}_2 &= \frac{1}{m}(F_a - F_e) \\
\dot{x}_3 &= \frac{\beta_e}{(V_o + A_1 x_1)}\left[G_c \sqrt{P_P - x_3} \cdot V_i(f) - Q_l - A_1 x_2 \right],
\end{aligned} \tag{3.15}$$

where x_1 is the cylinder displacement (stroke), x_2 is the cylinder velocity, x_3 is the actuation pressure (P_1), $G_c (= C_d w\sqrt{2/\rho} K_g)$ is the control flow gain, and Q_l is the leakage flow rate in the outlet reed valve, which is zero while discharging. Since the output of interest here is the actuation force, the output is $y = A_1 x_3 - A_2 P_2$ from Eq. **3.3** . Governing equation (Eq. **3.15**) also indicates that the control input ($V_i(f)$) appears explicitly in the output (zero relative degree). Based on this system model, two separate controllers are designed for two governing motions of actuator, during the fill and actuation stage.

3.3.1 Fill Stage ($x \le x_s$)

During the fill stage, open-loop Bang-Bang control is utilized based on the concept of minimum time control resulting from the shortest fill time requirement.

$$J = \int_0^{t_f} dt = t_f$$
$$\textit{subject to } u_{\min} \le u(t) \le u_{\max} \qquad \textbf{(}3.16\textbf{)}$$

Application of the Pontryagin's minimum principle leads to following open-loop fill solution, which is to apply the maximum flow rate until the end of fill.

$$V_i = V_i(f_{\max}). \qquad \textbf{(}3.17\textbf{)}$$

The maximum pulse frequency ($f_{\max}$) for maximum desired fill volume can be calculated based on the open-loop experimental results. Hence, time-based open-loop control can be adopted during the fill stage.

3.3.2 Actuation Stage ($x > x_s$)

In order to develop the nonlinear force tracking control law during the actuation stage, a sliding mode controller is proposed.

$$u = u_{eq} + u_{switching} \tag{3.18}$$

where u_{eq} is the equivalent feedback control input to reach the state on the sliding surface and $u_{switching}$ is the discontinuous control input to keep the state on the sliding surface ensuring the robustness. Unlike the standard tacking control problem, equivalent control input term, however, can be ruled out for AT shift control since initial state (i.e., initial force) is always coincident with the desired reference trajectory, as shown in Figure **3-9** .

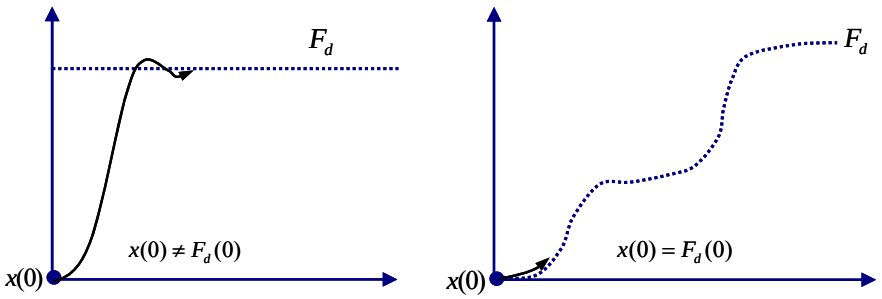

(a) standard (b) AT shift control

Figure 3-9: Graphical interpretation of two tracking control problems

Now, define the sliding surface for the derived system model ($n = 3$).

$$s = \left(\frac{d}{dt} + \lambda \right)^{n-1} \cdot e = \ddot{e} + 2\lambda\dot{e} + \lambda^2 e \tag{3.19}$$

where e is a force tracking error between the desired actuation force (F_d) and the actual actuation force (i.e., $e = F_d - F_a$), and λ is the strictly positive constant. This controller

design requires many differentiation operators, which is impractical in controller implementation. This difficulty can be reduced using a reduced order sliding surface ($s = e$) with only the third equation of Eq. **3.15** based on the fact that the control input ($V_i(f)$) appears explicitly in the output state (zero relative degree). Once the PHP actuator generates the sufficient control flow rate (Q_c) satisfying the sliding mode condition, the tracking error can be converging along the sliding surface by the discontinuous control law (switching control law)

$$u_{switching} = sign(s). \qquad \textbf{(}3.20\textbf{)}$$

This simple but effective controller can be interpreted physically by defining that the sliding surface is the tracking error. As illustrating in Figure **3-10** , if the actual force is lower than the desired actuation force ($e > 0$), it is clear that the actual force will be raised by increasing actuation pressure through the supplied flow rate (Q_c). If the actual force is higher than the desired force ($e < 0$), the actual force will be slightly dropped due to the leakage flow in the outlet reed valve. As a result, the actual force can track the desired force between two control modes, which are known as the 'sliding mode'.

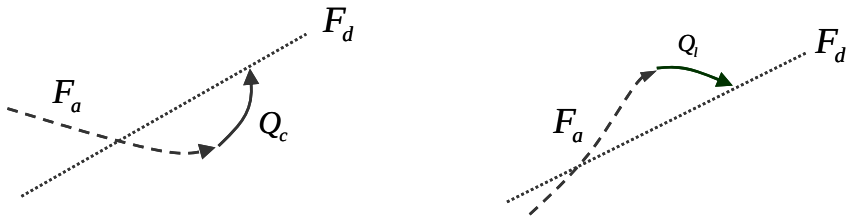

(a) $F_d - F_a > 0$ (b) $F_d - F_a < 0$

Figure 3-10: Physical interpretation of switching control action

The advantages of this switching controller are such that it does not require not only cylinder position and velocity feedback but also much gain tuning. An additional advantage of this switching controller is the elimination of the pulse frequency modulation (in short, PFM), which is typically required to convert the designed continuous control input into pulse input. For example, the Lyapunov-based nonlinear controller has been used for designing a continuous control input [Sohl, 1999]. In a similar manner, the control law for piezoelectric-hydraulic pump actuator can be designed using the Lyapunov direct method.

$$Q_c = \frac{V_o + A_1 x}{A_1 \beta_e}\left[\dot{F}_d + k_2 e + \dot{x}\left[\frac{A_1^2 \beta_e}{V_o + A_1 x}\right]\right] \qquad (3.21)$$

In fact, this continuous control input is identical to the equivalent feedback input of sliding mode controller. It needs to be converted into the pulse signal to drive the piezo-hydraulic pump through the pulse frequency modulation. Furthermore, the controller requires the position (x) and velocity of piston ($\dot{x}$) information in addition to pressure. Many nonlinear controllers with continuous control input have been reported using nonlinear, adaptive and robust control theory. Critical implementation issue of these controllers is the requirement of full state feedback ($x, \dot{x}, \text{and } P_1$). This is not cost-effective and impractical for AT shift control. In addition, since the signal condition of all state variables is affected by noise due to pulse modulation, the tracking performance is also degraded. In order to implement this switching control input for pulse-driven PHP actuator, simple modulating scheme is needed such that the PHP actuator will possess aforementioned switching modes;

- On mode: $V_i = V_i(f_c)$ if $u = +1$
- Off mode: $V_i = 0$ if $u = -1$. **(**3.22**)**

3.3.3 Sliding Mode Condition

Once the piezoelectric -hydraulic pump generates sufficient controlled flow rate (Q_c), the tracking error can be asymptotically converged along $s = 0$. This convergence ability of the force tracking error during the actuation stage should be proven mathematically. If the actuation force trajectory is assumed to be a differentiable function, the derivative of actuation force defined in Eq. **3.3** yields the following equation since accumulator pressure (P_2) is constant.

$$\dot{F}_a = A_1\dot{P}_1 - A_2\dot{P}_2 = A_1\dot{P}_1 \quad \textbf{(}3.23\textbf{)}$$

By denoting control flow rate $Q_c (= G_c\sqrt{P_P - x_3}\cdot V_i(f))$ and substituting Eq. **3.15** into Eq. **3.23** yields:

$$\dot{F}_a = A_1\left[\frac{\beta_e}{(V_o + A_1 x)}(Q_c - Q_l - A_1\dot{x})\right] \quad \textbf{(}3.24\textbf{)}$$

Based on Eq. **3.22,** Eq. **3.24** can be re-written as follows:

$$\dot{F}_a = \begin{cases} -\dfrac{A_1^2\beta_e}{(V_o + A_1 x)}\dot{x} + \dfrac{A_1\beta_e}{V_o + A_1 x}Q_c = -A_1\alpha\dot{x} + \alpha Q_c, & u = +1, \\ -\dfrac{A_1^2\beta_e}{(V_o + A_1 x)}\dot{x} - \dfrac{A_1\beta_e}{V_o + A_1 x}Q_l = -A_1\alpha\dot{x} - \alpha Q_l, & u = -1. \end{cases} \quad \textbf{(}3.25\textbf{)}$$

where α is positive parameters defined as follows:

$$\alpha = \frac{A_1 \beta_e}{(V_o + A_1 x)} \tag{3.26}$$

We also define the following Lyapunov function:

$$V = \frac{1}{2} s^2 \tag{3.27}$$

The sliding surface $s \equiv 0$ is reached within a finite time when the following sliding condition for the positive constant (η) is satisfied [Slotine, 1991].

$$s\dot{s} \le -\eta |s| \tag{3.28}$$

From Eq. **3.23**, the derivative of the sliding surface becomes

$$\dot{s} = \dot{F}_d - A_1 \dot{P}_1 \tag{3.29}$$

Substituting Eq. **3.29** and Eq. **3.19** into Eq. **3.28** results in the following equations:

$$s\dot{s} = \begin{cases} s\left(-\alpha Q_c + A_1 \alpha \dot{x} + \dot{F}_d\right) & , u = +1, \\ s\left(\alpha Q_l + A_1 \alpha \dot{x} + \dot{F}_d\right) & , u = -1. \end{cases} \tag{3.30}$$

Next, assume that the bounded α, Q_c, Q_l, and $\dot{F}_d$ can be chosen for a given positive η such that

$$\alpha Q_l + A_1 \alpha \dot{x} + \dot{F}_d > \eta \tag{3.31}$$

$$-\alpha Q_c + A_1 \alpha \dot{x} + \dot{F}_d < -\eta. \tag{3.32}$$

Then, if $s < 0$ (i.e., $u = sign(s) = -1$), the following condition can be always true from Eq. **3.30** and Eq. **3.31**.

$$s(\alpha Q_l + A_1 \alpha \dot{x} + \dot{F}_d) < \eta s < 0. \tag{3.33}$$

Also, if $s > 0$ (i.e., $u = sign(s) = +1$), this condition becomes.

$$s(-\alpha Q_c + A_1 \alpha \dot{x} + \dot{F}_d) < -\eta s < 0. \quad \textbf{(}3.34\textbf{)}$$

In both cases, the sliding condition (Eq. **3.28**) is always satisfied.

It can be shown that $\alpha, Q_l, \dot{x}$, and $\dot{F}_d$ are explicitly bounded to satisfy the sliding condition. First, note that the derivative of reference force ($\dot{F}_d$) consists of only positive gradients since the negative slope tracking control is generally not required in AT shift control, Since I can design $F_d(t)$ with the finite Lipschitz constant K such that $0 < \left|\dot{F}_d(t)\right| \le K < \infty$ on the control time interval [t_1, t_2], $F_d(t)$ must be Lipschitz continuous, which implies that the derivative of $X(t)$ is bounded with positive Lipschitz constant K defined as

$$\frac{\left|X(t_2) - X(t_1)\right|}{t_2 - t_1} \le K \quad for\ t_1 < t_2 \quad \textbf{(}3.35\textbf{)}$$

Since and the stroke of the hydraulic cylinder is also physically limited (i.e., $x_0 \le x(t) \le x_s$) and and the stroke is changed smoothly after contacting the second spring (band brake), by the same token, it must be Lipschitz continuous function during the control interval.

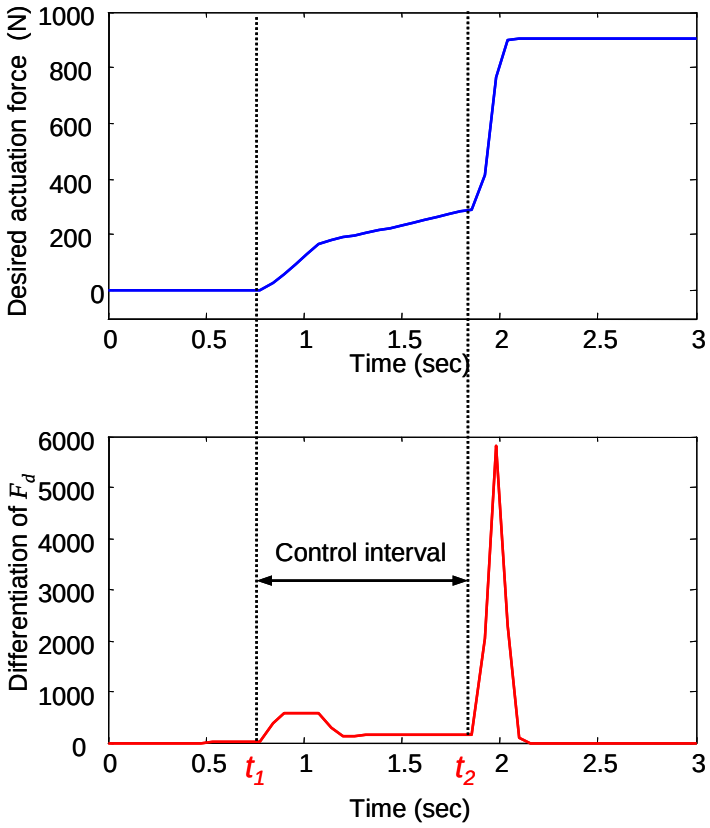

Figure 3-11: Typical desired actuation pressure trajectory used in the current AT

Next, the ram area of hydraulic cylinder and control volume must be a finite value due to the design constraint. The effective bulk modulus in hydraulic compliance, however, has uncertainties due to the pressure variation and uncertain entrapped air, as shown in Figure **3-12** [Waton, 1989].

$$\beta_{e\min} \le \beta_e(t) \le \beta_{e\max} \tag{3.36}$$

Hence, parameter α can be bounded by following expressions

$$0 < \alpha_{\min} \le \frac{A_1 \beta_e}{(V_o + A_1 x_1)} \le \alpha_{\max} \tag{3.37}$$

where $\alpha_{\min} = \frac{A_1 \beta_{e\min}}{(V_o + A_1 x_s)}$ $\alpha_{\max} = \frac{A_1 \beta_{e\max}}{(V_o + A_1 x_0)}$. Bounds Eq. **3.37** can be rewritten by other bounded form

$$\sigma^{-1} \le \frac{\hat{\alpha}}{\alpha} \le \sigma \tag{3.38}$$

where $\hat{\alpha} = \sqrt{(\alpha_{\max} \cdot \alpha_{\min})}$ is the estimate of α as the geometric mean of the bounds, $\sigma = \sqrt{(\alpha_{\max} / \alpha_{\min})}$.

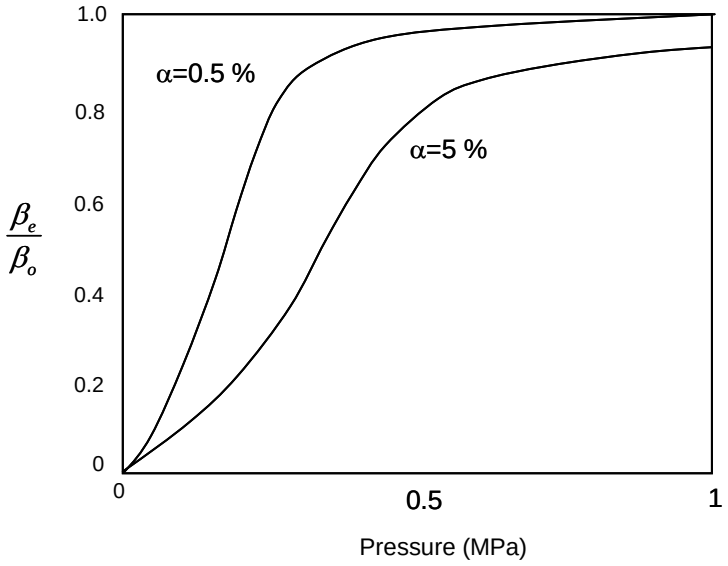

Figure 3-12: Effect of the ratio of entrapped air to fluid (α) on fluid bulk modulus

Finally, when pump off, the actuating pressure P_1 is also always higher than initial accumulator pressure P_2. Hence, the leakage flow in outlet reed valve Q_l $(= G_l \sqrt{P_1 - P_2})$ is also bounded by the maximum leakage flow rare $Q_{l\max}$ that can occur at the maximum pressure differences. Consequently, the proposed sliding mode controller guarantees bounded input/bounded output (BIBO) stability.

3.4 Experimental Validation

3.4.1 Controller Implementation

Control experiment is performed to validate the effectiveness of proposed controller. The experimental set-up for implementation consists of a dSPACE system, a TTL pulse generator, a two-level driver, and the piezoelectric-hydraulic pump based actuator, as shown in Figure **3-13**. Designed control law will be implemented in the dSPACE system. A high resolution pressure transducer also will be used to measure and calculate the actuation force. Figure **3-14** shows the photograph of the overall control experimental setup. Once the control starts, the maximum pulse frequency ($f_{\max}$), 200 Hz, is first applied to the PHP-based actuator to fill the dead stroke fill volume and the actuation force calculated from measured pressure will be sent to the dSPACE system. The measured pressure is filtered using a low-pass filter (cutoff frequency of 20 Hz) because it contains fine pressure ripples caused by pulse driven actuation of pump. According to the control law of Eq. **3.20** and Eq. **3.22,** the feedback control input voltage (V_i) is determined after the fill stage. This control input should be pulse voltage with constant amplitude and varying frequency. It enables us to use a different driver (e. g., switching type driver) for large PZT stack transducer. Compared with a linear power amplifier, this cutting-edge driver features compact structure, higher efficiency and superior compensation capability for large capacitive loads (i.e., 30 μF of PZT stack) at high frequencies, which are appropriate for automotive applications.

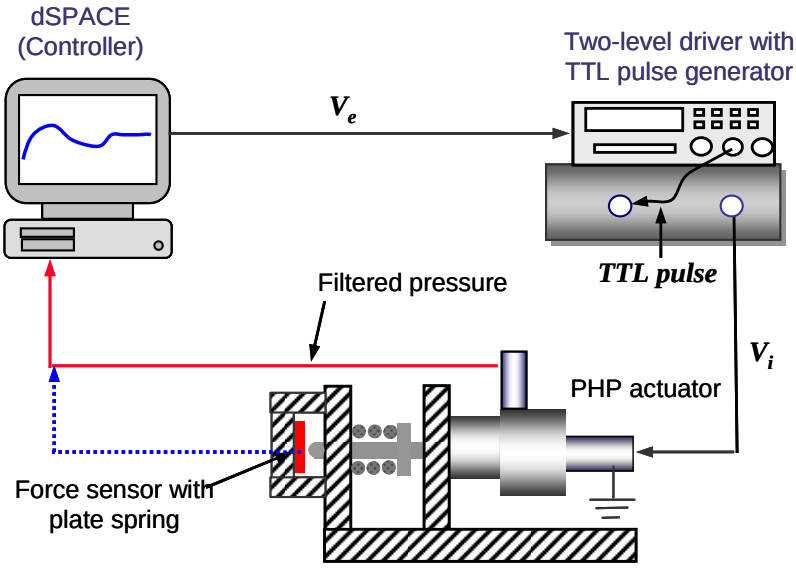

Figure 3-13: Configuration diagram of control experiment set-up

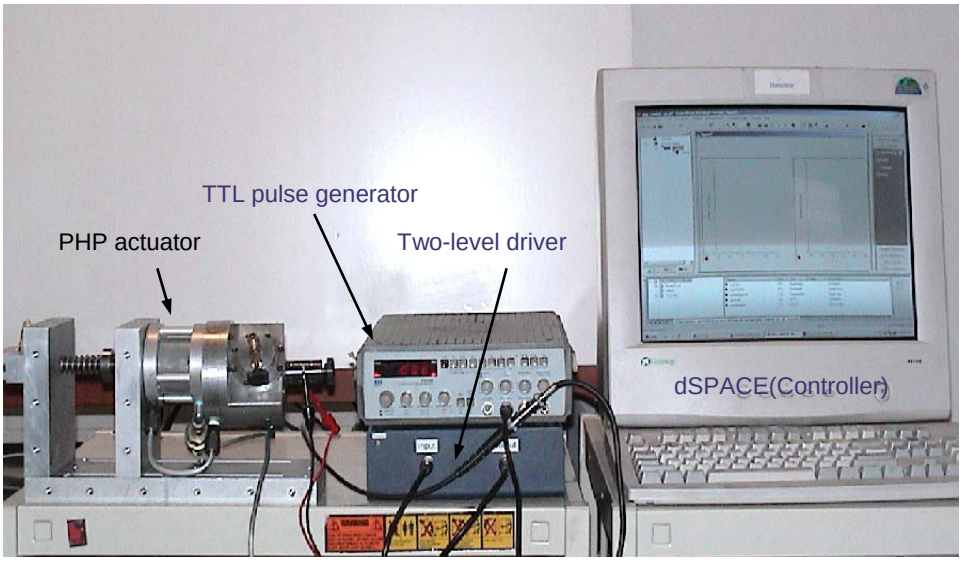

Figure 3-14: Photograph of overall control experiment set-up

Implementation of the control law requires an intermediate stage since the customized driver has to be driven by transistor–transistor logic (in short, TTL) pulse. Therefore, the control input should be converted into the equivalent control (V_e), which in turn will be an input to the TTL pulse generator. The final control pulse input voltage will be eventually applied to the PZT stack through the switching driver in short circuit. Obviously, it will be identical to the original control input (V_i). Voltage-controlled frequency (in short, VCF) function of TTL pulse generator is used to convert control frequency of control input into the equivalent control input voltage. According to the sensitivity curve, as shown in Figure **3-15**, pulse frequency of the control input will be proportionally converted into the equivalent control input voltage,.

$$V_e = 0.05 f_c \qquad \textbf{(}3.39\textbf{)}$$

where f_c is the control pulse frequency, which will be TTL pulse frequency.

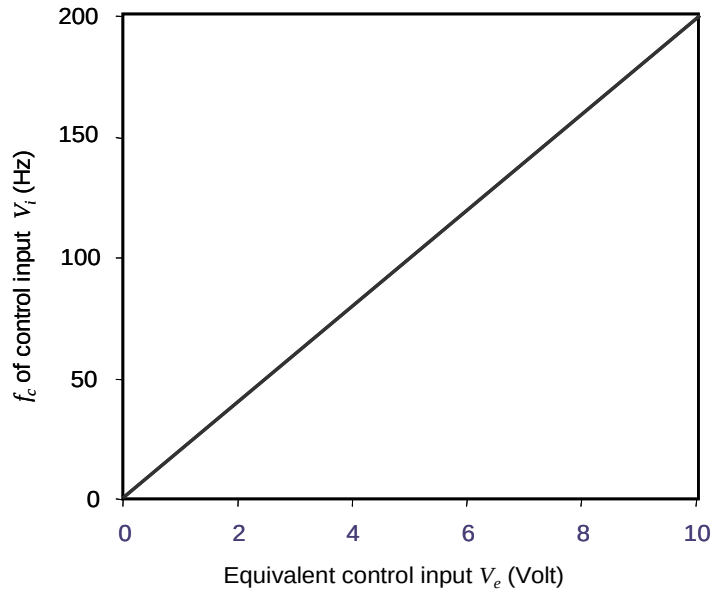

Figure 3-15: Sensitivity curve for voltage-controlled frequency (VCF) implementation

The aforementioned controller implementation procedure is illustrated by the wave forms of the various control signals in Figure **3-16** .

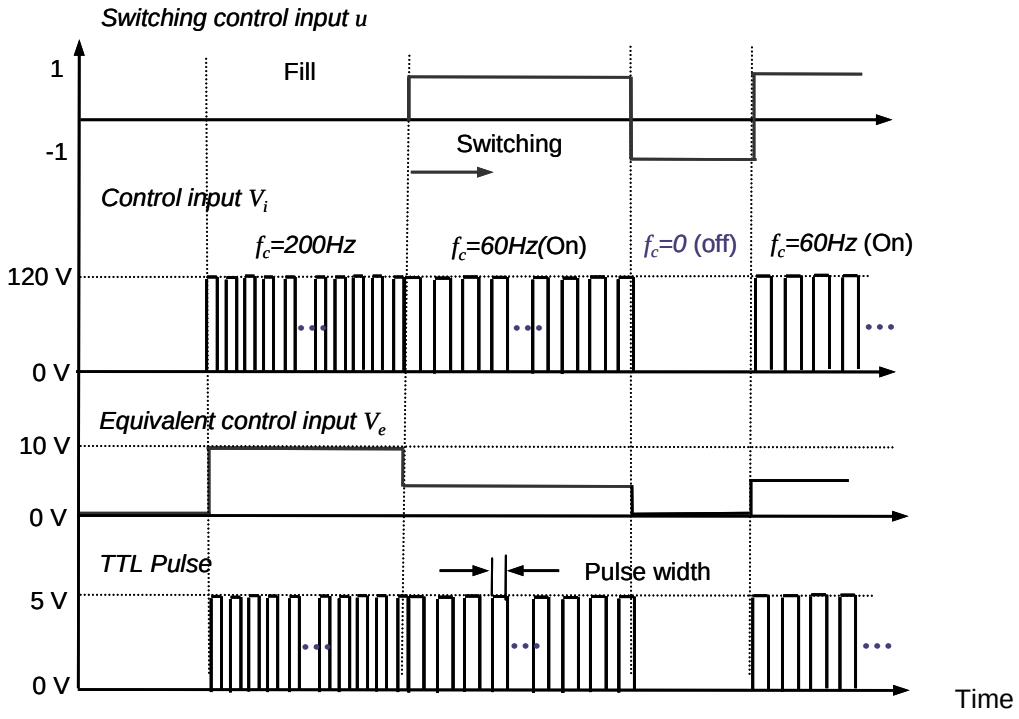

Figure 3-16: Wave forms of individual control signals

The example TTL pulse of 100 Hz is illustrated in Figure **3-17**. Since the opening duration time of reed valve is directly related to the pressure characteristic and its ability to generate dead-head pressure [Tan, 2005], an optimum pulse width of TTL pulse input is determined. Based on the experimental results illustrating in Chapter **2**, the duty ratio of TTL pulse is chosen to be 60 %, since it shows the largest pressure difference under normal operational conditions.

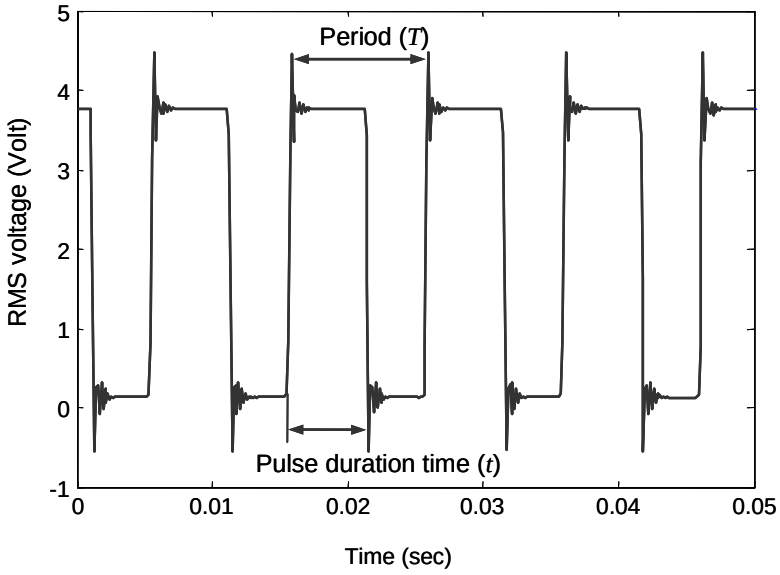

Figure 3-17: TTL pulse for two-level driver: 60 % duty ratio, rise and fall time (<24ns)

The driver switches a large capacitive load between low level (e.g., 0 Volt) and high level (e.g., 120 Volt to 150 Volt) according to the TTL pulse**.** With this different topology, this driver can provide sufficient current required for producing fast rise/fall time ($250\ \mu\text{sec}$) [Dynamic Structure & Materials, LLC]. The overall controller implementation can be represented by the block diagram, as shown in Figure **3-18**.

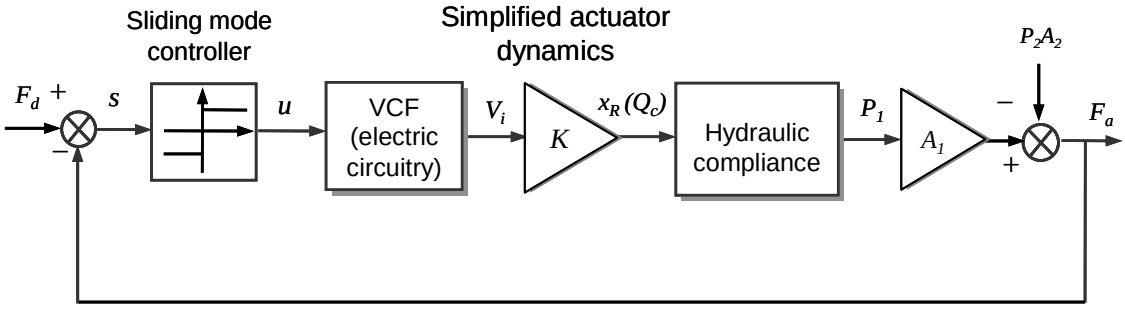

Figure 3-18: Block diagram for actuation force tracking control

Finally, the proposed controller is coded in MATLAB/Simulink and a dSPACE® (model: 1103 board) is used to perform the real time control task, as shown in Figure **3-19** . The real time workshop (RTW) module in the dSPACE® system converts the controller in Simulink into an executable C code and downloads it into the microprocessor built in the dSPACE® board. The sampling rate was set to be 1000 μsec . The dSAPCE® system converts analog inputs (i.e., from pressure or force transducer) into digital inputs using built-in A/D converter with 16-bit output resolution. The digital output (i.e., equivalent control input) is converted into analog output voltage through the built-in D/A converter.

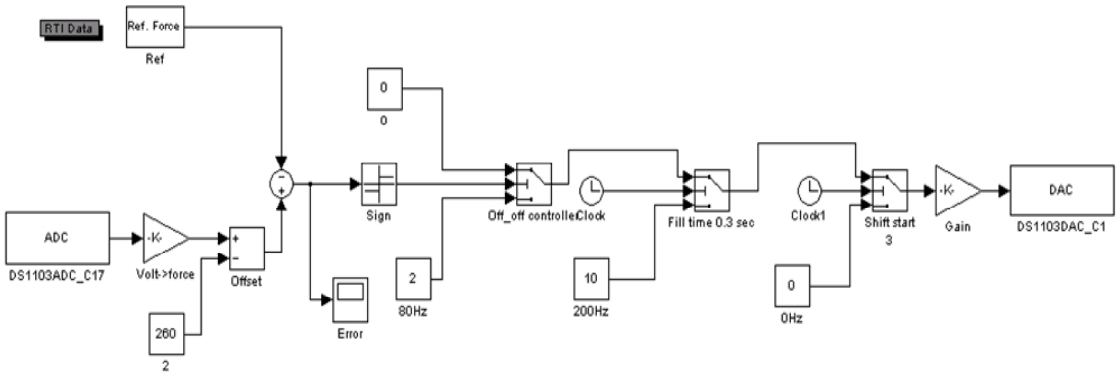

Figure 3-19: Switching controller coded in MATLAB/Simulink

The open-loop control responses are first investigated to confirm the voltage-controlled frequency (VCF) implementation, as shown in Figure **3-20** . With varying equivalent control input voltages, the TTL pulse generator can successfully generate the corresponding pulse frequencies. In addition, it can be shown that the similar actuation force with the desired force trajectory can be produced by even open-loop control, and self-locking capability of actuation force is confirmed after turning off the PHP actuator.

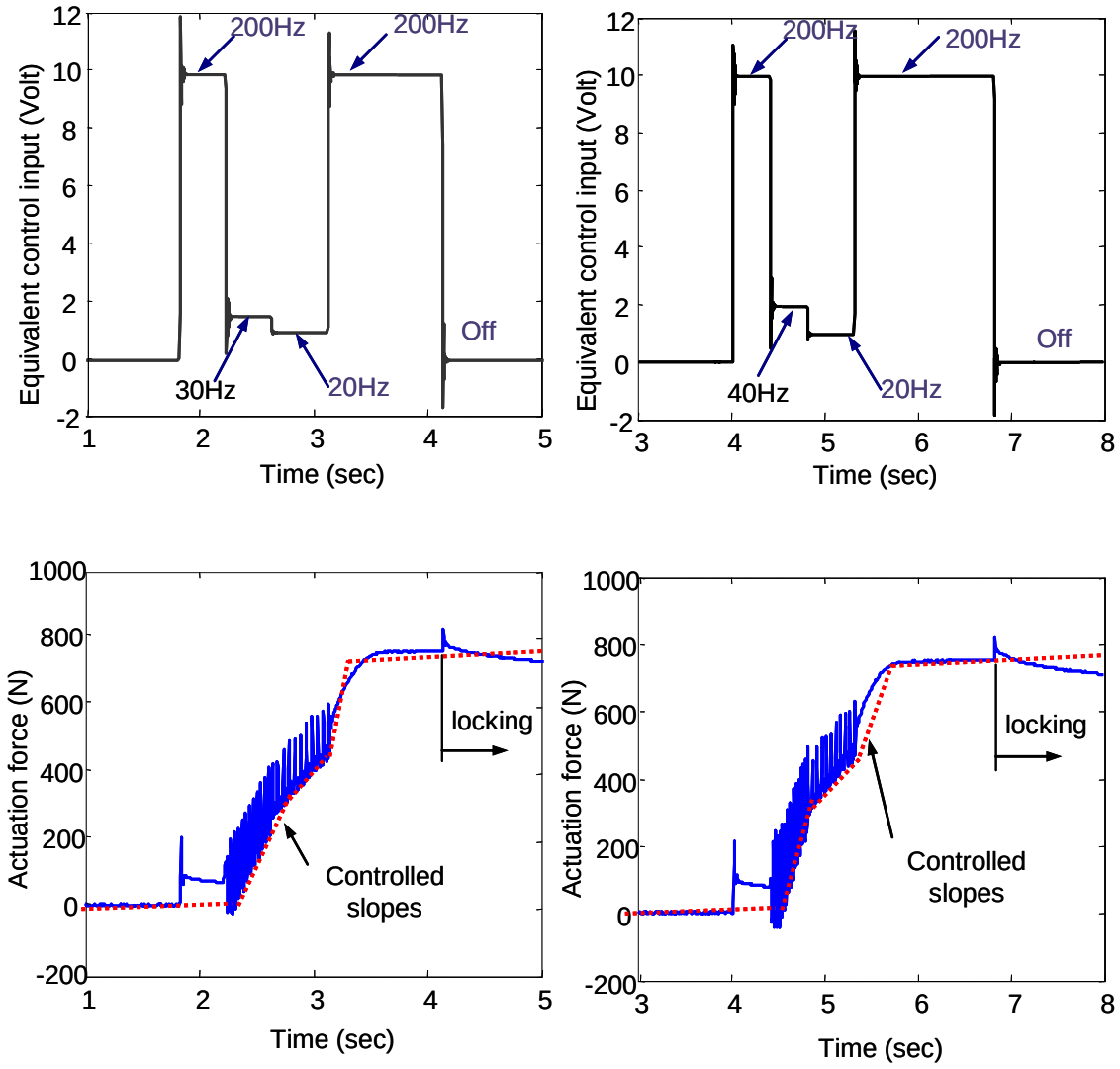

Figure 3-20: Open-loop actuation force control responses (P_2 = 0.55 MPa, V_i = 120)

3.4.2 Actuation Pressure Tracking Control Results

Control experiments and simulations are conducted to validate the proposed control approach. The initial accumulator pressure is set to be 0.55 MPa and control input voltage of 120 V is applied. Maximum pulse frequency for filling the dead-stroke volume of hydraulic cylinder is initially scheduled as 200 Hz (i.e., 10 V) for 0.35 sec and the control frequency f_c is set to be 60 Hz (i.e., 3 V) to generate the required control flow rate satisfying the following sliding mode condition derived from Eq. 3.32.

$$Q_c > \frac{1}{\alpha}(\eta + A_1\alpha\dot{x} + \dot{F}_d) \tag{3.40}$$

Under the normal control conditions (accumulator pressure of 0.55 MPa, $\beta_e \approx 150\,\text{MPa}$), required control flow rate Q_c is calculated to be 4 cc/s for large η $(10 \text{ to } 1000)$, which can be generated at pulse frequency of 40 Hz, as confirmed in the flow rate evaluation result in Chapter **2**. The desired force trajectory is determined based on the developed performance of PHP actuator described in Chapter **2**. For example, a maximum actuation force of 700 N in the reference trajectory is corresponding to dead-head pressure of 0.38 MPa under 0.55 MPa accumulator pressure.

Examples of the actuation pressure tracking control response are illustrated in Figure **3-21**. All parameters, dimensions, and gains for simulation are listed in the Table **3-1**. The controlled actuation force can successfully track the desired reference trajectory in both simulation and experiment. A relatively large tracking error around two second is due to the insufficient control flow rate. In other words, the slope (i.e., derivative) of desired trajectory ($\dot{F}_d$) becomes much higher, while control flow rate is

fixed (Eq. **3.40**). However, this is acceptable in AT shift control, since this higher force is typically not required for shift transient control but is to prevent the slippage of friction elements (i.e., locking) for safety reasons. Chattering with lower switching frequency (about 10 Hz) is occurring in experimental result.

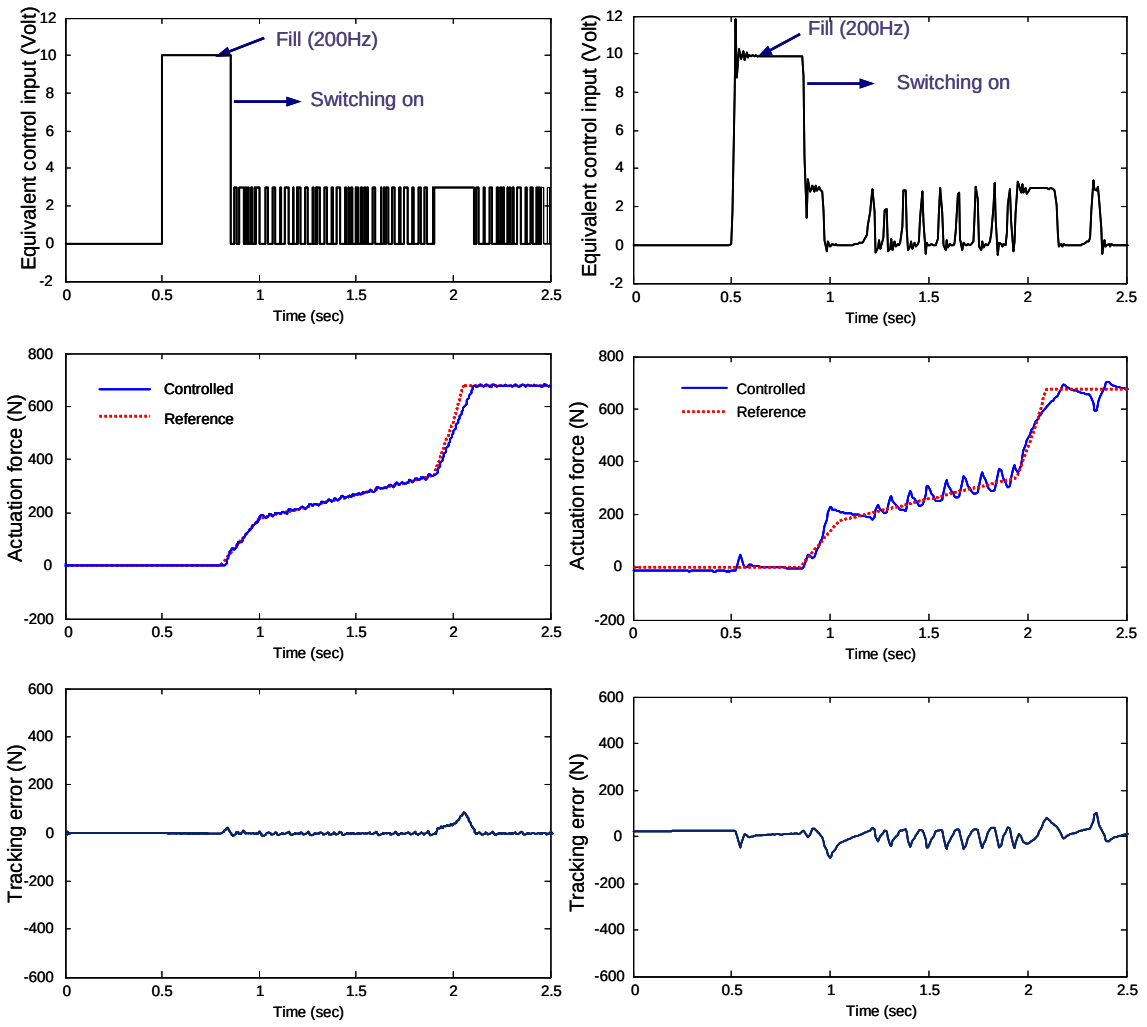

(a) simulation (ideal case) (b) experiment

Figure 3-21: Pressure tracking control responses of band brake actuation system with PHP actuator ($P_2 = 0.55$ MPa, $V_i = 120$ V, $f_c = 60$ Hz)

3.4.2.1 Chattering Phenomenon

The chattering phenomenon illustrated in Figure **3-21** is undesirable in practice, for it can excite the low frequency dynamics of friction elements. Accordingly, the reason for this chattering has to be identified and resolved. Note that the fine switching action itself shown in ideal case of simulation shown in Figure **3-21** (a) is *not* called 'chattering' since the switching is intended for guaranteeing the robustness and its frequency tends to infinity [Utkin ,1999]. Two well-known traditional methods are first used to resolve the chattering. The higher sampling frequency is set to be $100\,\mu$sec to prevent 'discretization chatter' due to digital controller. The sign function is also replaced with following saturation function with boundary layer thickness.

$$sat(s/\Phi) = \begin{cases} s/\Phi & if\ |y| \le 1 \\ sign(s/\Phi) & otherwise \end{cases} \tag{3.41}$$

where Φ is a positive constant. Experimental results using these methods are shown in Figure **3-22**. However, these methods turned out to be not effective to resolve this chattering with finite switching frequency. In the case of using saturation function, tracking error is not converged to zero, which means it deviated from the zero in the middle of the desired trajectory.

The other possible reason for this chattering is the fast actuator dynamics, which involves simplified reed valve and unmodeled electric circuit dynamics. These fast dynamics are known as the major factor leading to deterioration of the perfect switching in sliding mode control [Utkin and Lee, 2006]. It is often excited by the fast switching control input.

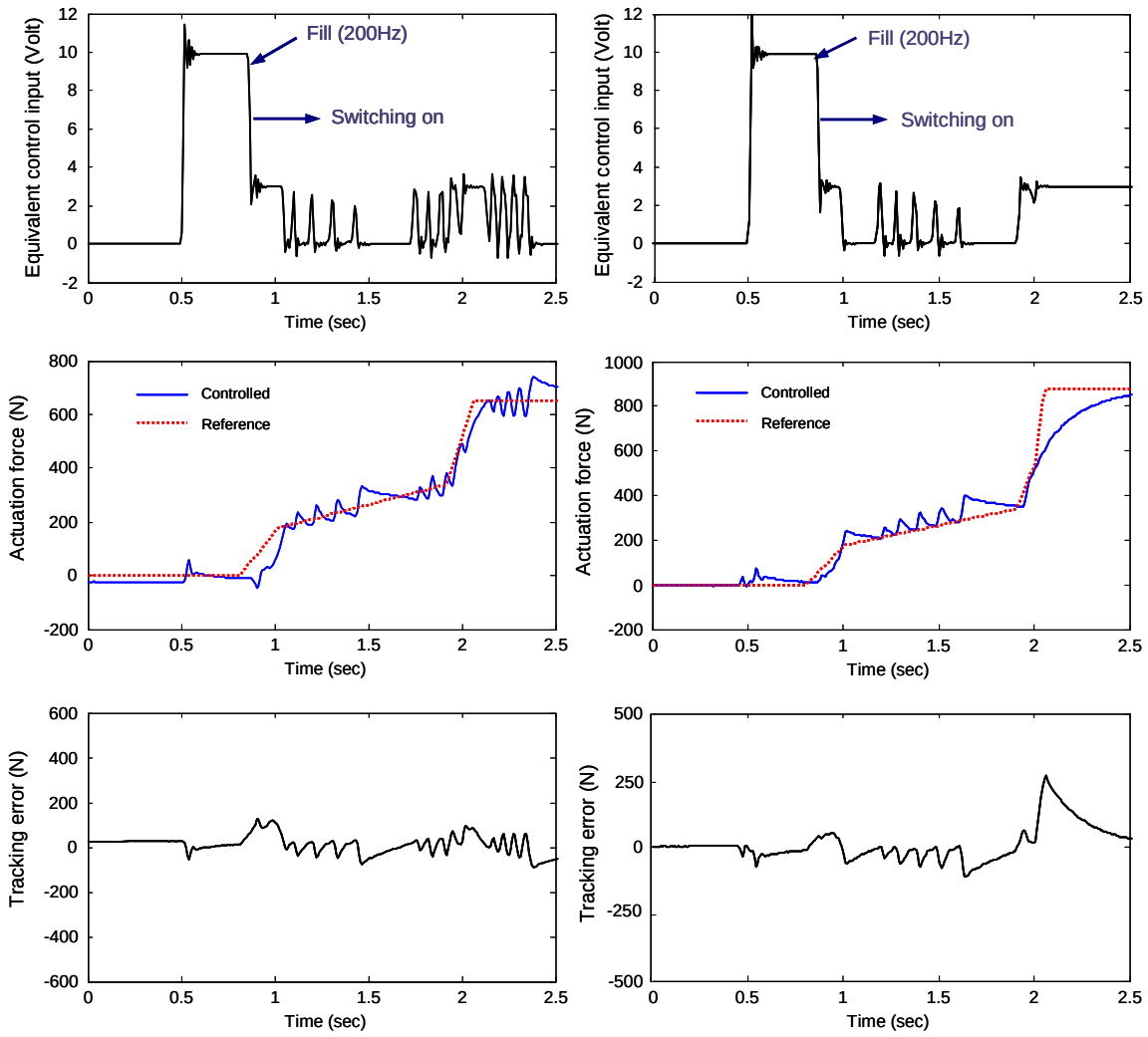

(a) higher sampling time (b) saturation function (Φ=10)

Figure 3-22: Pressure tracking control responses of band brake actuation system with higher sampling rate and saturation function (P_2 = 0.55 MPa, V_i = 120 V, f_c = 60 Hz)

The fast actuator dynamics can be take into account in the closed control loop as follows;

$$w(s) = \frac{1}{(s+1)^n} u(s) \tag{3.42}$$

where $w(s)$ and $u(s)$ are Laplace transforms of $w(t)$ and $u(t)$. Then, actual control input captured by dynamic signal analyzer will be delayed continuous input $w(t)$, instead of discontinuous $u(t)$, as shown in Figure **3-23** . From the shape of transient response, the effects of neglected actuator dynamics can be considered by assuming as the second-order system with rise time (t_r=0.02 sec).

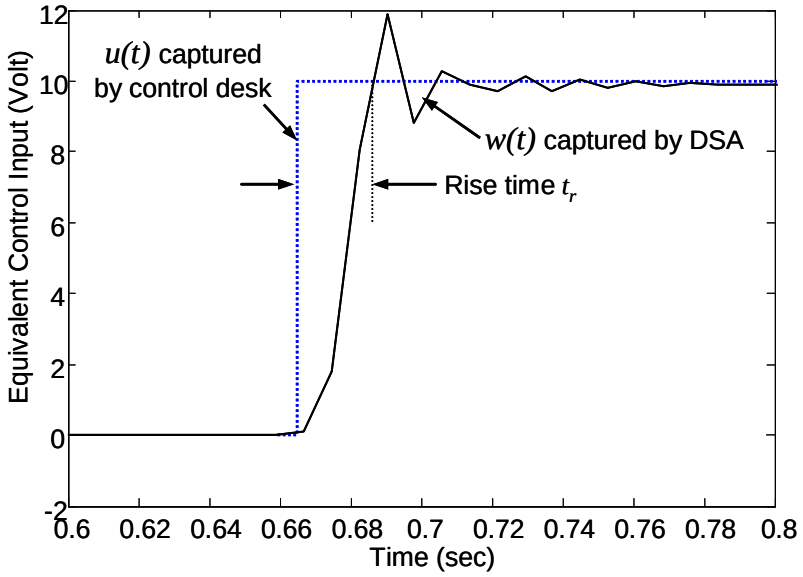

Figure 3-23: Actual control input representing unmodeled actuator dynamics

By taking into account the second-order actuator dynamics, lower switching frequency shows good agreement between the simulation and experiment results, as shown in Figure **3-24**. To further investigate the effect of actuator dynamics on chattering, the rise time is adjusted by changing the cut-off frequency for low-pass filtering. As shown in Figure **3-25**, the chattering frequency is increased from 10 Hz to 20 Hz when the cut-off frequency is changed from 20 Hz to 40 Hz, which leads in the reduction of rise time. Therefore, we can conclude that the chattering is mainly caused

by the unmodeled actuator and electric circuit dynamics neglected in the stage of the controller design.

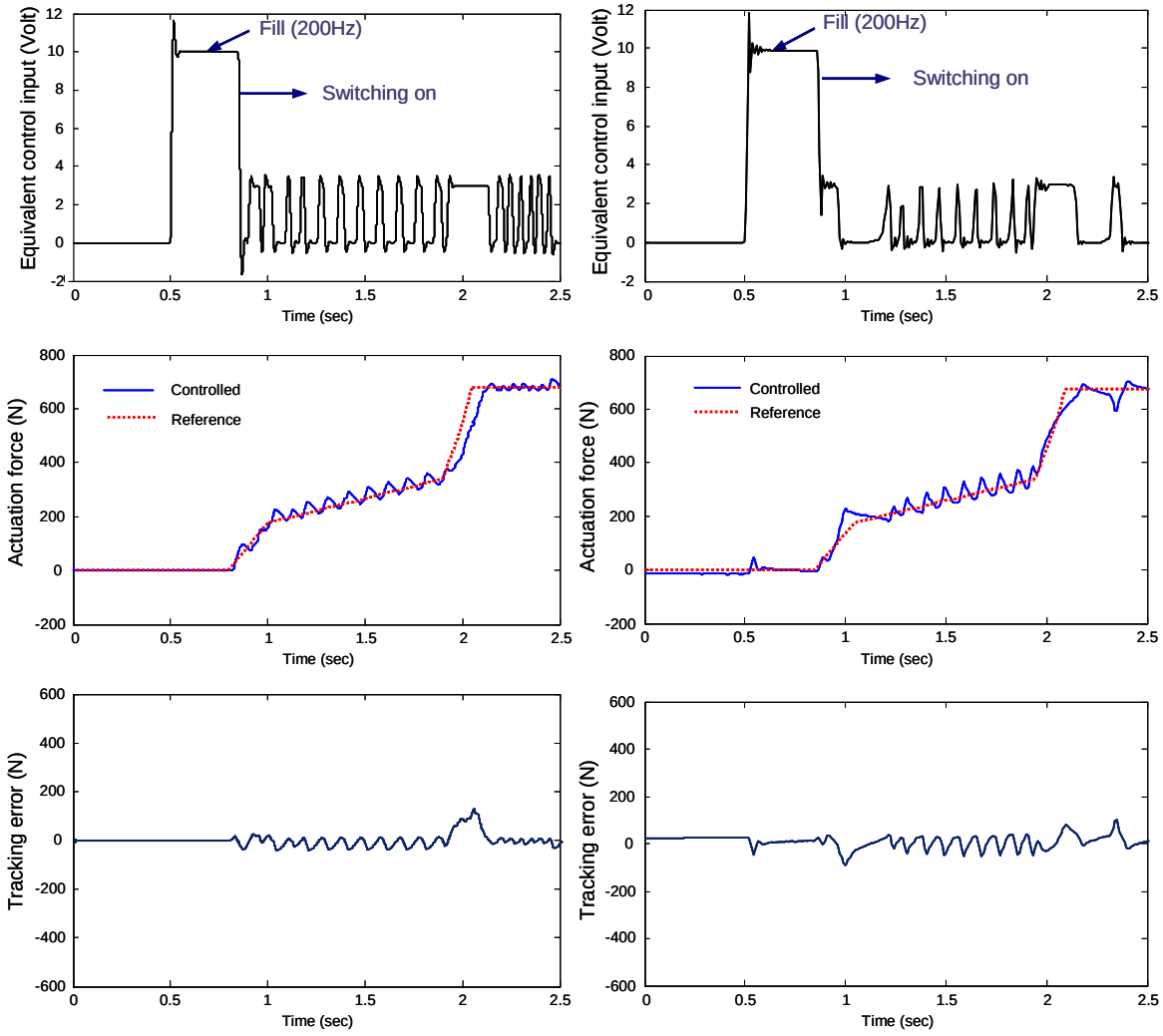

(a) simulation (b) experiment

Figure 3-24: Pressure tracking control responses of band brake actuation system with actuator dynamics ($P_2 = 0.55$ MPa, $V_i = 120$ V, $f_c = 60$ Hz)

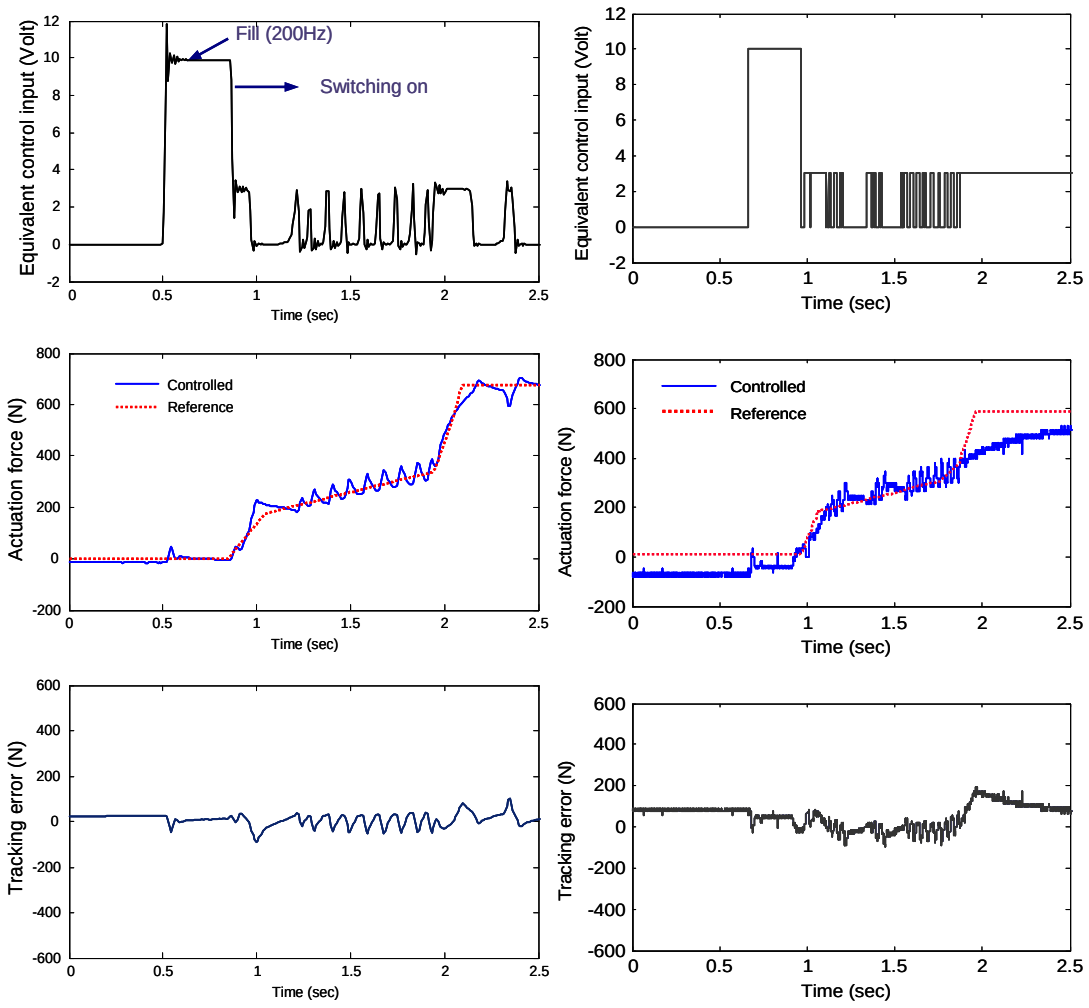

(a) 20 Hz (b) 40 Hz

Figure 3-25: Pressure tracking control responses of band brake actuation system with different cut-off frequency for low-pass filter (P_2 = 0.55 MPa, V_i = 120 V, f_c = 60 Hz)

3.4.2.2 Tracking Performance for Different Trajectories

The tracking performance of controller is further investigated by using different desired trajectories. As noted in Chapter **1,** the actuation force has to be controllable to

adjust the braking torque of friction elements during the inertia phase Based on this fact, different trajectories consist of different gradients in the middle of trajectory are implemented. While the trajectory is changed, the controller still shows good tracking performance, as shown in Figure **3-26**.

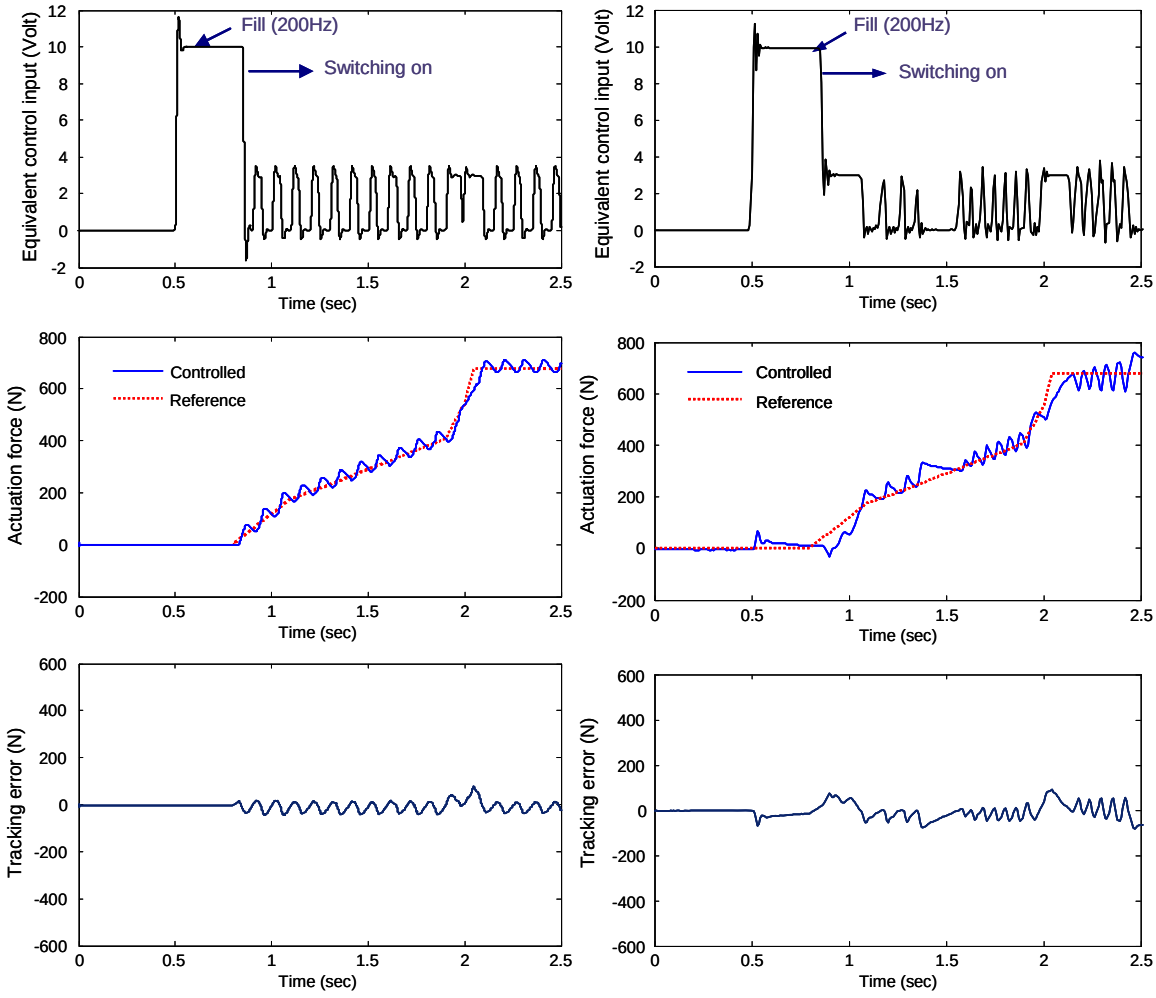

(a) simulation (b) experiment

Figure 3-26: Pressure tracking control responses of band brake actuation system with different desired trajectory (P_2 = 0.55 MPa, V_i = 120 V, f_c = 60 Hz)

3.4.2.3 Effect of the Effective Bulk Modulus Uncertainty

The effect of effective bulk modulus (β_e) uncertainty on the tracking performance is examined since it will be varying with pressure variations and the entrapped air during the operation of the hydraulic systems. The nominal effective bulk modulus (β_{nom}) for accumulator pressure of 0.55 MPa is set to be 3.5e8. In order to generate the lower effective bulk modulus, lower accumulator pressure (0.4 MPa) is utilized. Due to the lower effective bulk modulus, the hydraulic compliance of the working fluid becomes higher value, which in turn causes lower pumping pressure [Kim et al., 2007] and this may lead to insufficient control flow rate and lower dead-head pressure. Figure **3-27** shows the effect of lower effective bulk modulus ($\beta_e/\beta_{nom} = 0.7$) using lower accumulator pressure, which will affect the control flow rate ($Q_c = G_c\sqrt{P_P - P_1}\cdot V_i(f)$). As a result, a slightly under fill situation is observed at the beginning of the tracking control due to the insufficient fill volume and saturation also occurs at the end of control. However, the controller can still track the reference well in inertia phase, for the sliding mode condition is still valid although the controlled flow rate has changed. This result indicates that the proposed controller can be robust against the variation of effective bulk modulus.

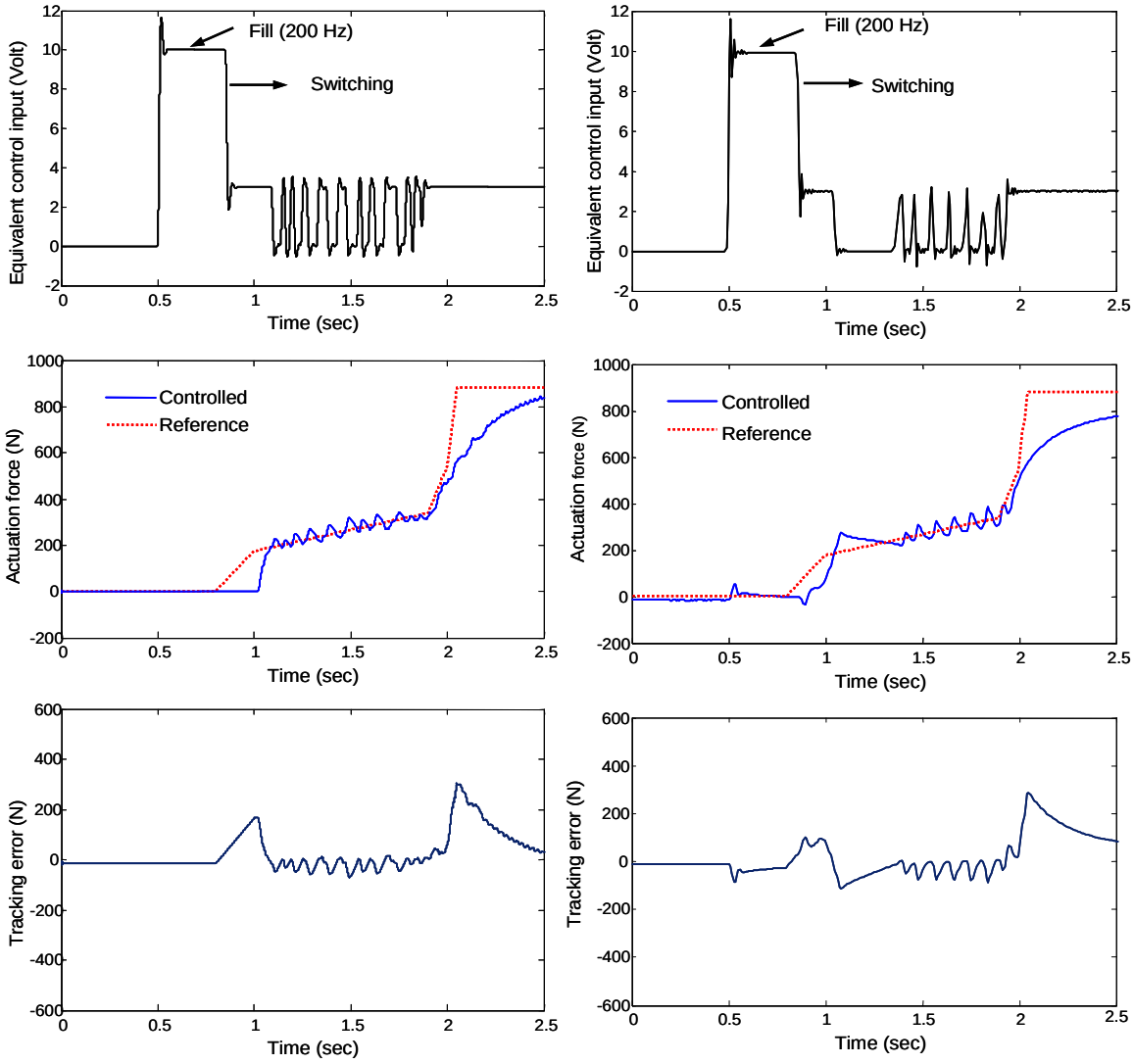

(a) simulation (b) experiment

Figure 3-27: Pressure tracking control responses of band brake actuation system with lower accumulator pressure (P_2 = 0.4 MPa, V_i = 120 V, f_c = 60 Hz)

3.4.2.4 Effect of the Control Frequency

The only parameter to be tuned in this controller is the frequency of control input (f_c). In order to investigate the effect of varying control frequency on tracking

performance, equivalent control input voltage is changed from 3 Volt (60 Hz) to 1.5 Volt (30 Hz) and 4 Volt (80 Hz), respectively. As shown in Figure **3-28**, chattering amplitude is reduced in case of lower control frequency, while it is increased for higher control frequency, since the control flow rate acts as switching gain.

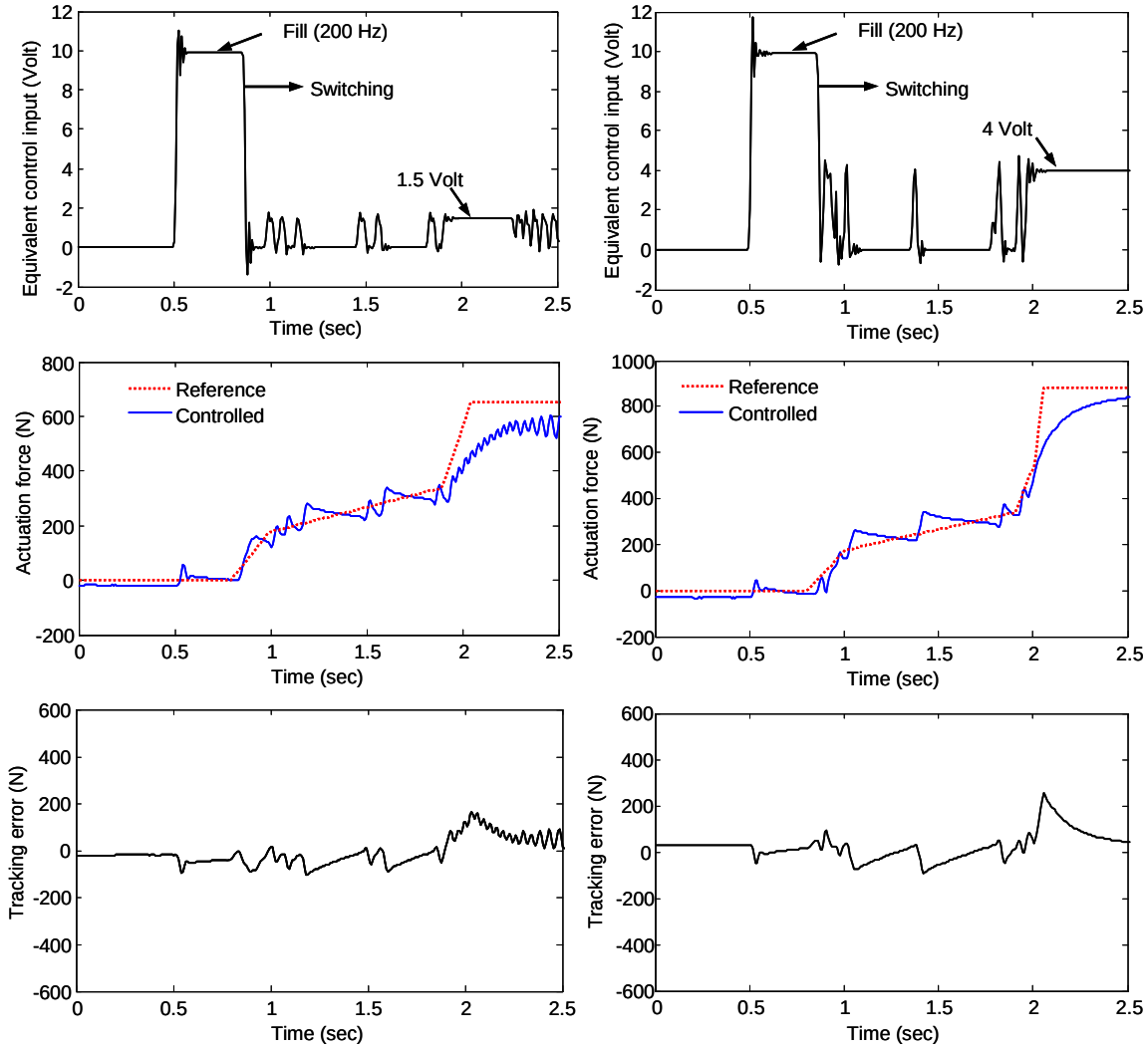

(a) 30 Hz (b) 80 Hz

Figure 3-28: Pressure tracking control responses of band brake actuation system with different control frequencies (P_2 = 0.55 MPa, V_i = 120 V, f_c = 60 Hz)

3.4.2.5 Effect of Friction Force

In general, force transducer is not cost-effective for AT applications, although the measurement can be more directly use for feedback. Therefore, pressure measurement and tracking are used in the controller design. The pressure sensors are more cost-effective, and are easier to be installed inside the AT. However, since the friction force can affect the force tracking performance using pressure feedback and tracking [Liu et al., 2000], measured actuation force during the pressure tracking control is compared with actuation force calculated from actuation pressure to confirm the effect of the friction force. A piezoelectric material based piezo-type force transducer (model: PCB® 208C03) is installed at the front of cylinder piston, as shown in Figure **3-29**.

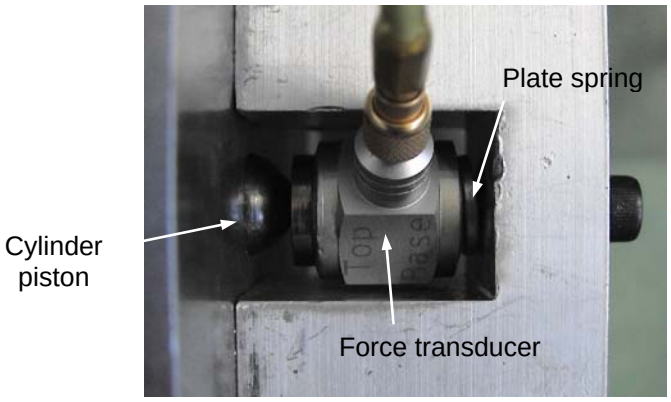

Figure 3-29: Piezo type force transducer to estimate the friction force

The comparison result between the controlled force calculated from pressure and the measured actual force is illustrated in Figure **3-30**. The discrepancy is largely due to the friction force in the hydraulic cylinder neglected in system model. However, this friction force can be compensated by the global feedback controller in the automatic transmission shift control. A feedback controller of turbine speed of the AT during the inertia phase

has been recently developed. Once the closed-loop controller is established within the AT, friction force in actuation system can be compensated by treating it as the disturbance. From the results, it can be seen that the chattering amplitude in the direct measured actual force is smaller than that of the calculated actuation force; which could be the result of unmodeled damping in the system.

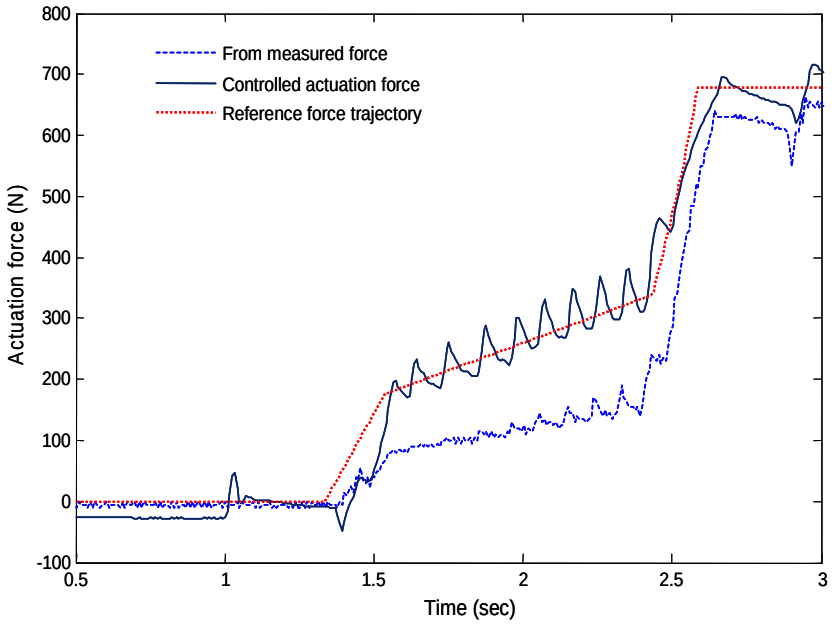

Figure 3-30: Comparison of measure forces: controlled actuation force calculated from actuation pressure and measured actuation force

3.5 Actual Actuation Force Tracking Control

Since actual force feedback control could be effective way to compensate the friction force in hydraulic cylinder, actual force tracking control using on-site force transducer is presented in this section.

3.5.1 On-site Force Transducer

On-site force transducer is customized using FlexiForce® sensor for tracking the actual actuation force affected by friction force. Figure **3-31** illustrates the outlook of prototype transducer, which consists of DC power supply (3 to 5 Volt), converting circuit, FlexiForce® sensor, which features cost-effective, easy-to use, and compact size. Small puck (ϕ 9 mm) is also needed to prevent the damage of sensing area. Details about transducer are described in Appendix **A**.

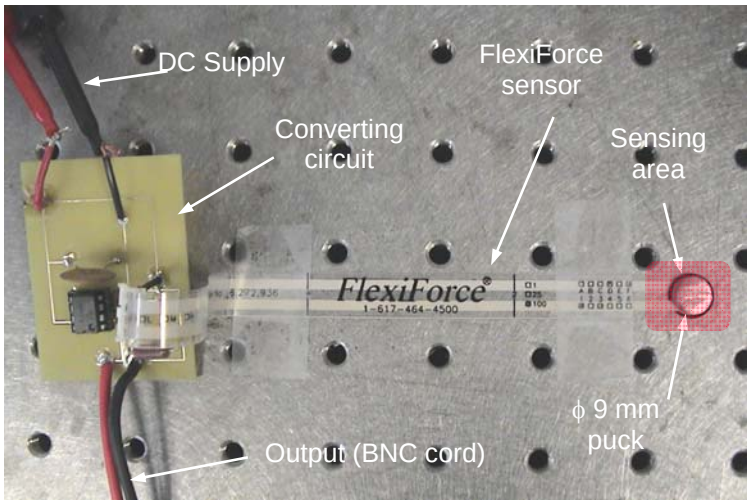

Figure 3-31: Prototype force transducer for actuation force tracking control

3.5.2 Actual Force Tracking Control Results

Like the actuation pressure tracking control, the representative responses of actuation force tracking control are illustrated in Figure **3-32**. Initial accumulator pressure is set to be 0.55 MPa, and amplitude of control input voltage is fixed to be 120

Volt. Maximum pulse frequency for filling the dead-stroke volume of hydraulic cylinder is initially scheduled as 200 Hz (i.e., 10 Volt) for 0.3 sec and the control frequency f_c is set to be 60 Hz (i.e., 3 Volt). In actual force tracking control, the desired force trajectory is modified to be slightly different from the case of pressure tracking control, considering the lower level of force due to the friction force. Accordingly, the maximum desired trajectory after two seconds is determined as 500 N. Figure **3-32** (a) shows the tracking result using commercial piezo type force transducer. Tracking control responses using prototype force transducer is compared in the Figure **3-32** (b). Since the results for two transducers are in good agreement, the feasibility of new force transducer is confirmed. However, the chattering frequency becomes further lower than pressure tracking control (i.e., 10 Hz $\rightarrow$ 5 Hz) in both cases. The main reason for this further lower switching frequency is the different off-switching mechanisms. The actuation pressure is able to drop quickly in off-switching mode. Contrary to the actuation pressure, measured actual force turned out to be unable to drop quickly. Lower switching frequency is largely due to this asymmetrical behavior. However, this lower chattering frequency is attributable to the reduction of chattering amplitude, as shown in the illustrative example. The possible reason for this slow off-switching is the inertia of cylinder piston and friction force between the cylinder and the piston. The exact cause will be further investigated in the future.

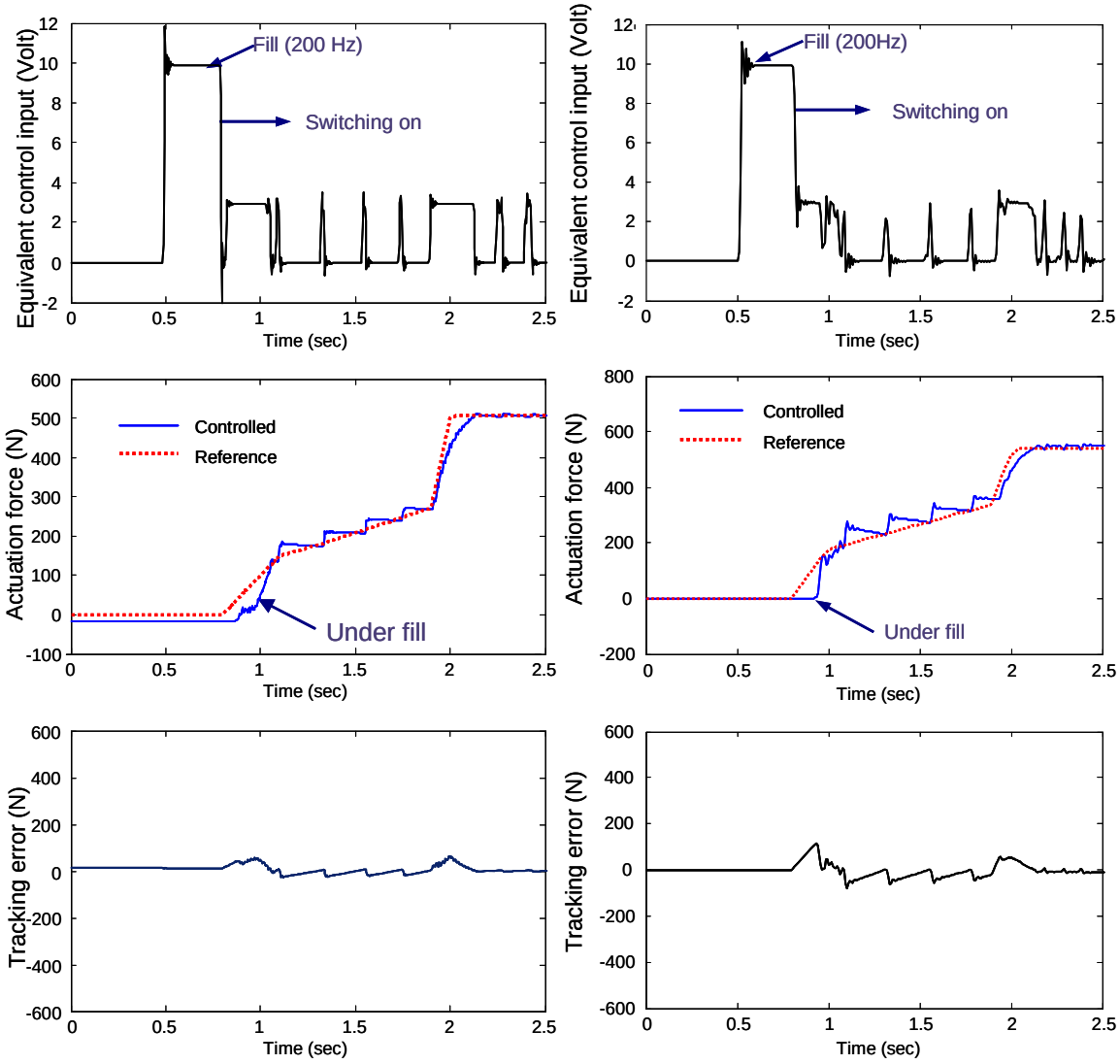

(a) using piezo force transducer (b) using prototype force transducer

Figure 3-32: Force tracking control responses of band brake actuation system with different force transducers (P_2 = 0.55 MPa, V_i = 120 V, f_c = 60 Hz)

Like the pressure tracking control, different desired trajectory is used to investigate the tracking performance of controller in Figure **3-33**. The switching controller can track the different desired trajectories.

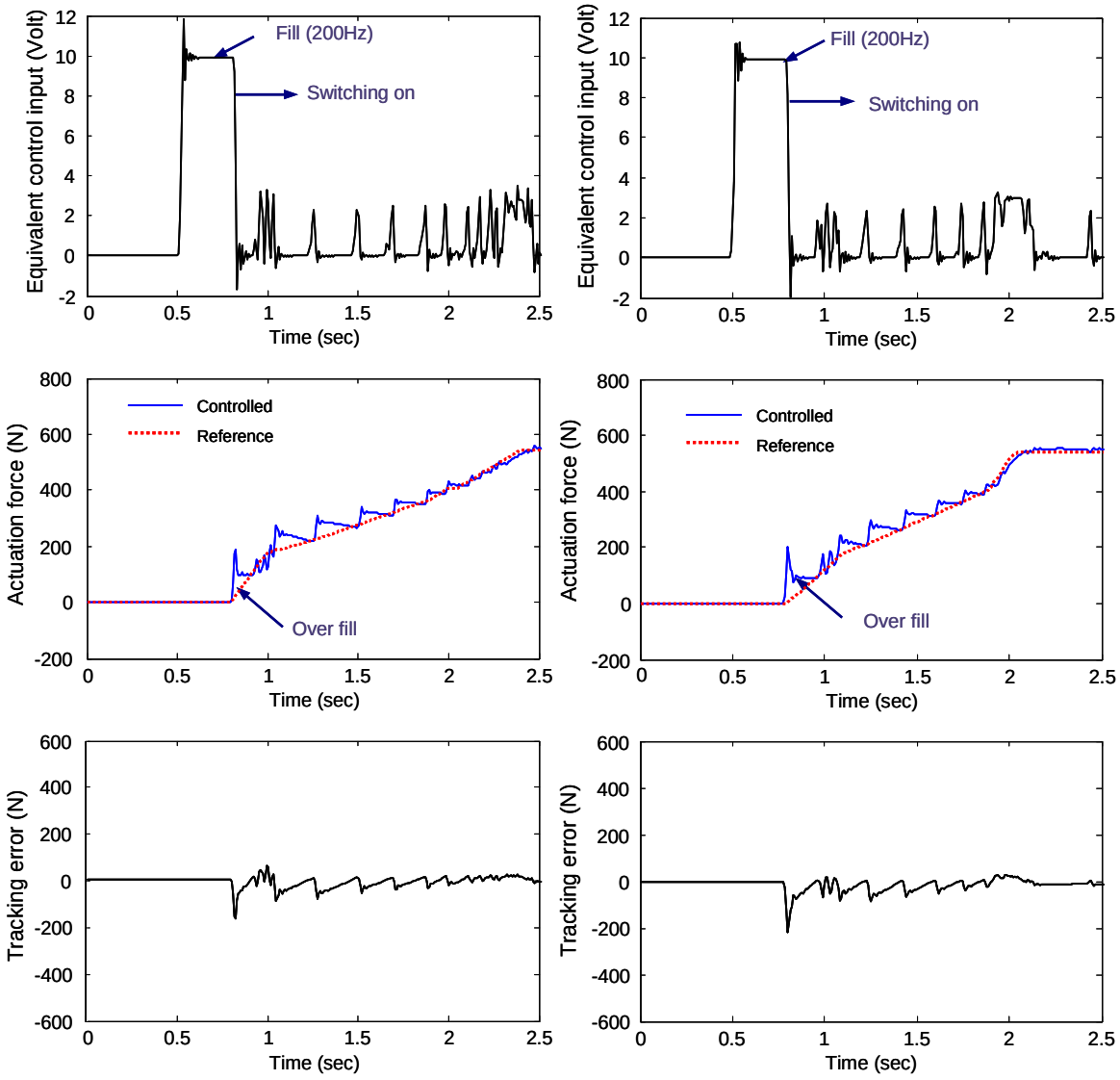

Figure 3-33: Force tracking control responses of band brake actuation system for different desired trajectories (P_2 = 0.55 MPa, V_i = 120 V, f_c = 60 Hz)

Tracking response for special function such as ramp trajectory is shown in Figure **3-34**. Proposed controller turned out to be effective for tracking the trajectory that consists of smooth gradient.

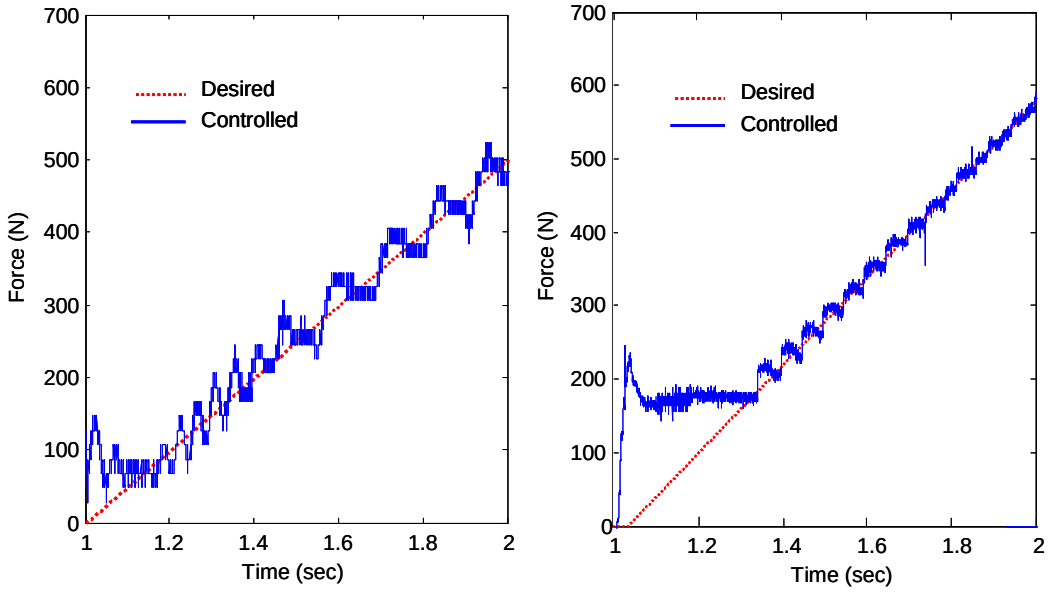

(a) actuation force (pressure) tracking (b) actual force tracking

Figure 3-34: Ramp responses of force tracking control (P_2 = 0.55 MPa, V_i = 120 V, f_c = 60 Hz)

Finally, the necessity of consistent fill control is introduced. As shown from Figure **3-21** to Figure **3-34**, fill volume is not as constant as scheduled due to the difficulty in setting the desired fill stoke. It could be varying with many factors, such as tolerance stack-up of hardware components. If the same fill control time is applied even though the fill volume has been changed, over-fill or under-fill will occur at the beginning stage of feedback control. This undesired phenomenon can be eliminated by the correct fill, which can lead the smallest maximum tracking error as shown in Figure **3-35**. Consequently, closed-loop fill control is required for consistent correct filling.

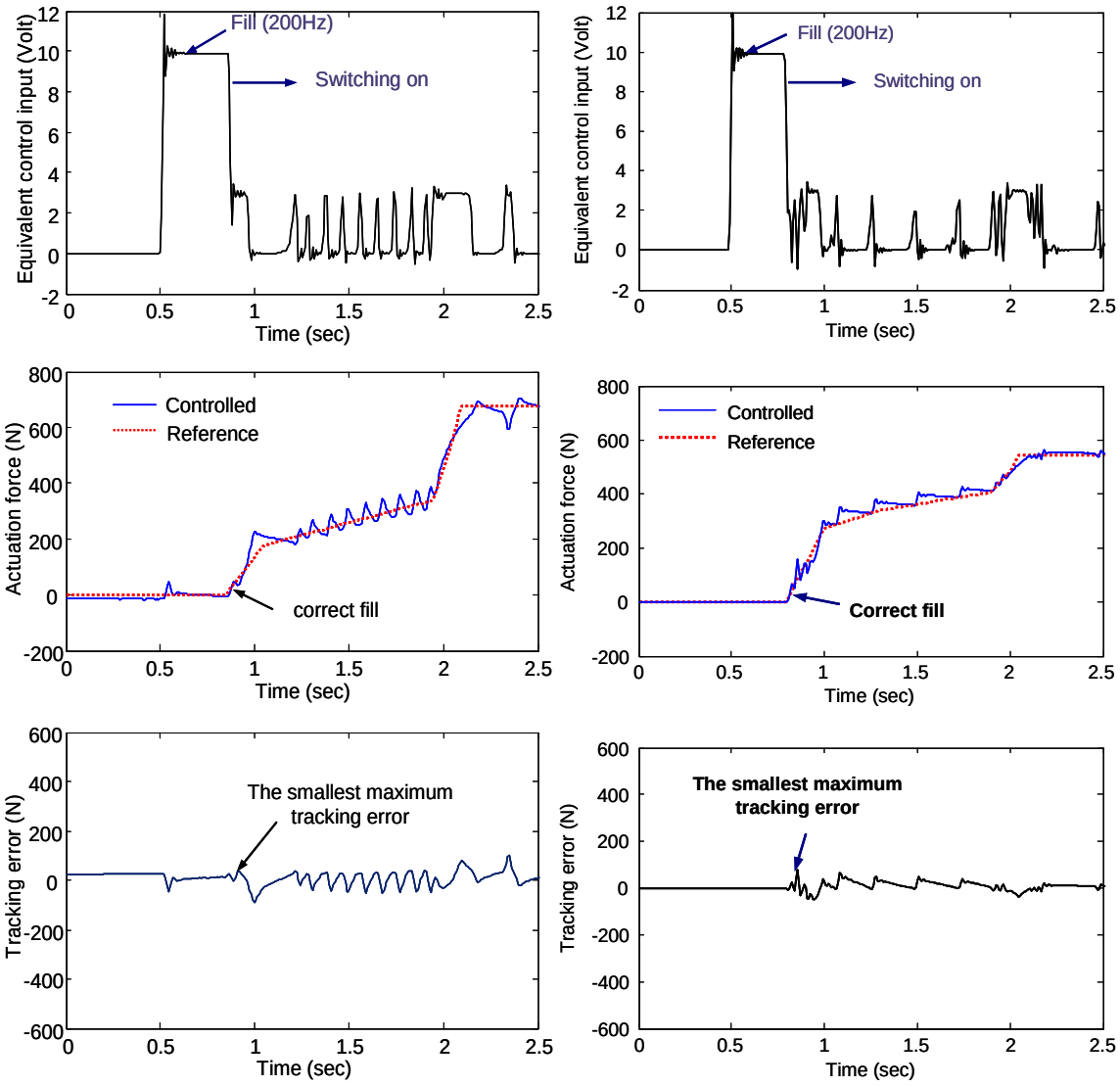

(a) actuation pressure tracking (b) actual force tracking

Figure 3-35: Force tracking control responses of band brake actuation system illustrating correct fill (P_2 = 0.55 MPa, V_i = 120 V, f_c = 60 Hz)

Table 3-1: Simulation parameters, dimensions, and gains for actuation force control

Symbol	Items (SI unit)	Nominal value
A_1	Ram (effective) area of head side in double-acting hydraulic cylinder (m^2)	0.002
A_2	Ram area (effective) area of rod side in double-acting hydraulic cylinder (m^2)	0.0019
C_d	Discharge coefficient	0.6
c_1,c_2	Damping constant of return spring and band brake (N·s/m)	1 (assumed)
P_c	Pressure of pumping chamber (MPa)	1.2
P_2	Pressure of accumulator (MPa)	0.55
K_g	Control gain	0.0045
G_l	Leakage flow gain	2×10^{-7}
k_1	Spring constant of return spring (N/m)	39
k_2	Spring constant of band brake (N/m)	3×10^{5} (assumed)
k_p	Stiffness of PZT stack transducer (N/m)	
m	Effective mass of hydraulic cylinder (kg)	0.01
V_o	Control volume of head side in double-acting cylinder (m^3)	8×10^{-4}
w	Reed orifice area gradient	0.0094
x_o	Pre-loaded length of return spring (m)	0.003
x_s	Dead (fill) stroke (m)	0.004
x_R	Opening displacement of reed valves (m)	0.001
β_e	Effective bulk modulus of working fluid (MPa)	400
ρ_c	Density of hydraulic oil (kg/m^3)	860

3.6 Chapter Summary and Conclusions

In this chapter, control issues for the piezoelectric-hydraulic pump actuator are first discussed. For model–based controller design, a system model was developed. A switching sliding mode controller for force tracking control of the PHP based actuator is designed based on the sliding mode theory, and implemented on an experimental test bed. Promising force tracking control results are demonstrated through simulation and experimental efforts. It is concluded that this nonlinear switching controller;

- Can achieve the desired trajectory tracking performance,
- Does not require much gain tuning,
- Can be robust to the small variation of effective bulk modulus,
- Does not require cylinder position (displacement) and velocity feedback,
- Is appropriate for the pulse-driven PHP actuator.

This chapter confirmed the potential of utilizing the PHP-based actuator as a new controllable actuation system for AT friction elements.

.

Chapter 4

Application to Automatic Transmission Shift Control

The PHP actuator and controller presented in Chapter **2** and Chapter **3** are applied to the automatic transmission shift control scenario to examine the effectiveness of the new power-by-wire actuation concept. To do this, an automotive power train model is first presented in Section **4.1** and Section **4.2**, respectively. The real time power train model, which includes engine, test-bed AT, and drivelines for half car is synthesized to develop the hardware-in-the-loop simulation (in, short, HILS) model using the modeling framework, state charts. Details of the power train model are described. For the purpose of illustration, the power on 1 → 2 shift using band brake as on-coming friction element and one-way clutch (in short, OWC) as off-going friction element (synchronizing control) is provided as a test scenario for evaluating the actuator performance. To achieve the enhanced shift performance, adaptive fill volume control is designed to prevent the over-fill in Section **4.3**. With developed real time power train model and PHP actuator, the architecture of the HILS is constructed, and its successful use in the development of AT shift control system is presented to demonstrate the feasibility and benefits of using the new PHP actuator (Section **4.4)**. Finally, the global shift controller for the inertia phase is proposed in Section **4.5**. Using the genetic algorithm (in short, GA), the turbine acceleration during the inertia phase is regulated by learning the desired force trajectory to be tracked by the PHP actuator.

4.1 Power train Model

The schematic of an automotive power train used in this research is illustrated in Figure **4-1**. It consists of three main components: the engine, AT with differentials (frequently referred as trans-axle), and the driveline of a quarter car system. The impeller of the torque converter is connected with the engine and the turbine of the torque converter is connected to the input shaft of the AT. The forward clutch is constantly engaged to transmit the engine torque during the N → D (i.e., Neutral → Drive position) shift operation. A planetary gear set used in this AT is the combination of two compound planetary gears and features high torque capacity/weight ratio. A drum of the band brake is connected with a second (rear) sun gear (S2) and a one-way clutch is connected with a first (front) ring gear through a second carrier. Output rotational speed is finally reduced by the transfer drive gear with final gear ratio (in short, FGR).

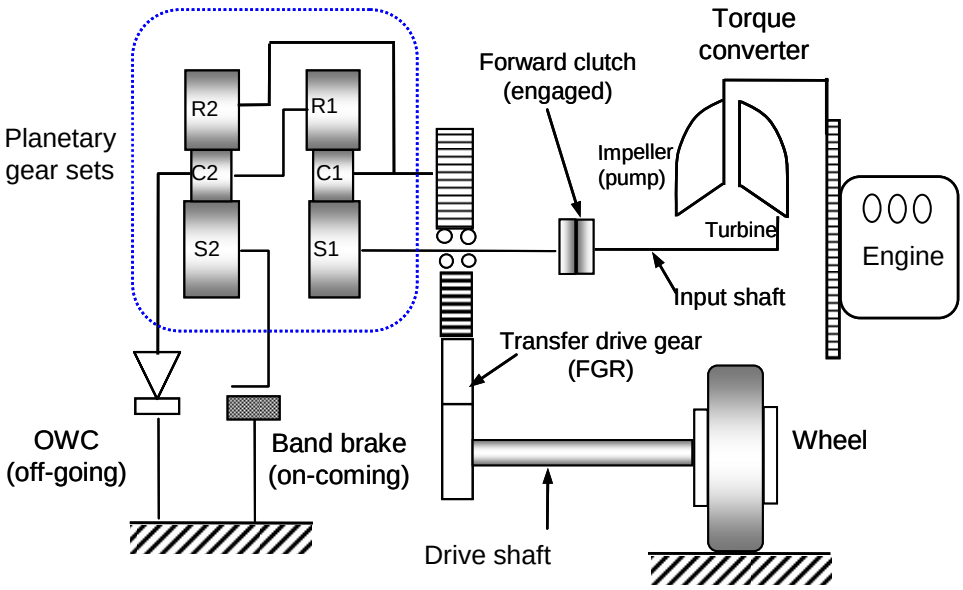

Figure 4-1: Schematic of power trains: engine, trans-axle (1 → 2 up shift) and driveline

4.1.1 Engine and Torque Converter

A static experimental data (torque map) of DOHC gasoline engine (2000 cc) is adopted. Static engine torque can be characterized by a function of throttle opening angle (θ_{th}) and engine rotational speed (ω_E), as shown in Figure **4-2** .

$$T_{ES} = f(\omega_E, \theta_{th}) \tag{4.1}$$

The experimental data on static engine torque map are listed in Appendix **C**.

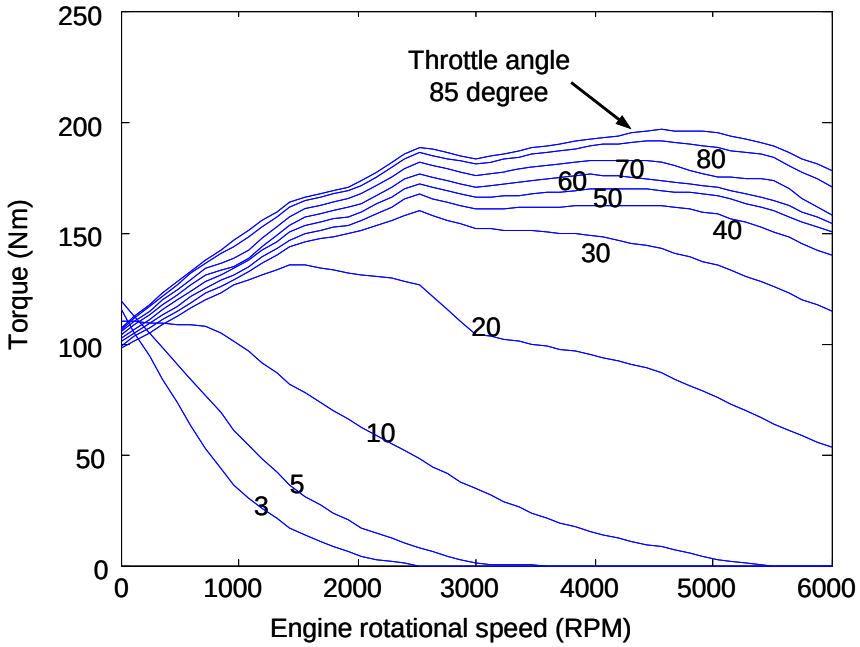

Figure 4-2: Static DOHC gasoline engine (2000 cc) torque map for engine model

In a dynamic response, there exists a response lag (transport delay), which results from the engine mechanism. For the four cylinder combustion engine, an instantaneous engine torque is generated after two revolutions.

$$T_E = \frac{e^{-T_{DE}s}}{1+\tau_E s} T_{ES} \tag{4.2}$$

where τ_E is the time constant (0.1 sec). T_{DE} is the lag time of the engine torque, which is assumed to be a constant (0.15 second) in this research.

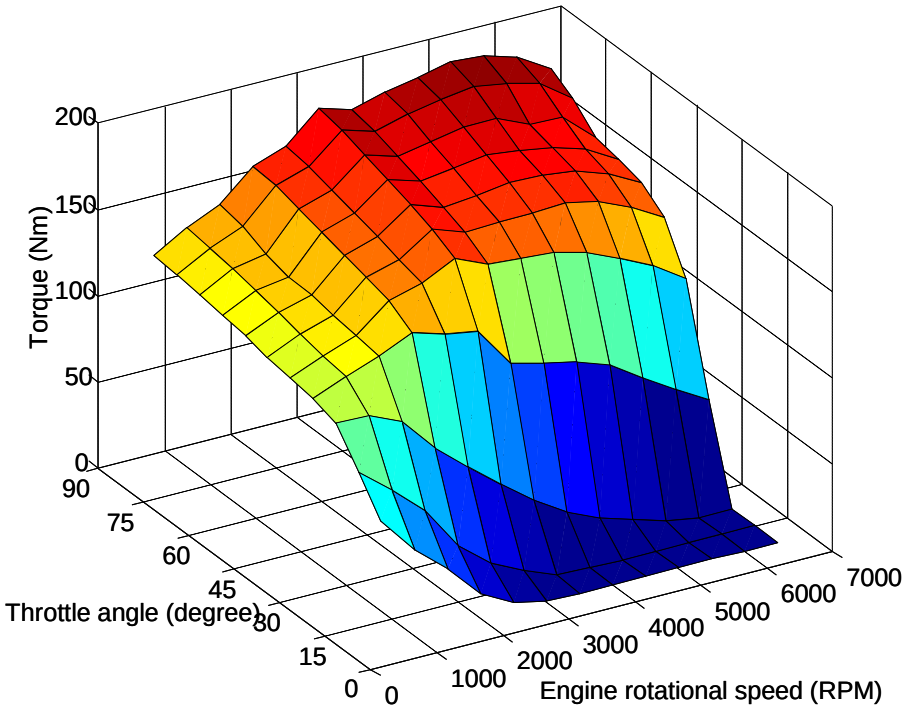

Figure 4-3: 3-dimensional representation of engine torque map

For the torque converter model, a steady-state performance curve is adopted to match with the DOHC gasoline engine (2000 cc). This curve is obtained from the performance test data and can be characterized by the torque ratio (R_t) and the torque capacity factor (C_f) as a function of speed ratio (r), as shown in Figure **4-4** .

$$T_I = C_f(r)\omega_E{}^2, \qquad T_T = R_t(r)T_I \tag{4.3}$$

where

$$r = \frac{\omega_T}{\omega_E}, \quad R_t(r) = \begin{cases} t_1 + t_2 r + t_3 r^2 + t_4 r^3 & r < 0.85 \\ 0.99 & r \geq 0.85 \end{cases} \qquad \textbf{(4.4)}$$

The coefficients for torque ratio ($t_i, i = 1 \cdots 4$) and the torque capacity factor (C_f) are listed in Appendix **C**. From Eq. **4.3**, the steady-state impeller torque (T_I) and the turbine torque (T_T) can be calculated with different speed ratio. Here, we assume that lock-up clutch built inside the torque converter is not engaged and the torque amplification function is always activated during the 1 → 2 shift.

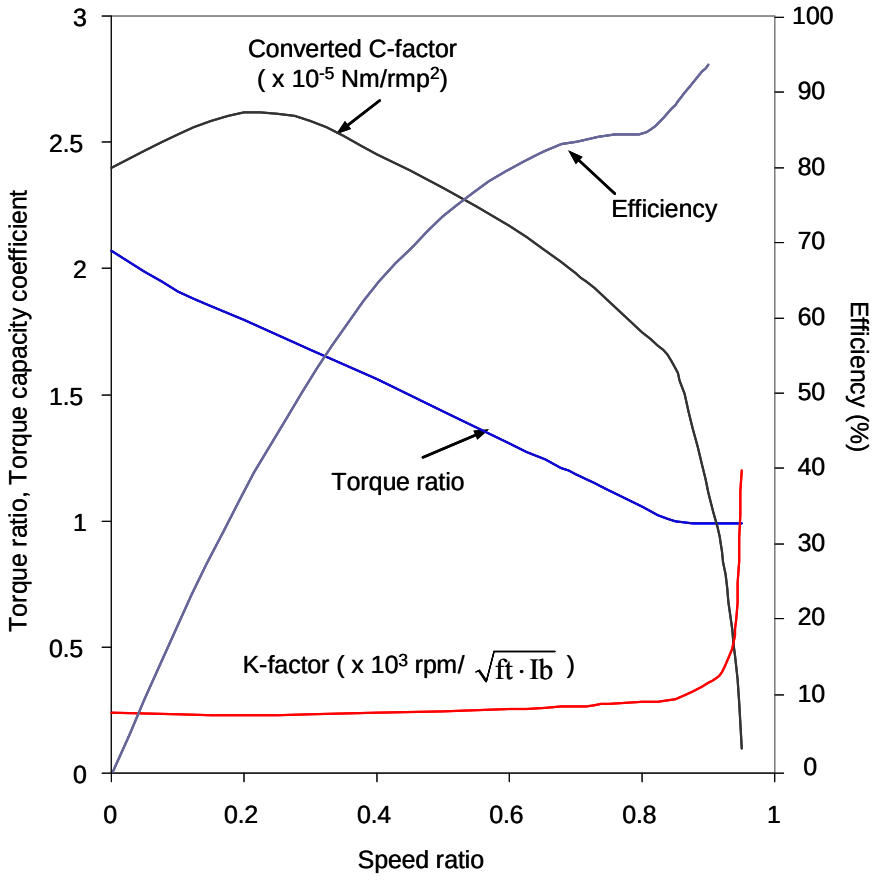

Figure 4-4: Static experimental data for engine and torque converter model

4.1.2 Planetary Gear Sets

Figure **4-5** represents the two-simple type compound planetary gear sets of Ford AT model (4F27E) used in this thesis. The torque relationships in planetary gear sets become:

$$T_{R1} = r_1 T_{S1} \tag{4.5}$$

$$T_{R2} = r_2 T_{S2} \tag{4.6}$$

where r_1 and r_2 are gear ratio (i.e. $r_1 = Z_{R1}/Z_{S1}$, $r_2 = Z_{R2}/Z_{S2}$). The kinematic relationship in planetary gear sets can be defined as:

$$\Psi(1+r_1)\dot{\omega}_{OUT} = \dot{\omega}_{S1} + r_1\dot{\omega}_{R1} \tag{4.7}$$

$$(1+r_2)\dot{\omega}_{R1} = \dot{\omega}_{S2} + \Psi r_2\dot{\omega}_{OUT} \tag{4.8}$$

where Ψ is the final gear ratio (FGR).

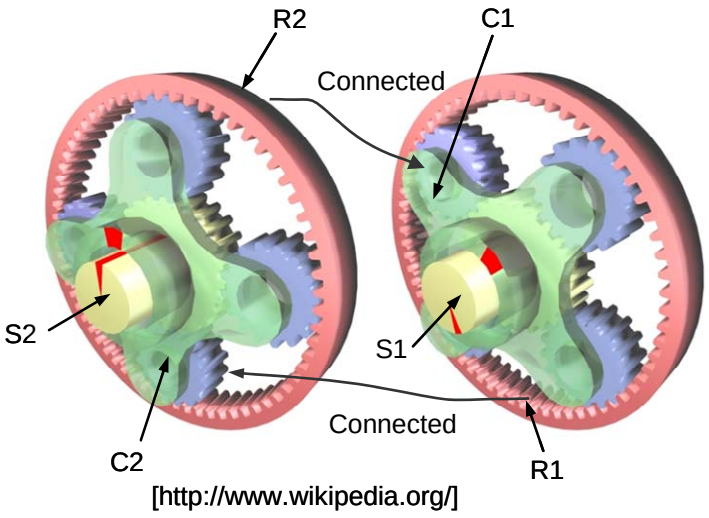

Figure 4-5: Two-simple type planetary gear sets used in Ford model (4F27E)

4.1.3 Friction Elements: Band Brake and One-Way Clutch

The wet band brake consists of a band, a drum and anchor. The gap between the drum and band is lubricated with ATF (automatic transmission fluid), as shown in Figure **4-7** (a). The drum is directly connected to a planetary gear set. The static relationship between the generated braking torque capacity (T_B) and applied net actuation force (F_a) on the band for the energizing mode is generally used to model [Fanella, 1994].

$$T_B = \begin{cases} R_d(e^{\mu(v)\cdot a} - 1)\cdot F_a & \text{for energizing engagement} \\ R_d(1 - e^{-\mu(v)\cdot a})\cdot F_a & \text{for de-energizing engagement} \end{cases} \quad \textbf{(}4.9\textbf{)}$$

where a is the contact angle ($2\pi \sim 4\pi$), R_d is the radii of drum, $\mu(v)$ is the friction coefficient which is varying with temperature, slip speed etc. In this research, $\mu(v)$ is assumed to be the function of the slip speed and independent of temperature as follows:

$$\mu(v) = b_1 + b_2 \cdot v + b_3 \cdot v^2 + b_4 \cdot v^3 \quad \textbf{(}4.10\textbf{)}$$

where v is the slip speed of drum connected with the sun gear of the second planetary gear set (*S2*), and $b_{i,} i = 1 \ldots 4$ are coefficient. When the band brake is engaged by actuation systems, band engagement dynamics significantly affects the AT shift quality because output torque heavily depends on the band brake torque during the inertia phase. Therefore, the dynamic band model has been developed by many researchers. For instance, Fujii et al. [2000] has developed new friction element model based on the first principles of a self-energizing mechanism. An advanced modeling method using neural network was also developed by using experimental result as training data [Cao and

Wang, 2004]. Figure **4-6** shows the typical dynamic relationship between applied pressure and generated band brake torque, showing some response delay caused by further stroking (i. e., compression of friction pad or deformation).

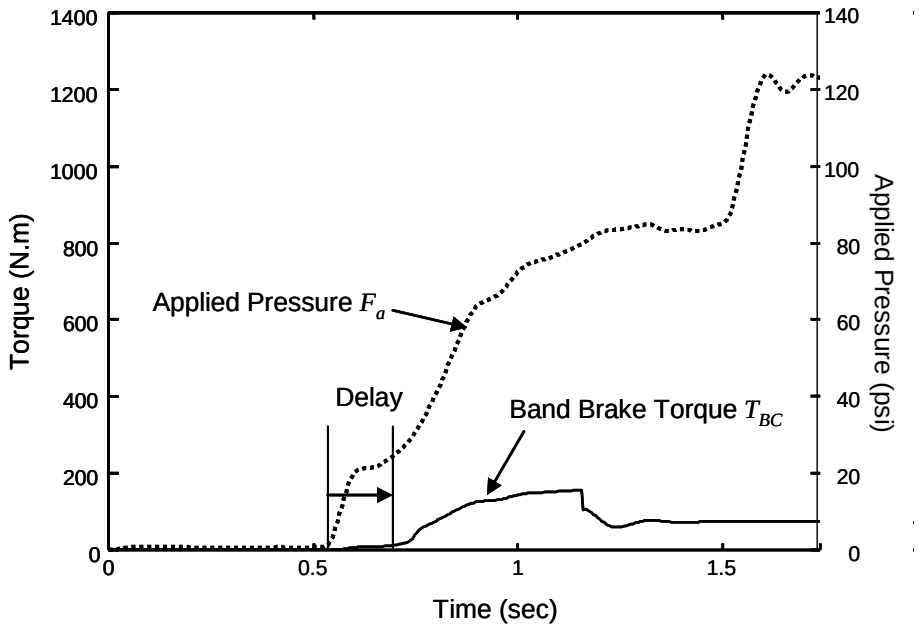

Figure 4-6: Typical dynamic characteristic between pressure and band brake torque [Cao and Wang, 2004]

While these models were successfully validated through the experimental studies, they are not suitable for real-time analysis with the overall power train model. In this research, the band brake torque is assumed to be characterized by following second order system based on the response shown in Figure **4-6** .

$$T_B(s) = \frac{k\omega_n^{\,2}}{s^2 + 2\xi\omega_n s + \omega_n^{\,2}} F_a(s) \tag{4.11}$$

where $T_B(s)$ and $F_a(s)$ are the Laplace operator of T_B and F_a, k is the proportionality constant defined in Eq. 4.9, ω_n is the natural frequency that has to be tuned so that the

delay time should be in the range of 0.2 sec. The direction of braking torque capacity also should be considered because of the slip of the friction elements during the torque and inertia phase. When the brake is slipping, the band brake torque (T_{BC}) is determined by the direction of the second sun gear speed as follows:

$$T_{BC} = sign(\omega_{S2})T_B \quad \textbf{(}4.12\textbf{)}$$

where $sign(x) = \begin{cases} 1 & (x > 0) \\ -1 & (x < 0) \end{cases}$, and ω_{S2} is the angular velocity of the second sun gear.

When the one-way clutch is overrunning, the reaction torque of the one-way clutch becomes zero since the one-way clutch is designed to transmit the torque only in one direction, as shown in Figure **4-7** (b).

$$T_{OWC} = \begin{Bmatrix} T_{OWC} \ if \ \omega_{R1} = 0 \\ 0 \quad if \ \omega_{R1} > 0 \end{Bmatrix} \quad \textbf{(}4.13\textbf{)}$$

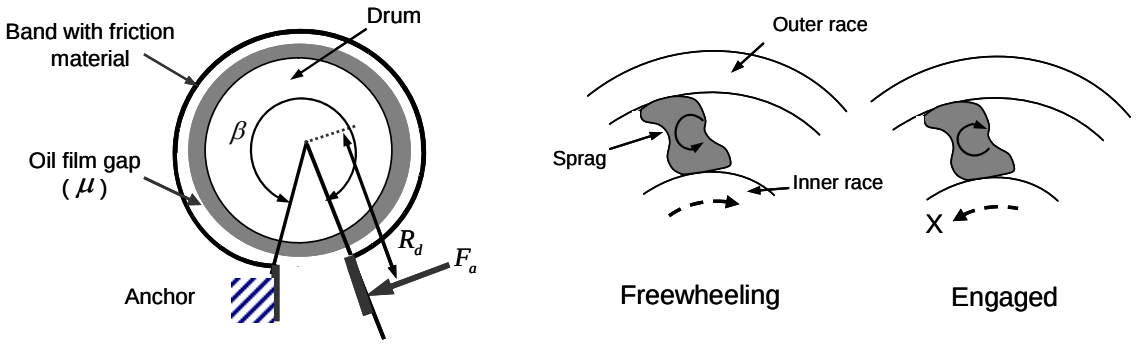

(a) band brake (b) sprag type one-way clutch

Figure 4-7: Schematic of friction elements (band brake and one-way clutch)

4.1.4 Road Load Torque

Road load can be expressed by summing up the rolling resistance (R_r), air resistance (R_w), acceleration resistance (R_a), and gradient resistance (R_g).

$$T_{LOAD} = (R_w + R_a + R_g + R_r) \cdot r_t \tag{4.14}$$

where r_t is the tire radius. Assuming that the vehicle is driving with constant speed and the road is not inclined, Eq. **4.14** can be reduced by follows;

$$T_{LOAD} = (R_a + R_r) \cdot r_t = (\frac{\rho_a}{2} C_a A_V \cdot V_H{}^2 + \mu_r m_V) \cdot r_t \tag{4.15}$$

where ρ_a is the air density, C_a is the coefficient of aerodynamic resistance, A_V is the frontal area of vehicle, V_H is the vehicle speed, m_V is the vehicle mass, and μ_r represents the coefficient of rolling resistance, which is a function of vehicle speed, tire inner pressure, as shown in Figure **4-8 (b).** In this research, the rolling resistance coefficient is assumed to be constant, since the discrepancy is small to be negligible.

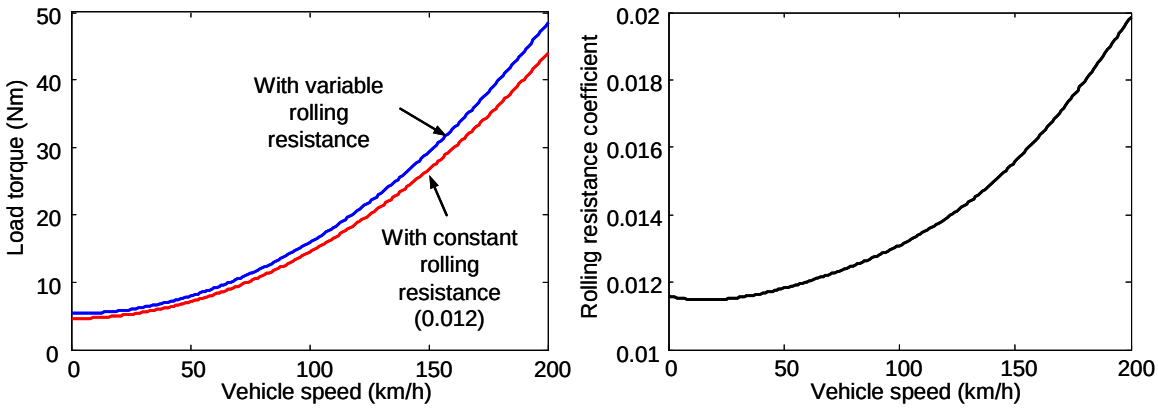

(a) road load curve (b) rolling resistance coefficient

Figure 4-8: Characteristic of road load torque

4.2 Power-on 1→2 Up Shift Model

4.2.1 Derivation of Governing Equations

The governing equations of motion for individual inertia elements described in Figure **4-9** can be expressed as follows:

- Engine and impeller (pump):

$$I_E\dot{\omega}_E = T_E - T_I \quad \textbf{(}4.16\textbf{)}$$

- Turbine (input) shaft:

$$I_T\dot{\omega}_T = T_T - T_F \quad \textbf{(}4.17\textbf{)}$$

- Sun gear of the first planetary gear set (*S1*):

$$I_{S1}\dot{\omega}_{S1} = T_F - T_{S1} \quad \textbf{(}4.18\textbf{)}$$

- Ring gear of the first planetary gear set (*R1*):

$$I_{R1}\dot{\omega}_{R1} = T_{S2} + T_{R2} - T_{OWC} - T_{R1} \quad \textbf{(}4.19\textbf{)}$$

- Sun gear of the second planetary gear set (*S2*):

$$I_{S2}\dot{\omega}_{S2} = -T_{S2} - T_B \quad \textbf{(}4.20\textbf{)}$$

- Ring gear of the second planetary gear set (*R2*):

$$I_{R2}\dot{\omega}_{R2} = T_{S1} + T_{R1} - T_{R2} - \frac{T_{OUT}}{\Psi} \quad \textbf{(}4.21\textbf{)}$$

- Output shaft:

$$I_V\dot{\omega}_{OUT} = T_{OUT} - T_{LOAD} \quad \textbf{(}4.22\textbf{)}$$

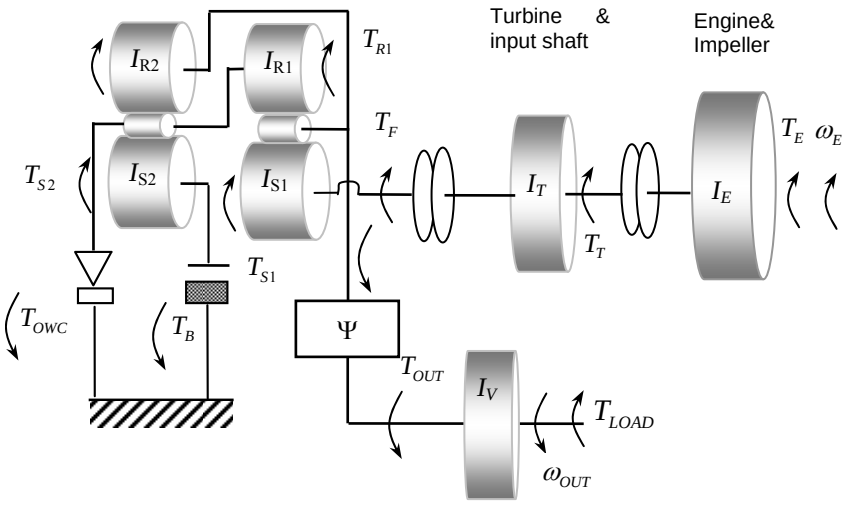

Figure 4-9: Simplified inertia model for the P/on up 1→2 shift model

Since the ring gear of the second planetary gear set (*R2*) and the output shaft are connected with each other, the eliminating of $\dot{\omega}_{R2}$ and T_{OUT} in Eq. **4.21** yields the following equation:

$$I_{EQV}\dot{\omega}_{OUT} = \Psi(T_{S1} + T_{R1} - T_{R2}) - T_{LOAD} \quad \textbf{(}4.23\textbf{)}$$

where $I_{EQV} = I_V + \Psi^2 I_{R2}$.

Since we are not interested in the internal torques ($T_{S1}, T_{R1}, T_{S2}, T_{R2}$), these torques could be eliminated by using kinematic constraints (Eq. **4.5** and Eq. **4.6**) as follows:

$$T_{R1} - T_{R2} = r_1 T_{S1} - r_2 T_{S2} \quad \textbf{(}4.24\textbf{)}$$

Substituting Eq. **4.18** Eq. **4.19** and Eq. **4.20** into Eq. **4.23** and Eq. **4.24**, respectively, the torque balance equations can be reduced to the following two equations:

$$r_1 I_{S1}\dot{\omega}_{S1} - (1+r_2) I_{S2}\dot{\omega}_{S2} - I_{R1}\dot{\omega}_{R1} = r_1 T_F + (r_2+1) T_B + T_{OWC} \quad \textbf{(4.25)}$$

$$I_{EQV}\dot{\omega}_{OUT} + \Psi(I_{S1}\dot{\omega}_{S1} + I_{S2}\dot{\omega}_{S2} + I_{R1}\dot{\omega}_{R1}) = \Psi(T_F - T_B - T_{OWC}) - T_{LOAD} \quad \textbf{(4.26)}$$

During the 1 → 2 up shift, the unknown forward clutch torque (T_F) and $\dot{\omega}_{S1}$ can be eliminated because the forward clutch is always engaged to transmit turbine torque (constraint). By replacing T_F with $I_T\dot{\omega}_T - T_T$ and $\dot{\omega}_{S1}$ with $\dot{\omega}_T$ in Eq. **4.25** and Eq. **4.26**, the governing equations can be further modified.

In summary, the final governing equations are as follows:

$$\begin{gathered} r_1(I_{S1}+I_T)\dot{\omega}_{S1} - (1+r_2) I_{S2}\dot{\omega}_{S2} - I_{R1}\dot{\omega}_{R1} = r_1 T_T + (r_2+1) T_B + T_{OWC} \\ I_{EQV}\dot{\omega}_{OUT} + \Psi\{(I_{S1}+I_T)\dot{\omega}_T + I_{S2}\dot{\omega}_{S2} + I_{R1}\dot{\omega}_{R1}\} = \Psi(T_T - T_B - T_{OWC}) - T_{LOAD} \\ \Psi(1+r_1)\dot{\omega}_{OUT} = \dot{\omega}_{S1} + r_1\dot{\omega}_{R1} \\ (1+r_2)\dot{\omega}_{R1} = \dot{\omega}_{S2} + \Psi r_2\dot{\omega}_{OUT} \end{gathered} \quad \textbf{(4.27)}$$

The 1 → 2 up shift can be divided into several states according to the velocity sign of the sun gear and ring gear of the planetary gear sets as shown in Table **4-1**. Each state is also classified by its degree of freedom (in short, DOF) of dynamics. Torque phase has 1-DOF which is described as the rotational speed of the first ring gear connected with input shaft. Meanwhile, inertia phase has 2-DOF.

Table 4-1: Classification of the gear state during 1 → 2 shift

Ring gear	Sun gear	Gear state	Degree of freedom
$\omega_{R1} = 0$	$\omega_{S2} = 0$	N/A	
	$\omega_{S2} \neq 0$	First gear & torque phase	1
$\omega_{R1} \neq 0$	$\omega_{S2} = 0$	Second gear	1
	$\omega_{S2} \neq 0$	Inertia phase	2

4.2.2 Simulation of the Power-on 1→2 Up Shift

4.2.2.1 Introduction of State Chart

As described in the previous section, AT shift dynamics can be characterized by state transition system. The use of the finite state machine (in short, FSM) modeling technique as a modeling framework will reflect the event-driven nature of automatic transmission in which each gear state includes unique governing equations. With this modeling frame, state chart is proposed as a visual formalism for the modeling of complex systems [Harel, 1987]. In fact, state chart is an example of finite state machine. It is suitable to describe state transition systems such as AT shift dynamics due to its hierarchical approach to express dynamic behavior. Based on this modeling concept, power on 1→2 up shift model for each state and phase is derived. The detail procedures and derived governing equations are described in Appendix **B**.

With the derived equations, the overall 1 → 2 up shift event can be represented by the state chart, as shown in Figure **4-10**. In this figure, each state is described by boxes consisting governing equations. Transition between states is described by an arrow line and transition condition is put above that line. According to the transition condition, each state can be sequentially switched. For instance, if the angular velocity of the second sun gear ($\dot{\omega}_{S2}$) is changed from negative to positive, the transition from inertia phase to 2nd gear state occurrs. This state chart can be easily implemented by using Stateflow® toolbox in MATLAB/Simulink®. This modeling technique also enables us to conduct real time simulation or hardware-in-the-loop simulation (in short, HILS), for it can

provide extremely fast CPU executing time [Ferreira et. al., 2004]. For each gear state, the turbine acceleration ($\dot{\omega}_T$) can be first calculated from a derived governing equation consisting of known torques such as the turbine torque (T_T), the band brake torque (T_{BC}), the one-way clutch torque (T_{TOWC}), and the road load torque (T_{LOAD}). Next, using pre-calculated $\dot{\omega}_T$, other unknown torques and variables can be sequentially determined. The state variables of interest (i.e., the angular velocities such as $\omega_T, \omega_{OUT}, \omega_{S2}$ etc) also can be obtained by numerically integrating their angular accelerations ($\dot{\omega}_T, \dot{\omega}_{OUT}, \dot{\omega}_{S2}$) in the upper-level block diagram.

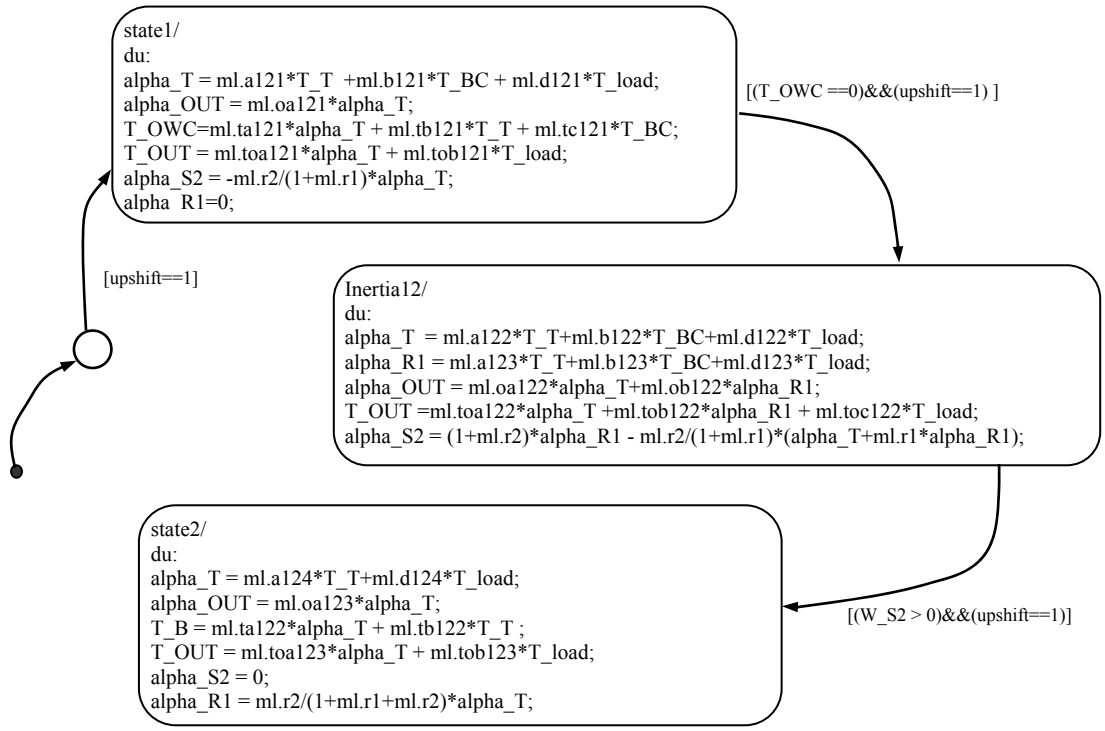

Figure 4-10: State chart for power on 1 → 2 up shift simulation of A/T

4.2.2.2 Simulation Results

Figure **4-11** shows the overall block diagram for power/on 1 → 2 up shift simulation model using Simulink® with Stateflow®. The PHP actuator and the sliding mode force tracking controller presented in Chapters **2** and **3** are also integrated with power train and power/on 1 → 2 up shift model. The 5th-order Dormand-Prince solver is used for numerical integration, and the fixed step size of 100 μsec is used to achieve the real time capability. The required parameters are provided by the Ford Motor Company, which are listed in Appendix **C**.

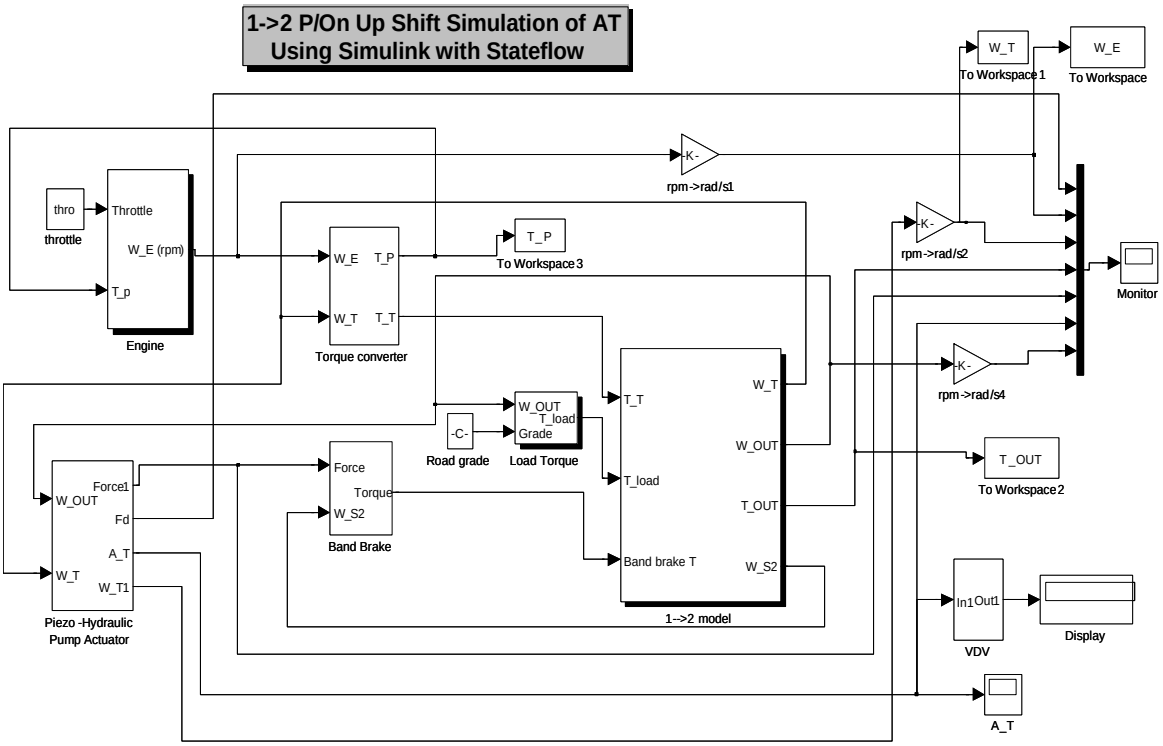

Figure 4-11: Power on 1→2 up shift simulation model using Simulink® with Stateflow®

To represent the 1→2 up shift of AT, vehicle launching (starting) performance is first simulated and shown in Figure **4-12.** The throttle opening of this illustrative example is set to be 10 degree (medium) and the start of 1 → 2 up shift is scheduled when the output speed (ω_{OUT}) reaches a prescribed value in the shift pattern. The engine rpm hesitation phenomenon is generally observed after launching due to the characteristic curves of torque converter. The output torque is increased up to 1700 Nm and then dropped down afterwards.

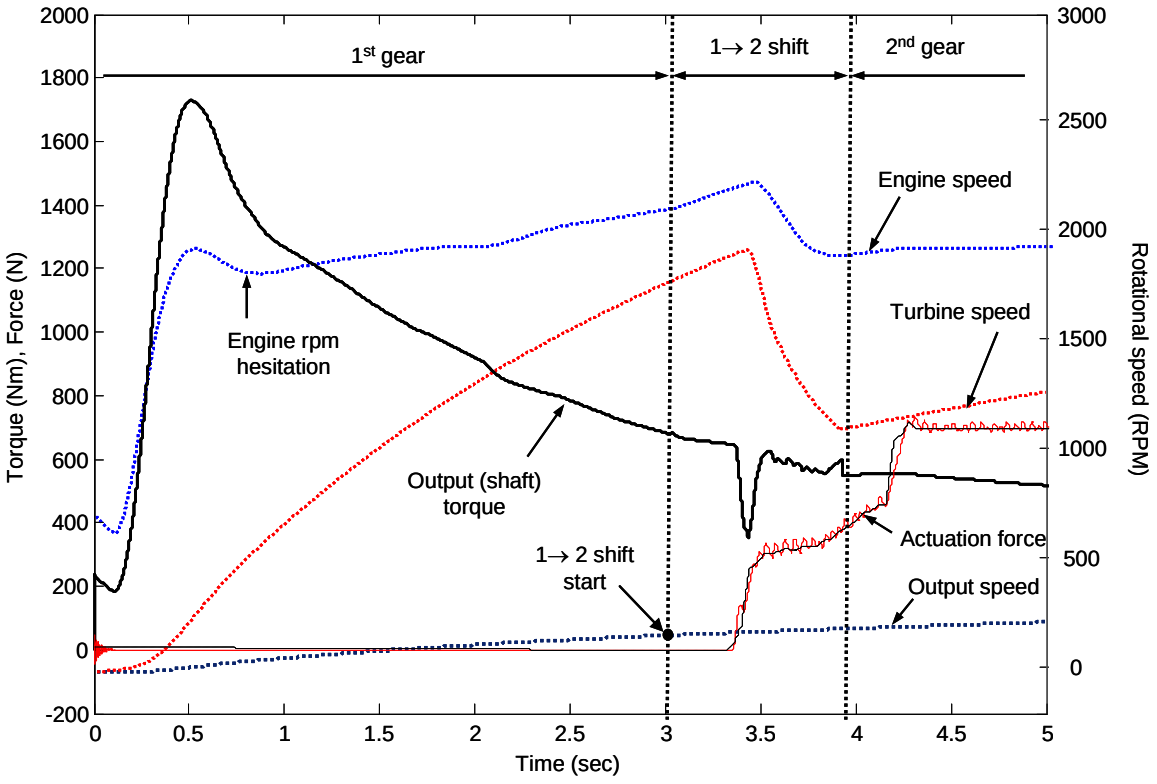

Figure 4-12: Simulation results of vehicle launching with the throttle opening of 10 degree

Open-loop 1 → 2 up shift control using the nonlinear force tracking control on PHP actuator is presented from 3 second to 4 second, as illustrated in Figure **4-12.** To evaluate the accuracy of the simulation model for 1 → 2 up shift control, detail simulation results are compared with vehicle test results in Figure **4-13**. Desired force trajectory used in Figure **4-12** and Figure **4-13** (b) is determined by the pressure profile in a vehicle test and the diameter of current servo cylinder ($\phi\, 0.038\, m$). In the current electro-hydraulic actuation system, the high pressure is commended at the beginning of control to fill the dead-stroke. However, the pressure does not generate during the fill stage in PHP actuator. On starting 1 → 2 up shift, the fill time for dead-stroke volume corresponding to 3.5 mm stroke is set to be 0.3 second. In both cases, at the onset of this torque phase, the output torque dropped (torque hole), which is inevitable since a part of the input (turbine) torque is re-routed through the on-coming friction element (e.g., band brake).

The inertia phase is characterized by sudden increase of output torque caused by the gear ratio change within a very short period of time, in general 0.5 second, and the decelerating of engine speed. This transient torque eventually goes down to the second gear torque level. This inertia phase is also called speed phase since the engine speed and turbine speed has to be changed by new gear ratio. The output vehicle speed will be gradually increasing due to the relatively larger inertia of vehicle. As observed, the simulation results show good agreement with the vehicle test results.

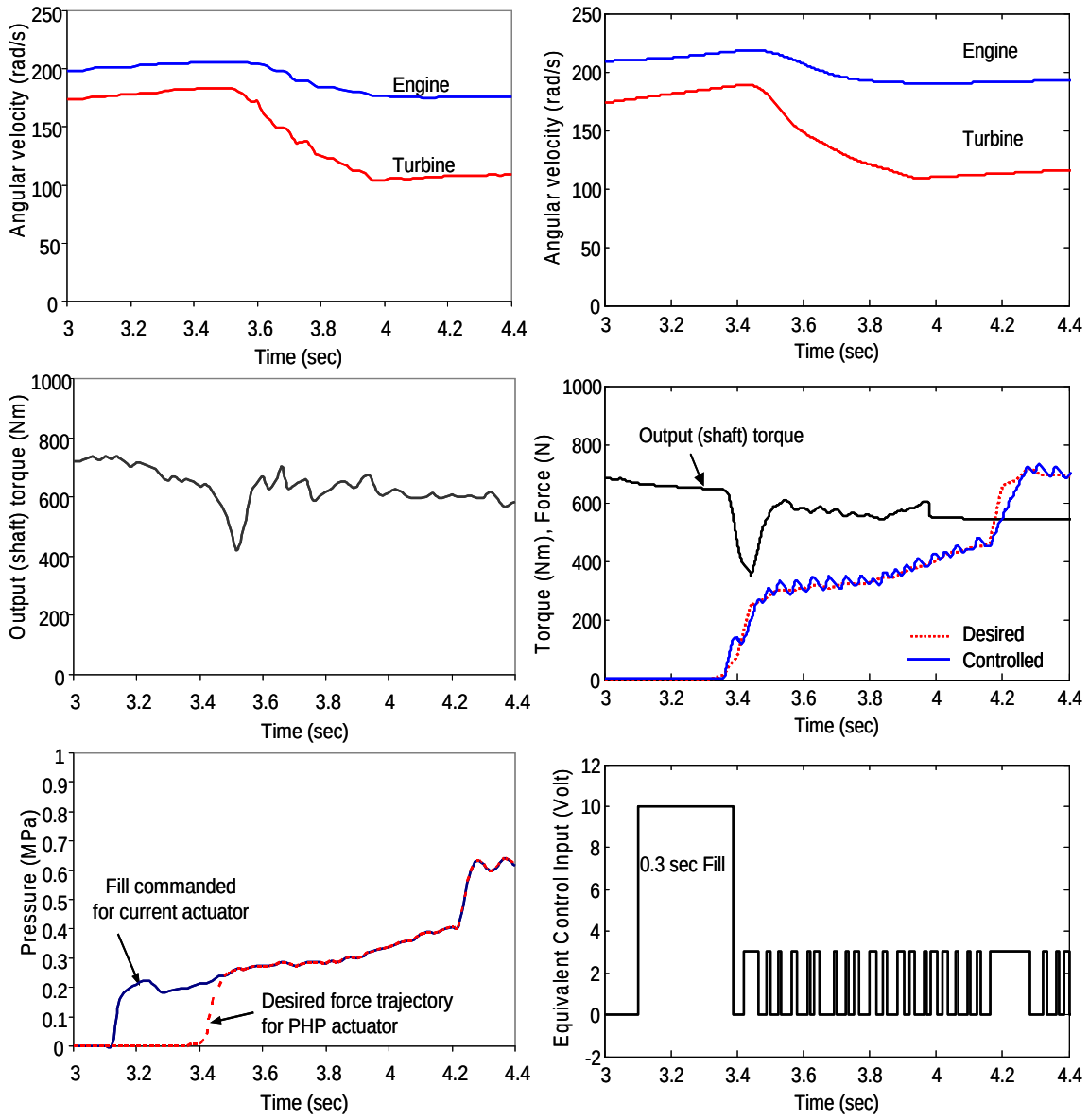

(a) vehicle test (b) off-line simulation

Figure 4-13: Vehicle test results [Ford, 2008] and simulation results of power-on 1→2 up shift control with the throttle opening of 10 degree

To further validate the shift model, other responses of interested states are investigated, as shown in Figure **4-14**. When the initial negative reaction torque of one-way clutch (T_{OWC}) becomes zero and negative band brake torque is applied, the onset of

inertia phase occurrs around 3.4 second and the first ring gear and the second sun gear will be slipping (i.e., 2-DOF), as shown in Figure **4-14** (a) and (b). Also, when the negative angular velocity of the second sun gear becomes zero (i.e., band brake is fully engaged), negative braking torque becomes positive.

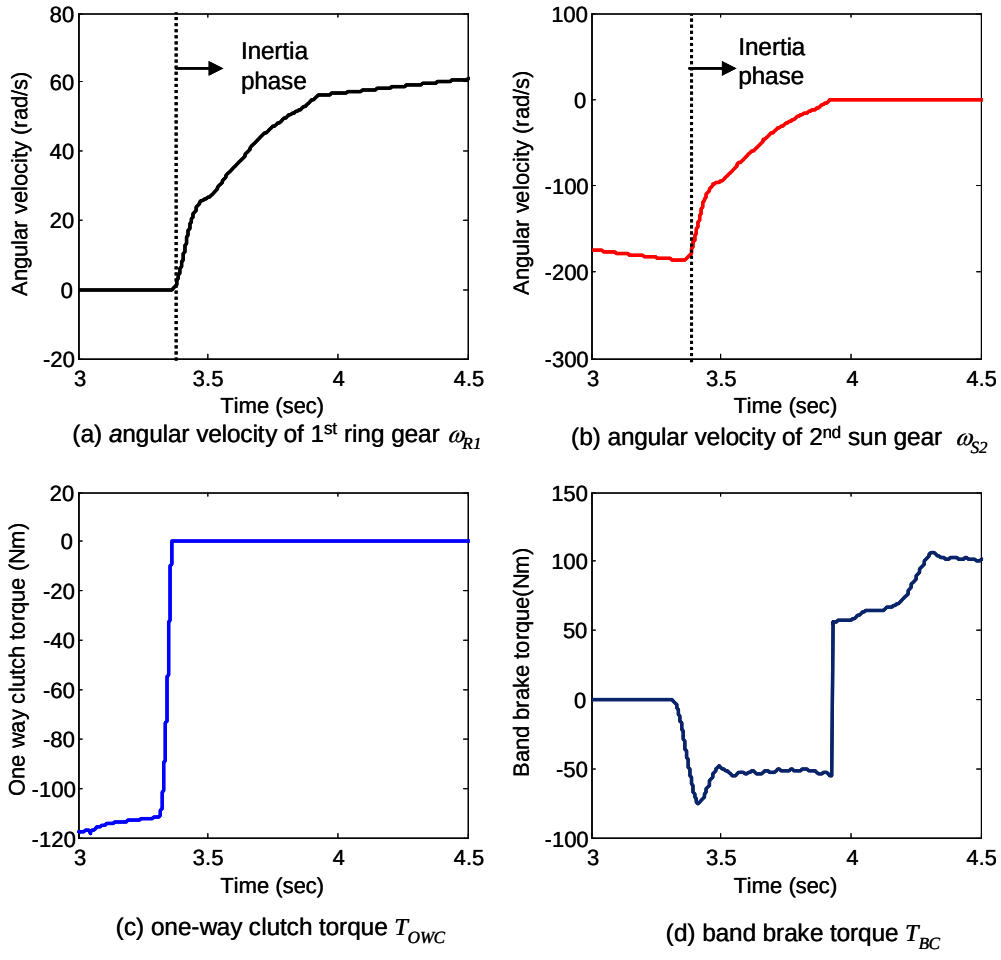

Figure 4-14: Simulation result for other responses of interested states

More simulation results of power-on 1 → 2 up shift control are shown in Figure **4-15**. Throttle opening is changed from 10 % to 20 % and 5 %, respectively. The

level of angular velocity and output torque depends on the throttle opening. The inertia phase duration also varies with the throttle opening.

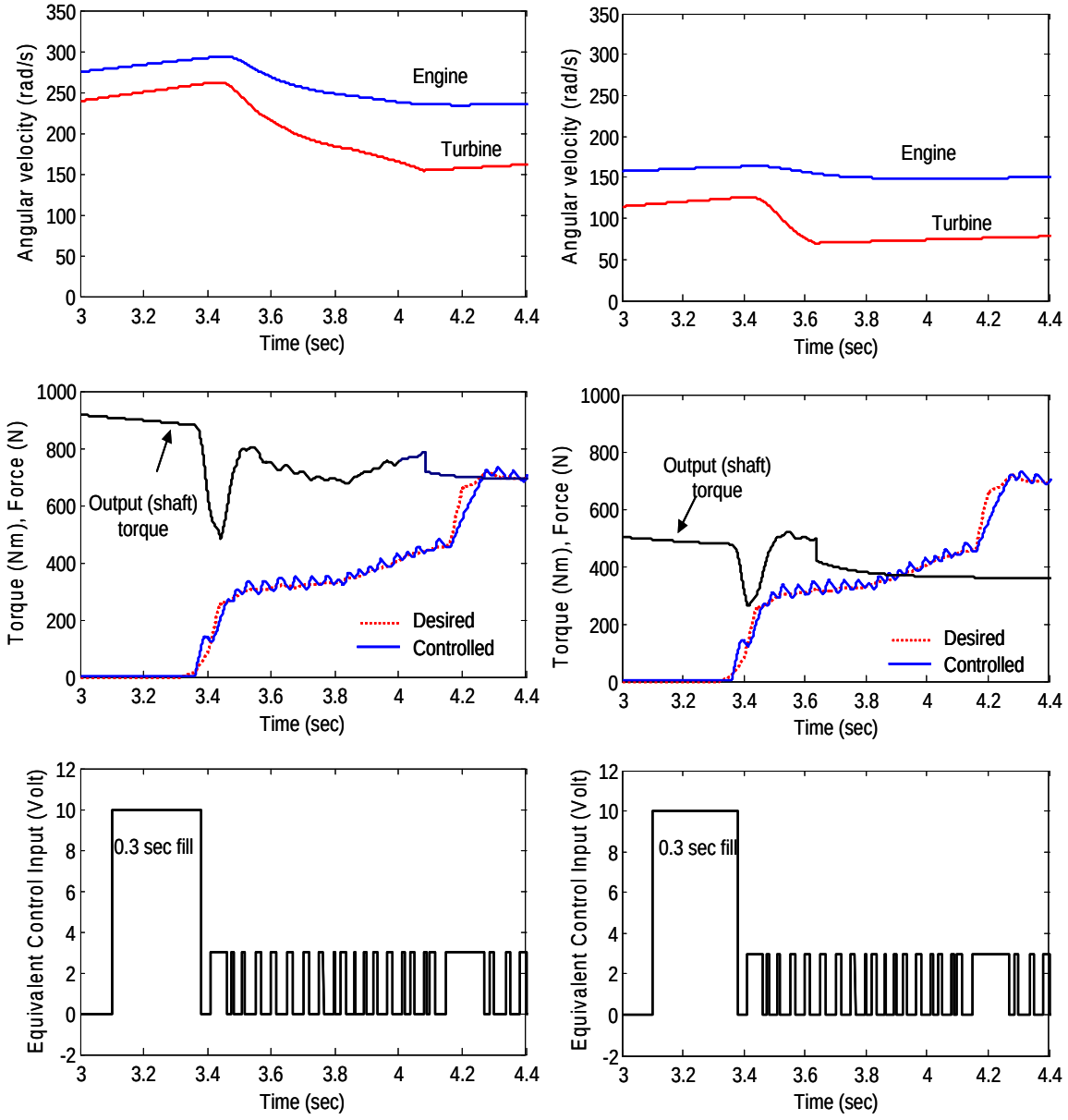

(a) 20 degree (b) 5 degree

Figure 4-15: Simulation results of power-on 1→2 up shift control with respect to different throttle openings (•••: desired;—: controlled)

4.3 Fill Volume Adapting Scheme for Torque Phase Control

4.3.1 Motivation

While the proposed sliding mode control proposed in Chapter **3** has shown promising features in force tracking performance, some issues still need to be addressed for automatic transmission applications. In particular, transition stage control (i.e., from fill stage to actuation stage) is a challenging issue. For instance, if the fill volume is slightly changed due to uncertainties such as the wear of band or tolerance stack-up of components, over-fill or under-fill can occur. This adverse phenomenon will lead to large tracking error in the beginning of the force tracking control.

Figure **4-16** shows simulation result illustrating over-fill spike originated from the intended variation of fill volume. To produce the over-fill spike, the open-loop fill control is set to be finished at 0.3 second, while the fill stroke is changed from nominal 3.5 mm to 3.2 mm and 3.0 mm, respectively. This unwanted overfill spike will decrease the duration of torque phase and cause the peak of output torque. Consequently, this *ad-hoc* fill controller has to be enhanced to ensure consistent shift quality over the life of the AT, which implies robust performance against the varying fill volume.

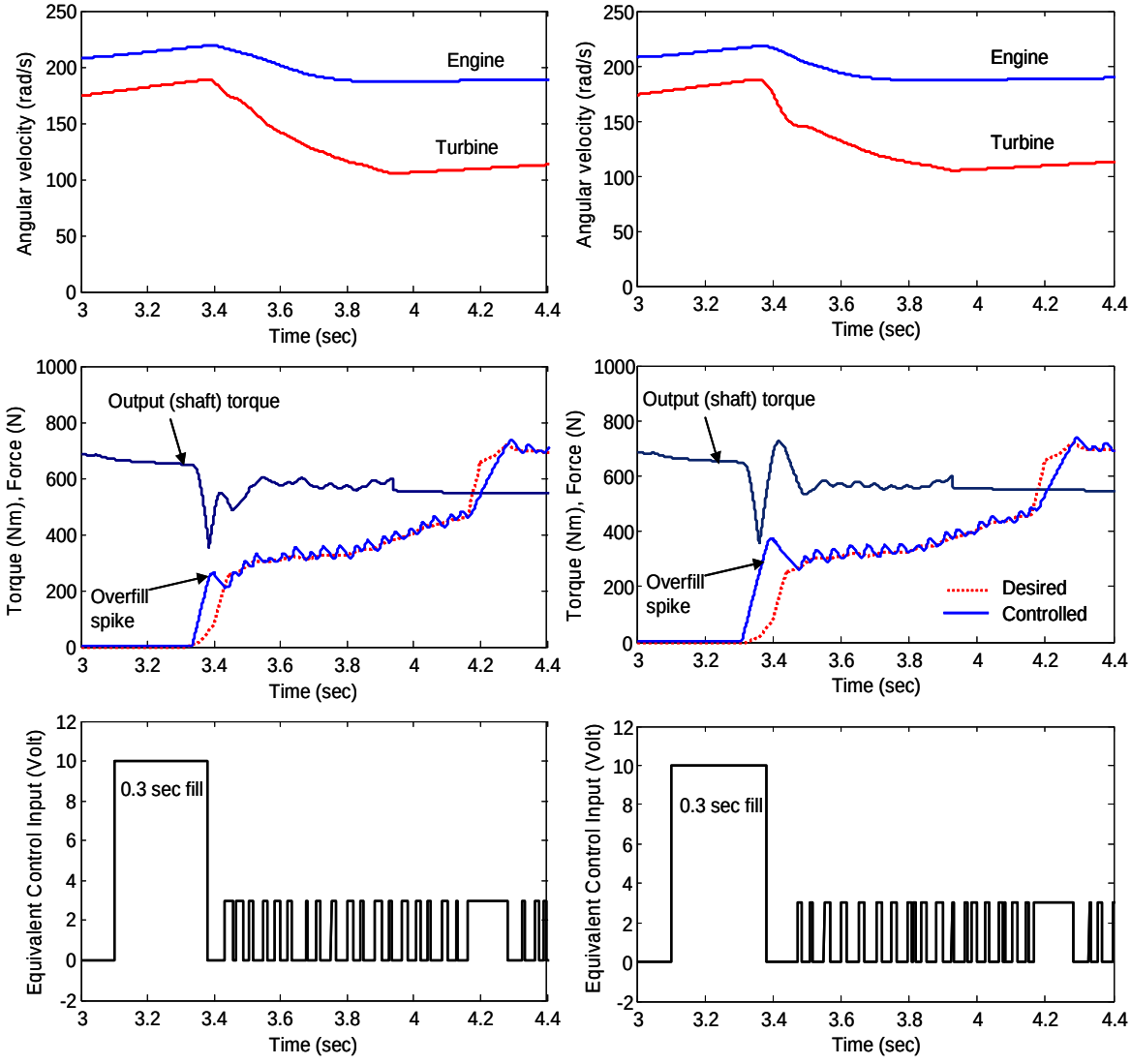

(a) 3.2 mm fill stroke (b) 3.0 mm fill stroke

Figure 4-16: Simulation results of power-on 1 → 2 up shift control using nonlinear force tracking control of PHP actuator : over fill cases (•••: desired;—: controlled)

To prevent the unwanted over-fill spike, learning algorithms of the fill volume have been developed such that the next shift event will achieve better shift quality [Zongxuan and Hebbale, 2005]. However, a critical disadvantage of learning methods is that they are not capable of preventing bad shift in the first event. Recently, another

approach has been performed to detect the end of fill with advanced transducer technology. Using position or flow rate transducer signal, the end of fill can be detected. However, flow rate signal has been proven unreliable due to noise. Furthermore, the over-fill spike is very sensitive to the variation of fill stroke, as shown in Figure **4-16**. Consequently, using position sensor is not applicable because position sensor itself is a component with tolerance. Hence, a more advanced detecting methodology should be developed for robust performance against the varying fill volume.

4.3.2 Detect the End of Fill Using Turbine Acceleration of AT

After filling the cylinder dead-stroke volume, the output torque starts to drop since the turbine input torque is transmitting through the on-coming band brake. While output torque would be a good feedback signal to use, reliable and cost-effective output torque transducers are not available in current AT. In this research, turbine acceleration of the AT is utilized to detect the end of fill, for turbine acceleration and actuation pressure provide information for the end of fill. The output torque equation during the torque phase is (see Appendix **B**)

$$T_{OUT} = C\dot{\omega}_T + T_{LOAD} \qquad \textbf{(}4.28\textbf{)}$$

It is clear that output torque is a explicit function of the turbine angular acceleration and load torque. However, like non-contact output torque sensor, hardware-based direct measurement of angular acceleration is not applicable.

4.3.3 Differentiation of Turbine Speed and Post-filtering

A natural alternative is to directly differentiate the angular velocity (rotational speed) obtained from the only available pick-up sensor in current AT. The backward-difference operator is mainly used to differentiate the velocity quantity.

$$\alpha(k) = \dot{\omega}(k) = \frac{\omega(k) - \omega(k-1)}{T_s} \quad \textbf{(}4.29\textbf{)}$$

where T_s is sampling (interrupt) time. Figure **4-17** shows the speed sensor widely used in current AT and the principle of speed measurement. The rotational speed will be calculated from the number of pulse induced by magnetic hall sensor.

$$\omega = \frac{60 \cdot M}{Z \cdot T_s}(rpm) \quad \textbf{(}4.30\textbf{)}$$

where M is the number of pulse, Z is the number of gear tooth, T_s is sampling time.

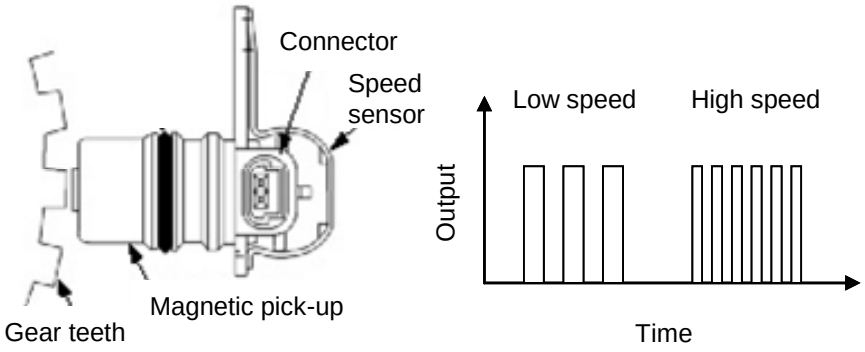

Figure 4-17: Principle of speed measurement in current automatic transmissions

To demonstrate the feasibility of new approach, actual measured rotational speed data (recorded sampling rate of 0.02 second) is used, as shown in Figure **4-18**. The measurement error $e(k)$ is defined by following expression and shown in lower graph.

$$e(k) = \omega(k) - \tilde{\omega}(k) \qquad \textbf{(}4.31\textbf{)}$$

where, $\omega(k)$ is the primary angular velocity and $\tilde{\omega}(k)$ represents the measured angular velocity . This measurement error, which is mainly caused by sampling, will act as noise in differentiation operation.

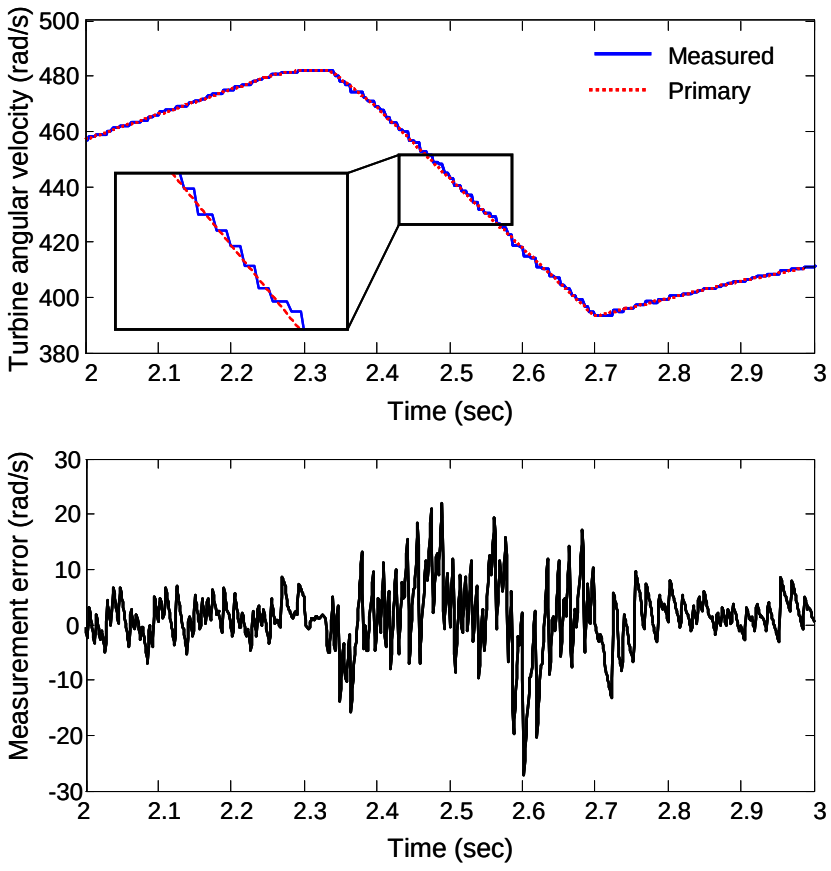

Figure 4-18: Sample measured data of turbine angular velocity and measurement error

Figure **4-19** shows the differentiation result of measured angular velocity without post-filtering. As expected, this is useless with large noise resulted from measurement error. The use of a longer interrupt period with high resolution sensor can be utilized to reduce such problems. However, longer sampling rate will lead to unwanted larger delay and the resolution is still insufficient to detect transient point.

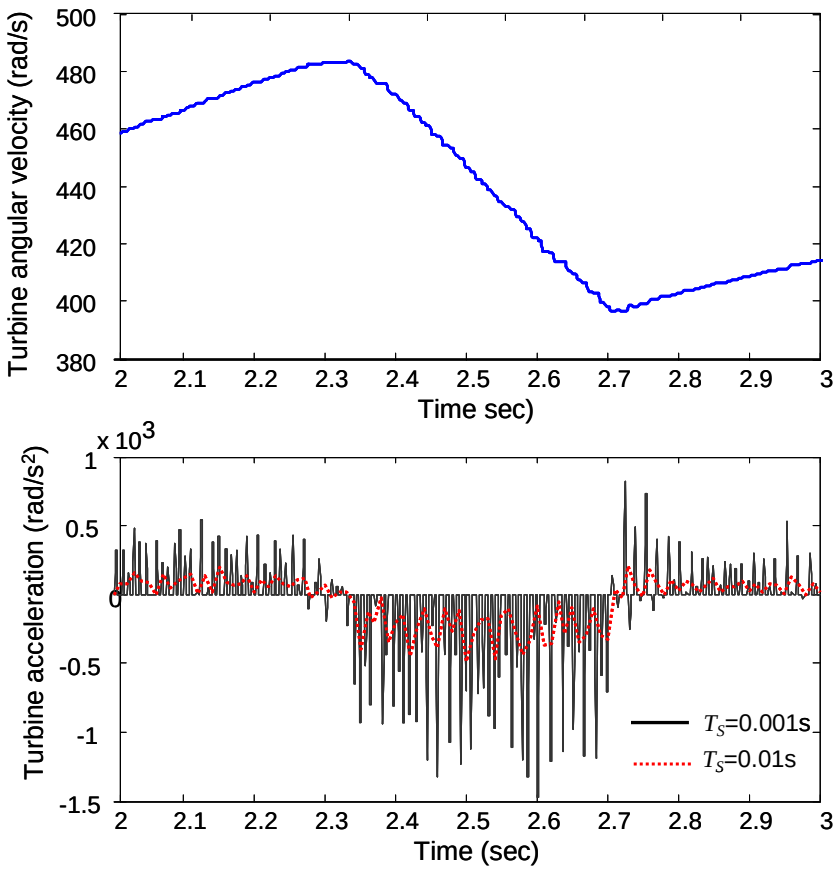

Figure 4-19: Differentiation result of measured angular velocity without post-filtering

To facilitate available acceleration, several post-filtering techniques, such as FIR and IIR low-pass filters, can be used to restore the corrupted measured velocity signal. However, conventional filtering solutions also will lead to large phase delay. The post

filtering result using FIR low-pass filter is illustrated in Figure **4-20**. Due to the large phase delay, it is also useless since the interested interval of torque phase in AT shift control is 100 ~ 200 ms. Indeed, the estimation of angular acceleration has been recognized as one of the most challenging tasks in the realization of many control applications [Gao and Ovaska, 2001]. Accordingly, more advanced filtering techniques are required.

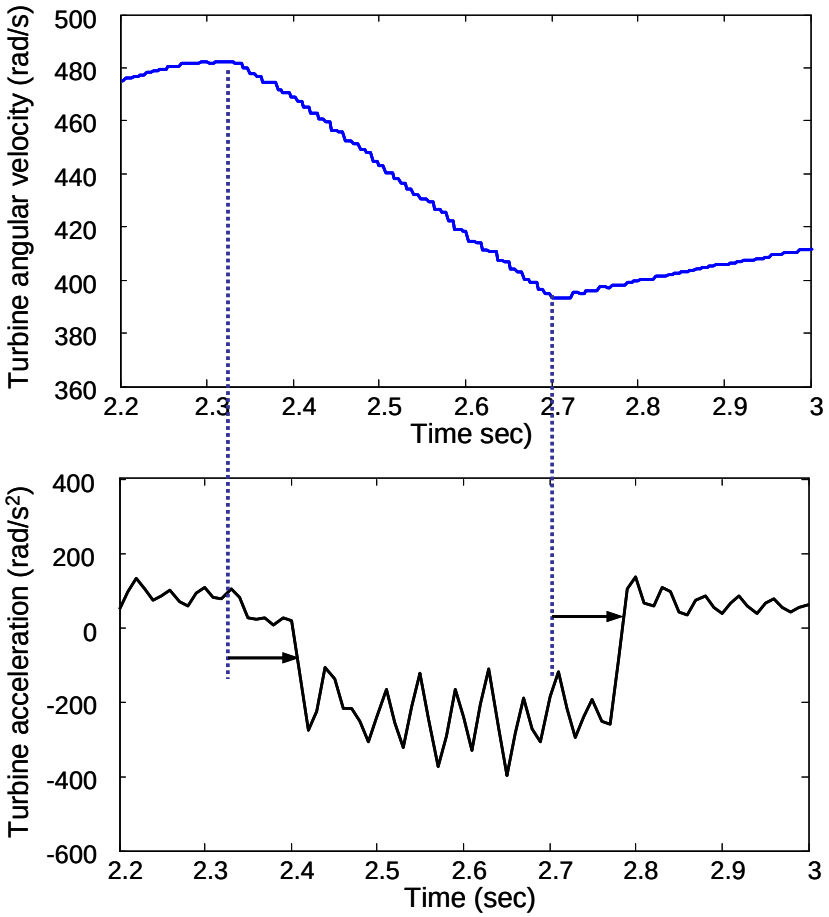

Figure 4-20: Phase-delayed differentiation result using low-pass (FIR) post-filtering

4.3.4 Neural Network – based Estimation

It has been recognized that neural networks are well suitable for nonlinear signal processing [Hines, 1997]. Figure **4-21** shows the structure of a single input adaptive transverse filter with time delay neural network (TDNN) used for estimation [Hines, 1997]. It can be observed that the tapped delay line is feeding not only to the current samples but also to the delayed samples. Thus, this neural network- based filter can be described as a nonlinear function of the stored sample data as follows;

$$\hat{\alpha}(k) = f[\tilde{\alpha}(k), \tilde{\alpha}(k-1), \cdots, \tilde{\alpha}(k-N)] \qquad \textbf{(}4.32\textbf{)}$$

where N is the order of neural network-based estimator, which is generally determined by empirical tuning (N = 5 in this case). The set of delayed data is the noisy acceleration samples and will be input to the neural networks, which means *on-line* training data. The set of delayed noisy data will be eventually averaged by the appropriate weights.

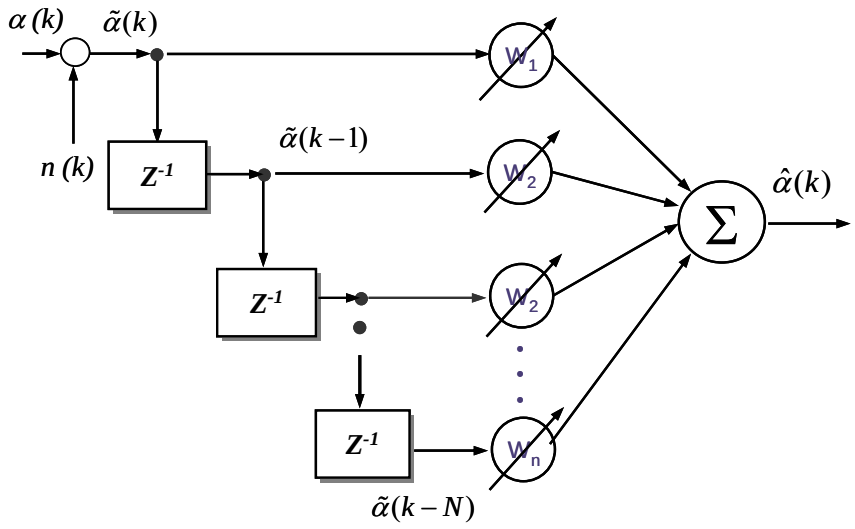

Figure 4-21: Schematic structure of single input adaptive transverse filter

In this thesis, the adaptive weighting of coefficients is performed by using optimization algorithms such as the error back-propagation (BP) algorithm [Passino, 2004]. The root mean square error defined in Eq. **4.33** is considered as the cost function to be minimized. It will gradually learn to attenuate the noise $n(k)$ and eventually restore the primary acceleration.

$$E = \sqrt{\frac{1}{n}\sum_{k=1}^{n}\sum_{j=1}^{m}(\alpha_j^{(k)} - y_j^{(k)})^2} \qquad \textbf{(}4.33\textbf{)}$$

The structure of neural network for BP algorithm is shown in Figure **4-22**. x_i is the input patterns and *n* is the number of input nodes (= 6). z_s represents the output at *s-th* hidden neuron and *h* is the number of neurons at hidden layer (= 5). The output *y* ($\hat{\alpha}$) at the output layer is given by

$$y_j = f_2(W_{sj} z_s) = f_2(W_{sj}\, f_1(W_{is} x_i)) \qquad \textbf{(}4.34\textbf{)}$$

where z_s is the activation at the hidden neurons. f_2 is the activation function at the output neurons, and f_1 is the activation function at the hidden neurons. W_{is} and W_{sj} are the weight *i-th* input to *s-th* hidden and *s-th* hidden to the output, respectively. These weights will be adaptively updated by error back propagation algorithm. To derive the BP algorithm, differentiation of activation functions is essentially required as follows;

$$\frac{\partial E}{\partial W_{js}} = -\sum_{k=1}^{P}\delta_{2j}^{(k)} z_s^{(k)} \ , \ \delta_{2j}^{(k)} = (\alpha_j^{(k)} - y_j^{(k)})\, f_2^{'}(net_j^{(k)}) \qquad \textbf{(}4.35\textbf{)}$$

$$\frac{\partial E}{\partial W_{si}} = -\sum_{k=1}^{P}\delta_{2s}^{(k)} x_i^{(k)} \ , \ \delta_{1s}^{(k)} = f_1^{'}(net_s^{(k)})\sum_{j=1}^{m} W_{js}\delta_{2j}^{(k)} \qquad \textbf{(}4.36\textbf{)}$$

The detailed error back propagation steps are described in Appendix **D**.

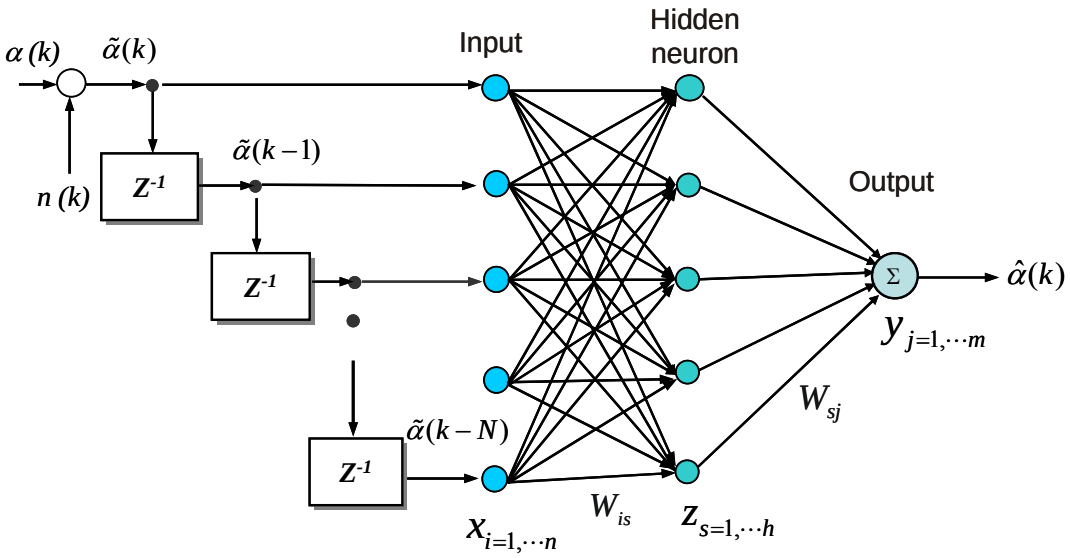

Figure 4-22: Structure of neural network-based filter using BP algorithm

The activation functions (f_1 and f_2) are selected to be logistic and linear function, respectively, as shown in Figure **4-23**.

$$f_1(x) = \frac{1}{1+e^{-\beta x}},\ f_2(x) = x \qquad \textbf{(4.37)}$$

where β is slope of logistic function (= 1).

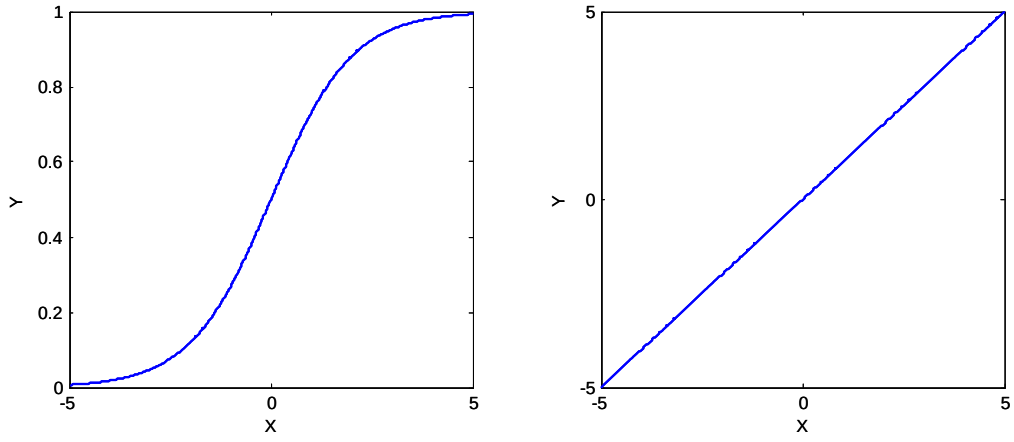

(a) f_1 (logistic) (b) f_2 (linear)

Figure 4-23: Activation functions used for BP algorithm

The estimation results of using the TDNN-based filtering approach is illustrated in Figure **4-24**. Critical point indicating the end of fill can be detected by comparing two sampled data as follows;

$$\left|\alpha(k)-\alpha(k-1)\right| > \alpha_r \qquad \textbf{(}4.38\textbf{)}$$

If the difference between the two sampled data is greater than the acceleration signal ripple α_r, this point can be represented as a slope changing point. As seen, the resolution of the turbine acceleration using this advanced filtering method is adequate to detect the critical point. RMS error is also converged, as shown in Figure **4-25**.

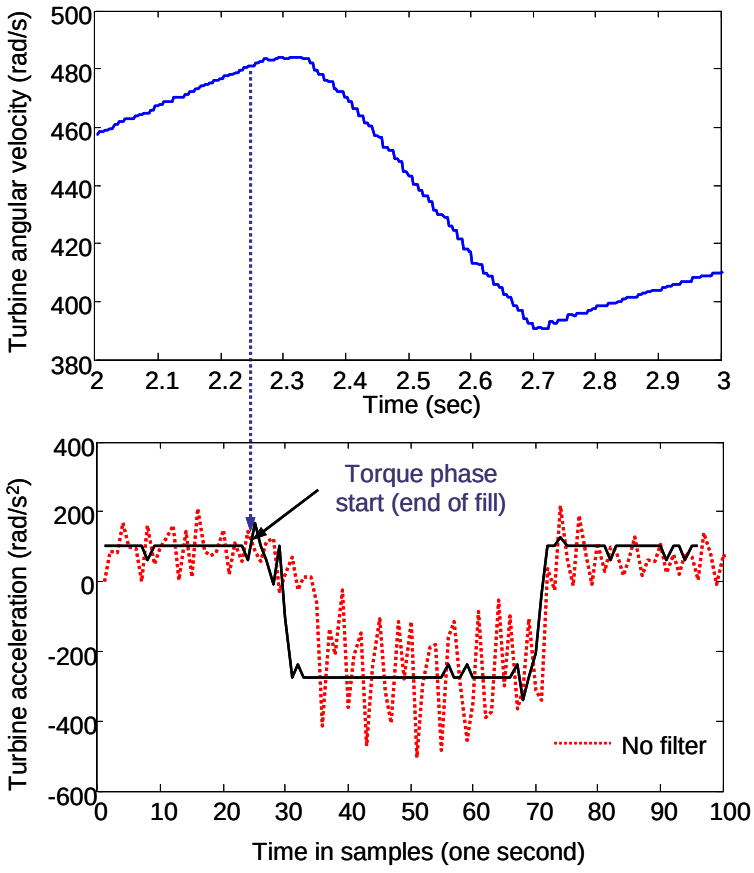

Figure 4-24: Estimation result using TDNN-based filtering (•••:without filtering)

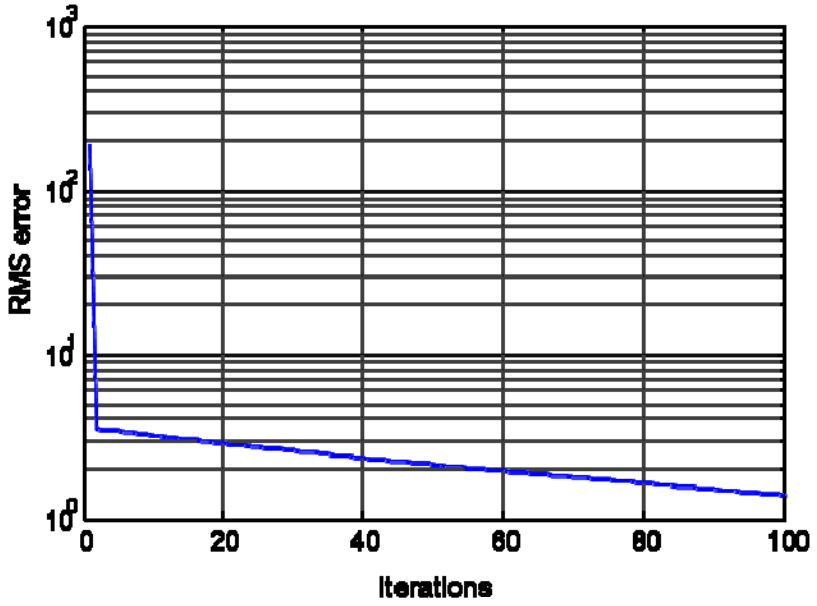

Figure 4-25: The history of converged RMS error

Nonlinear logistic activation function such as f_1 will be difficult to implement in the AT control unit (in short, TCU). In real applications, we can either use a linearized activation function or modifying the TCU subroutine library. For the purpose of comparison, the logistic function for f_1 is changed to a linear function (i.e., both activation functions are linear), as shown in Figure **4-26**.

$$f_1(x) = 0.1x + 0.5 \qquad (4.39)$$

The estimation result with the linear activation function is plotted in Figure **4-27**. Compared with the original logistic function, the shape of the filtered acceleration is more naive, which result in slightly delayed detecting. However, the discrepancy is so small.

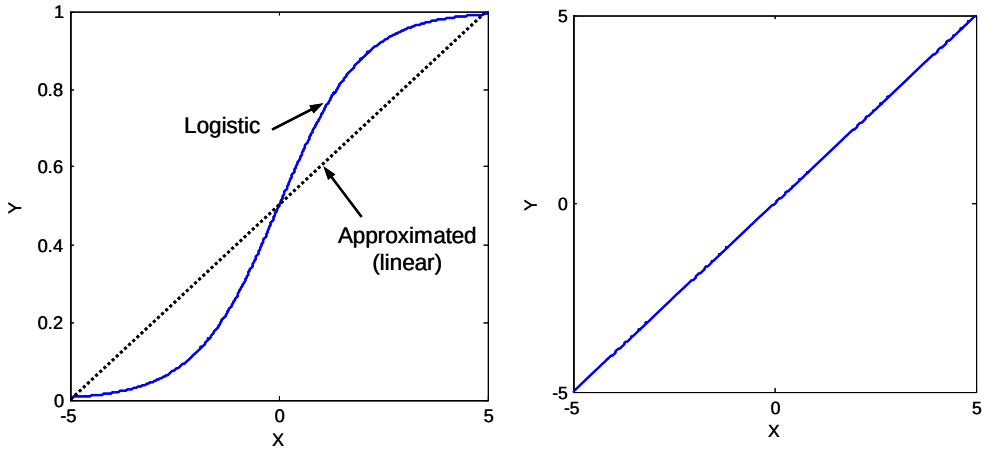

(a) f_1 (linear) (b) f_2 (linear)

Figure 4-26: Approximated activation functions used for activation function f_1

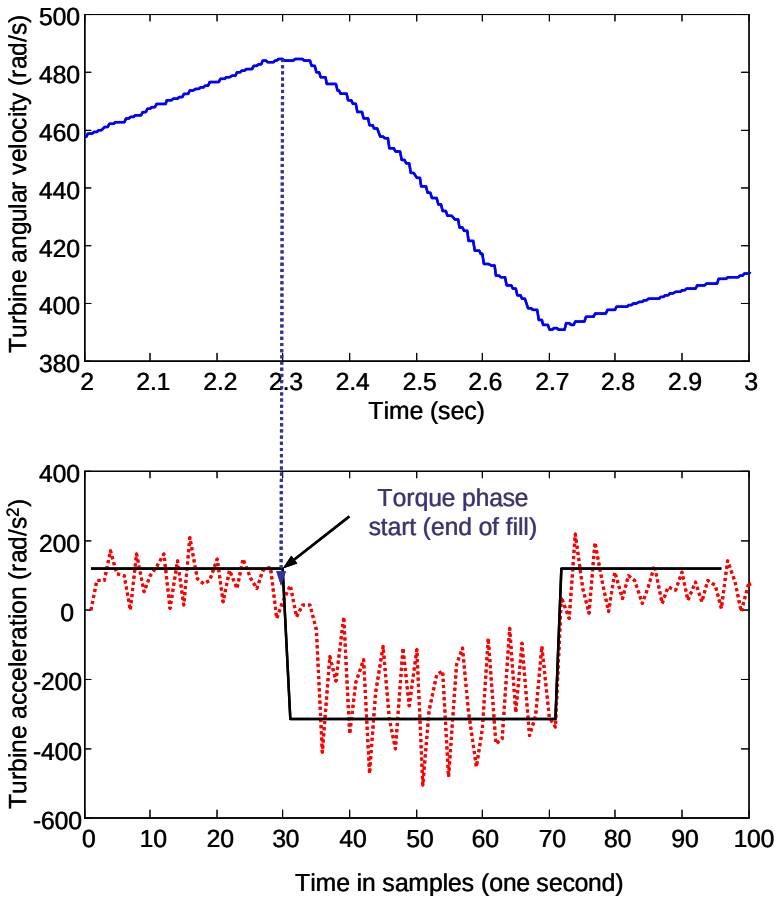

Figure 4-27: Filtering with approximated activation function (•••: without filtering)

While the neural network-based filter shows the promising performance, on-line estimation using the BP algorithm requires large computation efforts for built-in TCU in vehicles. Filtering also can be performed by *off-line*. Pre-determined weights using the BP algorithm can be used for weights in Figure **4-21**. For instance, filtering result using pre-determined weight (Eq. **4.40**) shows similar filtering result, as shown in Figure **4-28**.

$$\mathbf{W} = [0.1\ 0.1\ 0.1\ 0.1\ 0.1\ 0.2] \qquad \textbf{(}4.40\textbf{)}$$

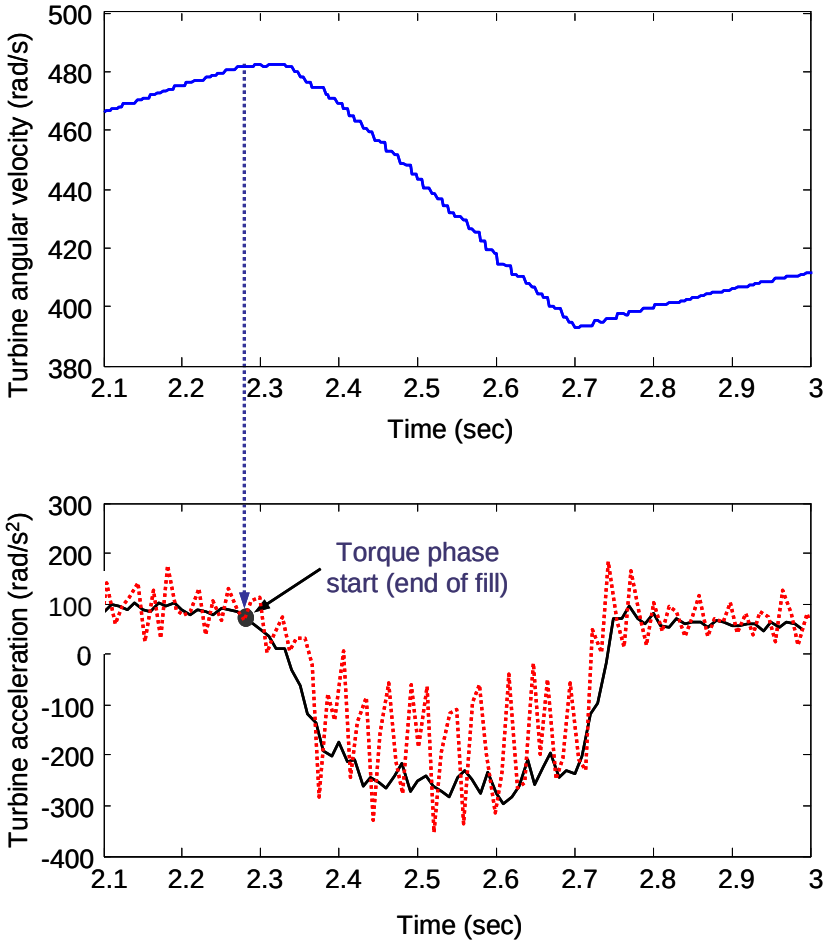

Figure 4-28: Estimation result with pre-determined weights (•••: without filtering)

4.3.5 Simulation Result and Discussions

To emulate the measurement error of turbine speed, random noise is added to the turbine angular velocity in the simulation model, as shown in Figure **4-29**. In addition, zero order hold is used to emulate the interrupt period of 0.01 second, which is commonly used in the AT control unit. As a result, differentiated turbine acceleration contains unwanted noise and has to be filtered.

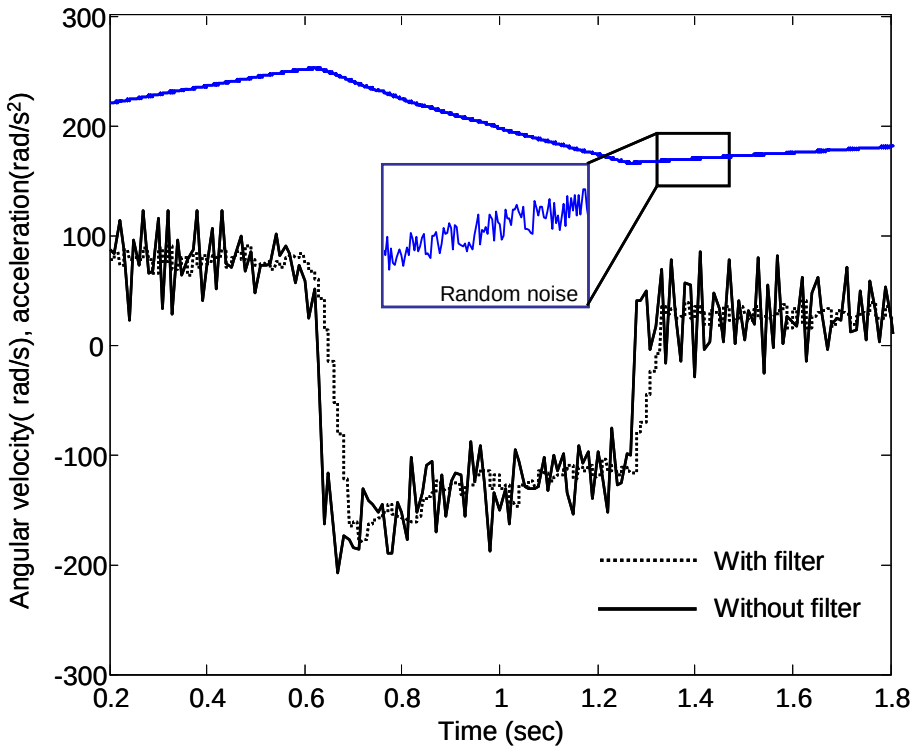

Figure 4-29: Simulated turbine acceleration considering the measurement error in turbine angular velocity (•••: with filter;—: without filter)

The simulation result of torque phase control for the case of overfill is shown in Figure **4-30.** Fixed fill time of 0.3 second can be successfully adjusted by detecting the

end of fill in the turbine acceleration. Because of this fill volume adapting control strategy, the over-fill spike in the actuation force and the output torque can be reduced.

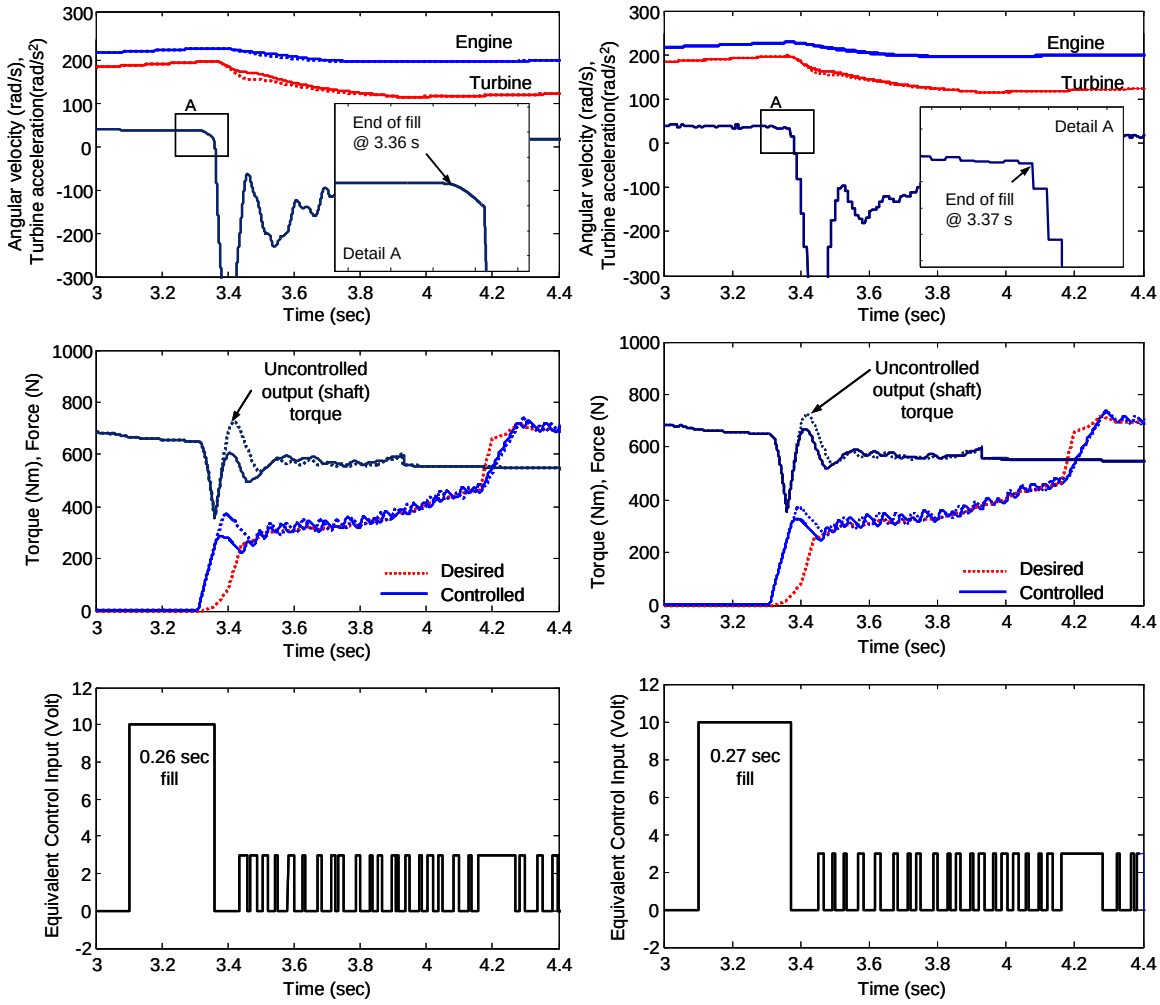

(a) ideal case (b) with measurement noise

Figure 4-30: Torque phase control result for fill stroke of 3.0 mm (•••: uncontrolled)

4.4 Hardware-in-the-loop Simulation

Building upon the off-line simulation model described earlier, the hardware-in-the-loop simulation is performed by replacing the actuator model with the PHP actuator hardware. Recently, hardware-in-the-loop simulation (HILS) systems have been recognized as one of the most powerful tools for rapid development of power train control systems since engineers can identify and resolve the problems earlier in the development cycle [Mianzo, 2000]. In this thesis, the feasibility of the proposed actuation system with the controller is evaluated via HILS.

4.4.1 Configuration of HILS

The HILS environment consists of the simulation module and physical hardware for the band brake actuation system, as shown in Figure **4-31**. The dSPACE® (model: DS1103) control board that is built the Texas Instruments TMS320C31 floating-point DSP processor is used as a rapid control prototyping tool for implementing the real time control task. The procedure for the HILS is summarized as follows:

1. Real time simulation model and controller is coded in MATLAB/Simulink®. The turbine and engine rotational speed signal (ω_E, ω_T), which are available sensing signals in current AT, are also adopted for determining the shift schedule and shift control law.
2. The real time workshop (RTW) module in the dSPACE® system builds the real time models and controller. Then, it converts them into an executable C code and downloads it into the microprocessor built in the DSP board.

3. The digital output (i.e., equivalent control input) determined by the micro-processor is converted into analog output voltage through the built-in D/A converter.
4. The control input drives the piezoelectric-hydraulic pump based actuator through the driver, which in turn generates the actuation force (pressure). The dSAPCE® system converts analog inputs (i.e., from pressure or force transducer) into digital inputs using built-in A/D converter with 16-bit output resolution.

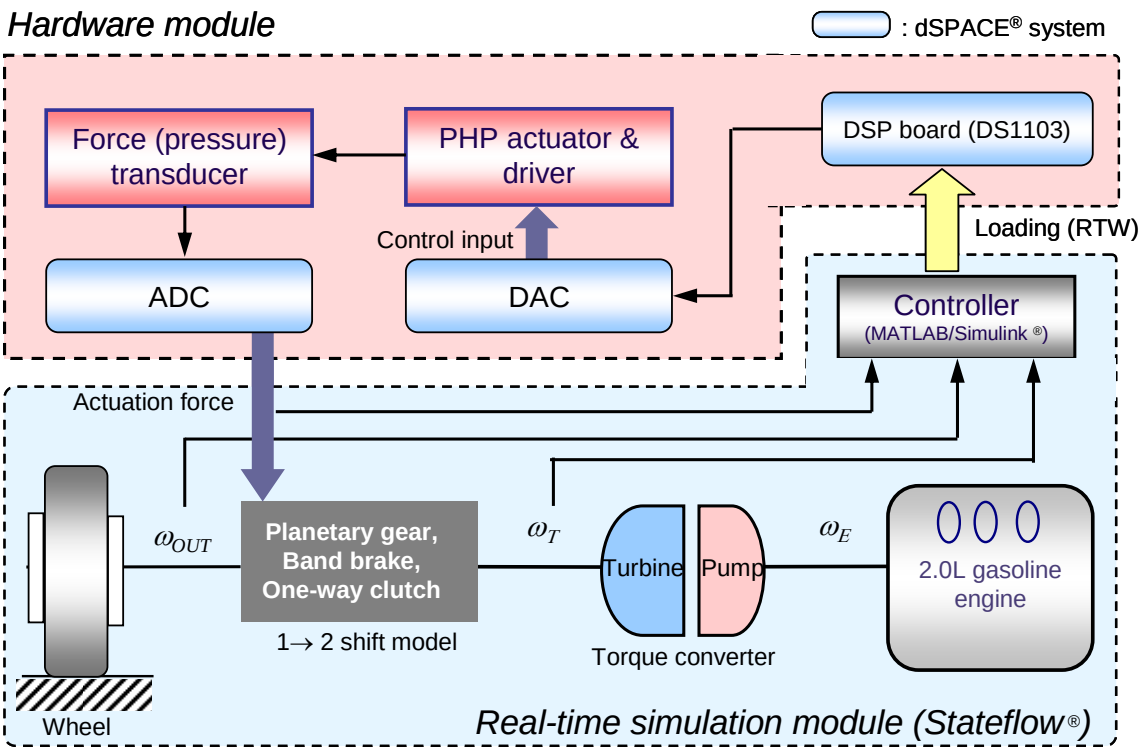

Figure 4-31: Hardware-in-the-loop simulation(HILS) platform

To avoid overrunning, the CPU executing time has to be within the sampling (interrupt) time *T*, as shown in Figure **4-32** [dSPACE, 2007]. Therefore, the executing time is first of all examined. Dormand-Prince (5-th order) method with fixed step size of

100 μsec is used for numerical integration. The executing time per one numerical integration step is approximately 50 μsec using Stateflow®. In this case, numerical integration can be performed more than 10 times within the sampling time of 1000 μsec. As a result, the total executing time is 500 μsec, which is less than the sampling time of 1000 μsec.

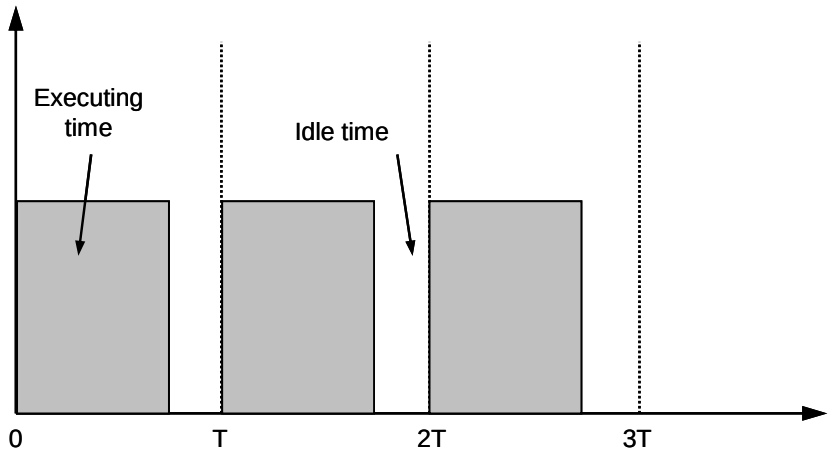

Figure 4-32: Diagram for illustrating real-time control experiment

Figure **4-33** shows the overall outlook of the hardware-in-the-loop simulation system, which includes controller with dSPACE system, PHP actuator and drivers. To represent the entire stroke, the plate spring with a small additional stroke (about 0.5 mm) is introduced at the front of the piston of hydraulic cylinder to emulate the band brake, for the actual band brake can be slightly deformed due to the band elongation and the compression of a friction pad. With this element, the piston will be nearly stopped after stroking (i.e., fully compressed). For actual force tracking control, a customized force transducer is also attached on the plate spring to measure the actual actuation force.

Accumulator pressure is set to be same as actuation tracking control described in Chapter **3**, which is 0.55 MPa.

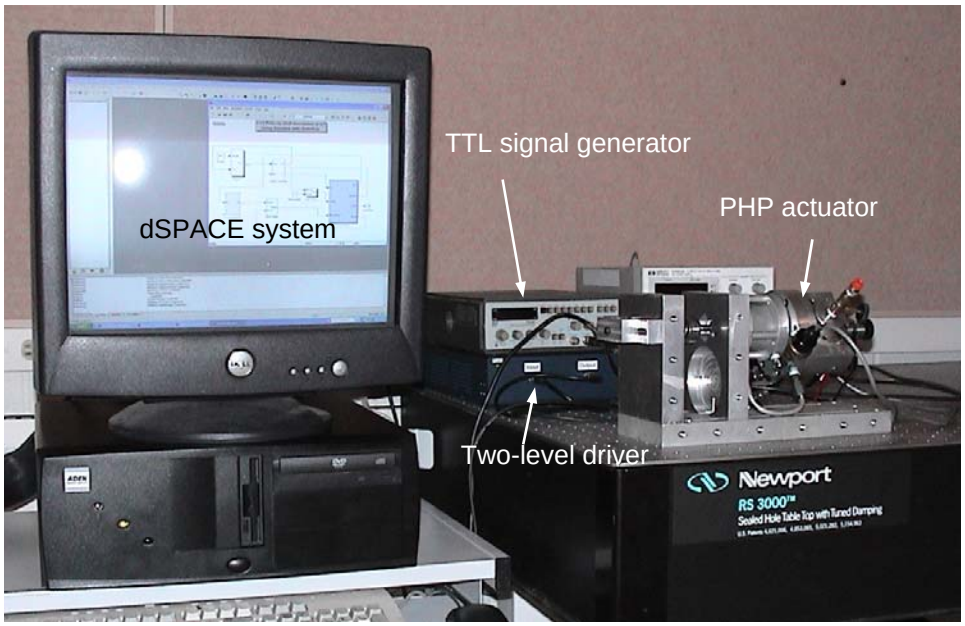

Top view of HILS stand

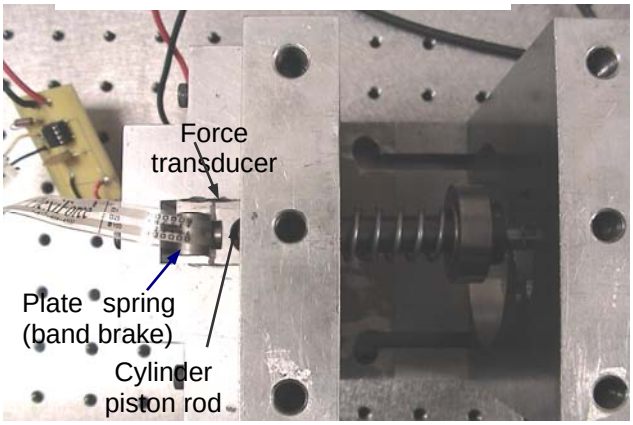

Figure 4-33: Overall outlook of hardware-in-the-loop simulation (HILS) system

4.4.2 Results and Discussion

Figure **4-34** shows the effect of numerical integration methods on HILS performance. While the proposed model could be operated in real time without overrunning, there are, however, significant discrepancies between the two responses of shaft torque. In case of the use of Runge-Kutta method (4^{th} order), output (shaft) torque is significantly differ from the off-line simulation results. This problem was resolved by selecting a higher order numerical integration method such as Dormand-Prince method (5^{th} order).

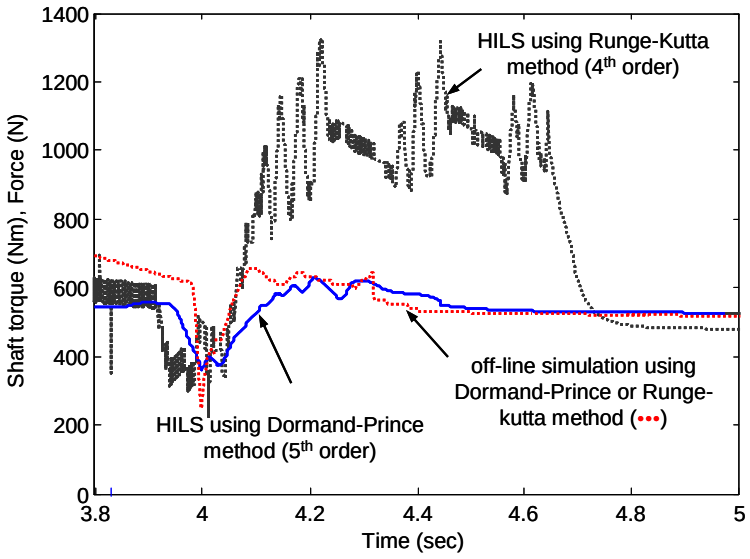

Figure 4-34: Effect of numerical integration methods on HILS performance

The typical real time HILS results using two tracking methods (pressure and force tracking) are shown in Figure **4-35** and Figure **4-36**. These illustrative examples are for the 10° of throttle opening in AT model. The controller successfully tracked the

desired trajectory determined from vehicle test results in both cases. The HILS results are also in good agreement with the vehicle test result (Figure **4-13**).

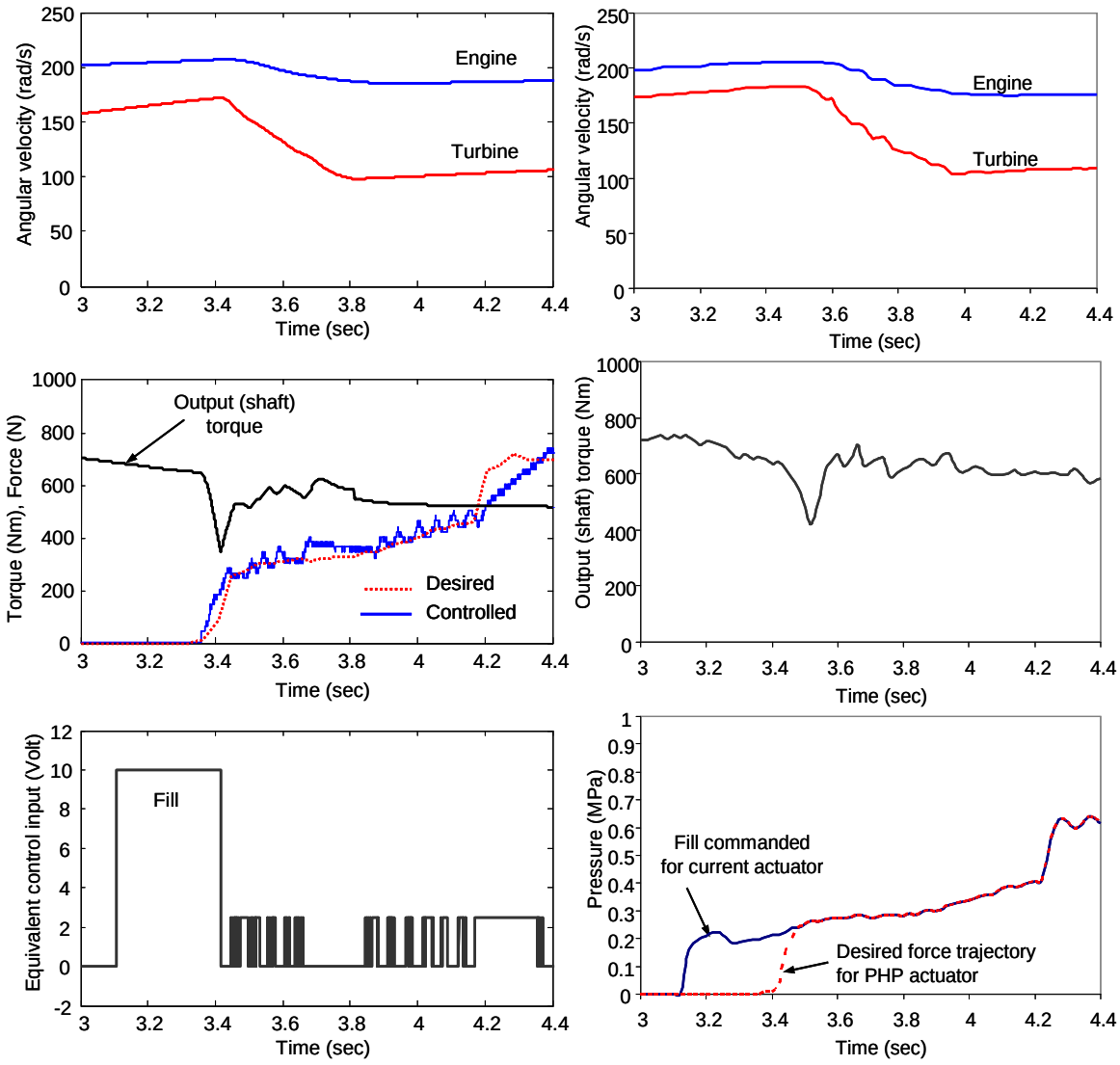

(a) HILS (b) vehicle test

Figure 4-35: HILS with actuation pressure tracking control result and comparison with vehicle test results: $\theta_{th} = 10^{\circ}$

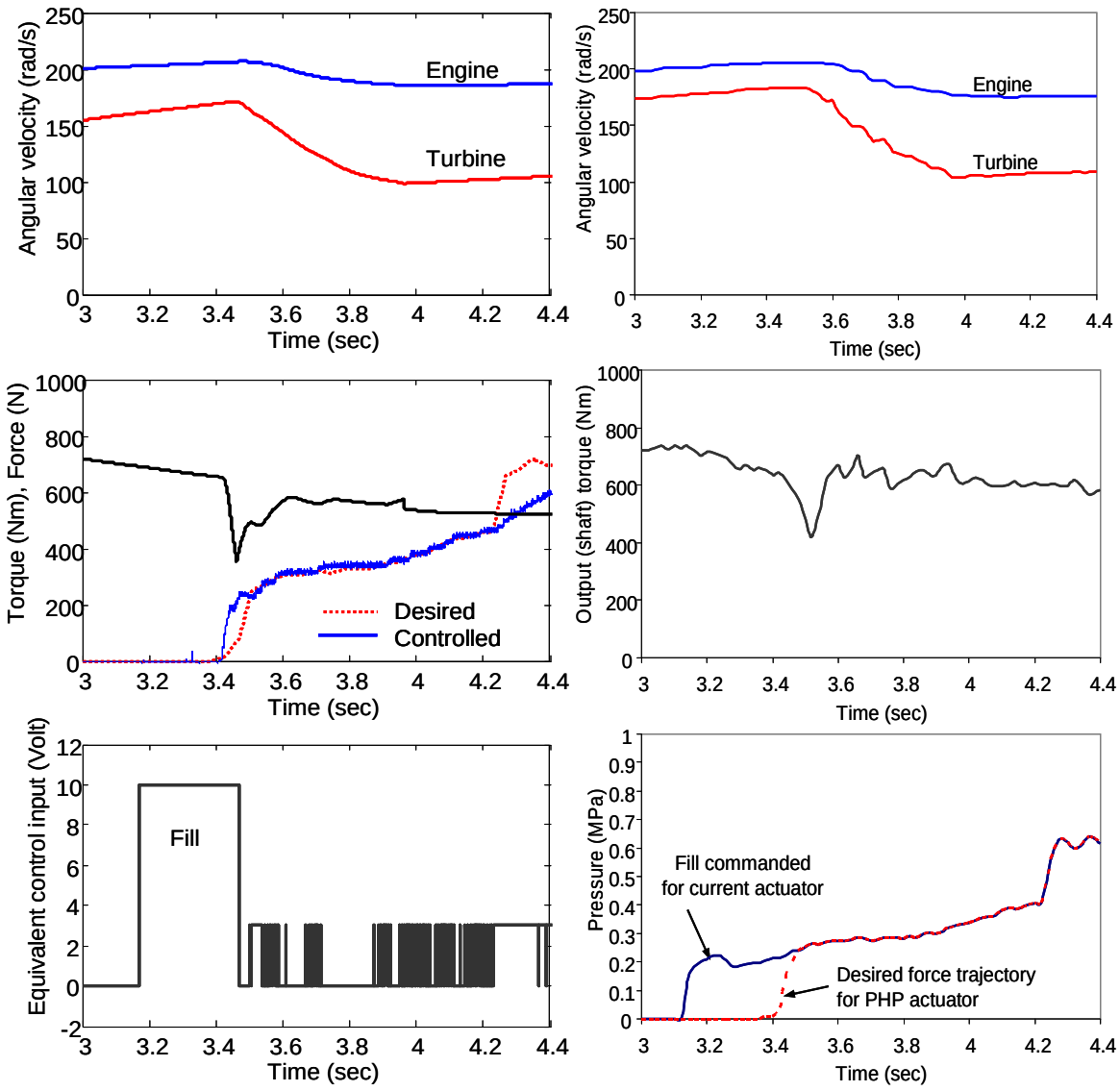

(a) HILS (b) vehicle test

Figure 4-36: HILS with actual force tracking control result and comparison with vehicle test results: $\theta_{th} = 10^{\circ}$

HILS performance with respect to different throttle openings are investigated. Like the off-line simulation results, throttle angles are set to be 5°, 10°, and 15°, respectively, in Figure **4-37** , Figure **4-38** , and Figure **4-39**. The HILS results are in

good agreement with the off-line simulation results. After engaging (i.e., locking after 4.2 second), the HILS results show some discrepancy with off-line simulation results due to the rather insufficient dead-head pressure. Actual force tracking using force transducer is preferable to actuation force tracking because of the better resolution.

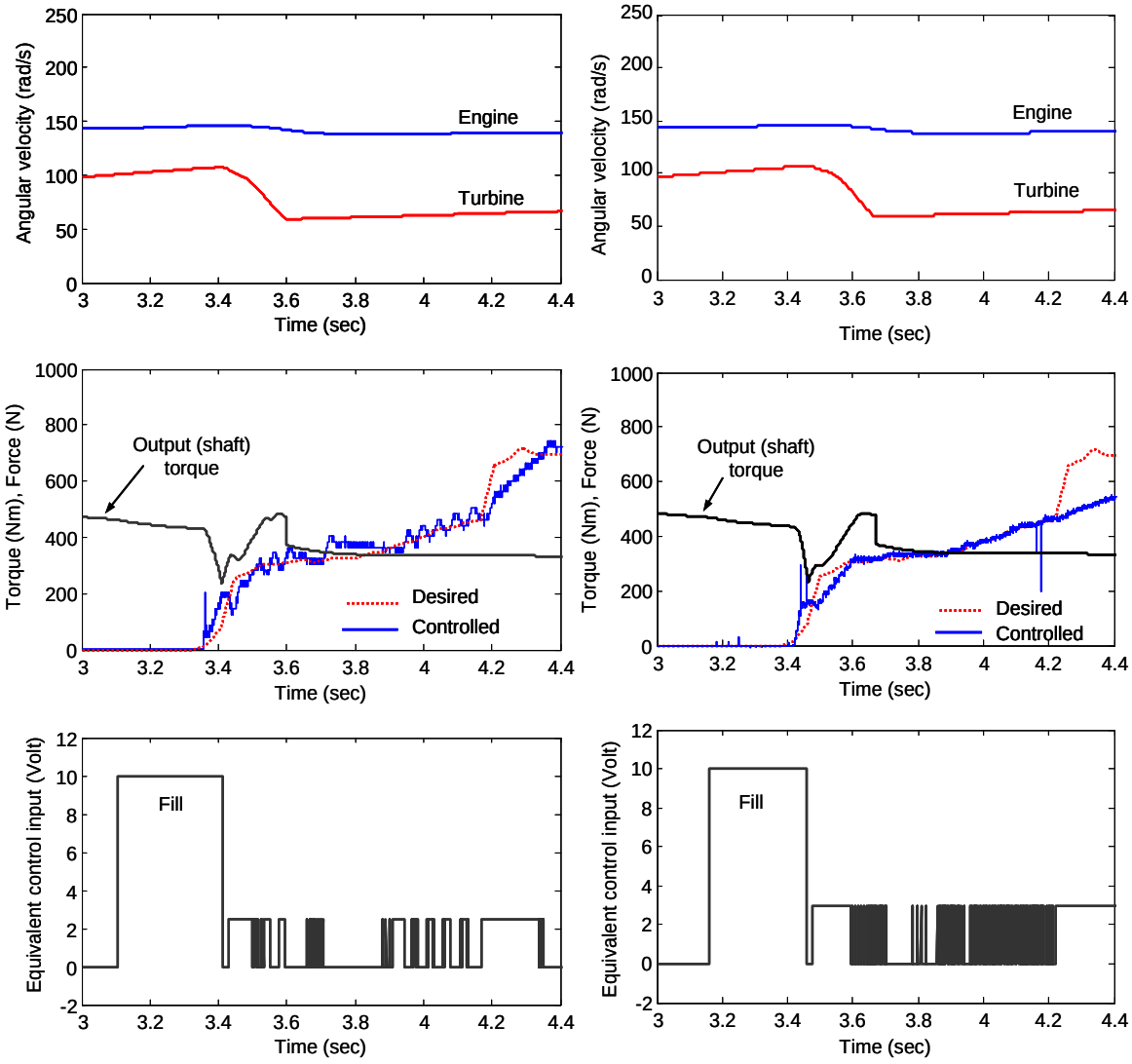

(a) actuation pressure tracking (b) actual force tracking

Figure 4-37: HILS result with respect to two tracking methods: $\theta_{th} = 5^{\circ}$ (•••: desired;—: controlled)

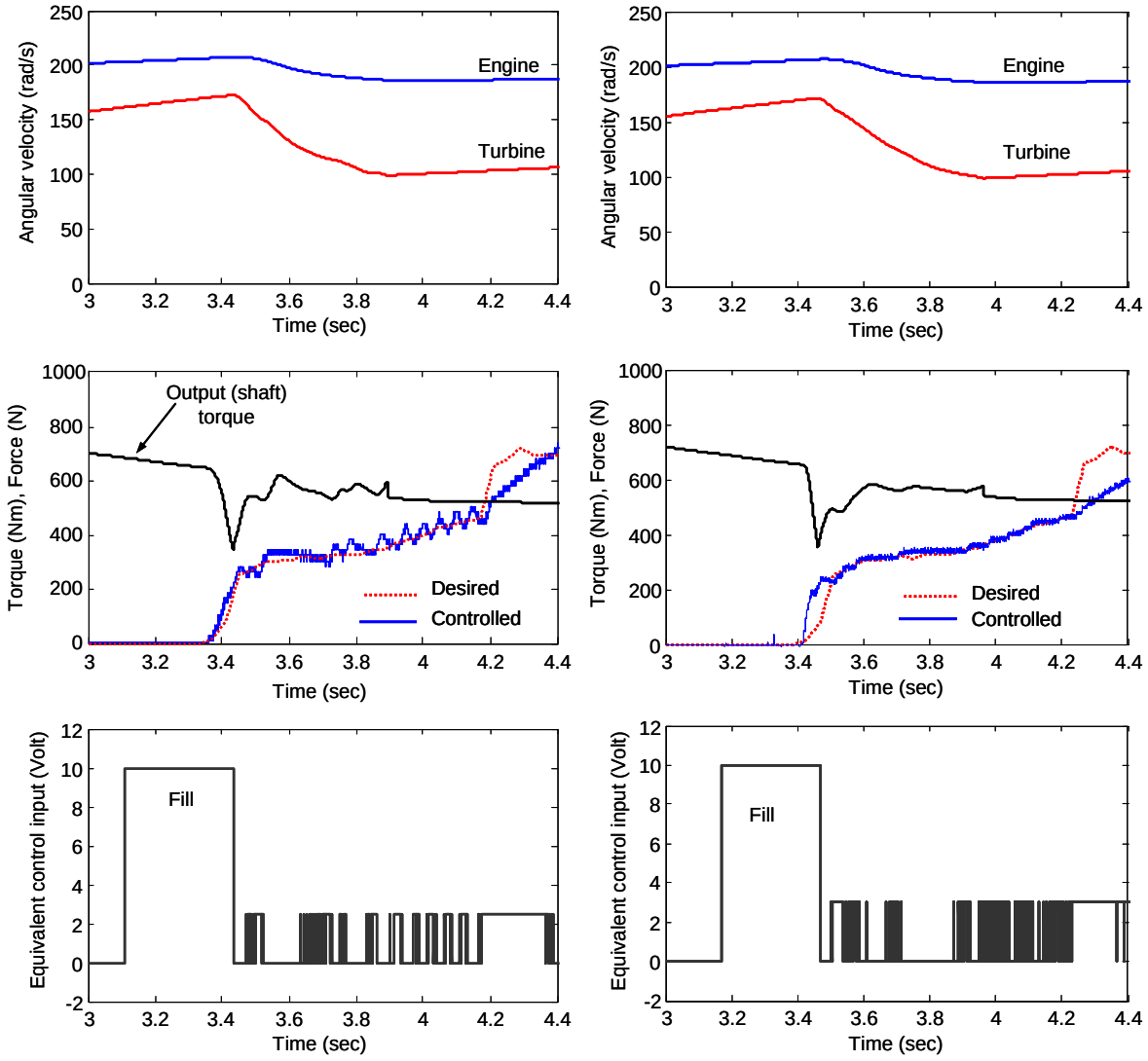

(a) actuation pressure tracking (b) actual force tracking

Figure 4-38: HILS result with respect to two tracking methods: $\theta_{th} = 10^{\circ}$ (•••: desired;—: controlled)

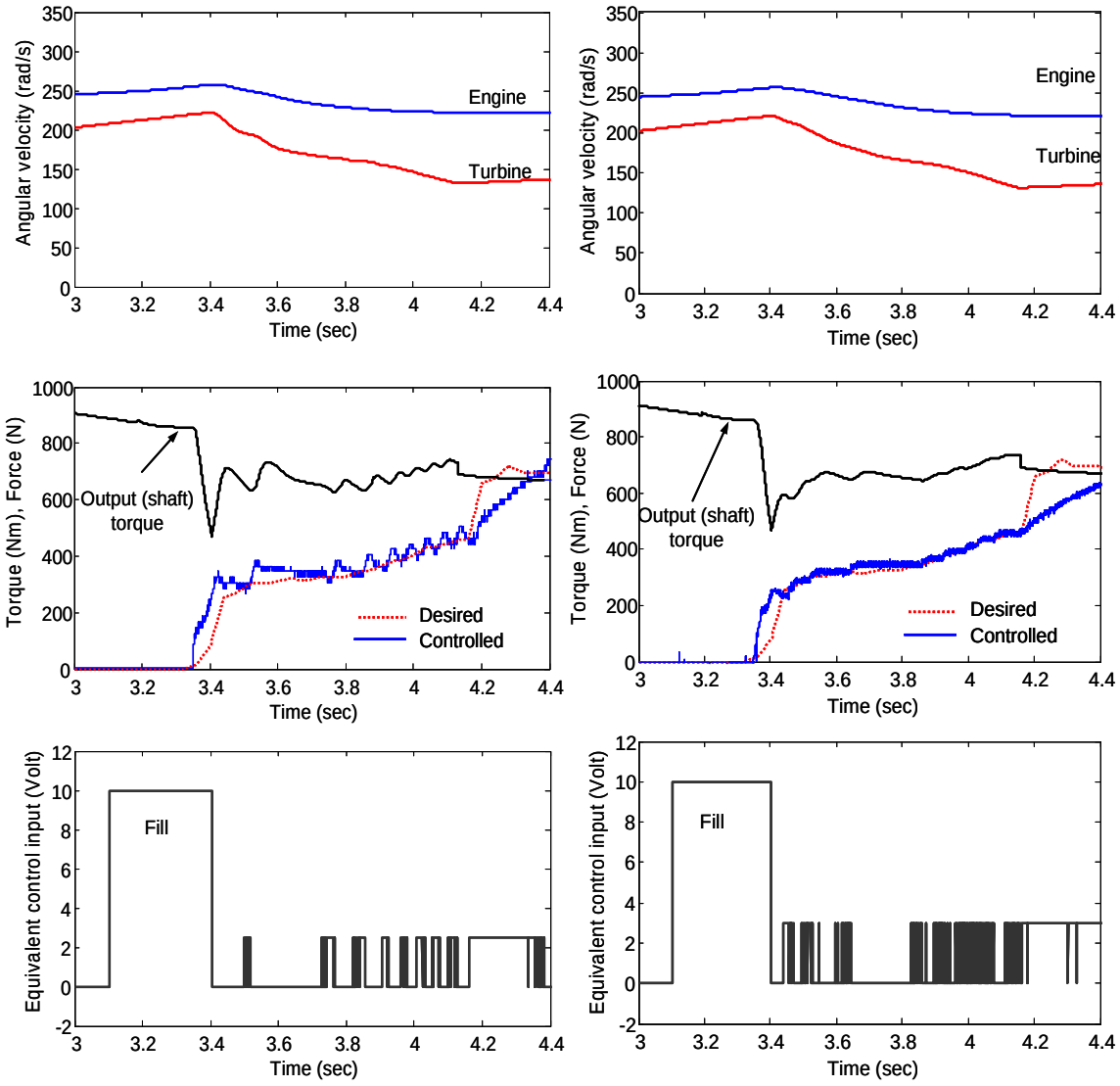

(a) actuation pressure tracking (b) actual force tracking

Figure 4-39: HILS result with respect to two tracking methods: $\theta_{th} = 15^{\circ}$ (in the middle •••: desired;—: controlled)

Next, HILS performance with fill volume adapting scheme are investigated in Figure **4-40** and Figure **4-41**. To present the unwanted over-fill scenario, fill strokes are intentionally set to be 3.0 mm and 2.8 mm, respectively. In both cases, the original fixed

fill time of 0.3 second is adjusted to 0.27 second and 0.24 second, respectively. Consequently, the overfill spike in actuation force and the output torque is reduced because of the successful prevention of the excessive overfill. The effectiveness of the fill volume adapting scheme is validated through the HILS.

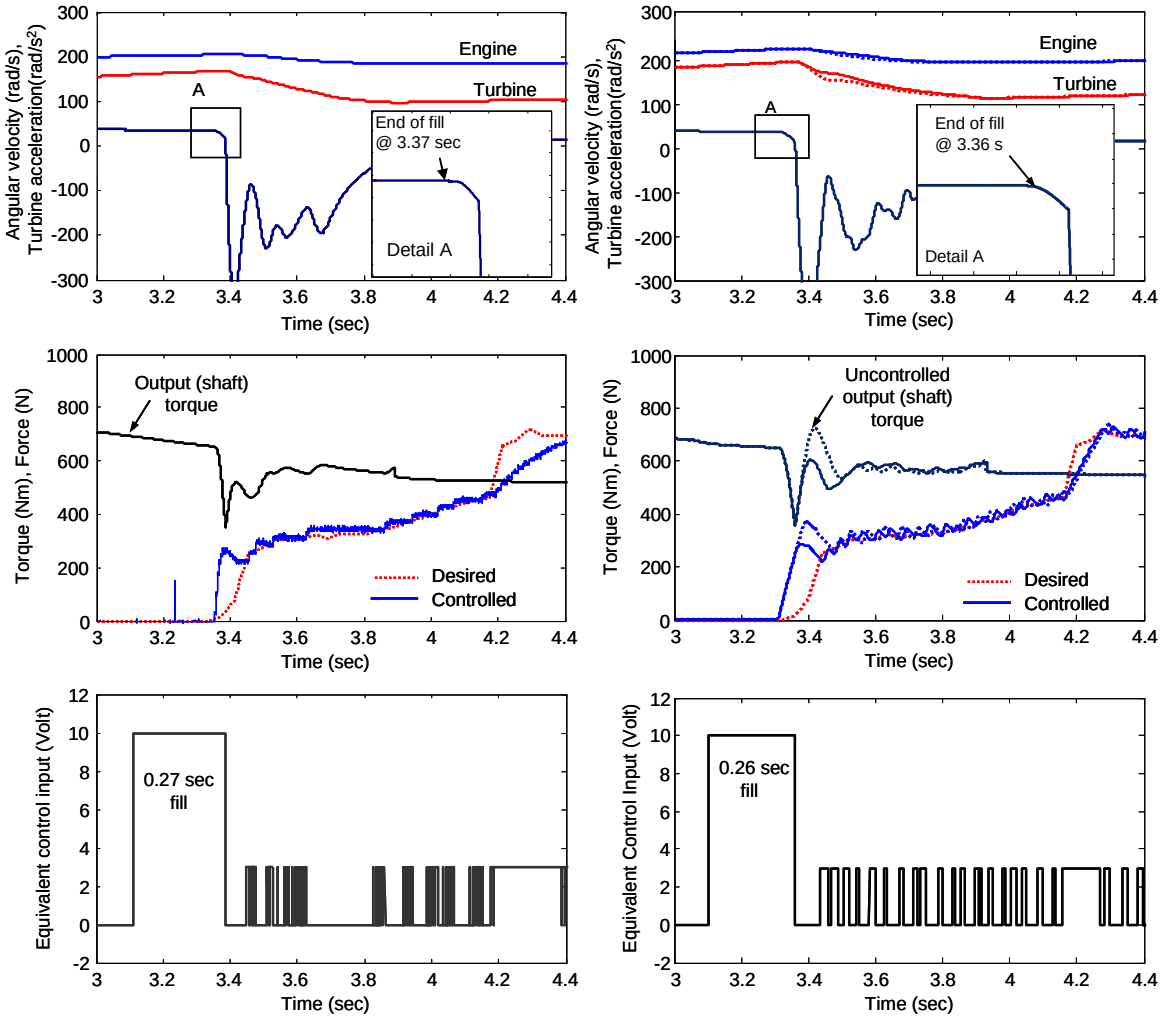

(a) HILS (b) simulation (---: uncontrolled)

Figure 4-40: Fill volume adapting control result and comparison with offline simulation results: $\theta_{th} = 10^{\circ}$, fill stroke = 3.0 mm

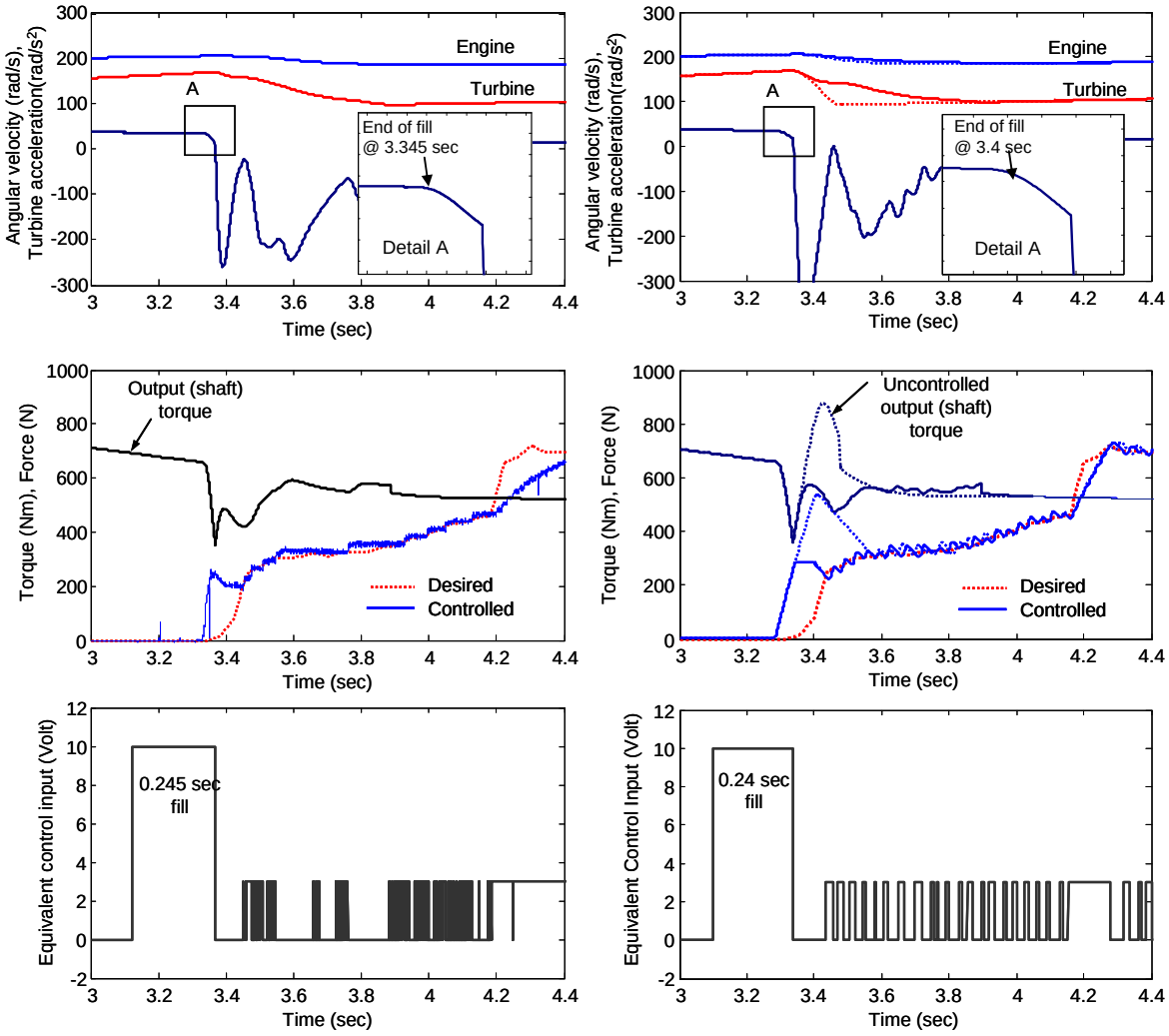

(a) HILS (b) simulation (---: uncontrolled)

Figure 4-41: Fill volume adapting control result and comparison with offline simulation results: $\theta_{th} = 10^{\circ}$, fill stroke = 2.8 mm

The effect of friction force is also investigated by measuring simultaneously the actual actuation force. As shown in Figure **4-42**, the slight discrepancy between two forces is small during the actuation stage, which implies that the friction force have little

effect on the actuation force. Chattering amplitude in the controlled actuation pressure is also rather dissipated by the friction in the hydraulic cylinder.

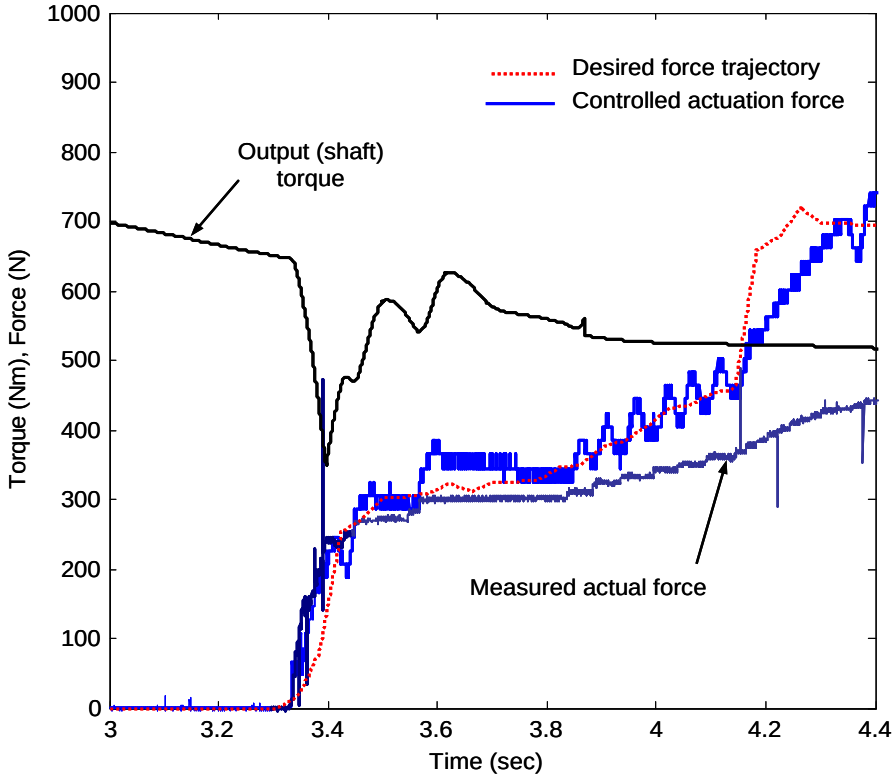

Figure 4-42: Comparison of measured forces: controlled actuation pressure and actual force affected by friction force (•••: desired;—: controlled actuation force from pressure)

Finally, self-locking capability is examined. The details for self-locking are described in Appendix **E**. As demonstrating in Figure **4-43**, the actuation force could be remaining after reaching steady-state, while the driving voltage for the PHP actuator is off.

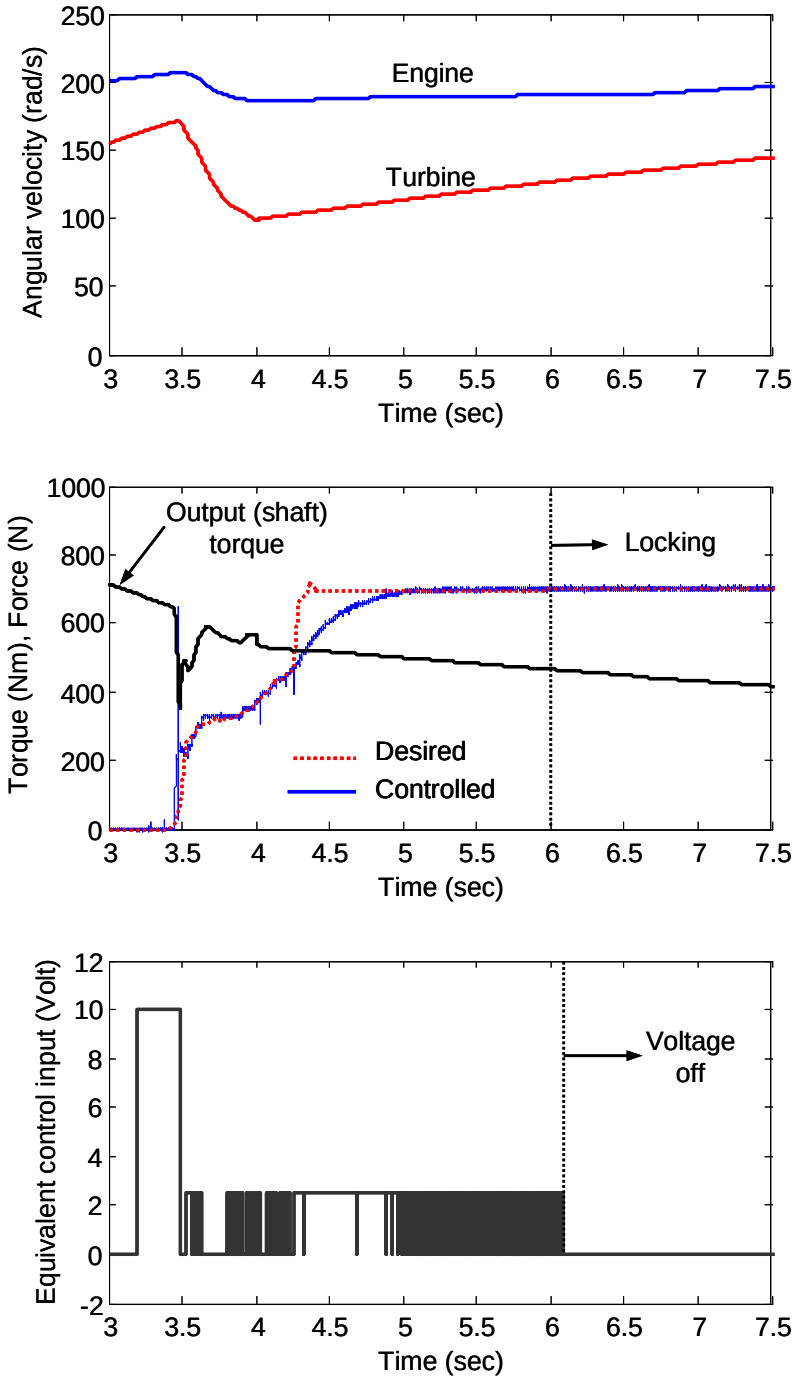

Figure 4-43: HILS with actual force tracking control result illustrating self-locking capability: $\theta_{th} = 10^{\circ}$

4.5 Intelligent Inertia Phase Control

4.5.1 Motivation

Since the basic function of the shift control is to achieve a smooth shift with consistent shift quality under all shift conditions, the evaluation of shift quality has to be introduced. While it has been well recognized that the most critical factors that can affect shift quality include friction materials, actuator force (pressure), and response time, the shift quality is, however, difficult to define or measure as a subjective function. Some metrics have been used to evaluate shift quality. According to Schwab [1994], shift quality can be assessed by the sum of the following sub cost functions:

$$\begin{aligned} J_1 &= abs[T_{Beginning\ of\ torque\ phase} - \min(T_{OUT})] \\ J_2 &= abs[\max(T_{OUT}) - T_{End\ of\ inertia\ phase}] \\ J_3 &= abs(torque\ \ phase\ duration - 125) \\ J_4 &= abs(inertia\ \ phase\ duration - 250) \\ J_5 &= \sum_{i=1}^{4} \alpha_i J_i, \text{where,} \alpha \text{ is weighting factor} \end{aligned} \quad \textbf{(}4.41\textbf{)}$$

where J_1 penalizes the torque dropping (hole) during the torque phase, and J_2 represents the overshoot of output torque. J_3 and J_4 stand for the torque phase duration time and the inertia duration time (t_2 and t_3). These parameters for evaluating shift control performance are indicated in Figure **4-44**. On the other hand, simpler vibration dose value has been typically used to evaluate the shift control performance, with emphasis on J_2 in Eq. 4.41 [Megli et. al., 1999].

$$VDV = \left[\int \bar{\alpha}^4 dt\right]^{1/4} = \left[\int \left(\frac{T_{OUT}}{I_V}\right) dt\right]^{1/4} \quad \textbf{(4.42)}$$

where $\bar{\alpha}$ is the filtered acceleration obtained from vehicle accelerometer. In this research, similar *VDV* is introduced based on the fact that turbine acceleration is closely related with the output torque in the inertia phase.

$$VDV = \left[\int_{ss}^{sf} \bar{\alpha}_T^4 dt\right]^{1/4} \; rad/s^2 \quad (4.43)$$

where $\bar{\alpha}_T$ is the filtered turbine acceleration. *ss* and *sf* stand for shift start and shift finish, respectively.

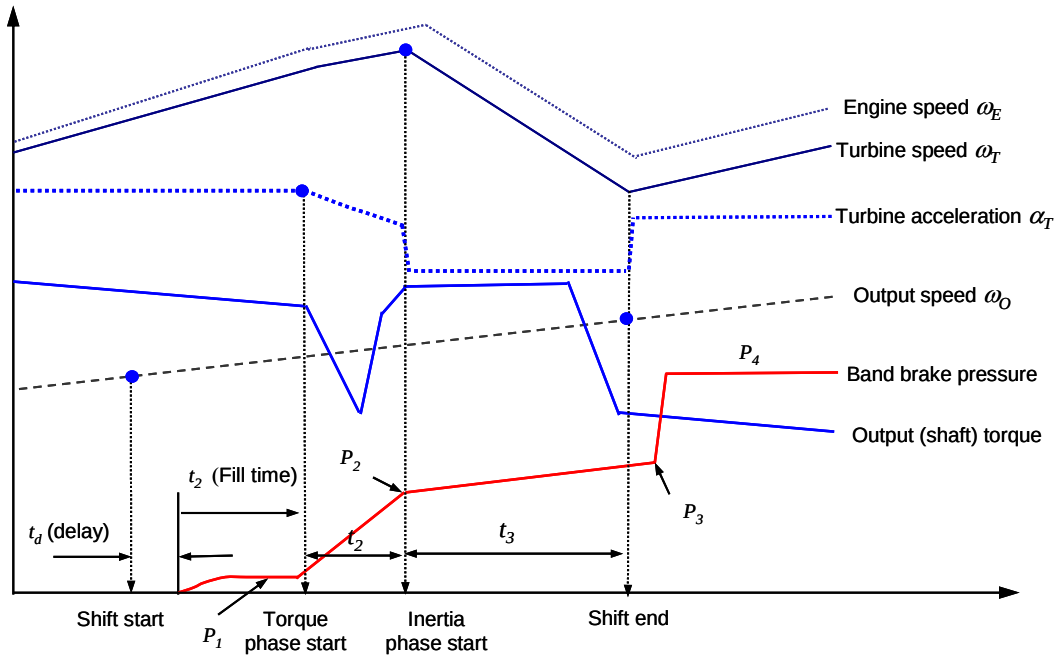

Figure 4-44: Power on 1-2 up shift control diagram of typical AT using band brake as on-coming member and one way clutch (OWC) as off-going member

During the inertia phase (i.e., t_3 in Figure **4-44**), closed-loop control is typically required to achieve robust shift control. However, industrial applications of AT shift control have been performed through open-loop, event-driven, and look-up table actions, while feedback control has been commonly proposed in AT shift controls [Zongxuan and Hebbale, 2005]. The main reason for this technical limitation is the difficulty of using cost-effective and reliable sensors in AT. For example, cost-effective non-contacting output torque transducers are still not available in current AT. Consequently, only PID feedback control of turbine rotational speed (or turbine acceleration) during the inertia phase has been developed, for shift quality is closely correlated to the duration time of the inertia phase. The other reason is the difficulty of using robust feedback control. For instance, the control gains for PID control of turbine speed is currently tuning by trial and error because AT model is highly nonlinear. As a result, it is not robust against parameter variations, disturbances, and wide operation conditions. To overcome these limitations, learning control has been recently studied. According to many research efforts [Yoon, 1999, and Cao et al, 2005], the optimum force (pressure) trajectory can be adaptively updated for next shift event through the reliable calibrations or learning algorithm. In order to update the desired force trajectory, the parameterization of desired trajectory with key parameters has to be performed [Han et. al., 2003]. Since P_2 and P_3 in Figure **4-44** are typically the critical parameters for determining the shift quality, P_2 and P_3 are selected as parameters to be updated for changing the desired force trajectory in this research. Figure **4-45** illustrates the importance of parameters P_2 and P_3. *VDV* will be deviated from the target value (i.e. minimum value) with different P_2 and P_3.

Therefore, performance index *VDV* should be minimized to regulate the turbine angular acceleration by changing the desired force trajectory.

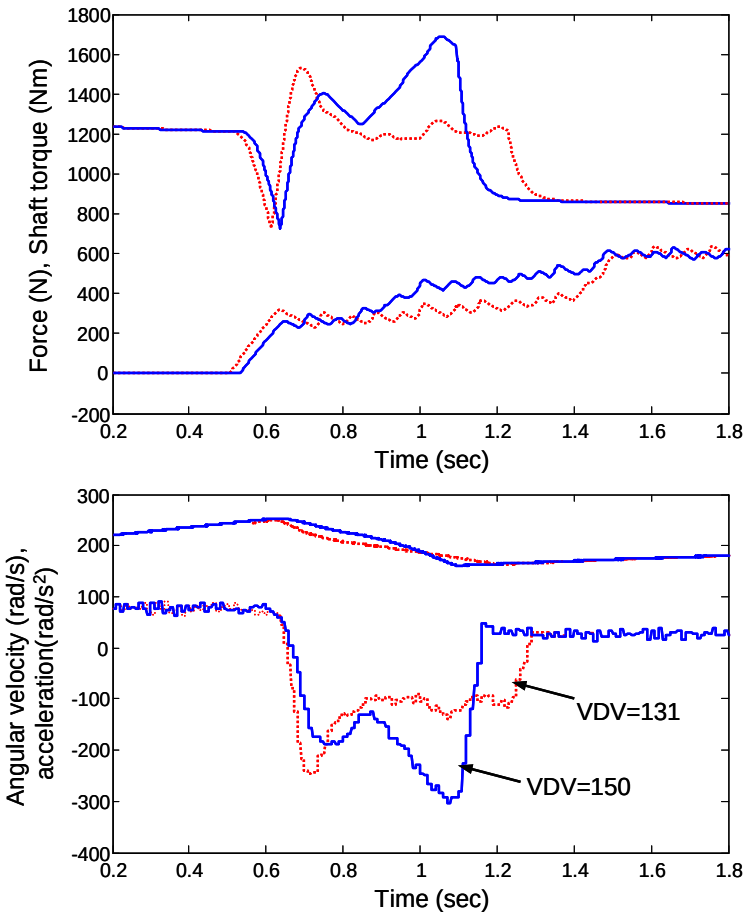

Figure 4-45: Simulation result of AT shift control with deviating turbine acceleration

4.5.2 Intelligent Inertia Phase Control Using Genetic Algorithm (GA)

In this research, an intelligent genetic algorithm (in short, GA) is employed to learn the desired trajectory. Figure **4-46** shows the flowchart for intelligent torque phase control. Performance index *VDV* calculated from turbine acceleration is bounded with target ranges.

$$VDV_{Lower} \le VDV \le VDV_{Upper} \tag{4.44}$$

If calculated *VDV* is deviated from the desired range, P_2 and P_3 in desired force trajectory shown in Figure **4-44** will be updated by learning algorithm. The main advantage of bounding is that unnecessary learning near the desired value, which can lead to chattering of the control parameter, may be avoided. The optimization toolbox (GAOT Ver.5) developed by Christopher et al. [1995] is employed for GA learning algorithm.

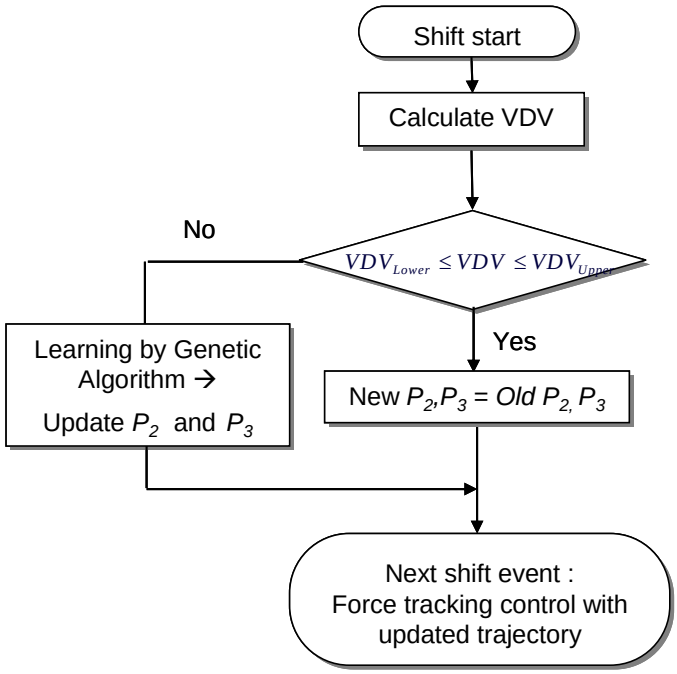

Figure 4-46: Flowchart for intelligent control of torque phase

The GA has a very simple structure: we first generate initial random population using bounds to be optimally selected, evaluate it, and start creating new populations by applying generic operators so called crossover and mutation. Contrary to the conventional methods, one of the main advantages of GA is that it does not require well-defined objective function, most suitable for highly nonlinear system. In addition, since

GA performs search in a population of points, and is based on probabilistic transition rules, it is less likely to converse to local minima or maxima, which can be the pitfall of conventional methods based on the sensitivity information [Passino, 2004]. Accordingly, learning with GA can successfully end up with an optimization problem of the objective function *VDV* as follows;

$$\begin{aligned} &\text{Maximization } VDV^{-1} \\ &\text{Bounded to } P_{2\_lower} \le P_2 \le P_{2\_upper}, P_{3\_lower} \le P_3 \le P_{3\_upper}, \end{aligned} \tag{4.45}$$

Since the genetic algorithm can handle only the maximization problem, the objective function is set to be the inverse of the *VDV*. To demonstrate the effectiveness of proposed intelligent control, harsh shifts shown in Figure **4-45** is learned with bounds ($157\ N \le P_2 \le 251\ N$, $319\ N \le P_3 \le 455\ N$) and initial population size (5 in this case). As shown in Figure **4-47**, best population (i.e., object function *VDV*) can quickly converged to the optimum value of 115.5 within five iterations.

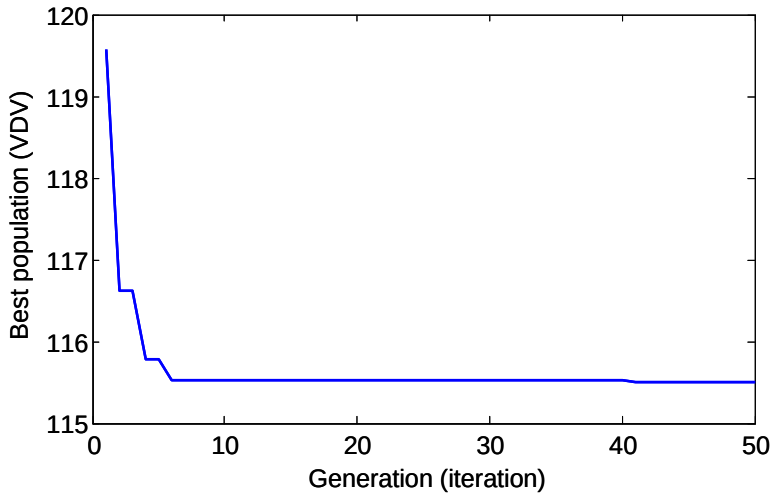

Figure 4-47: The converging history of population (object function *VDV*)

After learning, two important parameters (P_2 and P_3) are successfully updated by 182 N and 325 N, respectively. Figure **4-48** and Figure **4-49** show the intelligent control result using new force trajectory consisting of updated parameter P_2 and P_3. *VDV* is calculated to be 115, which is identical to the converged objective function.

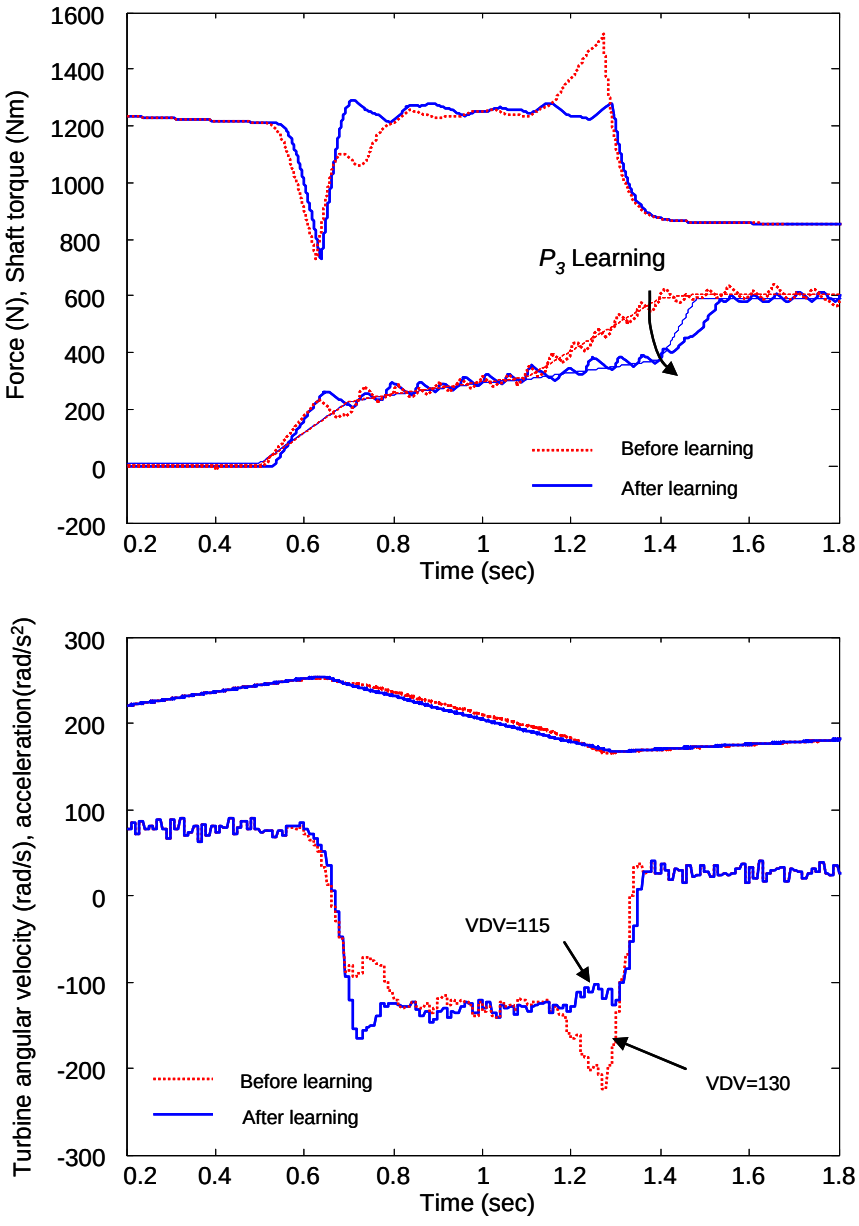

Figure 4-48: Intelligent control result for turbine acceleration regulation (P_3 learning)

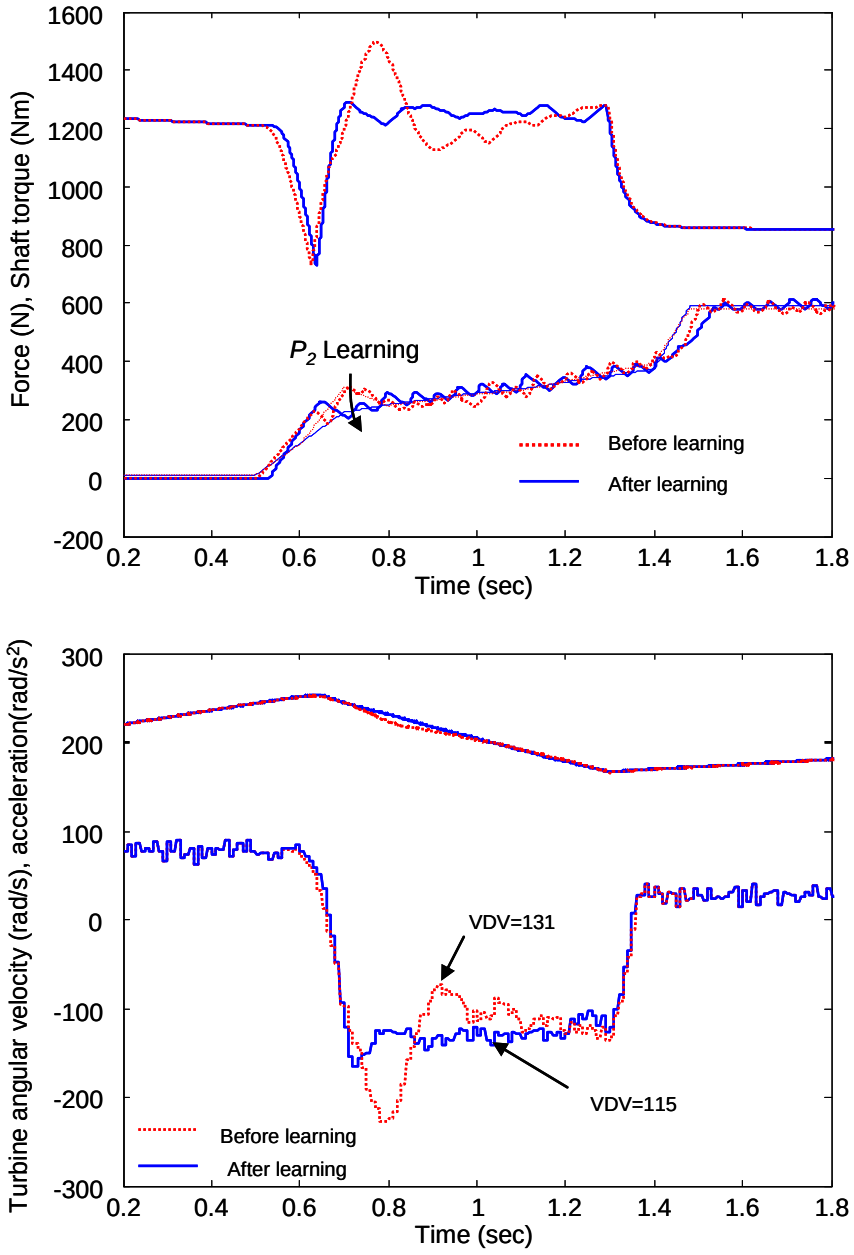

Figure 4-49: Intelligent control result for turbine acceleration regulation (P_2 learning)

4.6 Chapter Summary and Conclusions

In this chapter, the application of the PHP actuator is extended to an AT test-bed to validate the feasibility of the new power-by-wire actuation concept. The typical power train model with 4-speed AT for compact-size passenger car is first synthesized to develop the real time simulation capability for HILS using Stateflow®. For simplicity, only the power on $1 \rightarrow 2$ up shift simulation model is developed. In addition, fill volume adapting strategy is integrated with the tracking controller to prevent the overfill spike that will negatively affect shift performance. For detecting the end of fill, turbine acceleration information of AT is utilized, and neural network-based estimation technique is introduced to restore the corrupted measurement signal. Building upon the fast off-line simulation model, the HILS is performed by replacing the actuator model with the actual PHP actuator hardware. For the global shift controller to control the output torque of AT during the inertia phase of the shift, intelligent control using GA algorithm is proposed to update adaptively the desired force trajectory to be tracked by the PHP actuator.

The results of this chapter indicate that the PHP actuator with the nonlinear sliding mode force tracking controller can be effective for the shift control of AT, and its performance can be further improved by a simple fill volume adaptive scheme and a GA based inertia phase control algorithm. Furthermore, the use of HILS can expand the utility of the real-time power train model for controller development and design of power train systems.

Chapter 5

Conclusion and Recommendations

5.1 Summary of Research Efforts

The primary objective of this research is to develop a piezoelectric-hydraulic pump actuator and control system to achieve a new power-by-wire concept that can potentially replace current the electro-hydraulic actuation systems used in automotive transmissions. Based on the performance requirements of band brake actuation for AT, a prototype piezoelectric-hydraulic pump based actuation system is first developed (Chapter **2**). The compact stand-alone actuator's performance is then evaluated through a series of experiments and analysis. The maximum flow rate of 20 cc/s with a corresponding fill time of 0.3 second and a desired deadhead pressure (0.45 MPa) are achieved. From these evaluation results, it is concluded that the performance of the new piezoelectric-hydraulic pump actuator is adequate for AT shift control. In addition to successful development of the prototype, two secondary research results have been achieved during the research process. With the derived piezoelectric impedance model, a new online monitoring method of the effective bulk modulus of working fluid is first presented. Also, the effect of Helmholtz resonance on the volumetric efficiency of the piezoelectric-hydraulic pump is first recognized. Based on derived analytical model and simulation results, the main parameter for shifting the Helmholtz resonant frequency is identified and evaluated experimentally. Large cavity in the double-acting hydraulic

cylinder turned out to be acting as an Helmholtz resonator. Simple design modifications using the Helmholtz resonator allow us to improve the volumetric efficiency of the piezoelectric-hydraulic pump at relatively lower frequency ranges.

In the research presented in Chapter **3**, the nonlinear sliding mode controller is developed for actuation force tracking control of the piezoelectric-hydraulic pump (PHP) based actuator for an automatic transmission (AT) friction element. With a derived governing equation of motion of the PHP-band brake actuation system, a simple but effective switching control law is synthesized based on the sliding mode theory. To demonstrate the effectiveness of proposed controller, its force tracking performance for smooth engaging of friction elements is validated experimentally. A power on 1 → 2 shift using band brake as on-coming friction element and one-way clutch as off-going friction element (synchronizing control) is performed. In addition, implementation methods using switching type driver is first established, which can be appropriate for other pulse-driven actuator in view of the efficiency.

In Chapter **4**, the PHP actuator is applied to automatic transmission shift control to validate the effectiveness of the new power-by-wire actuation concept. A real time power train model, which includes engine, test-bed AT, and drivelines for half car is first synthesized to develop the model for hardware-in-the-loop simulation using the modeling framework, state charts. In addition to the development of required model, both torque phase control to prevent the over-fill and new turbine acceleration regulating control for AT shift controller are designed to achieve the enhanced shift performance. In order to address the overfill problem, detecting of the end of fill using turbine acceleration of AT is first proposed using advanced filtering method, neural network-

based estimation. Finally, with the developed real time power train model and the PHP actuator, the HILS architecture is constructed, and its successful use in development of AT shift control system is presented to demonstrate the feasibility of the new PHP actuator.

5.2 Summary of Major Contributions

- This research first demonstrated the potential of PHP-based actuator as a new controllable actuation system for AT friction elements. The proposed nonlinear force control methodology could successfully track the desired force trajectory for AT shift control with acceptable tracking error.
- PHP actuator also provides the fundamental concept for the new pressure control system of fluid power systems, eliminating three traditional hydraulic components (oil pump, regulating valve, and control valve). It can be a critical piece of technology that will provide breakthrough in the development of the new alternative pressure control systems.
- The major impact of the new effective bulk modulus measuring method is that it makes on-line monitoring possible. Current methods normally require precision testing equipments consisting of many complex components and cannot be used in real-time. With this new transducer unit, the hydraulic compliance can be easily updated with adaptive schemes, which will provide more robust tracking performance of the hydraulic control systems.

- It has been demonstrated that it is possible to build more reliable power train models based on the HILS that is capable of real time execution. The proposed HILS can be a valuable tool in the development of automotive transmissions and operating control systems and software.
- In general, transition control of the friction element for AT shift is a challenging issue. In this research, the basic approach using feedback sensing signal is first suggested for fill volume adaptation.

5.3 Recommendations for Future Research

Although the present research has demonstrated the feasibility of new piezoelectric-hydraulic pump based actuation system for successful AT control, there are still many issues requiring attention and research in the future.

One future task item will be to examine the durability of the PZT stack transducer. Although the PZT stack transducers have been successfully applied in various industry applications, such as diesel engine injection valve actuator, the durability of the PZT stack transducer has to be evaluated to prevent unexpected failure or damage within the life of AT.

One of the main issues to be properly addressed in the future is the enhanced controllability of the PHP actuator, focusing on the reduction of chattering in the output actuation force. The chattering is undesirable in practice, since it may excite the low frequency dynamics of friction elements. Further investigation of the reasons for chattering to occur is first of all recommended. If the effect of the unmodeled actuator

dynamics is for the main reason for chattering, as predicted in this thesis, the design of new control laws considering actuator dynamics can be one of the potential solutions. The use of higher order sliding surfaces may also be able to alleviate chattering.

If the PHP actuator will have to be employed with other applications such as positioning control systems, the PHP actuator has to be further developed to perform the general tracking control (e.g., bi-directional or sinusoidal tracking) since the PHP actuator is developed for only the AT shift control (one-directional actuation application).

When it comes to the application to AT shift control, the HILS of intelligent inertia phase control should be further performed. The design of more robust shift controller is also required for enhanced shift performance. While the HILS has been shown to be an effective tool, actual dynamo experiments may still be helpful since they can be more accurate in evaluating the overall performance of the controller and actuator.

Finally, the achieved research results can be extended into other general friction elements, such as dry type clutches used in a dual clutch transmission (in short, DCT) and hybrid electric vehicles (in short, HEV), and other applications where large stroke and high actuation force are required. In particular, HEV are currently being developed by numerous automotive companies due to their significant potential in enhancing fuel economy and emissions. The clutch that connects the engine and inverter (or motors) is one of the key elements in most hybrid vehicle configurations. Accordingly, the reliable clutch actuation system is essential in HEVs.

Bibliography

Alleyne, A., Liu, R., and Wright, H., 1998, "On the limitations of Force Tracking Control for Hydraulic Active Suspensions," *Proceedings of the American Control Conference*, No. 0-7803-4530-4.

APC International, Ltd., 2006, *Piezoelectric Ceramics: Principles and Applications.*

Belanger, P. R., 1992, "Estimation of angular velocity and acceleration from shaft encoder measurements," *IEEE International conference of Robotics and Automation*, pp. 585 ~ 592.

Bosch, 1993, *Automotive Handbook 3rd Ed.*, Society of Automobile Engineers, USA.

Cadou, C., Zhang, B., 2003, "Performance Modeling of a Piezo-hydraulic Actuator," *Journal of Intelligent Material systems & Structures.* Vol.14, pp. 149 ~160.

Cao, M., Wang, K.W., Fujii, Y., Tobler, W., 2004, "Advanced hybrid neural network automotive friction component model for power train system dynamic analysis. Part 2: system simulation," IMechE Journal of Automobile Engineering, Vol.218 Part D, pp. 845 ~ 857.

Cao, M., Wang, K.W., Fujii, Y., Tobler, W., 2005, "Development of a Friction Component Model for Automotive Power train System Analysis and Shift Controller Design based on Parallel-Modulated Neural Networks," ASME Journal of Dynamic Systems, Measurement, and Control, 127(3), pp. 382-405.

Chapman, E. G., Herdic, S. L., Keller, C. A., Lynch, C. S., 2005, "Development of Miniaturized Piezo-Hydraulic Pumps," *Smart Structures and Materials 2005: Proceedings of SPIE,* Vol. 5762, pp. 299~310.

Chen, Liang, Fanping, Sun and Rogers, C. A., 1996, "Electro-mechanical impedance modeling of active material systems," Smart Materials and Structures, 5, pp. 171-186.

Chen, C. T., 1984, *Linear System Theory and Design*, Oxford University Press.

Chiang M. H., Lee, L. W., Huang, K. S., 2005, "Development of a Hydraulic-Piezoelectric Actuator for Hybrid Positioning Control with Large Stroke, High Loading and Sub-Micrometer Accuracy," *Proceedings of the IEEE International Conference on Mechatronics,* No. 0-7803-8998-0.

Cho, D., and Hedrick, J. K., 1989, "Automotive Power train Modeling for Control," ASME Journal of Dynamic Systems, Measurement, and Control, Vol.111, pp. 568 ~ 575.

Choi, S. B., Yoo, J. K., Cho, M. S. and Lee, Y. S., 2005, "Position control of a cylinder system using a piezoactuator-driven pump," Mechatronics Vol.15, No.2, pp.239-249.

Chopra, I., 2002, "Review of State of Art of Smart Structures and Integrated Systems", AIAA Journal, Vol. 40, No. 11, pp. 2145 ~ 2187.

Christopher R. H., Jeffery A. J., and Michael G. Kay, "A Genetic Algorithm for Function Optimization: A Matlab Implementation," North Carolina State University IE-TR 95-09, 1995.

Deiss, H., Krimmel, H. and Horsak, G., 2006, "Innovative Driveline System Technology," SAE Technical Paper No.2006-21-0026.

dSPACE Release 5.3 *User's guide*, 2007, dSPACE® GmbH.

Dupere, I. D. J., Dowling, A. P., 2005, "The Use of Helmholtz Resonators in a Practical Combustor," ASME Journal of Engineering for Gas Turbines and Power, Vol. 127, pp.268 ~ 275.

Dynamic Structures and Materials, LLC (DSM: http://www.dynamic-structures.com/), Technical note on Two Level Driver.

Eryilmaz, B. and Wilson, B. H., 2001, "Improved Tracking Control of Hydraulic Systems," Journal of Dynamic Systems, Measurement and Control, 123(3):457-462.

Ellison, J., Sirohi, J., and Chopra, I., 2005, "Investigation of active materials as driving elements of a hydraulic hybrid actuator," Smart Structures and Materials: Proceedings of SPIE, Vol. 5746, pp. 274 ~ 289.

Fanella, R., 1994, Design of band in "*Design Practices: Passenger Car Automatic Transmissions,"* 3rd edition, Society of Automotive Engineers, New York, pp. 419 ~ 426.

Ferreira, J. A., Almeida, F. G., Quintas, M. R., Oliveira, J. P. E, 2004, "Hybrid models for hardware-in-the-loop simulation of hydraulic systems Part 1: theory," IMechE Journal of Automobile Engineering, Vol.218 Part D, pp. 465 ~ 474.

Ferreira, J. A., Almeida, F. G., Quintas, M. R., Oliveira, J. P. E, 2004, "Hybrid models for hardware-in-the-loop simulation of hydraulic systems Part 2: experiments," IMechE Journal of Automobile Engineering, Vol.218 Part D, pp. 475 ~ 484.

Fishman, K. L. and Machmer, D., 1994, "Testing Techniques for the Measurement of Bulk Modulus," Journal of Testing and Evaluation, 22 (2):161-167.

Ford Motor Co., 2006, *Maintenance Manual of 4F27E AT*.

Fujii, Y., Tobler, W. E., Snyder, T. D., 2000, "Prediction of wet band brake dynamic engagement behavior Part 2: experimental model validation," IMechE Journal of Automobile Engineering, Vol.215 Part D, pp. 603 ~ 611.

Fujii, Y., Tobler, W. E., Clausing, E. M., Megli, T. W., Haghgooie, M., 2002, "Application of dynamic band brake model for enhanced drivetrain simulation," IMechE Journal of Automobile Engineering, Vol.216 Part D, pp. 873 ~ 881.

Gao, X. Z., and Ovaska S. J., 2001, "Acceleration signal estimation using neural networks", Measurement Science and Technology, Vol. 12, pp. 1611 ~ 1619.

Gu, X. Takabayashi, H., Fujii, T., Nishida, M., and Ishikawa, K., 2006, "Latest Technologies Applied to Automatic Transmission Maji-Band™," SAE Technical Paper 2006-01-0356.

Gogola, M., and Goldfarb, M., 1999, "Design of a PZT-Actuated Proportional Drum Brake," IEEE/ASME Transactions on mechatronics, Vol. 4, No. 4, pp. 409 ~ 416.

Hahn, J. O., Hur, J. W., Choi, G. W., Cho, Y. M. and Lee, K. I., 2002, "Self-learning approach to automatic transmission shift control in a commercial construction vehicle during the inertia phase," IMechE Journal of Automobile Engineering, Vol.216 Part D, pp. 909 ~ 919.

Han, Woo-sung and Yi, S. J., 2002, "A study of shift control using the clutch pressure pattern in automatic transmission," IMechE Journal of Automobile Engineering, Vol.217 Part D, pp. 289~298.

Harel, D., 1987, "Statecharts: a visual formalism for complex systems," Science of Computer Programming 8, pp. 231 ~ 274.

Hebbale, K. V., and Kao, C. K., 1995, "Adaptive Control of Shifts in Automatic Transmissions," Proceedings of the ASME international Mechanical Engineering Congress and Exposition.

Hines, J. W., 1997, *Fuzzy and Neural Applications in Engineering*, John Wiley & Sons.

Hirose, S., Ikuta, K. and Umetani, Y., 1989, "Development of a Shape Memory Alloy Actuators: Performance Assessment and Introduction of a New Composing Approach," Advanced Robotics, vol. 3, No. 1, pp.3~16.

Houghton International Inc., 2008, Hydrolubric® High Water Content Fluids (HWCF) brochure (http://www.houghtonintl.com)

IEEE, 1978, *IEEE Standard on Piezoelectricity* ANSI/IEEE Std176-1987.

Janen, J. F., Lind, R. F., Chesser, J. B., Love, L. J., 2003, "Design, analysis, fabrication, and testing of a novel piezoelectric pump," Oak Ridge National Laboratory Project Report No. ORNL-2003/188.

Jinghong, Y., Zhaoneng, C. and Yuanzhang, L., 1994, "The Variation of oil Effective Bulk Modulus with Pressure in Hydraulic System," ASME Journal of Dynamic Systems, Measurement, and Control, Vol. 116, pp. 146~150.

John Shaju, Cadou, C., Yoo, Jin-Hyeong, Wereley, N. M., 2006, "Application of CFD in the Design and Analysis of a Piezoelectric Hydraulic Pump," Journal *of Intelligent Material systems & Structures.* Vol.17, pp. 967 ~ 979.

Kalish, Yury, Henein, N. A., 2007, "Stress analysis of multilayer piezoelectric actuators for diesel fuel injection subjected to pulse voltage excitation," *Smart Structures and Materials 2001: Proceedings of SPIE,* Vol. 6527, No. 65270T-1.

Karassik, Igor J.; Messina, Joseph P.; Cooper, Paul; Heald, Charles C., 2001, Pump *Handbook (3rd Edition),* McGraw-Hill.

Keller, 2004, Novel Concepts in Piezohydraulic Pump Design, M.S. Thesis, Mechanical Department, Georgia Institute of Technology.

Khalil, H. K., 1996, *Nonlinear Systems* 2nd ed., Prentice-Hall.

Kim, Gi-Woo and Wang, K.W., 2007a, "Piezoelectric-Hydraulic Pump Based Brake Actuation system for Automotive Transmission Control," *Smart Structures and Materials 2007: Proceedings of SPIE,* Vol. 6525, 65251E.

Kim, Gi-Woo and Wang, K. W., 2007b, "On-line Monitoring of Fluid Effective Bulk Modulus Using Piezoelectric Transducer Impedance," ASME International Mechanical Engineering Congress & Exposition, No.IMECE2007-41864.

Kim, Gi-Woo and Wang, K. W., 2008, "Nonlinear Force Feedback Control of Piezoelectric-Hydraulic Pump Actuator for Automatic Transmission Shift Control", *Smart Structures and Materials 2008: Proceedings of SPIE* No. 6930-9.

Kim, Gi-Woo and Wang, K. W., 2009, "Power-By-Wire Piezoelectric-Hydraulic Pump Actuator for Automotive Transmission Shift Control", SAE 2009 World Congress, Technical paper No. 09PFL-0042.

Kinsler, L. E., Frey, A. R., Coppeans, A. B., and Sanders, J. V., 2000, *Fundamentals of Acoustics*, Wiley, New York, 4th ed.

Konishi, K., Yoshimura, T., Hashimoto, K. and Yamamoto, N., 1993, "Hydraulic actuators driven by piezoelectric elements (1st report, trial piezoelectric pump and its maximum power)," Journal of Japanese Society of Mechanical Engineering (C) 59, pp.213-220.

Kotwicki, A. J., 1982, "Dynamic Models for Torque Converter Equipped Vehicles," SAE Paper No.820393.

Lee, D. G., Or, S. W. and Carman, G. P., 2004, "Design of a piezoelectric-hydraulic pump with active valves," *Journal of Intelligent Material systems & Structures.* Vol.15, pp. 107~115.

Lhermet, N., Delas, O., Claeyssen, F., 2006, "Magnetostrictive pump with piezo active valves for more electrical aircraft," 10th International Conference on New Actuator, P144, pp. 964 ~ 967.

Liang, C., Sun F., and Rogers, C. A., 1996, "Electro-mechanical impedance modeling of active material systems," *Journal of Smart Materials and Structures,* Vol. 5, pp. 171-186.

Lindner, D. K., Vujic, N. and Leo, D. J., 2001, "Comparison of drive amplifiers for piezoelectric actuators," *Smart Structures and Materials 2001: Proceedings of SPIE,* Vol. 4332, pp. 281~291.

Lindner, J. E., and Anderson, E. H., 2003, "Design and Testing of Piezoelectric-Hydraulic Actuators," *Smart Structures and Materials 2001: Proceedings of SPIE,* Vol. 5054, pp. 96 ~ 107.

Liu, R. and Alleyne, A., 2000, "Nonlinear force/pressure tracking of an electro-hydraulic actuator," ASME Journal of Dynamic Systems, Measurement and Control, Vol. 122, pp. 232 ~ 237.

Manring, N. D., 1997, "The Effective Fluid Bulk Modulus Within a Hydrostatic Transmission," ASME Journal of Dynamic Systems, Measurement and Control, 119:462-465.

Manring, N. D., 2005, *Hydraulic Control Systems*, Wiley.

Masmoudi, R. A., Hedrick, J. K., 1992, " Estimation of Vehicle shaft Torque Using Nonlinear Observers," ASME Journal of Dynamic Systems, Measurement and Control, Intelligent Material systems & Structures, Vol. 114, pp. 394 ~ 400.

Mauck, L. D. and Lynch, C. S., 1999, "Piezoelectric hydraulic pump," Proceeding of the 6th SPIE conference on Smart Structures and Integrated Systems, Newport Beach, CA 3668, pp. 844-852.

Mauck, L. D. and Lynch, C. S., 2000, "Piezoelectric Hydraulic Pump Development," *Journal of Intelligent Material Systems and Structures*. Vol.11, pp. 758~764.

McCloy, D., and Martin, H. R., 1980, *Control of Fluid Power: Analysis and Design*, Ellis Horwood Limited, Chichester, England, 2nd ed.

Megli, T. W., Haghgooie, M., and Colvin, D. S., 1999, "Shift characteristics of 4-speed automatic transmission," SAE technical paper 1999-01-1060.

Merrit, H. E., 1967, *Hydraulic Control Systems*, Wiley.

Mianzo, L., 2000, "A Transmission Model for Hardware-in-the-loop Power train Control System Software Development," *Proceedings of the 2000 IEEE International Conference,* No. 0-7803-6562-3.

Mitrovic, M., Carman, G. P., Straub, F. K., 2000, "Durability Properties of Piezoelectric Stack Actuators under Combined Electro-Mechanical Loading," *Smart Structures and Materials 2000: Proceedings of SPIE,* Vol. 3992, pp. 217 ~ 232.

Moura, J. T., Elmali, H., and Olgac, N., 1997, "Sliding Mode Control With Sliding Perturbation Observer," ASME Journal of Dynamic Systems, Measurement and Control, Intelligent Material systems & Structures, Vol. 119, pp. 657 ~ 665.

Nasser, K., Leo, D. J. and Cundey, H. H., 2000, "Compact Piezohydraulic Actuation System," *Smart Structures and Materials 2000: Proceedings of SPIE,* Vol. 3991, pp. 312~322.

Neelakantan, V. A., Washington, G. N., Bucknor, N. K., 2005, " Two-stage actuation system using DC motors and piezoelectric actuators for controllable industrial and automotive brakes and clutches," *Smart Structures and Materials 2005: Proceedings of SPIE,* Vol. 5762, pp. 275~286.

Neelakantan, V. A., Washington, G. N., Bucknor, N. K., 2007, " Model Predictive Control of a Two Stage Actuation System using Piezoelectric Actuators for Controllable Industrial and Automotive Brakes and Clutches" *Journal of Intelligent Material Systems and Structures,* Vol. 19 , pp. 845~857.

Niezrecki, C., Schueller, J., and Balasubramanian, K., 2004, "Piezoelectric-based Fluid Bulk Modulus Sensor," *Journal of Intelligent Material systems & Structures*, Vol.15, pp.893 ~ 899.

Niezrecki, C., Brei, D., and Balakrishnan, S., 2001, "Piezoelectric Actuation: State of the Art," The Shock and Vibration Digest, Vol.33, No. 4, pp. 269 ~ 280.

Niksefat, N., Wu C. Q., and Sepehri, N., 2001, "Design of a Lyapunov Controller for an Electroc-hydraulic Actuator during Contact Tasks," ASME Journal of Dynamic Systems, Measurement and Control, Intelligent Material systems & Structures, Vol. 123, pp. 299 ~ 307.

Nguyen, T., Leavitt, J., Jabbari, F., and Bobrow, J. E., 2007, "Accurate sliding-Mode control of Pneumatic systems Using Low-Cost Solenoid Valves," IEEE/ASME Transactions on Mechatronics, Vol 12, No. 2, pp. 216~219

Oates, W. S., Mauck, L. D and Lynch, C. S., 2000, "PZT Piston Driven Hydraulic Pump Development," Proceedings of the 2000 12th IEEE International Symposium on Applications of Ferroelectrics. Vol. 2, pp. 733~736.

Oates, W. S., and Lynch, C. S., 2001, "Piezoelectric Hydraulic Pump System Dynamic Model," *Journal of Intelligent Material Systems and Structures*. Vol.12, pp. 737 ~ 744.

O'Neill, Conal and Burchfield, John, 2007, "Kinetic Ceramics Piezoelectric Hydraulic Pumps," *Proceedings of SPIE,* Vol. 6527, No. 65270I-1.

Ovaska, S. J., Valiviita, S., 1998, "Angular Acceleration Measurement: A Review", IEEE Transactions on Instrumentation and Measurement, Vol. 47, No. 5, 1211 ~ 1217.

Park, C. H., 2001, "On the Circuit Model of Piezoceramics," *Journal of Intelligent Material systems & Structures.* Vol.12, pp. 515 ~ 522.

Park, J. H., Yoshida, K., Yokota, S., 1999, "Resonantly driven piezoelectric micropump fabrication of a micropump having high power density," Mechatronics Vol. 9, pp. 687 ~ 702.

Passino, K. M., 2004, *Intelligent Control: Biomimicry for Optimization, Adaptation, and Decision-Making in Computer control and Automation*, Springer-Verlag, London, UK.

Peairs, D. M., Park, Gyu-hae and Inman, D. J., 2004, "Improving accessibility of the Impedance-based Structural Health Monitoring Method," Journal of Intelligent Material systems & Structures, 15:129-139.

Piezomechanik GmbH, 2007, *Electronic supplies for piezomechanics: An introduction.*

Piezo Systems, Inc, (http://www.piezo.com/).

Paul, A. K., Mishra, J. K., Radke, M. G., 1994, "Reduced Order Sliding Mode Control for Pneumatic Actuator," IEEE Transactions on Control Systems Technology, Vol. 2, No. 3, pp. 271~276.

Prechtl, E. F., and Hall, S. R., 1999, "Design of a high efficiency, large stroke, electromechanical actuator," Smart Materials and Structures, Vol. 8, pp. 13 ~ 30.

Rinderknecht, D., Hickerson, A. I., Gharib, M., 2005, "A valveless micro impedance pump driven by electromagnetic actuation," Journal of Micromechanics and Microengineering Vol.15, pp. 861 ~ 866.

Schwab, L. F., 1994, "Development of a shift quality metric for an automatic transmission," SAE Technical Paper No. 941009.

Shen X., Zhang J., Barth E. J., and Goldfarb M., 2006, "Nonlinear Model-Based Control of Pulse Width Modulated Pneumatic Servo Systems," ASME Journal of Dynamic Systems, Measurement and Control, Intelligent Material systems & Structures, Vol. 128, pp. 663 ~ 669.

Sherrit, S., Bao, X., Cohen, Y. B., Chang, Z., 2004, "Resonance Analysis of High Temperature Piezoelectric Materials for Actuation and Sensing," *Smart Structures and Materials: Proceedings of SPIE,* Vol. 5387, No. 5387-58.

Sirohi, J. and Chopra, I., 2001a, "Compact Piezo-hydraulic Hybrid Actuator," *Twelfth International Conference on Adaptive Structures and Technologies*, University of Maryland, Technomic Publishing Co, Lancaster, UK.

Sirohi, J. and Chopra, I., 2001b, "Development of a Compact Piezoelectric-Hydraulic Hybrid Actuator," *Smart Structures and Materials: Proceedings of SPIE,* Vol. 4327, pp. 401 ~ 412.

Sirohi, J. and Chopra, I., 2003a, "Design and Development of a High Pumping Frequency Piezoelectric-Hydraulic Hybrid Actuator," *Journal of Intelligent Material systems & Structures.* Vol.14, pp. 135~147.

Sirohi, J., Cadou, C., and Chopra, I., 2003b, "Frequency Domain Modeling of a Piezohydraulic Actuator," 44th AIAA /ASME/ ASCE/ ASC Structure, Structural Dynamics, and Materials Conference, Paper No. AIAA 2003-1641.

Slotine, J. E., Li W., 1991, *Applied Nonlinear Control*, Prentice Hall, New Jersey.

Sneed, R. C, Smith, R. R., Cash, M. F., Anderson, E. H., 2007, "Smart-Material Based Hydraulic Pump System for Actuation of a Morphing Wing," 48th AIAA /ASME/ ASCE/ ASC Structure, Structural Dynamics, and Materials Conference, Paper No. AIAA 2007-1702.

Sohl, G., and Bobrow J. E., 1999, "Experiments and Simulations on the Nonlinear Control of a Hydraulic Servosystem," IEEE Transactions on control systems technology, Vol. 7, No. 2, pp. 238 ~ 247.

Stateflow® 6.5 *User's guide*, 1997, The Mathworks.

Sun Hong, and Chiu, G. T. C, 1999, "Nonlinear Observer Based Force Control of Electro-Hydraulic Actuators," *Proceedings of the American Control Conference,* No. 0-7803-4990-6.

Tan, H., Hurst, W. and Leo, D. J., 2002, "Performance of a Piezohydraulic Actuation System with Active Valves," *Smart Structures and Materials 2002: Proceedings of SPIE,* Vol. 4701, pp. 537~551.

Tan, H., Hurst, W. and Leo, D. J., 2005, "Performance modeling of a piezohydraulic actuation system with active valves," Journal of Smart Materials and Structures, Vol. 14, pp. 91 ~ 110.

Tieck, R. M., Carman, G. P., Lin, Y., O'Neill, C., 2005, "Characterization of a Piezohydrualic Actuator," *Smart Structures and Materials 2005: Proceedings of SPIE,* Vol. 5764, pp. 671~679.

Tekscan , Inc., FlexiForce® sensor brochure (http://www.tekscan.com/flexiforce.html)

Turner, A. J., Ramsay, K., 2004, "Review and Development of Electomechanical Actuators for Improved Transmission Control and Efficiency," SAE Technical Paper No.2004-01-1322.

Turner, A. J., Ramsay, K., Clark, R. E., Howe, D., 2006, "Development of High Force Electromechanical Linear Actuator for Shift-By-Wire Automated Manual Transmissions," SAE Technical Paper No.2006-01-0360.

Utkin, Vadim and Guldner Jürgen, Shi Jingxin, 1999, *Sliding Mode Control in Electromechanical Systems*, CRC Press.

Utkin, Vadim and Lee, Hoon 2006, "Chattering problem in sliding mode control systems", 2nd IFAC Conference on Analysis and Design of Hybrid Systems, pp. 346 ~ 350.

Wang, Y., Kraska, M., and Ortmann, W., 2001, "Dynamic modeling of a variable force solenoid and a clutch for hydraulic control in vehicle transmission system," *Proceedings of the American Control Conference,* No. 0-7803-6459-3, pp. 1789 ~ 1793.

Watton, J., 1989, *Fluid Power Systems*, pp.29-33, Prentice Hall, New York.

Winchell, F., J., and Route, W. D., 1998, "Ratio Changing the Passenger Car Automatic Transmission," *Design Practices: Passenger Car Automatic Transmissions",* Society of Automotive Engineers, Vol.5, pp. 79~105.

Yi, K., Shin, B. K., Lee, K. I., 2000, "Estimation of Turbine Torque of automatic Transmissions Using Nonlinear Observers", ASME Journal of Dynamic Systems, Measurement and Control, Intelligent Material systems & Structures, Vol. 122, pp. 276 ~ 283.

Yury Kalish, Naeim A. Henein, 2007, "Stress analysis of multilayer piezoelectric actuators for diesel fuel injection subjected to square pulse voltage excitation", *Smart Structures and Materials 2007: Proceedings of SPIE* No. 65270T-1.

Yoo, J. H., Sirohi, J., Wereley, N. M., Chopra, I., 2003, "A magnetorheological hydraulic actuator driven by a piezopump," ASME International Mechanical Engineering Congress & Exposition, No. IMECE2003-43315.

Yoon, A, Khargonekar, P., and Hebbale, K., 1997, "Design of Computer Experiments for Open-loop Control and Robustness Analysis of Clutch-to-Clutch Shifts in Automatic Transmissions," *Proceedings of the American Control Conference,* No. 0-7803-3832-4.

Zhang, N., Liu, D. K., Jeyakumaran, J. M., and Villanueva, L., 2002, "Modeling of dynamic characteristics of an automatic transmission during shift changes," IMechE Journal of Systems and Control Engineering, Vol.216, pp. 331~341.

Zhou, Su-Wei, Rogers, C. A., 1995, "Heat Generation, Temperature, and Thermal Stress of Structurally Integrated Piezo-Actuators," *Journal of Intelligent Material systems & Structures.* Vol.6, pp. 327 ~ 379.

Zongxuan, S., and Hebbale, K., 2005, "Challenges and Opportunities in Automotive Transmission Control," American Control Conference, pp.3284~3289.

Appendix A

On-site Force Transducer Unit Using FlexiForce® Sensor

A.1 Fabrication of Prototype Transducer

To implement this force transducer on automotive applications, output and input has to be DC Voltage for interfacing with TCU (transmission control unit). This will lead to use a force-to-voltage converting (drive) circuit [Tekscan]. Figure **A-1** shows one of the available converting circuits, which is using simple OP amp chip. FlexiForce® sensor can be represented by variable resistance (R_S). Tuning resistance (R_F) is used to adjust the output voltage (V_{out}) or sensitivity.

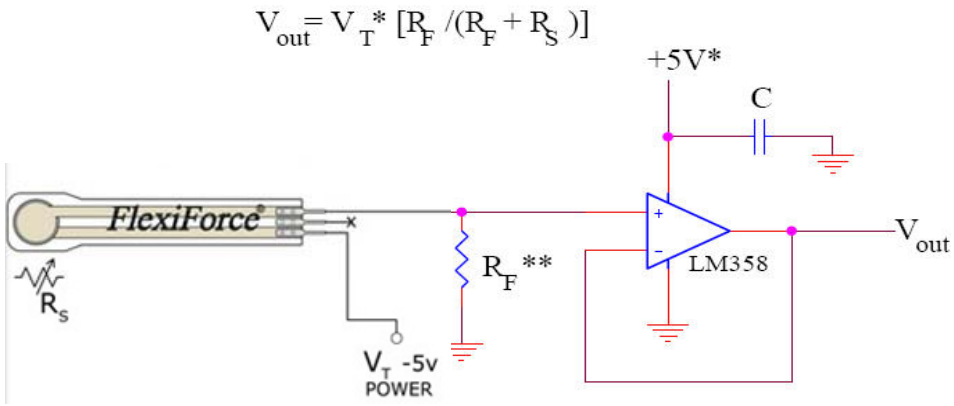

Figure A-1: Force-to-voltage converting circuit using OP amp chip (LM358)

A.2 Calibration

To calibrate the prototype transducer, a simple calibration device is set up using low friction air cylinder (ϕ 31 mm) actuated by air compressor (Max. 120 psi capacity) and reliable piezo type force sensor (Model : PCB 208C03). Calibration results are plotted in Figure **A-2** . Black diamond dots represent the specification of piezo type force sensor obtained from vendor. Blue triangular dots represent the calibration data that has to be matched with the specification. However, there must be slight difference between two curves due to the friction force in calibration device. In this preliminary study, this friction force is assumed to be negligible.

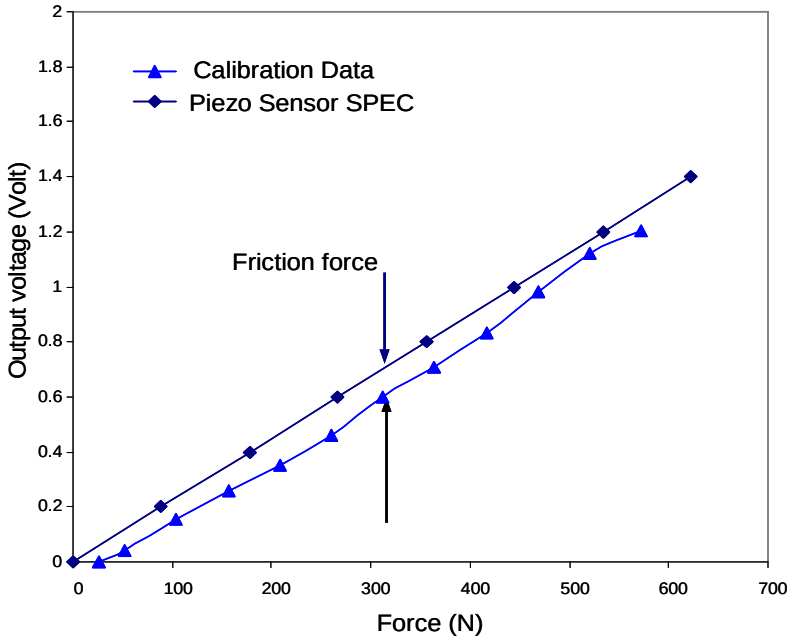

Figure A-2: Calibration result of prototype force transducer using calibration device

A.3 Sensitivity Curve

To obtain a sensitivity curve, step responses are first plotted with respect to different applying force using tuning resistance of 18 KΩ and drive voltage of 3 V. All steady-state voltages are collected to plot the sensitivity curve. The obtained sensitivity curve plotted in Figure **A-3** . Prototype force transducer shows good sensitivity, which is sufficient for force tracking control, and can be fitted by following equation

$$y = 496.6x - 93 \tag{A.1}$$

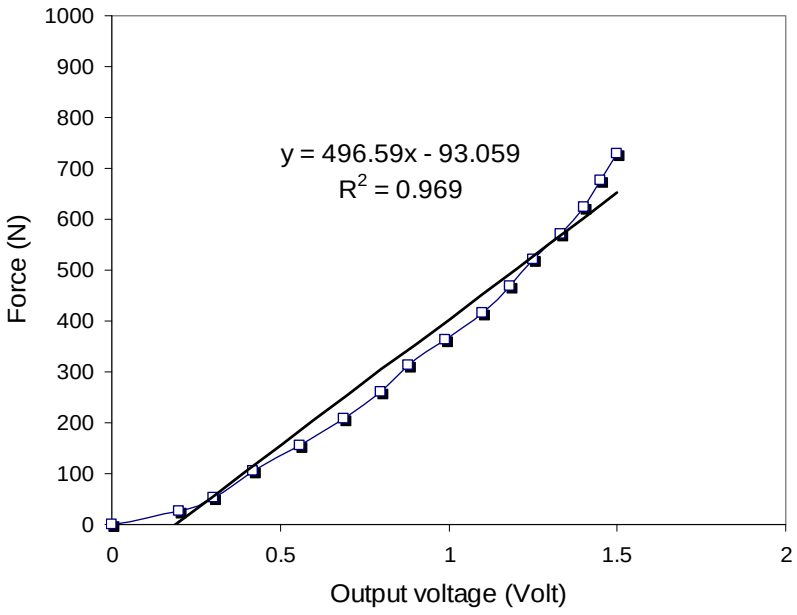

Figure A-3: Sensitivity curve for prototype force transducer using FlexiForce® sensor

Appendix B

Derivation of Power/on Up 1→2 Up Shift Model

The governing equations derived in Chapter 4 are summarized as followings:

$$\begin{aligned} r_1(I_{S1}+I_T)\dot{\omega}_{S1}-(1+r_2)I_{S2}\dot{\omega}_{S2}-I_{R1}\dot{\omega}_{R1} &= r_1T_T+(r_2+1)T_B+T_{OWC} \\ I_{EQV}\dot{\omega}_{OUT}+\Psi\left\{(I_{S1}+I_T)\dot{\omega}_T+I_{S2}\dot{\omega}_{S2}+I_{R1}\dot{\omega}_{R1}\right\} &= \Psi(T_T-T_B-T_{OWC})-T_{LOAD} \end{aligned} \quad \text{(B.1)}$$

In addition to governing equation, following three equations are required to drive the shift model for each phase.

$$\Psi(1+r_1)\dot{\omega}_{OUT}=\dot{\omega}_{S1}+r_1\dot{\omega}_{R1} \quad \text{(B.2)}$$

$$(1+r_2)\dot{\omega}_{R1}=\dot{\omega}_{S2}+\Psi r_2\dot{\omega}_{OUT} \quad \text{(B.3)}$$

$$I_V\dot{\omega}_{OUT}=T_{OUT}-T_{LOAD} \quad \text{(B.4)}$$

B.1 First Gear State and Torque Phase

In first gear state and torque phase, because of the one-way clutch, the first ring gear is constrained (i.e., $\dot{\omega}_{R1}=0$) and the turbine input torque is transmitted through the one-way clutch. When the 1 → 2 shift starts by shift commanding from the shift schedule, on-coming band brake starts engaging (i.e., torque phase including fill) and the torque capacity of the band brake is determined by the band brake (i.e., $T_B=T_{BC}$) because the second sun gear is not constrained ($\omega_{S2}\neq 0$, i.e., slip). In this these, the governing equations are solved directly for Stateflow® coding, instead of simultaneously numerical

solving. Hence, eliminating of $\dot{\omega}_{S2}$ and $\dot{\omega}_{OUT}$ in the governing equations yields following equations:

$$\dot{\omega}_T = C^{-1}[\Psi(1+r_1)T_T + \Psi r_2 T_{BC} - T_{LOAD}] = A_{121}T_T + B_{121}T_{BC} + C_{121}T_{LOAD} \qquad \text{(B.5)}$$

where $C = \Psi(1+r_1)(I_{S1}+I_T) + \dfrac{\Psi r_2^{\,2}}{1+r_1} I_{S2} + \dfrac{I_{EQV}}{\Psi(1+r_1)}$.

$$T_{OWC} = \{r_1(I_{S1}+I_T) + \frac{r_2(1+r_2)}{1+r_1} I_{S2}\}\dot{\omega}_T - r_1 T_T - (1+r_2)T_{BC} \qquad \text{(B.6)}$$

The transient output torque (T_{OUT}) and acceleration ($\dot{\omega}_{OUT}$) can be determined by the angular acceleration of each element (Eq. **B.3**) and load torque (Eq. **B.4**).

$$T_{OUT} = \frac{I_V}{\Psi(1+r_1)}\dot{\omega}_T + T_{LOAD} \qquad \text{(B.7)}$$

$$\dot{\omega}_{OUT} = \frac{1}{\Psi(1+r_1)}\dot{\omega}_T \qquad \text{(B.8)}$$

A general expression form for the output (shaft) torque (T_{OUT}) can be expressed in terms of the input turbine torque (T_T), the band brake torque (T_B), the load torque by substituting Eq. **B.5** into Eq. **B.7** :

$$T_{OUT} = a_{121}T_T + b_{121}T_{BC} + d_{121}T_{LOAD} \qquad \text{(B.9)}$$

As seen in Eq. **B.9**, the output torque is an explicit function of three torques. This useful relationship provides physical meaning of output torque drop in torque phase. The output torque starts inevitable dropping since the turbine input torque is transmitting through the on-coming band brake, which leads the negative band brake torque. Hence, the control of output torque is nearly challenging with the difficulty of using output torque transducer. As the band brake torque is increasing, one-way torque is decreasing until it

starts free-wheeling. The duration time is normally 0.1 to 0.2 second and there is no speed change in the engine and turbine speed.

B.2 Inertia (or Speed) Phase

The transition condition from the torque phase into the inertia phase is $T_{OWC} = 0$ or $\dot{\omega}_{R1} > 0$. Due to the slip, torques of friction elements should be replaced by $\omega_{R1} \neq 0, \omega_{S2} \neq 0$. After rearranging $\dot{\omega}_{S2}$ in terms of $\dot{\omega}_T$ and $\dot{\omega}_{R1}$ in Eq. **B.2** and Eq. **B.3**, substituting $\dot{\omega}_{S2}$ into Eq. **B.1** yields following equations:

$$\dot{\omega}_T = (A_{12}D_{12} + B_{12}C_{12})^{-1}\Big[(\Psi B_{12} + r_1 D_{12})T_T + \{(1+r_2)D_{12} - \Psi B_{12}\}T_{BC} - B_{12}T_{LOAD}\Big] \tag{B.10}$$

where $A_{12} = r_1(I_{S1} + I_T) + \dfrac{r_2(1+r_2)}{1+r_1} I_{S2}$, $B_{12} = \dfrac{(1+r_2)(1+r_1+r_2)}{1+r_1} I_{S2} + I_{R1}$,

$$C_{12} = \Psi(I_{S1} + I_T) - \frac{\Psi r_2}{1+r_2} I_{S2} + \frac{I_{EQV}}{\Psi(1+r_1)}, \quad D_{12} = \frac{\Psi(1+r_1+r_2)}{1+r_1} I_{S2} + \Psi I_{R1} + \frac{r_1}{\Psi(1+r_1)} I_{EQV}$$

$$\dot{\omega}_{R1} = (A_{12}D_{12} + B_{12}C_{12})^{-1}\Big[(\Psi A_{12} - r_1 C_{12})T_T - \{(1+r_2)C_{12} + \Psi A_{12}\}T_{BC} - A_{12}T_{LOAD}\Big] \tag{B.11}$$

$$T_{OUT} = \frac{I_V}{\Psi(1+r_1)}\dot{\omega}_T + \frac{r_1 I_V}{\Psi(1+r_1)}\dot{\omega}_{R1} + T_{LOAD} \tag{B.12}$$

$$\dot{\omega}_{OUT} = \frac{1}{\Psi(1+r_1)}(\dot{\omega}_T + r_1\dot{\omega}_{R1}) \tag{B.13}$$

During the inertia phase, the output torque is suddenly increased because of the gear ratio change and deceleration of engine inertia due to the relatively larger inertia of vehicle. Also, the output torque is mainly dependant of the band brake torque during the

inertia phase. The significance of this important fact enables us to control the output torque by modulating the actuation pressure for engaging torque of the band brake.

B.3 Second Gear State

The transition condition from the inertia phase into second gear state is $\omega_{S2} = 0$ because the rotational speed of the second sun gear connected with the drum of band brake will approach zero. Substituting this constraint ($\dot{\omega}_{S2} = 0$) into Eq. **B.3** and rearranging $\dot{\omega}_{R1}$ in terms of $\dot{\omega}_T$ yields following four equations:

$$\dot{\omega}_T = D^{-1}\left[\frac{\Psi(1+r_1+r_2)}{1+r_2}T_T - T_{LOAD}\right] \tag{B.14}$$

where $D = \frac{r_2(1+r_1+r_2)}{1+r_2}(I_{S1}+I_T) + \frac{(1+r_2)}{\Psi(1+r_1+r_2)}I_{EQV} + \frac{\Psi r_2^{\,2}}{(1+r_2)(1+r_1+r_2)}I_{R1}$

$$T_B = \frac{1}{1+r_2}\left[r_1(I_{S1}+I_T) - \frac{r_2}{1+r_1+r_2}I_{R1}\right]\dot{\omega}_T - \frac{r_1}{1+r_2}T_T \tag{B.15}$$

$$T_{OUT} = \frac{1+r_2}{\Psi(1+r_1+r_2)}I_V\dot{\omega}_T + T_{LOAD} \tag{B.16}$$

$$\dot{\omega}_{OUT} = \frac{1+r_2}{\Psi(1+r_1+r_2)}\dot{\omega}_T \tag{B.17}$$

.

Appendix C

MATLAB/Simulink® Models and Parameters for HILS

C.1 MATLAB/Simulink® Models

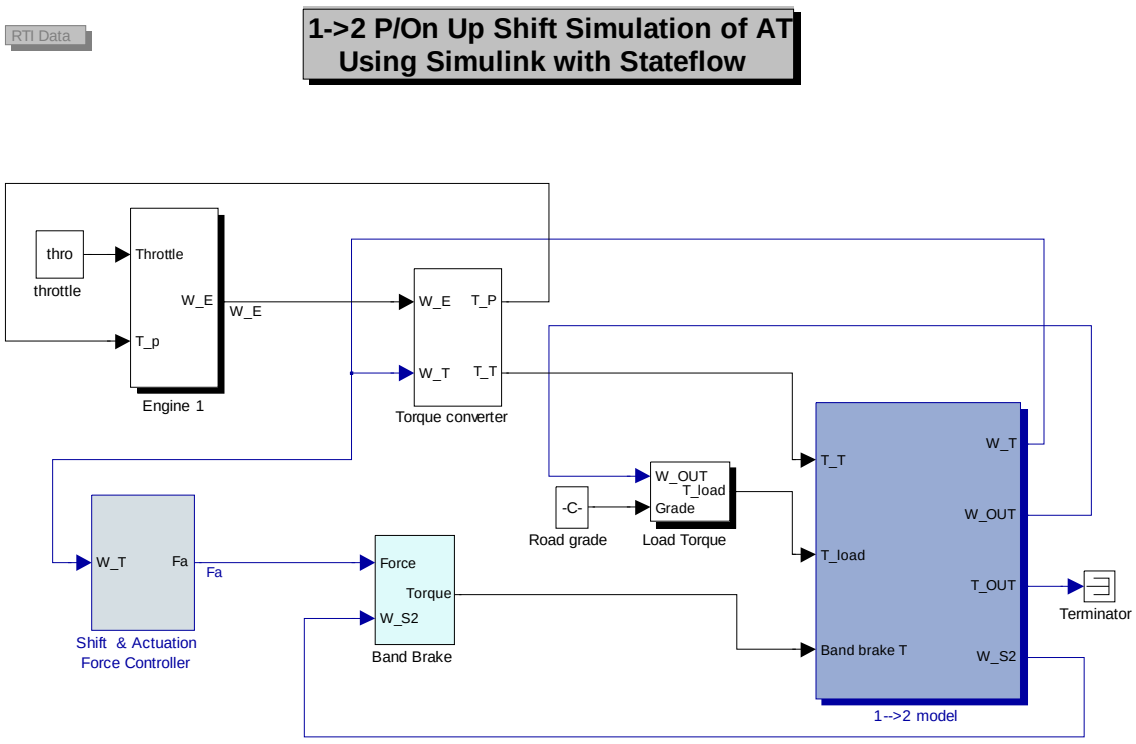

Figure C-1: Main MATLAB/Simulink® model for HILS

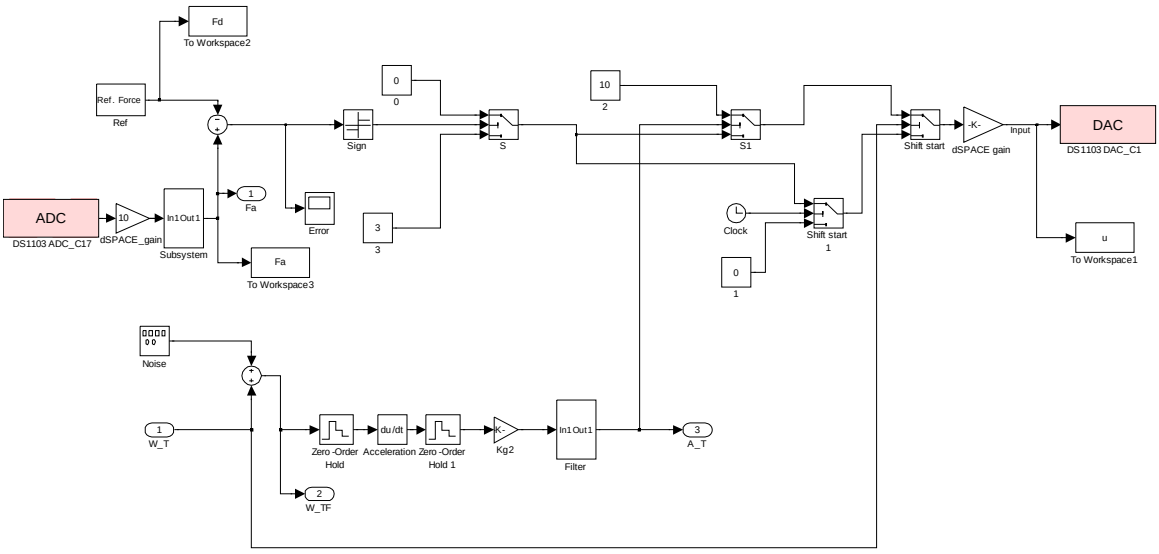

Figure C-2: AT shift and switching sliding mode controller

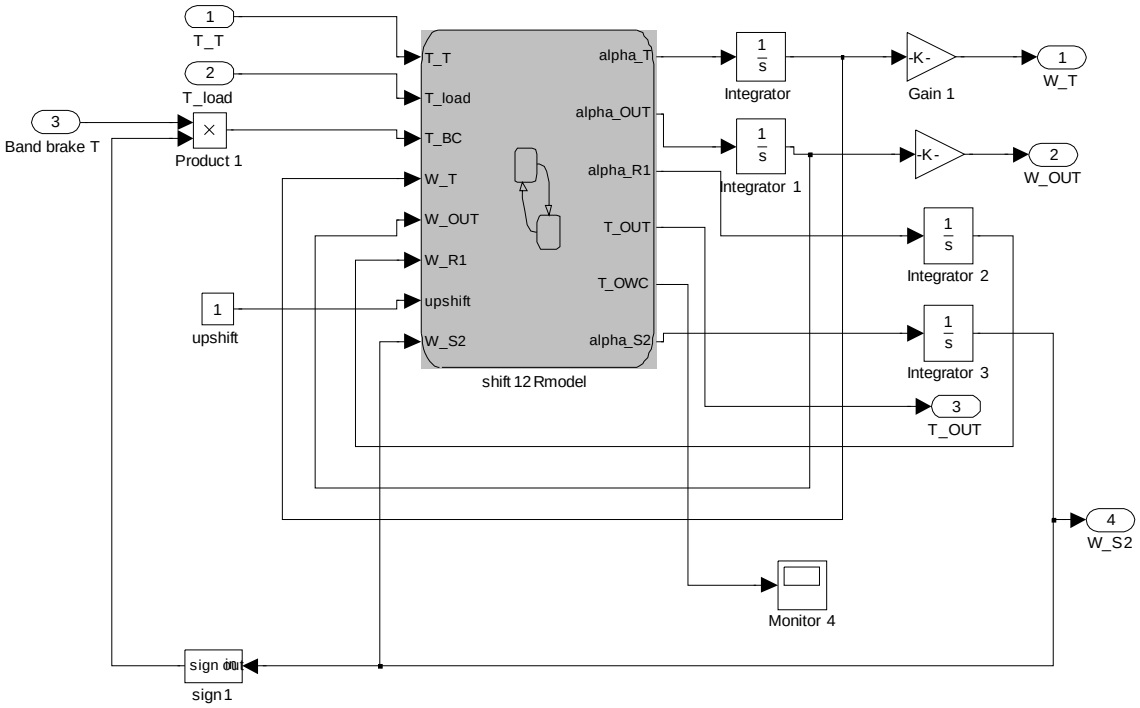

Figure C-3: Power on 1→2 up shift model with Stateflow® toolbox

C.2 Simulation Parameters for HILS

```
%---------- ----------Parameters for HILS of 1-2 up shift of AT ----------
%-------------------------------------------------  09/09/2008 ----------

%----------------------------------------  Ford 4F27E A/T ----------
%---------------------------------------------- Band Brake ----------
R=0.25;
Angle=340;
b1=0.14;
b2=-0.00372;
b3=0.0000228;
b4=-0.00000509;


%---------------------------------------- Planetary gear sets ----------

ZS1=49;                                  % No of gear tooth of first sun gear
ZR1=89;                                  % No of gear tooth of first ring gear
ZS2=37;                                  % No of gear tooth of second sun gear
ZR2=98;                                  % No of gear tooth of second ring gear
ZS3=100;                                 % No of gear tooth of transfer gear (drive)
ZR3=373;                                 % No of gear tooth of transfer gear (driven)
r1=ZR1/ZS1;                              % Gear ratio
r2=ZR2/ZS2;                              % Gear ratio
BE= ZR3/ZS3;                             % Final gear raio

%----------------------------------Load torque generation----------

r_tire = 0.3;                            % tire radius [m]
A_v = 2;                                 % frontal area of vehicle [m^2]
ro_a = 0.123;                            % air density [kg/m^3)
C_a = 0.33;                              % aerodynamic drag coefficient
M_v = 1500;                              % vehicle mass [kg]
mu_f = 0.01;                             % rolling resistance coefficient
grade = 0;                               % Load gradient [degree]

%----------------------------------Inertia (UNIT = Kg m^2)----------

IT=0.067;                                % turbine of T/C
IS1=0.0013;                              % first sun gear set
IR1=0.0027;                              % first ring gear set
IS2=0.008;                               % second sun gear
IR2=0.0107;                              % second ring gear
I_e = 0.1142;                            % engine

I_V = M_v*r_tire*r_tire;                 % vehicle
IEQV=I_V+BE^2*IR2;                       % equivalent vehicle
```

```
% 1st gear & torque phase

DET1=BE*(1+r1)*(IS1+IT)+((BE*r2^2)/(1+r1))*IS2+(IEQV/(BE*(1+r1)));

a121=(1/DET1)*(BE*(1+r1));
b121=(1/DET1)*(BE*r2);
c121 = 0;
d121=-(1/DET1);

ta121=r1*(IS1+IT)+(r2*(1+r2))/(1+r1)*IS2;
tb121=-r1;
tc121=-(1+r2);

toa121=I_V/(BE*(1+r1));
tob121=1;
oa121=1/(BE*(1+r1));

% Iertia phase during 1-2 shift

A12=r1*(IS1+IT)+(r2*(1+r2)*IS2)/(1+r1);
B12=((1+r2)*(1+r1+r2)*IS2)/(1+r1)+IR1;
C12=BE*(IS1+IT)-((BE*r2)*IS2)/(1+r2)+IEQV/(BE*(1+r1));
D12=BE*(1+r1+r2)/(1+r1)*IS2+BE*IR1+r1/(BE*(1+r1))*IEQV;
BC=(1/(A12*D12+B12*C12));
a122=BC*(BE*B12+r1*D12);
b122=BC*((1+r2)*D12-BE*B12);
c122=BC*(D12-BE*B12);
d122=-BC*B12;
a123=BC*(BE*A12-r1*C12);
b123=-BC*(BE*A12+(1+r2)*C12);
c123=-BC*(BE*A12+C12);
d123=-BC*A12;

toa122=(I_V/(BE*(1+r1)));
tob122=(r1*I_V)/(BE*(1+r1));
toc122=1;

oa122=1/(BE*(1+r1));
ob122=1/(BE*(1+r1))*r1;

% 2nd gear & torque phase

DET2=((BE*(1+r1+r2))/(1+r2))*(IS1+IT)+((1+r2)/(BE*(1+r1+r2)))*IEQV+((BE*r2^2)/((1+r2)*(1+r1+r
2)))*IR1;

a124=(1/DET2)*((BE*(1+r1+r2))/(1+r2));
b124=0;
c124=-(1/DET2)*((BE*r2)/(1+r2));
d124=-(1/DET2);

ta122=(1/(1+r2))*(r1*(IS1+IT)-(r2/(1+r1+r2))*IR1);
```

```
tb122=-(r1/(1+r2));
tc122=-(1/(1+r2));

toa123=((1+r2)/(BE*(1+r1+r2)))*I_V;
tob123=1;

oa123=(1+r2)/(BE*(1+r1+r2));

%-------------------------Initialize 1-2 model-------------------------
% 1: For light throttle
% 2: For medium throttle
% 3: For heavy throttle

sel=2;

switch sel
  case 1
    thro = 5;                                          % throttle opening
    init_eng_speed = 700*(pi/30);                      % initial engine RPM,
    init_alpha_T = 0 ;                                 % initial turbine acce
    S_S=120;                                           % shift start Wout (rpm)
  case 2
    thro = 10;                                         % throttle opening
    init_eng_speed = 700*(pi/30);                      % initial engine RPM,
    init_alpha_T = 0;                                  % initial turbine acce
    S_S=170;                                           % shift start Wout (rpm)
  case 3
    thro = 15;                                         % throttle opening
    init_eng_speed = 700*(pi/30);                      % initial engine RPM
    init_alpha_T = 0;                                  % initial turbine acce
    S_S=225;                                           % shift start Wout (rpm)
    otherwise
end

init_alpha_OUT = 0;

init_alpha_R1 = 0;

init_alpha_S2 = 0;


 %----static parameter : static engine map, torque converter static model,
% load data file for engine torque

Engine=[0   3 5 10  20  30  40  50  60  70  80 85;
500 71.6 89.6 108.6 113.0 115.4 117.8 120.2 122.6 125.0 127.3 128.5;
750 49.6 74.8 107.8 120.6 123.5 126.3 129.1 132.0 134.8 137.6 139.1;
1000 33.5 57.8 99.5 127.6 129.9 132.2 134.6 134.8 138.7 145.2 148.4;
1500 14.7 32.9 79.6 136.2 145.3 149.0 152.7 156.3 160.0 163.7 165.5;
2000 4.31 17.8 63.3 130.9 150.6 154.4 158.3 162.2 166.0 169.9 171.9;
2500 0 8.1 48.8 127.7 160.1 167.6 172.4 177.1 181.8 186.5 188.9;
3000 0  0.8 34.4 104.3 151.9 160.6 165.7 170.7 175.8 180.8 183.3;
```

```
3500 0  0.0 23.1 99.56 150.8 161.5 167.6 173.5 179.5 185.4 188.3;
4000 0  0.0 14.6 95.0 148.6 162.4 170.0 176.4 182.8 189.2 192.4;
4500 0  0.0 8.94 88.7 143.7 162.7 169.4 174.0 182.8 191.9 196.4;
5000 0  0.0 2.86 76.4 136.0 159.0 167.3 170.8 175.0 188.7 195.6;
5500 0  0.0 0.00 64.2 126.3 151.1 160.2 165.2 174.2 184.3 189.4;
6000 0  0.0 0.00 53.3 114.4 139.7 150.3 154.1 157.7 170.6 178.2];

% engine speed vector[rpm]
e_speed_v = Engine(2:size(Engine, 1), 1)';

% engine throttle opening vector
e_throttle_v = Engine(1, 2:size(Engine, 2));

%engine torque vector [Nm]
e_torque_v = Engine;

e_torque_v = e_torque_v(:, 2:size(e_torque_v, 2));

e_torque_v = e_torque_v(2:size(e_torque_v, 1), :);

%---------------------------------------- Torque converter ------------------------------------

%---------------Coefficients for regression equation of torque ratio

t1=2.072;
t2=-1.37;
t3=0.262;
t4=-0.192;

%-----------------------------------------------Coefficients for C-factor

speed_ratio = [0 0.1 0.2 0.3 0.4 0.5 0.6 0.7 0.75 0.8 0.85 0.9 0.92 0.94 0.95 0.96];

K_factor = [241.5 235.1 231.0 232.6 238.7 245.6 253.8 256.5 273.5 282.9 295 355.1 398.9 549.3
1200 5000];                          % unit: rpm/sqrt(ft.ib)

K_C = 1.37;                          % Correction factor for converting K-factor -> C-factor



%-----------------------------------Desired force trajectory-------------------------------

P_D = [-0.128 -0.146 -0.037 -0.256 -0.256 -0.256 -0.256 -0.256 -0.256 2 10,...
   32.227 34.698 38.654 38.892 39.496 41.235 39.771 41.492 41.675 41.858,...
   44.165 44.751 47.992 49.2 51.727 55.06 55.737 57.971 58.63 84.151,...
   86.536 92.047 89.172 89.191 88.715];                  % pressure unit: psi
```

Appendix D

Back Propagation Algorithm for TDNN-based Filter

STEP 1: Initialization

Generate training set by TDNN

Initialize weights of Wis and Wjs randomly

Stopping Criteria

STEP 2: **Forward Propagation**

Compute nets and zs for each hidden neuron, i=1,…,h:

$$net_s = \sum_{i=1}^{n} W_{is} x_i \quad \text{and} \quad z_s = f_1(net_s)$$

Compute netj and yj for each output neuron, j=1,…,m:

$$net_j = \sum_{s=1}^{h} W_{sj} z_s \quad \text{and} \quad y_j = f_2(net_j)$$

STEP 3: **Backward Propagation**

Compute δ_{2j} for each output neuron, j=1,…,m:

$$\delta_{2j}^{(k)} = (d_j^{(k)} - y_j^{(k)})\, f_2^{'}(net_j^{(k)})$$

Compute δ_{1s} for each hidden neuron, i=1,…h:

$$\delta_{1s}^{(k)} = f_1^{'}(net_s^{(k)}) \sum_{j=1}^{m} W_{js} \delta_{2j}^{(k)}$$

STEP 4: **Accumulate gradients over the input patterns**

$$\frac{\partial E}{\partial W_{sj}} = \sum_{k=1}^{P} (\delta_{2j} z_s)^{(k)} / \left\| z^{(k)} \right\|^2 , \quad \frac{\partial E}{\partial W_{is}} = \sum_{k=1}^{P} (\delta_{1s} x_i)^{(k)} / \left\| x^{(k)} \right\|^2$$

Note: For the numerical stability, the following rule for z and x vector is applied.

$$\left\| z^{(k)} \right\|^2 = \begin{cases} \left\| z^{(k)} \right\|^2 & if \ \left\| z^{(k)} \right\|^2 \geq 1 \\ 1 & if \ \left\| z^{(k)} \right\|^2 < 1 \end{cases}$$

STEP 5: **Update the weights**

$$W_{sj}^{(l+1)} = W_{sj}^{(l)} + lr\frac{\partial E}{\partial W_{sj}}$$

$$W_{is}^{(l+1)} = W_{is}^{(l)} + lr\frac{\partial E}{\partial W_{is}}$$

where, lr is the learning rate (0.005 and 0.1).

MATLAB Code

```
%-------Error Back Propogation Algorithm for TDNN-based filter---------
%%------------------ Generate the Input Patterns----------------------
close all
d=5;
x=delay_in(Td,d);

%---------------------Initialization ---------------------------------
RMS_Goal  = .001;
maxcycles = 100;
lr    = 0.0001;
hidden = 5;                                  % Number of hidden Layers

[inputs,patterns1]=size(x');
[outputs,patterns]=size(Td');

W1=0.5*randn(hidden,inputs+1);
W2=0.5*randn(outputs,hidden+1);

%------------------Back propagaion routine-----------------------------
[hidden,inputs1]=size(W1);
[outputs1,hidden1]=size(W2);
terms=outputs*patterns;                 %Number of error terms
RMS=zeros(1,maxcycles);                  %Output vector
LR=zeros(1,maxcycles);

X=[ones(1,patterns1);x'];
%h=1./(1+exp(-W1*X));                    %Hidden layer(Use logistic)
h=0.1*W1*X+0.5;                          %Hidden layer (Use linear)
H=[ones(1,patterns1);h];                %Input of output layer

output = W2*H;                           %Output (Use Linear function)

e = output-Td(length(Td)-5)';            %Error

RMS(1) = sqrt(sum(sum(e.^2))/terms);   % RMS Error
for i=2:maxcycles
   delta2 = e;                     % Differential is 1
```

```
    del_W2 = lr*delta2*H';
    delta1 = h.*(1-h).*(W2(:,2:hidden+1)'*delta2);
    del_W1 = lr*delta1*X';
    new_W1 = W1+del_W1;                          %Updating of weighting of hidden layer
    new_W2 = W2+del_W2;                          %Updating of weighting of output layer
    new_h = 1./(1+exp(-new_W1*X));
    new_H = [ones(1,patterns1);new_h];          % New output of hidden
    new_output = new_W2*new_H;                   % New output
    new_e = Td(length(Td)-5)-new_output;         % New Error
    RMS(i) = sqrt(sum(sum(new_e.^2))/terms);     % RMS Error

    if RMS(i)<RMS(i-1)
        W1 = new_W1;
        W2 = new_W2;
        e=new_e;
        h=new_h;
        H=new_H;

    end
end
RMS=nonzeros(RMS);
LR=nonzeros(LR);

%-----------------------------Post Processing--------------------------
semilogy(RMS);
ylabel('RMS Error');
xlabel('Cycles')
grid
xlabel('Time (sec)');
ylabel('Turbine angualr velocity(rad/s)');

X=[ones(1,patterns1); x'];
h=1./(1+exp(-W1*X));
H=[ones(1,patterns1);h];
output = W2*H;
figure;
plot(Td,'Red')
hold
plot(output,'Blue');
xlabel('Time (sec)');
ylabel('Turbine angualr acceleration (rad/s^2)');

%----------------------Sub Call Function for time delay matrix----------
function [xd] = delay_in(x,d);
[s,r]=size(x);
if r~=1
    error('The input vector must be a column vector.')
end
xd=[];
for i=1:d+1
    xd=[xd x(i:s-d+i-1)];
end
```

Appendix E

Miscellaneous Items for the PHP Actuator

E.1 Evaluation of Noise Level

To quantify the noise level of PHP actuator, sound pressure level (in short, SPL) is measured by using a microphone. Figure **E-1** shows the measurement locations for sound pressure level of PHP actuator. Based on the standard of SAE-J-1074 (Engine sound level measurement procedure), four microphones are located 50 cm from the longitudinal centers of the vertical planes forming the smallest rectangle to measure the sound pressure level. Air condenser type microphones (Larson-Davis laboratories model, sensitivity range of 4 ~ 8 mV/Pa) are used in this measurement. Figure **E-2** shows the noise test stand in anechoic chamber, where is a shielded room designed to attenuate sound waves (Vibrations and Acoustics Laboratory of University of Michigan). Background noise is not considered in this measurement. Driving pulse frequency for PHP actuator is fixed at 200 Hz and 60 Hz, corresponding to the fill and control frequency of PHP actuator, respectively. Measured sound pressures are shown in Figure **E-3** and Figure **E-4** . While sound pressures measured in each location show the nearly identical value (1.5 Pa) in both cases, sound pressures measured in parallel with PHP actuator (RH, LH) slightly higher, which implies that the sound energy is more intense in horizontal axis.

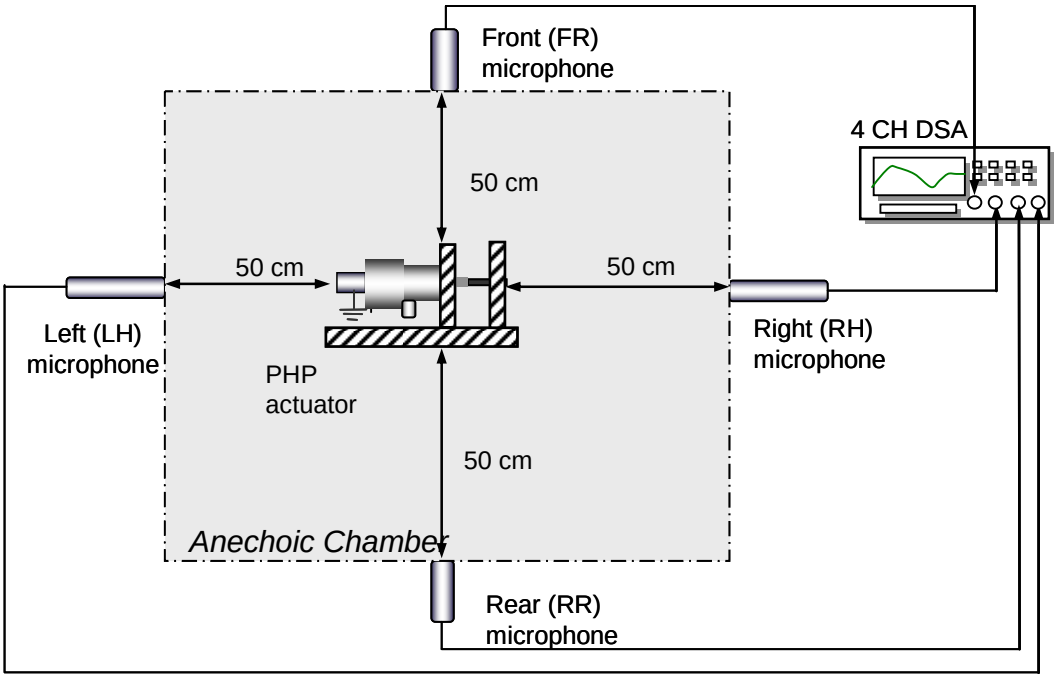

Figure E-1: Measurement location for sound pressure level of PHP actuator

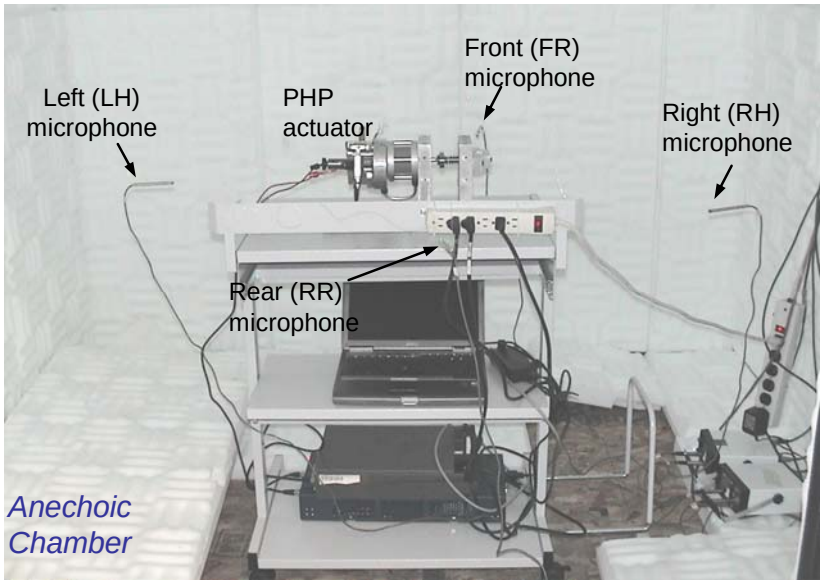

Figure E-2: Overall noise test stand located in anechoic chamber

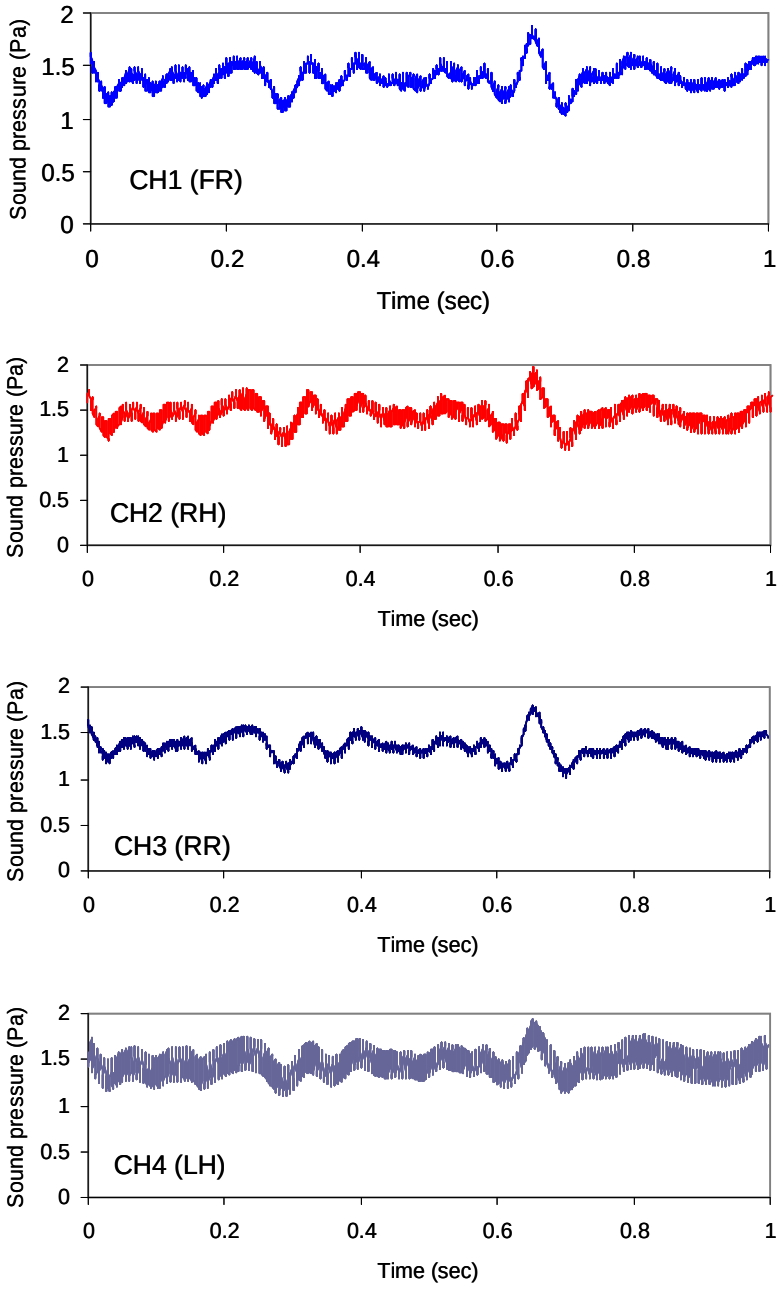

Figure E-3: RMS sound pressures measured in four measurement locations (200 Hz)

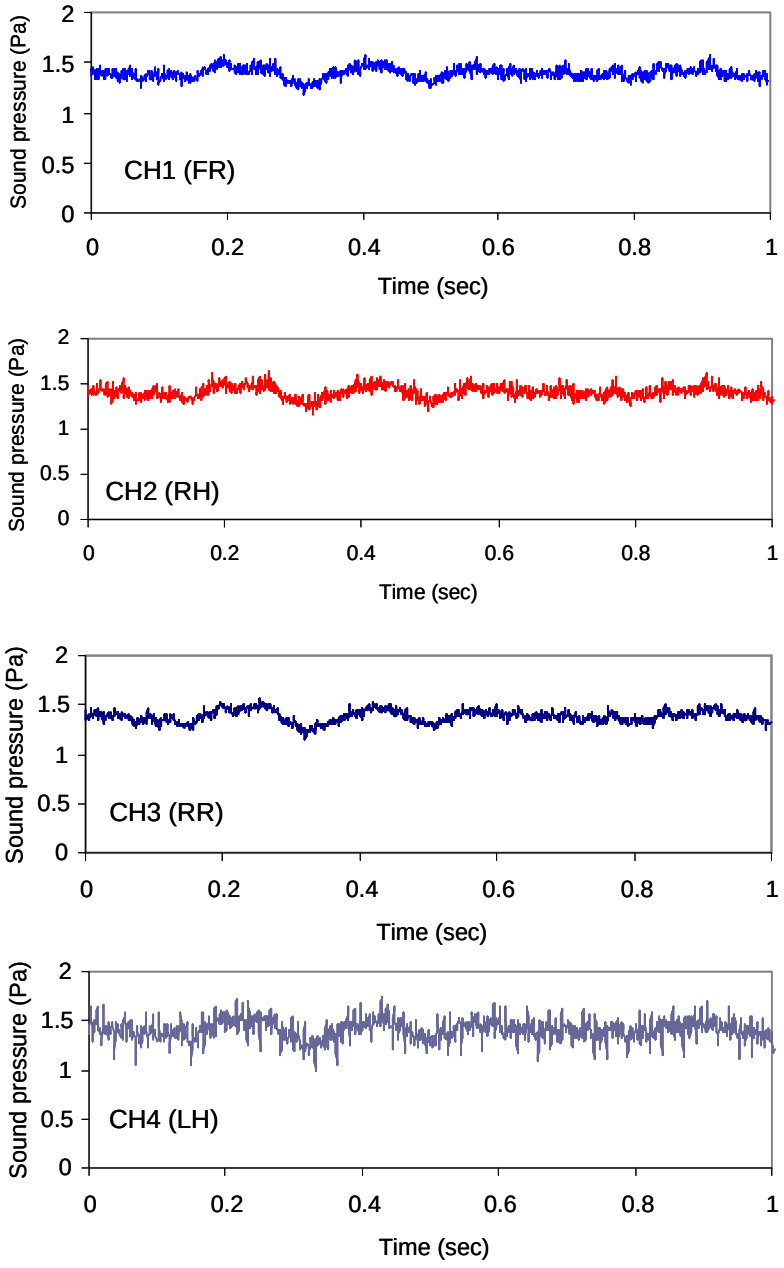

Figure E-4: RMS Sound pressures measured in four measurement locations (60 Hz)

Sound pressure level (SPL) can be present by a logarithmic measure of the RMS pressure of a sound relative to a reference value. As a result, it's measured in decibel as follows;

$$SPL = 10 \cdot Log_{10}\left[\frac{{P_{RMS}}^2}{{P_{ref}}^2}\right] \quad \text{dB} \tag{E.1}$$

where P_{RMS} is the measured RMS sound pressure, P_{ref} is the reference sound pressure. The commonly used reference sound pressure in air is $20\times10^{-6}\ Pa$, which is usually considered the threshold of human hearing. Then, the average level of four measurements can be determined by following Eq. **E.2**.

$$SPL = 10 \cdot Log_{10}\left[\left(10^{\frac{LH}{10}} + 10^{\frac{RH}{10}} + 10^{\frac{FR}{10}} + 10^{\frac{RR}{10}}\right)\Big/ 4\right] \quad \text{dB} \tag{E.2}$$

where $LH, RH, FR,$ and RR represent the sound pressure level measured by left, right, front, and rear microphones. Averaged sound pressure levels with respect to two driving pulse frequencies are illustrated in Figure **E-5**. Sound pressure level of PHP actuator can exceed 90 dB in both cases.

FFT analysis result for 200 Hz is also shown in Figure **E-6** . Since the basic noise source of PHP actuator is caused by contacting reed valves with stoppers, there are periodic peaks in the power spectrum. These noises are called structure-borne noise. Accordingly, adding damping materials in reed valve can be one of the feasible methods to reduce the SPL of PHP actuator.

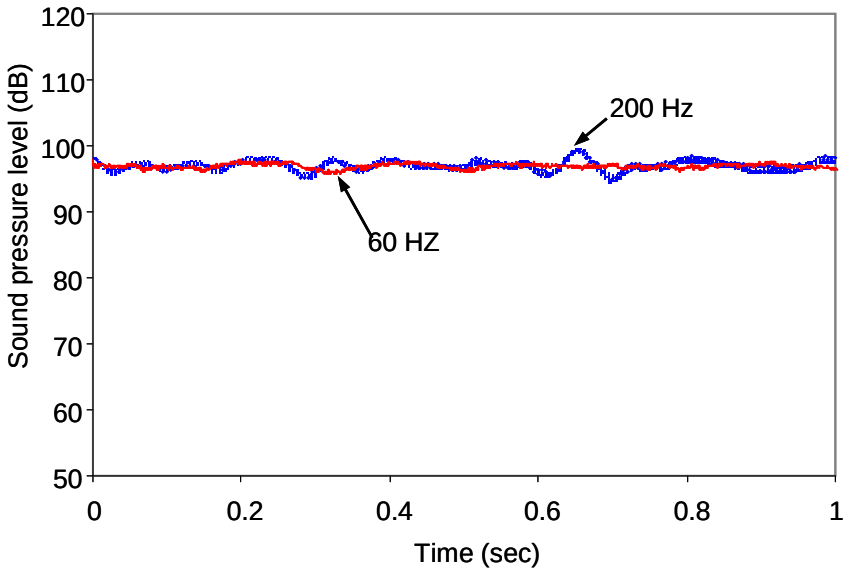

Figure E-5: Evaluation results of sound pressure level about two driving frequencies

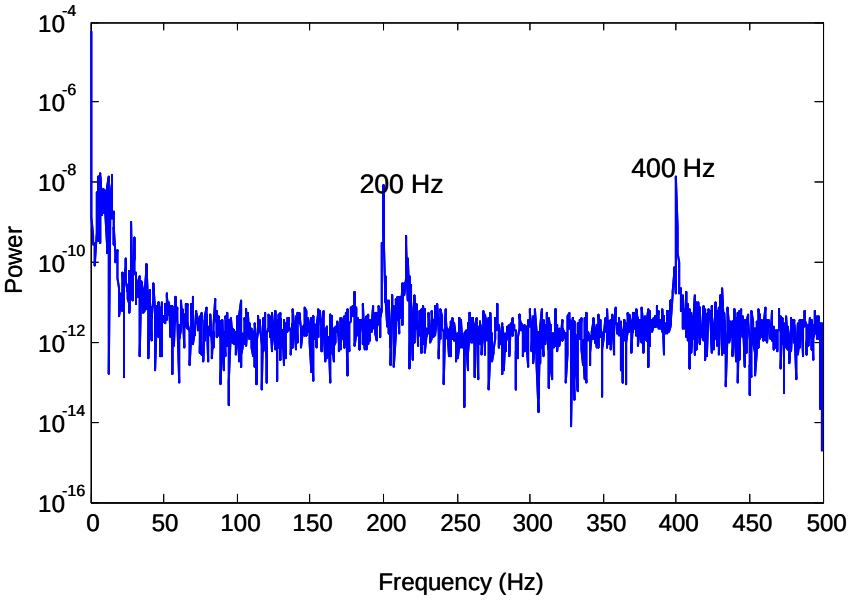

Figure E-6: FFT analysis result for driving pulse frequency of 200 Hz

E.2 Self-locking Capability

In friction element actuation system, there should have a self-locking mechanism to prevent the slippage. A typical available locking method is to apply much higher pressures (about 1.2 MPa) than actuation pressures (about 0.4 MPa). As a result, generated dead-head pressure of the prototype has to be enhanced. For instance, the loss of compliance in pumping chamber should be minimized by using more advanced design. Compared with the conventional actuation systems, there is an additional advantage in PHP actuator. While the power of PHP actuator is off after finishing the shift, the generated actuation force can still be remaining for locking due to the one-way valve (i. e., reed valve), as shown in Figure **E-7** . The duration of self-locking is sufficient for the next shift event.

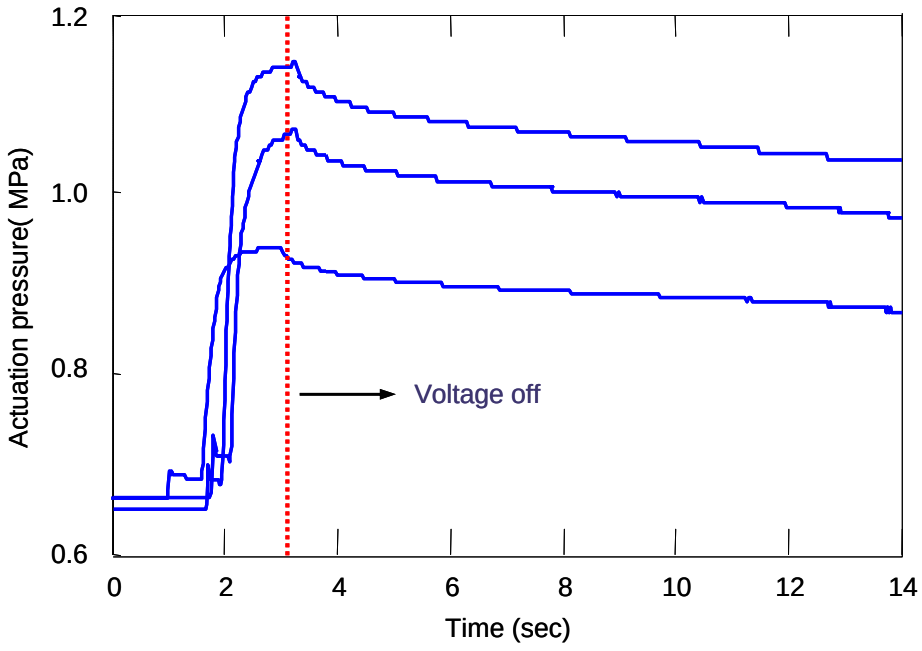

Figure E-7: Self-locking performance with respect to different actuation pressures

E.3 Flow Rate Performance with Check Valve

In fact, the operation of a check valve is identical to the reed valves. At relatively low frequency ranges (below 200Hz), the commercial check valve with more reliable durability can replace the reed valve. To evaluate the feasibility of the check valve as an substitute of reed valve, different one-way valve assemble is made by Lee company's check valve and its flow rate performance was evaluated, as shown in Figure **5-8** and Figure **5-9** , respectively.

(a) with check valve (b) with reed valve

(c) Detail A (Model: Lee®)

Figure 5-8: Different one-way valve assembles

Due to the narrow bandwidth of the check valve, flow rate cannot recover after some critical frequency ranges. For instance, flow rate becomes dropped at 150 Hz in case of the accumulator pressure of 0.7 MPa, as shown in Figure **5-9**. Compared with the reed valve presented in Chapter **2**, flow rate was also sensitive to the variation of the accumulator pressures.

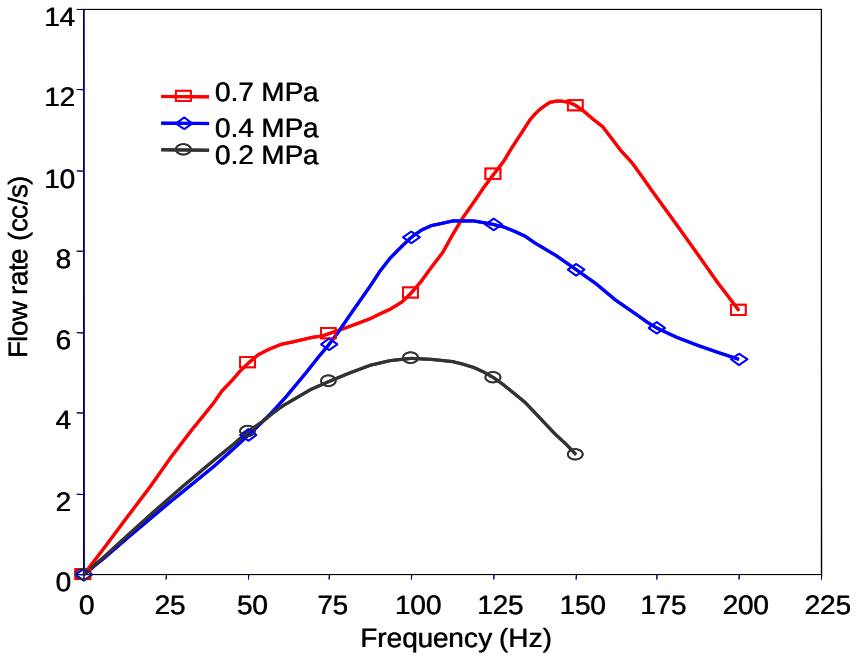

Figure 5-9: Flow rate with respect to different accumulator pressures

.

VITA

Gi-Woo Kim

Gi-Woo Kim received the B.S degree and M.S. degree in mechanical engineering department from the Inha University, Inchoen, South Korea, in 1994, and 1996, respectively. *Prior to* coming to the Pennsylvania State University in 2004, he worked for the Hyundai Motor Company, South Korea, from 1996 to 2004, serving as senior research engineer. His professional background includes the study of power-train simulation and control, fluid power systems, and smart material structures. His research area of expertise is transmission technologies, with an emphasis on automatic transmissions. During his time at Hyundai, he was awarded for a prize of excellence of achievements in 2003. To gain more strong academic background, combined with hands-on experience in industry field, he has been pursuing Ph. degree at the Pennsylvania State University since 2004. His research has been focusing on the development of advanced actuation systems featuring piezoelectric-hydraulic pump. Throughout his Ph. D program, he has published four conference papers, submitted two journal papers, and applied one patent. After completion of his degree, he will continue to work on his on-going research program with Ford Motors, serving as post doctoral fellow at the University of Michigan, Ann Arbor.